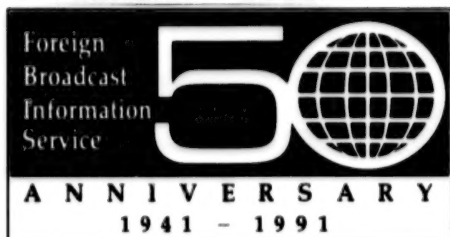


JPRS-JST-91-006
4 FEBRUARY 1991



JPRS Report

Science & Technology

Japan

**33RD SPACE S&T CONFERENCE
PART II**

JPRS-JST-91-006
4 FEBRUARY 1991

SCIENCE & TECHNOLOGY
JAPAN

33RD SPACE S&T CONFERENCE
PART II

906C3836 Tokyo DAI33KAI UCHU KAGAKU GIJUTSU RENGO KOENKAI KOENSHU in Japanese
31 Oct-2 Nov 89 pp 1-883

[Selected papers presented at the Proceedings of the 33rd Space Sciences and
Technology Conference held in Aichi Prefecture 31 Oct-2 Nov 89]

CONTENTS

Development of Feeder Command Receiver for ETS-VI [Ryoji Tanaka, Toyohito Okuyama, et al.].....	1
High-Precision Antenna Pointing Mechanism for ETS-VI [Eiichi Tsukada, Yoichi Kawakami, et al.].....	4
Development of K-Band Transponder System for Intersatellite Communications [Ryoji Tanaka, Shozo Nakasato, et al.].....	8
Effect of Soft Vibration on Direction of ETS-VI Antenna Reflector [Masazumi Ueha].....	13
Thermal Design of Antenna System for ETS-VI [Katsuhiko Nakajima].....	16
Antenna Pointing Control System for ETS-VI [Yoichi Kawakami, et al.].....	20
Structure of Multibeam Antenna for ETS-VI [Isao Otomo, et al.].....	24
Traveling Wave Tube Amplifier for ETS-VI [Hideo Makijima, Katsuhiko Yamamoto, et al.].....	27
Multibeam Transponder for ETS-VI [Masayoshi Tanaka, et al.].....	31

Satellite Switch for ETS-VI [Katsuhiro Araki, et al.].....	36
Development of Antenna Expansion Mechanism for S-Band Intersatellite Communications [Masato Tanaka, Shigeru Kimura, et al.].....	39
On-Orbit Calibration of Optical Sensors [Hideo Hino, Mitsuru Takei, et al.].....	42
Performance of Radiometer for ERS-1 Optical Sensor [Hideo Hino, Mitsuru Takei, et al.].....	47
Countermeasures Against Disturbances Caused by Optical Sensor Cooler [Hideo Hino, Mitsuru Takei, et al.].....	51
Development of Focusing Mechanism for ERS-1 Optical Sensor [Mitsuru Takei, Hiroki Ono, et al.].....	55
Conceptual Design for Advanced Microwave Radiometer [Akimichi Nitta, Yasuyuki Ito, et al.].....	58
System Parameters for Satellite-Mounted AVNIR [Go Masuda, Kiyotaka Yashiro, et al.].....	62
Examination of Mechanical System for AVNIR [Go Masuda, Kiyotaka Yashiro, et al.].....	65
Deployment Mechanism for Advanced Microwave Scanning Radiometer [Akimichi Nitta, Yasuyuki Ito, et al.].....	68
Ion Engine System for ETS-VI [Kenichi Kajiwara, Kazuo Sato, et al.].....	72
Development of Power Supply for ETS-VI Ion Engine [Kenichi Kajiwara, Kazuo Iwanami, et al.].....	75
Development of Ion Engine Thruster Control Units [Kenichi Kajiwara, Kazuo Iwanami, et al.].....	79
Propulsion Performance of Hall-Type Ion Thruster [Kimiya Komurasaki, Satoshi Ichikawa, et al.].....	83
Basic Experiments on Microwave Discharge Ion Thruster [Toshiaki Yasui, Hirokazu Tawara, et al.].....	86
Microwave Discharge Ion Engine [Yasuo Horiuchi, Arata Sashima, et al.].....	89
Propellant for 150 mN Ion Thruster [Hideki Yoshida, Hiromichi Kouchi, et al.].....	92

Characteristics Test on 150 mN Ion Thruster [Hideki Yoshida, Hiromichi Kouchi, et al.].....	97
Basic Experiments With High-Powered Stationary Plasma Jet [Takahisa Sakakibara, Hirokazu Tahara, et al.].....	100
Performance, Electromagnetic Field Distribution of Microwave- Heating Plasma Jet [Masao Yasufuku, Hirokazu Tahara, et al.].....	103
Discharge Mechanism of Semistationary MPD Thruster [Masanori Sasuki, Hirokazu Tahara, et al.].....	106
Characteristics of Electromagnetic Acceleration Using External Magnetic Field [Akihiro Samune, Yoshihiro Arakawa].....	109
Ignition Characteristics of MPD Arc Jet Thruster [Kenko Otsuka, Kazuo Uematsu, et al.].....	112
EM Development of MPD Thruster, Propellant Supply System for Mounting on SFU [Kyoichiro Suzuki, Hirokazu Suzuki, et al.].....	115
Correlation Between MPD Propulsion Characteristics, Flow Field [Takayuki Nakayama, Tatsuya Yoshida, et al.].....	119
Numerical Analysis of Axially Symmetric Flow in MPD Thruster [Osamu Kimura, Toshitaka Fujiwara].....	123
Specified Thrust Characteristics of 1 kW DC Arc Jet [Tetsuya Yamada, Kyoichito Miyakogi, et al.].....	126
Experimental Research on Low-Power Arc Jet Thruster [Yasuo Kawai, Osamu Kimura, et al.].....	129
Extended Operational Characteristics of Low-Input Arc Jet Thruster [Yuzuru Yasuda, Kenichi Onoue, et al.].....	132
Vibration Characteristics of 3.5 m ϕ Antenna for ETS-VI [Shokichi Misawa, Akira Meguro, et al.].....	135
Extension Test Method for ETS-VI Antenna Module [Akira Meguro].....	139
Ejection, Extension Characteristics of ETS-VI Primary Antenna Reflector [Akira Meguro, Hitoshi Miyoshi, et al.].....	143
Extension Test Method for 5 m ϕ Satellite Antenna [Yasumasa Hisada, Satoshi Kusama, et al.].....	147

Development of Synthetic Aperture Radar Antenna Retention, Release Mechanism [Hideo Hino, Mitsuru Takei, et al.].....	150
Orbital Extension Characteristics of ERS-1 Synthetic-Aperture Radar Antenna [Hideo Hino, Mitsuru Takei, et al.].....	153
Creation of Data Base for Research on Functionally Gradient Materials [Akio Moro, Yoshisato Ishibashi, et al.].....	156
High-Temperature Evaluation Test of Thermal Insulation Materials [Akinaga Kumakawa, Masaki Sasaki, et al.].....	159
Effects of Electron Beam on Polyimide, Polyetherimide [Ken Abe, Akira Onishi, et al.].....	163
Research on Deterioration of Paint, Bonding Agent for Space Use [Norihiko Kikuyama, Hideo Oba, et al.].....	166
Deterioration of Composite Resin Materials Caused by Atomic Oxygen [Takayuki Kamiyama, Toshi Sakakibara, et al.].....	169
Deterioration of Composite Materials at Low Temperatures [Seiichi Matsuoka, Akinori Nagao, et al.].....	172
Hydrogen Embrittlement of Ni-Radical Alloy for Liquid Hydrogen Fueled Rocket Engine [Kiyoshi Yokokawa, Yoshio Yamada].....	175
Research on Neutron CT Image Processing Method Using Small Cyclotron [Kazuo Maeno, Yutaka Hanaoka, et al.].....	179
Development of 32 GHz Traveling-Wave Tube Power Amplifier [Ryoji Tanaka, Toneo Kawanishi, et al.].....	182
Test Manufacture of 32 GHz Traveling-Wave Tube Power Amplifier [Ryoji Tanaka, Toneo Kawanishi, et al.].....	186
Thermal Analysis of Radiation-Cooled Four-Stage Collector for TWT [Susumu Atsukawa, Masao Kato, et al.].....	189
Study of PPM of 22 GHz TWT for Satellite-Mounted DBS [Masao Kato, Susumu Atsukawa, et al.].....	192
Precision Acquisition, Tracking System for Laser Communications Between Satellites [Hiroshi Arikawa, Yasumasa Kubota, et al.].....	195

Concept for Intersatellite Laser Communications [Hiroshi Arikawa, Yasumasa Kubota, et al.].....	199
Checkout System for Multibeam Satellite-Mounted Transponder [Koji Horikawa, Katsuhiko Araki, et al.].....	203
Command Decoder for Loading on Future Scientific Satellite [Tomonao Hayashi, Takamoto Ninomiya, et al.].....	208
Development of Aurora TV Camera for Scientific Satellite 'Akebono' [Takashi Oguchi, Eisuke Kaneda, et al.].....	212
Despun Mirror for 'Akebono' Satellite Imaging System [Kenji Hiraishi, Haruki Ayada, et al.].....	215
Development of Optical Communications Acquisition, Tracking System [Kenichi Takahara, Shitta Niimiya, et al.].....	218
Development of Antenna Directional Control System for Earth-Orbiting Spacecraft [Shinichi Otani, Tomomi Koseki, et al.].....	221
Development of Failure Resistance Onboard Processor [Keiichi Yamasaki, Toshio Kikuchi].....	225
Development of MUSES-A Attitude, Orbit Control Processor [Takamoto Ninomiya, Akito Watanabe].....	228
Development of Small Data Handling Unit for Satellite Use [Yoshinari Minami, Tadaaki Morimura, et al.].....	231
Rocket-Mounted Ku-Band TV Transmission Unit [Tomoki Hayashi, Koji Yokoyama, et al.].....	234
Current State of Development of Liquid Apogee Propulsion System (LAPS) [Akira Takano, Hideyuki Kobayashi, et al.].....	238
Pop Tests of Apogee Engine for ETS-VI [Yukio Kuroda, Makoto Tadano, et al.].....	240
Development of Liquid Apogee Engine for ETS-VI [Kazuo Kusaka, Tatsuo Kumagai, et al.].....	244
Extended Test of Mixed-Fuel Reproduction Cooling Engine [Hiroshi Miyajima, Shuichi Ueda, et al.].....	248
Dynamic Characteristics of LE-7 Liquid Acid Pump [Takashi Shimura, Mitsuo Watanabe, et al.].....	251
Simulation of LE-7 Activation Transient Characteristic (V) [Akio Kanmuri, Takeshi Karita, et al.].....	254

Model for 'Ionosphere Hole' Generation With Rocket Exhaust Products [Yoshiki Yamagiwa, Yoshio Ishikawa, et al.].....	257
Dynamic Characteristics of CW Laser Thruster [Hideki Moriai, Hiroshi Ohashi].....	261
Supersonic Flaw-Detecting Method for Exfoliation Between H-II SRB Liner, Propellant [Morio Shimizu, Katsuya Ito, et al.].....	264
Combustion Thrust Characteristics of Airbreathing Solid Rocket Motor [Akihiro Eguchi, Yutaka Kaneko, et al.].....	267
Combustion of Carbohydrates, Nitrogen Oxide in Solid Rocket Fuel [Ryoshi Moriyasu, Koichi Hayashi, et al.].....	270
Combustion Characteristics of Metal Added Hydrocarbon Rocket (III) [Hiroshi Sakamoto, Kazuo Sato, et al.].....	273
Development of Gas Jet Device for H-II Rocket [Akira Takano, Hideyuki Kobayashi, et al.].....	276
Development of Hydrazine Decomposition Catalyzer for Gas Jet Thruster [Akira Takano, Hideyuki Kobayashi, et al.].....	281
Development of Anilineless Hydrazine Anhydride for Gas Jet Thruster [Akira Takano, Hideyuki Kobayashi, et al.].....	284

Development of Feeder Command Receiver for ETS-VI

906C3836 Tokyo DAI33KAI UCHU KAGAKU GIJUTSU RENGO KOENKAI KOENSHU in Japanese
31 Oct-2 Nov 89 pp 468-469

[Article by Ryoji Tanaka, et al., National Space Development Agency; and
Toyohito Okuyama, et al., NEC Corp.]

[Text] 1. Introduction

This article describes the feeder command receiver (FL-CMDRX) that has been developed for the Engineering Test Satellite VI (ETS-VI). The FL-CMDRX is a component of the feeder link system (FLCE) for the experimental intersatellite communications equipment. It has been developed for ETS-VI use, based on the designs of the Ka-band tracking receiver and S-band TTC transmitter-receiver previously developed. Since the FL-CMDRX is an experimental apparatus, its development was implemented in such a form that an engineering model (EM) could be refurbished to make an operational model (OM). Development testing has already been completed.

2. Function

The FL-CMDRX is a Ka-band command receiver used during intersatellite communications experiments. It has the following functions:

- (1) It acquires a Ka-band ascending circuit command signal from the ground via an input filter and demodulates phasing.
- (2) It further PSK-demodulates the demodulated command base band signal and outputs it to the central unit as a PCM signal.
- (3) It has a telemetry output function to monitor an ON/OFF function and an operated condition by command.

A flow chart of the FL-CMDRX's functions is given in Figure 1.

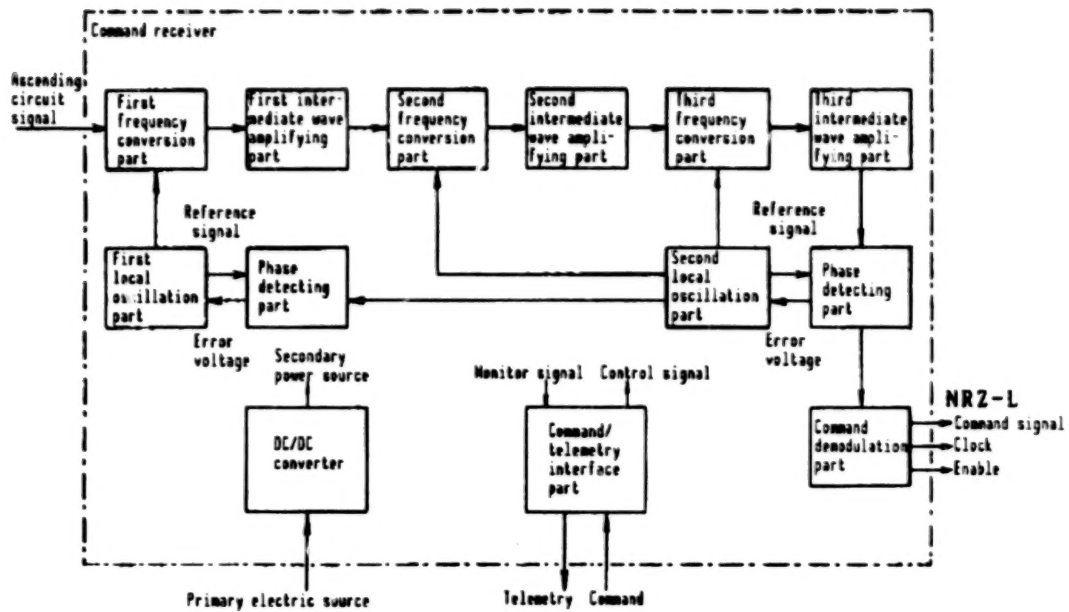


Figure 1. Flow Chart of FL-CMDRX Functions

3. Performance

The FL-CMDRX's primary performance characteristics are shown in Table 1 which also compares its specification values with actual development test results.

Table 1. Primary Performance Characteristics of FL-CMDRX

No.	Item	Specification value	Development test results
1.	Received frequency	29485.0 MHz ± 1 MHz	29485.0 MHz +2.9 MHz -4.4 MHz
2.	Dynamic range	-68 dBm--108 dBm	-60 dBm--114 dBm
3.	Received input signal sweeping speed	100 kHz/sec max	350 kHz/sec max
4.	Noise figure	Less than 13 dB (There is no LNA)	11.8 dB max
5.	Receiver input SWR	Less than 1.3	1.19 max
6.	Squelch level	Less than -112 dBm	-115 dBm max
7.	Optimum synchronizing frequency fluctuation	Less than ± 20 ppm	+3.3 ppm, -6.1 ppm max
8.	PLL bandwidth (2 BL)	More than 3 kHz	8.8 kHz min
9.	AGC bandwidth	More than 30 Hz	44 Hz min
10.	Command synchronization acquisition time	Less than 128 msec	100 msec max
11.	Command synchronization release time	Less than 47 msec	21 msec max
12.	Power consumption	Less than 8 W	5.3 W max
13.	Weight	Less than 3.19	2.7 kg (foam materials are excluded)

Figure 2. [not reproduced] is a photograph of the FL-CMDRX.

4. Characteristics

The FL-CMDRX has the following characteristics:

- (1) A triple superheterodyne system is adopted to ensure a wide acquisition frequency range for received input signals.
- (2) Fluctuations of the optimum synchronizing frequency are held down by providing temperature compensation.
- (3) Reductions in dimensions, weight, and power consumption were achieved through the use of HIC and MIC.

5. Conclusion

As mentioned above, the development test of the FL-CMDRX has been completed. The electronic performance test (temperature test included) and mechanical inspection have confirmed that the initially targeted performance and specification values were fully satisfied. It is planned that, after the completion of a system test, it will be refurbished to make it capable of withstanding the launch environment and will be quality certified as an on-board model.

Finally, thanks are due to those persons who kindly provided guidance in developing this device.

High-Precision Antenna Pointing Mechanism for ETS-VI

906C3836 Tokyo DAI33KAI UCHU KAGAKU GIJUTSU RENGO KOENKAI KOENSHU in Japanese
31 Oct-2 Nov 89 pp 470-471

[Article by Eiichi Tsukada, Human Interface Laboratories, NTT; Yoichi Kawakami, Radio System Laboratories, NTT; and Shojiro Miyake, Applied Electronics Laboratories, NTT]

[Text] 1. Introduction

A satellite-mounted multibeam communications system cannot dispense with an APM (antenna driving mechanism) that mechanically controls the driving of the reflector itself. Such a device is necessary to compensate for thermal deformation, which increases due to the enlargement of the antenna's caliber and the number of antennas mounted; to compensate for initial operating errors, and to secure a very high degree of antenna pointing precision.¹ An engineering model of an APM designed for an antenna system with a single beam width of about 0.3° and to make it possible to achieve driving control for a single unit at a level of precision of 10^{-3} , has been manufactured on an experimental basis and has been subjected to various tests. It has satisfied all its requirements. This article reports on the results of these tests.

2. Structure of Mechanism

The APM's basic specifications are shown in Table 1 and its external view is shown in Figure 1 [not reproduced]. The APM has the following characteristics:

- (1) The actuator uses a movable magnet system that can oscillate the coil assembly and magnetic circuit assembly. The mechanism's precision is improved by adopting a direct driving system that transmits the actuator's displacement to the reflector directly and not via a reduction gear.
- (2) The supporting mechanism is of a gimbal-mounted structure that can rotate around two D/C axles. It is designed to be lubrication-free. Its bearing part consists of four elastic bearings that utilize the flexibility of a cross spring in an attempt to extend its life and enhance its reliability in orbit. In particular, the elastic bearing is an integrated processed product made of a titanium alloy, the main structural material for the APM proper, so that it

Table 1. Basic Specifications of Satellite-Mounted APM

Item	Specification
Object to be driven	Auxiliary reflector
Load mass	About 2 kg
Load inertia	About 0.12 kg/m ²
Driving direction	DC/AC two axis (N-S and E-W)
Driving angle range	More than $\pm 1.25^\circ$ (N-S) More than $\pm 0.75^\circ$ (E-W)
Response frequency	0.2 Hz
Drive resolution	Within 0.002°
Maximum driving torque	More than 0.02 Nm
Maximum power consumption	Under 1 W
Interference between driving shafts	0.004°
Dimensions	250 x 250 x 85 mm
Weight	3.9 kg
Allowable load at locking time	More than 300 kg
Temperature range used	-40°C~+90°C
Vibrational environment conditions (random load)	19.5 Grms (2 min/axis)

is possible to provide stable support against the thermal cycle environment of a stationary orbit.

(3) The APM features a position feedback system that incorporates a noncontact displacement sensor, which has functions to sense the initial condition prior to operation and to return from an abnormal state to the normal condition.

(4) The APM has a built-in elastic plate pin lock hold/release mechanism, which functions to fix and protect the APM against vibration caused by launching and to release it after reaching orbit. This particular hold/release mechanism, which has a double tapered structure, was adopted after examining the holding function in terms of fixing position, fixing power, load reception and loosening, and the steady release function.

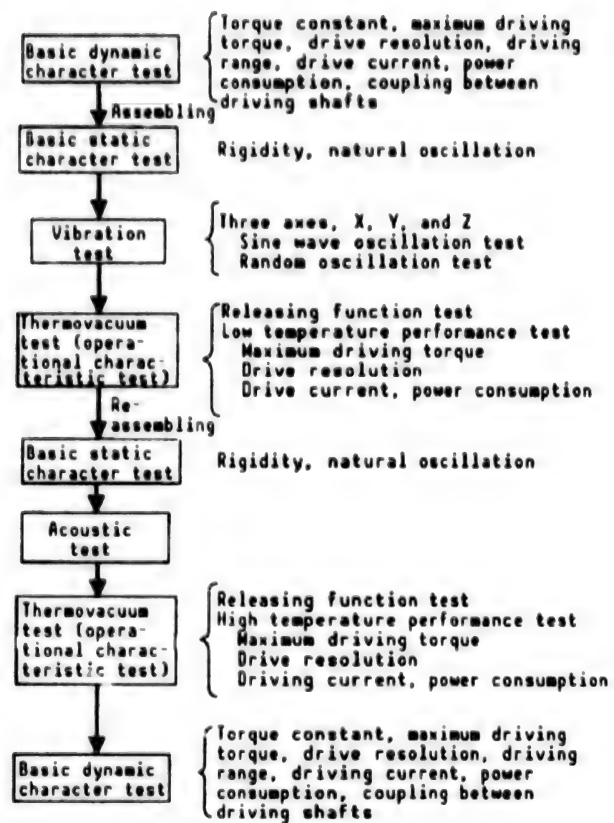


Figure 2. Test Flow and Principal Items

3. Character Test

The performance test and environmental test of a single unit of the APM were conducted according to the test flow diagram shown in Figure 2.

A gravity compensation device (canceler) was used in the dynamic character/performance characteristics test. The basic characteristics test was conducted at normal temperature in the atmosphere as a proving test and the thermovacuum test was conducted as a performance confirmation test within a specified temperature range in a vacuum chamber.

The performance characteristics test confirmed that the maximum driving torque was more than 0.025 Nm at a current of 0.138 A. The drive resolution was under 0.0001°, the drive ranges of the axes were 1.3° and 0.8°, and the tracking angle range, calculated from the beam deflection sensitivity, was more than 0.25°.

The static rigidity in the directions of three axes when locked was as high as 1.5~5.4 times that of the existing mechanism.^{2,3} The release function test in the thermovacuum chamber, which was conducted after the successful conclusion of the vibration test, confirmed that the lock was released exactly.

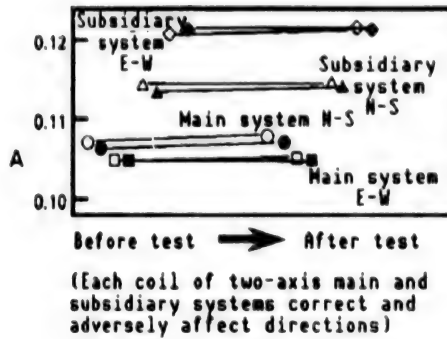


Figure 3. Changes in Torque Before and After Environmental Test
(Current difference to obtain driving torque of 0.02 Nm)

The torque variance of each drive coil before and after the environmental test is shown in Figure 3. Since the variance is as small as ± 0.5 percent, the environmental test confirmed that this presents no problems.

4. Conclusion

A compact, light APM with low power consumption for use on a satellite has been developed. This driving mechanism will be mounted on ETS-VI for use in multibeam satellite communications experiments.

References

1. Tsukada, et al., "Examination of Direct Drive-Type Antenna Pointing Mechanism," Space Science Technology Joint Lecture Meeting, No 28, 1984, p 330.
2. Ibid., "Satellite-Mounted High Precision Antenna Pointing Mechanism," Precision Engineering Society, 1986 Spring Convention, p 208.
3. Ibid., "Development of Antenna Control Device for Large Capacity Communications Satellite," Machinery Society, BULLETIN OF THESES, Vol 52 No 481, C 1986, p 2416.

Development of K-Band Transponder System for Intersatellite Communications

906C3836 Tokyo DAI33KAI UCHU KAGAKU GIJUTSU RENGO KOENKAI KOENSHU in Japanese
31 Oct-2 Nov 89 pp 472-473

[Article by Ryoji Tanaka, et al., National Space Development Agency; and Shozo Nakasato, et al., NEC Corp.]

[Text] 1. Introduction

An electric model (EM) of the experimental K-band intersatellite communications equipment (transponder system) to be mounted on Engineering Test Satellite VI (ETS-VI), which is scheduled to be launched in 1993, has been developed. This article will report on the realizability of the experimental intersatellite communications mission, based on the development test results that have been made available at this time.

2. Structure

This transponder system consists of two subsystems, feeder link equipment (FLCE) for intersatellite communications, and K-band intersatellite communications equipment—a KSA transponder. A functional flow chart of the transponder system is shown in Figure 1. The weight and power consumption of each subsystem in the EM are shown in Table 1. (No environmental measures are taken for the EM).

The structural characteristics of the transponder system are as follows:

- (1) Both the FLCE and KSA transponders are structured so they can make common use of the intermediate frequency, which in turn makes it possible to achieve a folded circuit.
- (2) The FLCE efficiently relays signals required by other mission apparatuses (SIC, OCE, TT, and C).
- (3) The folded circuits of the SIC and FLCE are able to perform coherent relaying.

Table 1. Weight and Power Consumption of Transponder (EM)

Name of component		Abbreviation	Weight (g)	Power consumption (W)
F	Feeder input filter 1	FL-INFIL1	211	—
	Feeder input filter 2	FL-INFIL2	192	—
L	Feeder receiver	FL-RX	1412	4.4
	Feeder L band branching filter	FL-LMUX	907	—
C	Feeder L band amplifier	FL-LAMP	722	1.39
	Feeder switch network 1	FL-SWN1	841	—
E	Feeder switch network 2	FL-SWN2	853	—
	Feeder up converter 1	FL-UPC1	990	3.93
	Feeder up converter 2	FL-UPC2	994	3.94
	Feeder waveguide switch 1	FL-WSW1	214	0.06
	Feeder waveguide switch 2	FL-WSW2	214	0.06
	Feeder waveguide switch 3	FL-WSW3	214	0.06
	Feeder waveguide switch 4	FL-WSW4	214	0.06
	Feeder power amplifier 1	FL-SSPA1	3170	34.0
	Feeder power amplifier 2	FL-SSPA2	3166	34.0
	Feeder output filter 1	FL-OUTFIL1	349	—
	Feeder output filter 2	FL-OUTFIL2	357	—
	Feeder hybrid	FL-HYB	30	—
	Feeder synthesizer	FL-SYNTH	5778	12.1
	Feeder command receiver	FL-CMDRX	2695	5.1
	Connection waveguide	FL-WG	1008	—
	Connection coaxial cable	FL-CBL	747	—
	FLCE Total	FL-XPDR	25277	96.7
KSA transponder	KSA diplexer	KSA-DIP	35	—
	KSA receiver	KSA-RX	1903	7.3
	KSA switch	KSA-SW	498	—
	KSA up converter	KSA-UPC	1170	6.0
	KSA power amplifier	KSA-SSPA	3027	36.5
	KSA connection waveguide	KSA-WG	104	—
	KSA connection coaxial cable	KSA-CBL	35	—
	KSA wire harness	KSA-HNS	372	—
	KSA transponder Total	KSA-XPDR	7143	49.8

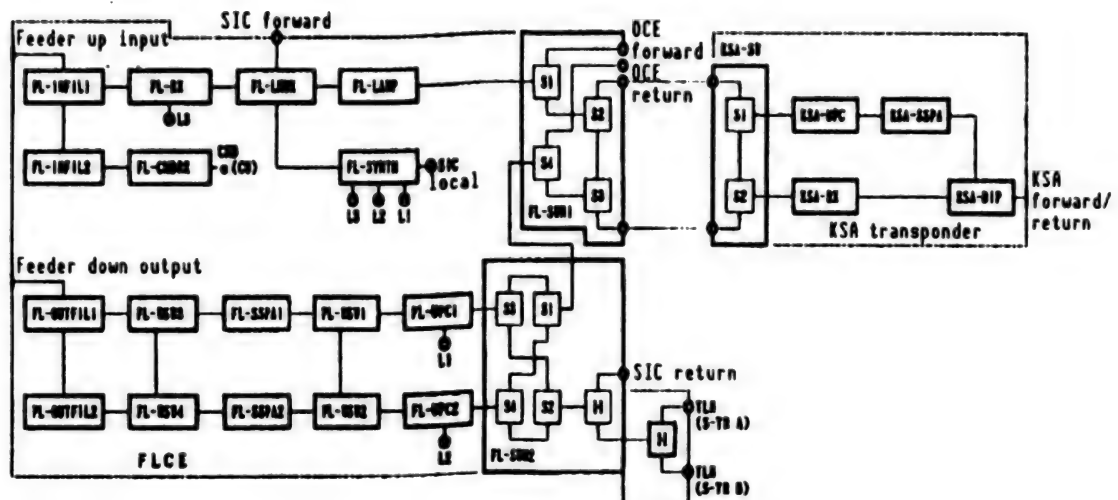


Figure 1. Functional Flow Chart for Transponder System

(4) A synthesizer like one that will be required for future data relay satellites has been mounted and is used in creating the station-originated redundant structure.

(5) The mission band command system features an independent structure that is separated from relay signals to improve reliability.

3. Development Method

The developmental sequence shown in Figure 2 was followed to ensure efficient development of the transponder system by effectively using the technologies accumulated so far.

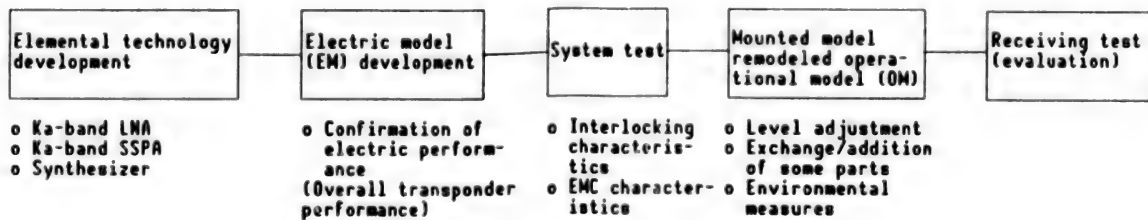


Figure 2. Sequence of Transponder System Development

4. Performance Parameters

The primary performance parameters of the FLCE and KSA transponder are shown in Table 2. The overall input/output characteristics of the KSA signal system are given in Figure 3, and a prediction for circuit signal attenuation is provided in Figure 4. For these parameters, actual performance almost achieved the targets, but some are still being improved and tested during the period of system tests in order to improve performance further.

Table 2. Primary Performance Parameters

Item	FLCE				KSA trans-ponder
	KSA/OCE	SIC	PIL	T&C	KSA
<u>Reception system up or return link</u>					
Carrier frequency(GHz)	29.772	29.8984	29.96325	29.485	32.555
Received signal level (dBm)	-90--60	-96--65	-95--65	-103--65	
Noise figure (dB)	6.8	6.7	6.7	15.8	
Linear amplification gain (dB)	61.5	40.4	—	—	
Saturated output level (dBm)	-4.3	(-24.8)	—	—	
In-signal band ripple (dBp-p)	0.1	0.1	—	—	
3 dB bandwidth (MHz)	62.6				
AM/PM (°/dB)	0.4	25.9	—	—	
—	—	—	—	—	
<u>Transmission system down or forward link</u>					
Carrier frequency(GHz)	19.938	20.1219	—	20.170	23.387
Input signal level(dBm)	-40--10	20.2455	—	1.35-	-40-
Linear amplification gain (dB)	-36--16.4	38.2	—	7.15	-10
Saturated output level (dBm)	56.8	(21.7)	—	13.1	55.3
In-signal band ripple (dBp-p)	33.4	0.15	—	(14.4)	35.0
3 dB bandwidth (MHz)	0.1	231.4	—	0.1	0.1
AM/PM (°/dB)	180	—	—	231.4	112
—	2.7	—	—	—	0.8

5. Conclusion

The development test of the FLCE and KSA transponder to be mounted on the ETS-VI has been completed, confirming that they almost satisfied the performance targets. System tests are currently being conducted. As a result of the system tests, the process of refurbishing the EM to make it into an OM will become more specific and the overall performance of the mission system will also be clarified. Finally, thanks are due to those persons who provided guidance in the development of the transponder system.

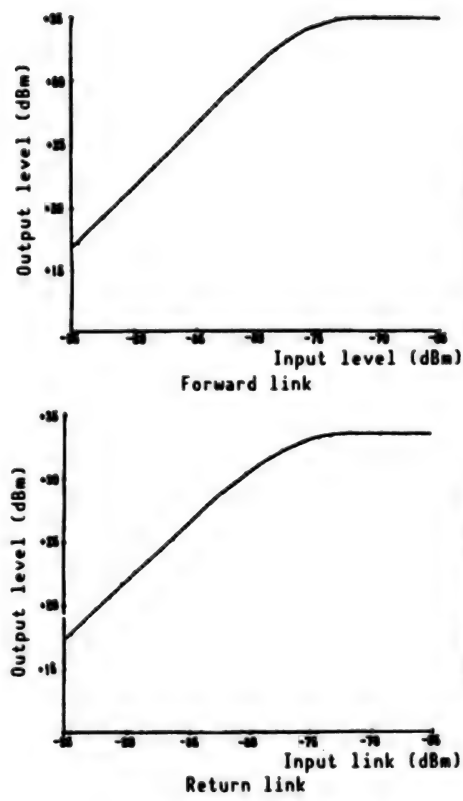


Figure 3. Overall KSA Input/Output Characteristics

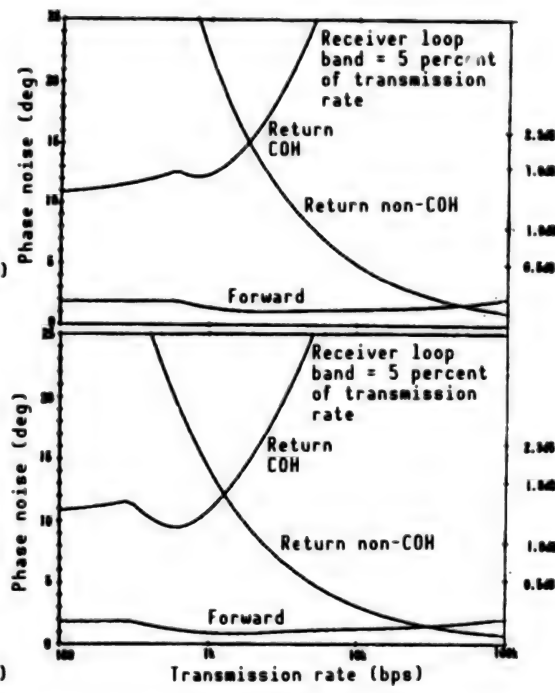


Figure 4. Circuit Signal Attenuation Volume Due to Station Transmitted Signal

Effect of Soft Vibration on Direction of ETS-VI Antenna Reflector

906C3836 Tokyo DAI33KAI UCHU KAGAKU GIJUTSU RENGO KOENKAI KOENSHU in Japanese
31 Oct-2 Nov 89 pp 474-475

[Article by Masazumi Ueha, Radio System Laboratories, NTT]

[Text] 1. Introduction

The Engineering Test Satellite VI (ETS-VI) will be equipped with a large main antenna reflector for multibeam satellite communications. Since this reflector is softer than conventional ones, it has been predicted that soft vibrations will affect the antenna's ability to achieve a high degree of pointing precision, for which the target is 0.015 degrees. This article reports on the use of a simulation to determine the antenna's directional variation at the time of orbit control when it is liable to be greatly affected by torque and also to assess the effects of unloading. Based on these results, the article will examine the degree of rigidity needed to keep directional variation due to soft vibrations of the main antenna reflector within a required range.

2. Pointing Control System and Reflector Vibration

As shown in Figure 1, the ETS-VI antenna pointing control system ensures a pointing precision of 0.015 degrees through a fine control process that uses the antenna driving control system rather than the less precise satellite attitude control system. Directional variation due to vibration of the main antenna reflector must be limited to no more than 1.0×10^{-3} . Assuming that the pointing variations of the two main antenna reflectors are most notable around the pitch axes where bending vibration, rather than natural vibration, is dominant, this discussion will focus on satellite dynamics around the pitch axes.

3. Directional Variation During Operation

Taking into account the fact that the effect of angular variation due to the vibration deformation of the main antenna reflector is doubled in terms of pointing directional variation, the volume given by formula (1) has been calculated by a simulation based on the conditions at the time of orbital control and unloading shown in (1) and (2).

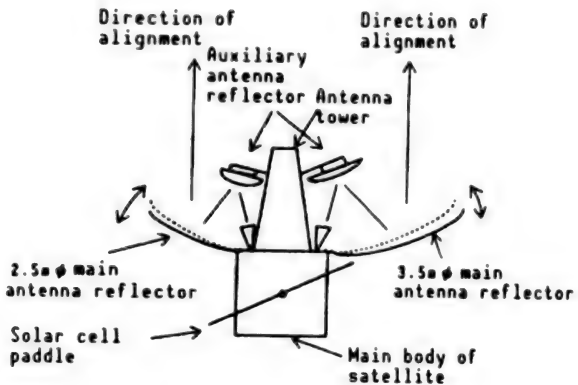


Figure 1. ETS-VI Pointing Control System and Reflector Vibration

$$\theta_A = 2 (\phi_A' + \phi_A R) \xi \quad (1)$$

ϕ_A : Primary intrinsic mode displacement of main antenna reflector

ϕ_A' : Primary intrinsic mode angular displacement of main antenna reflector

R : Distance between the satellite's center and a maximum displacement point

ξ : Mode coordinates

(1) During orbit control: A phasial stability method is used for the solar cell paddle's torsional oscillation and an amplitude stability method for the main antenna reflector's bending vibration.¹ A step disturbance torque of 1.2 Nm is applied to the satellite being controlled by an 0.2 Hz band attitude control system.

(2) During unloading: A rectangular pulse torque of a magnitude of 1 Nm and a duration of 0.4 second is applied to a satellite whose attitude control system is turned off temporarily.

The calculation results from (1) and (2) are shown in Table 1, which indicates that the pointing directional variations are within the range of required values.

Table 1. Calculation of Pointing Directional Variations During Operation

	3.5 mφ reflector	2.5 mφ reflector
(1)	1.0×10^{-4} deg	2.0×10^{-5} deg
(2)	1.2×10^{-4} deg	2.4×10^{-5} deg

4. Reflector Rigidity and Requirement for Pointing Precision

The variative quantity against the rectangular torque of moment M (Nm) and duration, Δt (s), was analyzed using natural vibration frequency as a parameter through the use of a model satellite with one main antenna reflector unit to determine the extent to which disturbance torque excites the soft vibration of a single main antenna reflector, thus resulting in greater variation. Since the rigidity of the semi-lifting mechanism, which is a connecting part with the satellite, is overriding, the mass distribution and mode form of the main antenna reflector does not depend on the natural vibration frequency and remains fixed. The results of calculating the variative quantity of the pointing direction for this condition are shown in Figures 2 and 3. In the figures, when $M\Delta t$ equals 0.4 Nms, the variative quantities are 3.3×10^{-4} degrees and 1.5×10^{-4} degrees for the present $3.5 \text{ m}\phi$ and $2.5 \text{ m}\phi$ main antenna reflectors, respectively. In order to secure the required pointing direction distribution values, the natural vibration frequency must be more than 1.2 Hz and 1.9 Hz, respectively.

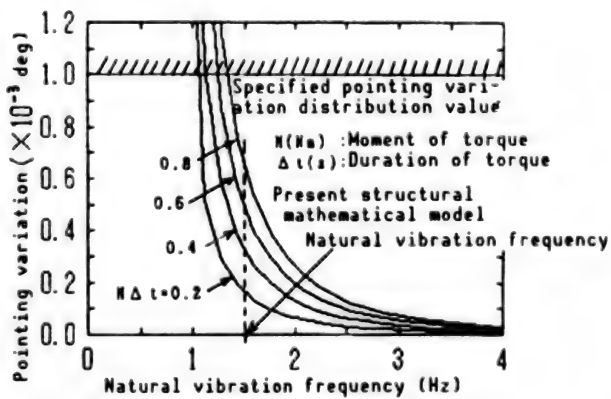


Figure 2. Rigidity of $3.5 \text{ m}\phi$ Main Antenna Reflector and Pointing Variation

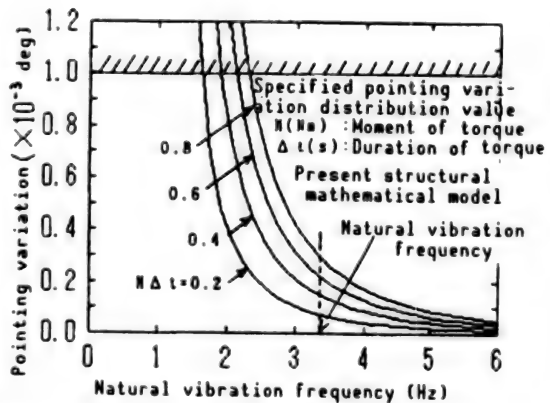


Figure 3. Rigidity of $2.5 \text{ m}\phi$ Main Antenna Reflector and Pointing Variation

5. Conclusion

Since the dynamic pointing directional variations due to vibration of the main antenna reflectors during operation of the ETS-VI are well within the required values, with the torque in an anticipated range, it has been proved that the rigidity of the present $3.5 \text{ m}\phi$ and $2.5 \text{ m}\phi$ main antenna reflectors is sufficient. Data from the tests of actual satellite-mounted multibeam communications systems will be evaluated in the future.

References

1. Ichikawa, Kawata, et al., "ETS-VI Attitude Control System Development (No 4)—Stationary Control/Orbit Control," Collection of Lectures From the 32nd Space Science and Technology Joint Lecture Meeting, 1989, pp 178-179.

Thermal Design of Antenna System for ETS-VI

906C3836 Tokyo DAI33KAI UCHU KAGAKU GIJUTSU RENGO KOENKAI KOENSHU in Japanese
31 Oct-2 Nov 89 pp 476-477

[Article by Katsuhiko Nakajima, et al., Radio System Laboratories, NTT]

[Text] 1. Introduction

The antenna system to be mounted on Engineering Test Satellite VI (ETS-VI), which will be used for fixed and mobile communications, must involve a tower-type arrangement. This is necessary to ensure that the temperature variation of the apparatuses, including the antenna tower, must be kept as narrow as possible in order to maintain the electronic performance of the main and auxiliary reflectors and the feeder system as well as to hold down directional beam variation due to thermal deformation. This article will report on the thermal control method selected for the antenna system based on these design requirements and the results of a thermal analysis.

2. Configuration of Antenna System

As shown in Figure 1, the antenna system consists of a 20 GHz band main reflector with an aperture of 3.5 m, a 30 GHz band main reflector with an aperture of 2.5 m, a 20 GHz band auxiliary reflector, a 30 GHz band auxiliary reflector, a 20 GHz cluster, a 30 GHz band cluster, an S-band horn, a C-band horn, a 20 GHz/S-band frequency selection sheet (FSS), a 30 GHz/C-band FSS, and an antenna tower. The main reflector's surface is a honeycomb sandwich plate covered with CFRP skin. Its back is supported by a trussed structure with CFRP tubes.

3. Thermal Control of Antenna System Components

3.1 Main Reflector

Since the main reflector is made of CFRP, it has a low degree of heat conductivity and little heat capacity. When the sun simultaneously irradiates part of the tower and the reflector itself, or if the satellite casts a shadow on the remaining part, a difference in temperature of about 200°C is generated on the surface, resulting in greater thermal deformation. In order to keep thermal deformation under 0.2 mm, an RMS structural examination was conducted

of the reflector surface's rigidity and the arrangement of support studs between the surface and the back structure. As a result, a thermal control method of painting the surface white and covering the back with a multilayered insulator (MLI) was adopted. Since this method makes it possible to equalize the temperature in the back structure through radiation heat exchange between the reflector's back side and the MLI, it effectively prevents thermal deformation.^{1,2}

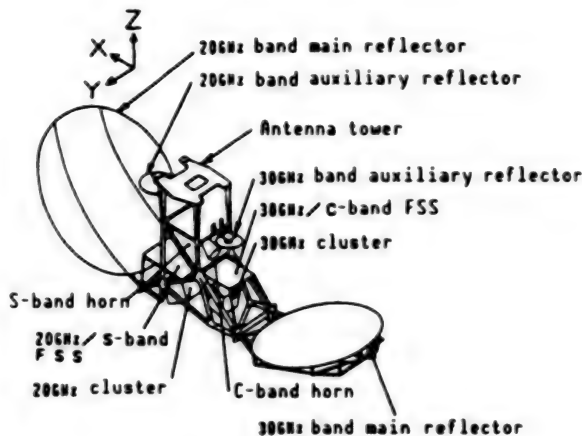


Figure 1. Structure of Antenna System

3.2 Auxiliary Reflector

The auxiliary reflector, which features a pointing control mechanism, controls temperature with a heater. This is because of the narrow operational temperature range and because it is entirely covered with MLI. The reflector surface is painted white to restrict a rise in temperature due to multiplex reflection from the main reflector.

3.3 Feeder System Components

The feeder system components are mounted on the tower. Since the MLI cannot be used for the wave filter part, it is necessary to satisfy the temperature conditions of the low temperature side. Therefore, a thermal control cover, which does not affect electronic characteristics, is used for the wave filter part, and the remaining parts are covered with MLI.

3.4 Antenna Tower

Since thermal deformation of the tower causes directional variation in the beams of the attached equipment, it is necessary to maintain a uniform configuration by keeping the temperature fluctuation range as narrow as possible. Except for the wave filter part, which has a thermal control cover, it was decided that thermal control of the tower would be effected by covering all around the truss, a main structure, with three-layered MLI and by painting the outermost layer black. This procedure facilitates analysis, testing, and evaluation of multiplex reflection.

4. Results of Thermal Analysis

Thermal analysis by the nodal point method was conducted to estimate the temperature of the antenna system components. A depiction of a mathematical thermal model is shown in Figure 2. Temperature estimation was based on a stationary thermal analysis of 22 cases where it was predicted that components would reach the highest or lowest temperature, together with three cases of diurnal variation transient analysis designed to forecast more realistic values of temperature fluctuations in an actual orbit.³ The cases of transient analyses are for the beginning and the end of satellite life in the vernal and autumnal equinoxes and for the end of satellite life in the summer solstice. As shown in Figure 3, the estimated temperatures of all antenna system components satisfy the design target temperature ranges for both nonoperational and operational times, proving that the selected thermal control methods are adequate.

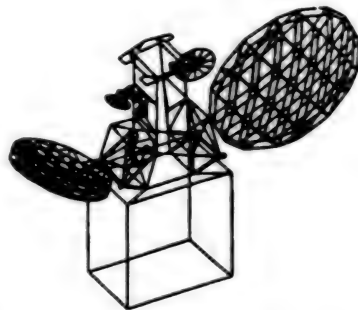


Figure 2. Depiction of Thermal Mathematical Model

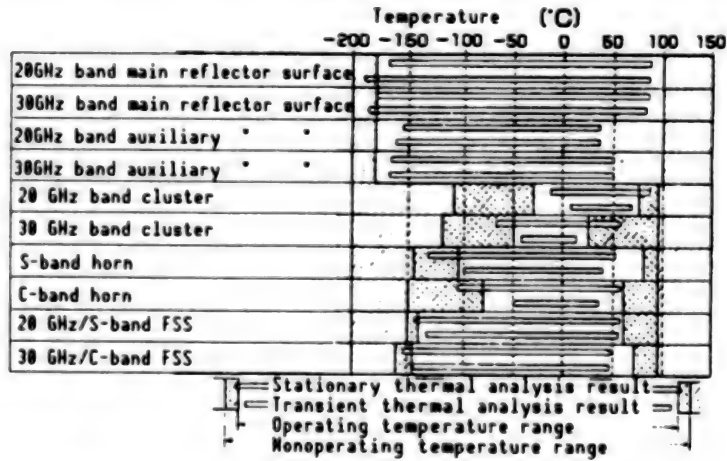


Figure 3. Design Target for Temperature Range and Thermal Analysis Results

5. Conclusion

This article described the thermal design for the antenna system for the fixed and mobile communications system to be mounted on ETS-VI and indicated that the component apparatuses satisfied the design target temperature ranges. The thermal testing of a single unit for each apparatus has already been completed

and the thermal mathematical model used for design is now being evaluated. Its results will be reported in due course.

References

1. Ohata, et al., "Examination of Thermal Deformation Control for Satellite-Mounted Reflector Surface," 30th Lecture Meeting Regarding Structural Strength, 1988.
2. Ohata, "Low Thermal Distortion of CFRP Surface Skin-Honeycomb Sandwich Plate," 31st Lecture Meeting Regarding Structural Strength, 1989.
3. Tsunoda, et al., "Examination of Thermal Control for ETS-VI-Mounted Fixed/Mobile Communications Antenna System and Thermal Test Methods," Shin Gakkai Study Meeting SAT88-39, 1988.

Antenna Pointing Control System for ETS-VI

906C3836 Tokyo DAI33KAI UCHU KAGAKU GIJUTSU RENGO KOENKAI KOENSHU in Japanese
31 Oct-2 Nov 89 pp 478-479

[Article by Yoichi Kawakami, et al., Radio System Laboratories, NTT]

[Text] 1. Introduction

Upgrading antenna pointing control precision is essential for the realization of multibeam satellite communications. This report will outline the antenna pointing control system to be mounted on the ETS-VI.

2. System Configuration

The requirements for the antenna pointing control system are shown in Table 1. In addition to pointing precision, the number of antennas controlled, beam composition, and the operating period during which control is needed are important factors in determining the configuration of the control system.

Table 1. Requirements for Control System

Item	Parameter
Pointing precision	Within 0.015 degrees
Number of antennas	2
Beam composition	Multibeam
Operating period	All times, including meal times

The antenna pointing control system configuration adopted for the ETS-VI is shown in Figure 1.¹ In order to prevent antenna misalignment, thermal deformation errors and attitude errors, which cause antenna pointing errors, an antenna driving control system that tracks beacon radiowaves from the ground was mounted on both the transmitting and receiving antennas. This control system consists of a radiowave sensor that detects the direction of the beacon radiowaves and an antenna driving mechanism that actuates the driving control circuit and rotates the reflectors. It works independently of the attitude control system.

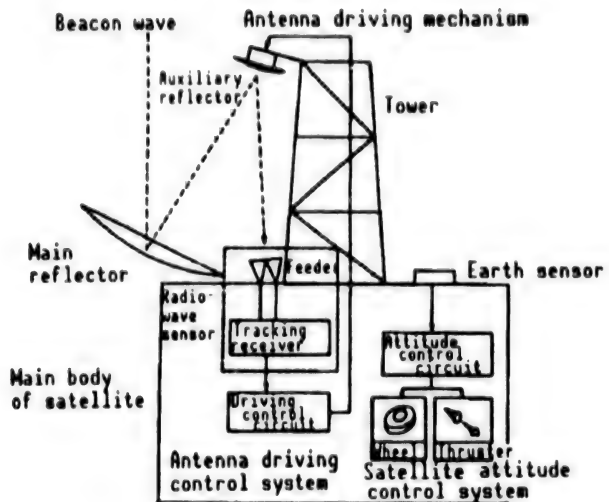


Figure 1. Configuration of Antenna Pointing Control System

In regard to antenna driving, main reflector driving and auxiliary reflector driving can be determined. Main reflector driving has superior electronic characteristics in that there is less antenna pattern distortion during driving. However, if its diameter is enlarged, its rigidity and the driving torque of the antenna driving mechanism must be increased, and such increases in mass will pose a problem. For the ETS-VI, therefore, it was decided to drive an auxiliary reflector whose inertial efficiency is one-hundredth to one-thousandth that of the main reflector. Further, the degradation of its electronic characteristics will be kept to a minimum by holding down the necessary driving range through an optimum setting of the driving center and a highly accurate alignment of the antenna system.

3. Pointing Error Distribution

The pointing error distribution system² established during the design of the antenna pointing control system are shown in Figure 2. When only the satellite's attitude control system is used, the overall antenna pointing error is about 0.2 degrees, but if the antenna driving control system is added, the error can be reduced to less than one-tenth. Residual errors after driving control include between-beam alignment error within the antenna system, thermal deformation error, the antenna driving control system's tracking error and the attitude error around the yaw axis, for which the driving control system cannot compensate. Antenna pointing precision can be ensured by designing the system so that these errors will be kept below designated values. With regard to the alignment and thermal deformation errors, in particular, which are expected to increase as the antenna is enlarged, it is possible to meet the requirements for distribution values by adopting strict design and evaluation standards, as compared with conventional methods, making alignment measurement more accurate and developing materials that have a low linear expansion rate.

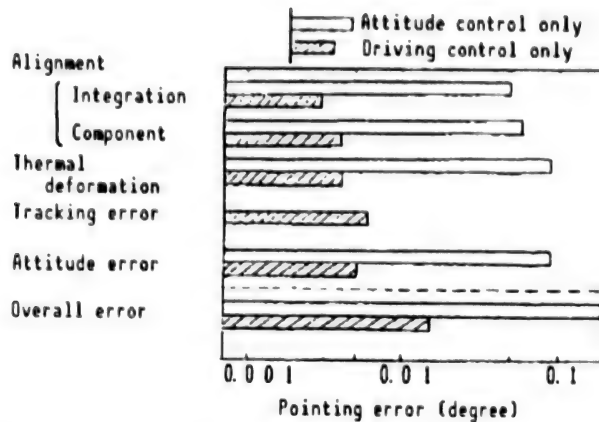


Figure 2. Antenna Pointing Error Distribution

4. Antenna Driving Control System Design

A block diagram of the antenna pointing control system is shown in Figure 3.³ The attitude control system and the antenna driving control system operate separately, but are coupled in terms of dynamics.¹ Therefore, the limit to which it is possible to design the antenna driving control system and the attitude control system separately was clarified by evaluating the interference between them. The antenna driving control system was then designed by setting the interface conditions, such as control band and attitude regulation, with the attitude control system. The antenna driving control system's control band was set at about 2 Hz to ensure the interface with the auxiliary reflector's structural design and to reduce weight.

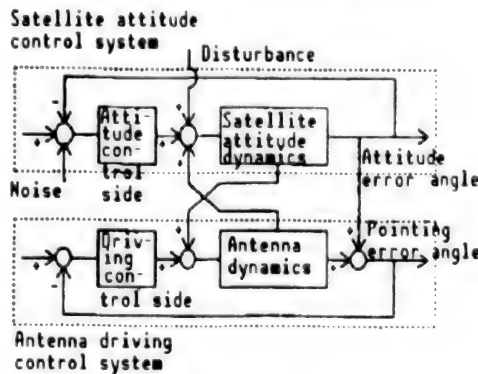


Figure 3. Block Diagram of Pointing Control System

It was determined that pointing error due to vibration of the main reflector is of little consequence. This determination was made by calculating exactly the interference with the driving control system. Furthermore, it was proved that the pointing error, obtained through analysis, due to main reflector vibration during adjustment of the satellite's orbit and unloading the wheel satisfies the distribution value requirement of 0.001 degrees.

A photograph of a 30 GHz auxiliary reflector assembly is shown in Figure 4 [not reproduced]. The antenna driving mechanism is mounted on the back of the auxiliary reflector and both the reflector and the driving mechanism are held

by two supporting booms. In order to ensure the control system's stability, the sensitivity of control precision to fluctuations in structural parameters was clarified. Also, structural design was carried out by setting nominal values and tolerances for natural vibration frequency, attenuation rates, angular displacement mode, and displacement mode as variables affecting the interface with the control system. As a result, a control characteristic of 0.002 degrees was obtained.

5. Conclusion

This article has touched on a number of the technological aspects concerning the process of designing the ETS-VI antenna pointing control system as well as the actual characteristics obtained.

The control characteristics of the antenna pointing control system will be evaluated in the future by using component elements that will be manufactured subsequently.

References

1. Kawakami, et al., Electronics Information Communication Society's Memorial National Convention, No 2273, 1987.
2. Ibid., Electronics Information Communication Society's Spring National Convention, B-238, 1989.
3. Hojo, et al., Ibid., B-184.

Structure of Multibeam Antenna for ETS-VI

906C3836 Tokyo DAI33KAI UCHU KAGAKU GIJUTSU RENGO KOENKAI KOENSHU in Japanese
31 Oct-2 Nov 89 pp 480-481

[Article by Isao Otomo, et al., Radio System Laboratories, NTT]

[Text] 1. Introduction

Previous reports on the multibeam antenna that will use the Ka-band (30/20 GHz), the C-band (6/4 GHz), and the S-band (2.6/2.5 GHz) to be mounted on the ETS-VI, which is scheduled to be launched in 1992, have dealt with the preliminary design of the antenna system's basic structure,¹ the principal technologies involved,² and the characteristics of the components. This article will describe the structure and characteristics of the antenna system that has been manufactured for the ETS-VI. It is based on an examination of this system.

2. Structure

The structure of the antenna system is shown in Figure 1. In this system, a reflector with a 3.5 m ϕ aperture sharing both the 20 GHz band and the S-band is placed on one side of the tower in the center, and a reflector with a 2.5 m ϕ aperture sharing both the 30 GHz band and the C-band is placed on the other side. Both reflectors separate the frequency bands with frequency selection sheets. The main and auxiliary reflectors are folded and kept on the tower's side during launch and unfolded in orbit.

Figure 2 [not reproduced] is a photograph of the actual ETS-VI antenna system in its storage position and Figure 3 [not reproduced] is a photograph of the system in its deployed configuration.

3. Characteristics

This antenna system's characteristics are as follows:

- (1) It has achieved a gain of 15 dB with the Ka-band, in contrast to the commercial communication satellite CS-3 which has a single-beam antenna.

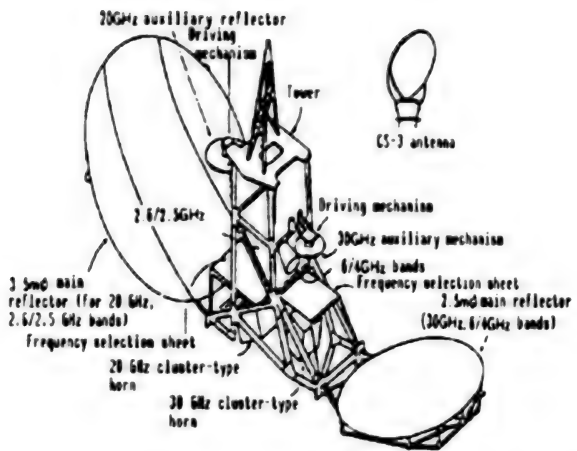


Figure 1. Structure of Antenna System for ETS-VI

Its multibeam antenna can cover all of Japan with 13 beams. This system also makes it possible to use the same frequency as the neighboring beam through the development of a cluster-type horn with superior side lobe characteristics as the primary radiator (Table 1).

Table 1. Parameters of Antenna System for ETS-VI

Item	ETS-VI	CS-3
Shape of beam	Ka-band: multibeam (13) C-band: single beam (1) S-band: multibeam (5)	Ka-band: shaped beam (1) C-band: single beam (1)
Aperture diameter	3.5 m ϕ 2.5 m ϕ	0.95 m ϕ
Antenna gain	Ka band: 48 dB C-band: 35 dB S-band: 31 dB	Ka band: 33 dB C-band: 25 dB
Expansion mechanism	Exists	None
Pointing precision	0.015°	0.2°
Weight per unit area	4.4 kg/m ²	13.0 kg/m ²

(2) The development of a highly reliable and highly accurate auxiliary reflector driving mechanism and a control algorithm confirmed that it was possible to create a driving control system capable of controlling the direction of the antenna beams with a high degree of precision, 0.015 degrees, by using the RF sensor's beacon radiowave detection signals.³

(3) The development of a wide-band, low-loss frequency selecting sheet has led us to establish two frequency sharing antenna building technologies that make it possible for the 3.5 m ϕ reflector to share the 30 GHz band and the S-band, and for the 2.5 m ϕ reflector to share the 30 GHz band and the C-band.

(4) It has been possible to reduce the weight and upgrade the precision of the system by developing a trussed structure that satisfies the strength requirements. The specular trussed structure⁴ also meets the electrical requirements through the use of proper specular materials. The weight of the 3.5 m ϕ and 2.5 m ϕ specular surfaces was reduced by about one-third per unit area to about 44 and 20 kg, respectively, compared with the 0.95 m ϕ specular surface of the CS-3 antenna. The precision of the 3.5 m ϕ and the 2.5 m ϕ specular surfaces was upgraded to as much as 0.17 and 0.14 RMS, respectively (about one-third that of the CS-3 in terms of specular precision with aperture) (Figure 4).

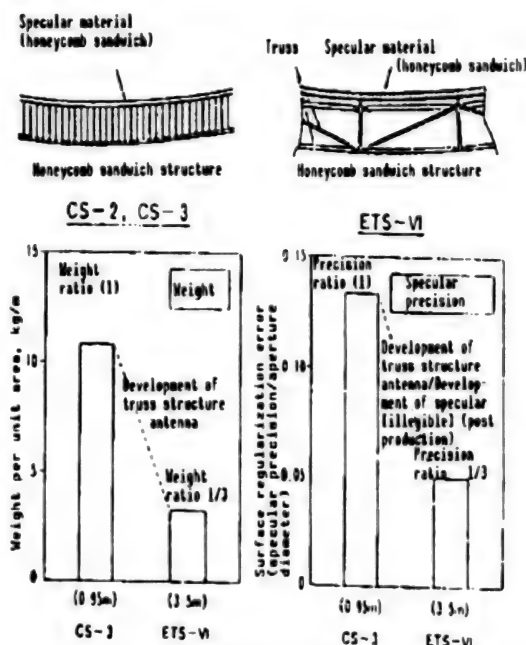


Figure 4. Trussed Specular Structure and Characteristics

4. Conclusion

This article has described the structure and characteristics of the ETS-VI antenna system. A program of system tests including electronic tests, integration tests, and environmental tests for vibration, shock, sound, and thermovacuum is currently under way. The results of these tests will be reported in due course.

References

1. Otomo, et al., SHINGAKU GIHO, SAT-84-47, 1984.
2. Ibid., 1988 Shingaku Spring National Convention, No SB-1-6.
3. Kawakami, et al., Preprints for this lecture meeting.
4. Yasaka, T., et al., IAF-86-201, 1986.

Traveling Wave Tube Amplifier for ETS-VI

906C3836 Tokyo DAI33KAI UCHU KAGAKU GIJUTSU RENGO KOENKAI KOENSHU in Japanese
31 Oct-2 Nov 89 pp 482-483

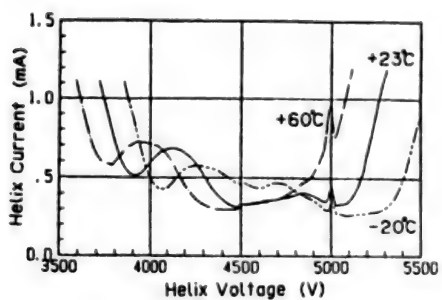
[Article by Hideo Makijima, et al., Radio System Laboratories, NTT; and
Katsuhiro Yamamoto, et al., Applied Electronics Laboratories, NTT]

[Text] 1. Introduction

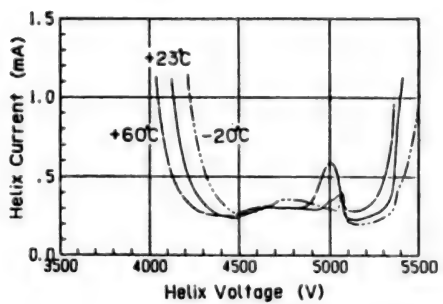
Efforts to reduce the weight and to upgrade the efficiency of a traveling wave tube amplifier to be mounted on ETS-VI by employing the technology for the traveling wave tube amplifier for the CS-3 have succeeded. The new traveling wave tube amplifier weighs 1,660 g and is 26 percent more efficient. This article discusses this new device.

2. Traveling Wave Tube

The traveling wave tube consists of an impregnant cathode, a speed taper helix slow wave circuit, a periodic magnet, and a two-step collector. Efforts were made to reduce its weight by shortening the length of the attenuator, optimizing the helix pitch profile and substantially shortening the length of the helix and the tube. The power required to heat the cathode was reduced to less than 80 percent of that for CS-3 by reducing the cathode's cubage without changing its electron release area and by strengthening the thermal radiation shield. The temperature stability of the helix current was improved through the development of a 2-17 system Sm Co magnet with a temperature coefficient (-0.02 percent/ $^{\circ}$ C) only half that of conventional magnets.^{3,4} The new magnet is used as a focusing magnet. The characteristics of helix voltage and helix current variation due to the effects of temperature are shown in Figure 1. The shortening of the helix length and the adoption of the low temperature coefficient magnet resulted in better electron beam transmission, a shorter helix internal diameter without causing the helix current to increase and better efficiency, eventually creating a wider band (17.7-21.2 GHz). With regard to the cathode, the impregnant cathode was the same as that used on the CS-3. The cathode operation temperature and screening conditions were so set to maintain an operational life more than 10 years, based on the results of the life expectancy test of the CS-3 traveling wave tube, which showed an operational life of more than 30,000 hours.



(1) Conventional magnet



(2) Low-temperature coefficient magnet

Figure 1. Helix Voltage, Helix Current Characteristics

3. Power Source

The power source consists of a pulse-width control boosting converter and a high-voltage series regulator, as shown in Figure 2. From a bus voltage of 31-50 V it provides a heater voltage and four other kinds of high voltages between 5,300 and 600 V. The transformer, coil, and condenser were miniaturized by amplifying the DC/DC converter's conversion frequency to 200 kHz. Also, introducing high-density mounting of hybrid ICs in the control circuits and using magnesium alloy for the container made it possible to reduce the weight of the power source.

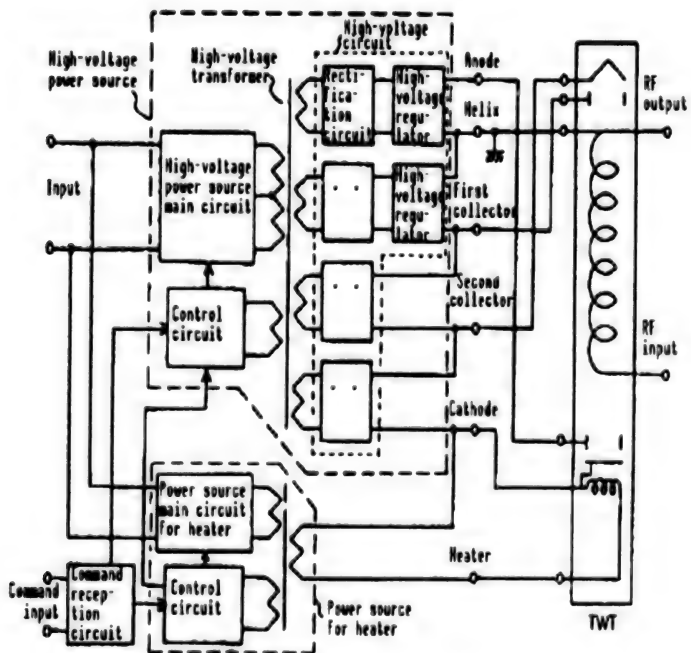


Figure 2. Structure of Power Source

In order to amplify the conversion frequency to 200 kHz, a high-speed high-voltage diode was developed and a MOSFET was used for the main switching element.⁵ In addition, in order to reduce loss due to the high-tension transformer's distributed capacity, which increases as the frequency becomes higher, the inductance of the transformer and choke coil was optimized. As a result, the weight of the power source was reduced to below half that of the device used on the CS-3 and its efficiency was improved.

4. Traveling Wave Tube Amplifier

Figures 3 and 4 show the weight and power consumption, respectively, of the traveling wave tube amplifier and compares these values with those for the CS-3. The weight was reduced to less than 60 percent and power consumption to 92 percent of the comparable figures for the CS-3. Figure 5 [not reproduced] is a photograph of the device.

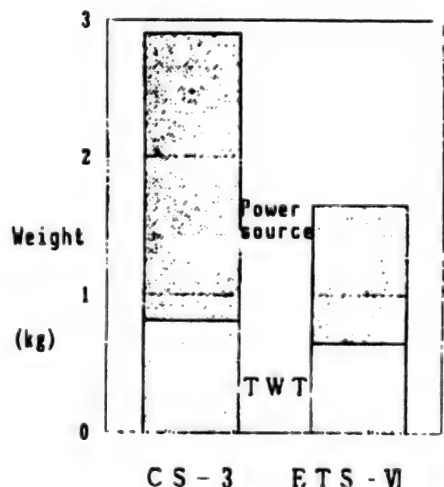


Figure 3. Weight of Traveling Wave Tube Amplifier

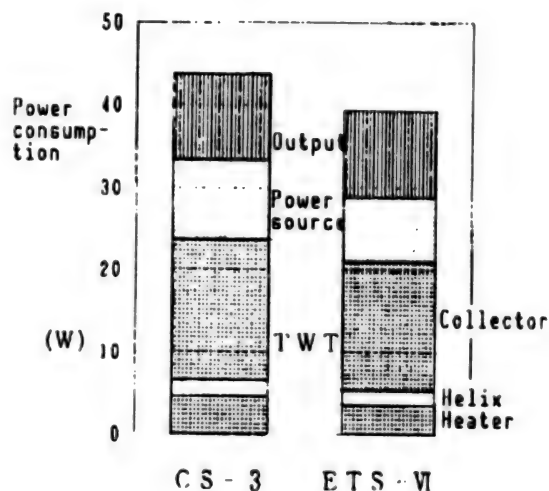


Figure 4. Power Consumption of Traveling Wave Tube Amplifier

5. Conclusion

The weight of the traveling wave tube amplifier was greatly reduced and its efficiency was improved by shortening the tube length and amplifying the power source conversion frequency. Additionally, its life has been extended by the screening method for the impregnant cathode, whose reliability was confirmed by the operation of the CS-3. Environmental and operational life stability have been further improved through the development of a low-temperature coefficient magnet and the enhanced stability of the helix voltage.

References

1. Tanaka, et al., UKAGIREN, 1989.
2. Ishibori, et al., TSUKEN JIPPO, Vol 11, 1985.
3. Kumasaka, et al., SHINGAKU GIHO, CPM83-36, 1983.
4. Kawashima, et al., Ibid., ED 86-126, 1986.
5. Kunihiro, et al., 1986 Shingaku General Convention, No 244, 1986.

Multibeam Transponder for ETS-VI

906C3836 Tokyo DAI33KAI UCHU KAGAKU GIJUTSU RENGO KOENKAI KOENSHU in Japanese
31 Oct-2 Nov 89 pp 484-485

[Article by Masayoshi Tanaka, et al., Radio System Laboratories, NTT]

[Text] 1. Introduction

A multibeam satellite communications system would be an effective way to increase the capacity and economy of satellite communications. One aspect of research and development in current satellite communications technology has involved the creation of a highly efficient, compact, and lightweight transponder that incorporates a satellite-mounted large-scale antenna and satellite switch. The transponder that is to be mounted on the Engineering Test Satellite VI (ETS-VI), which is scheduled to be launched in 1993, has recently been completed in anticipation of the confirmation of the satellite-mounted equipment technology and a proving space test of the multibeam satellite communications system. This article will describe the structure, functions, and characteristics of the satellite-mounted transponder.

2. System Outline

This system uses three frequency bands. For fixed satellite communications a 30/20 GHz band (Ka-band) and a 6/4 GHz band (C-band) are used, while for mobile satellite communications a 2.6/2.5 GHz band (S-band) is used. As shown in Figure 1, the Ka-band is a multibeam system capable of covering all of Japan with 13 beams. The C-band is a single beam system covering all of Japan with one beam, and the S-band is a multibeam system that covers Japanese coastal areas within the 200-nautical mile territorial limit with five beams.¹. The main transponder consists of transponders for these three frequency bands, a satellite switch (FI-SW) unique to the multibeam satellite communications system and control circuits. Additionally, the main transponder has a supervisory control circuit² that operates on an exclusive 30 GHz-band frequency that is separate from the satellite's own supervisory control circuit to transmit high-speed satellite switch control signals. The structure of the main transponder is shown in Figure 2.

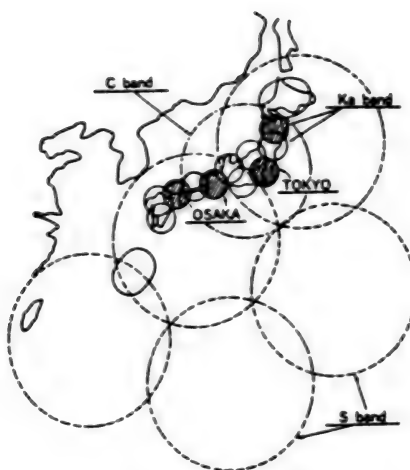


Figure 1. Arrangement of ETS-VI Beams

3. Reduction of Transponder's Dimensions and Weight

Since a large-capacity communications satellite requires a number of transponders, it is important to reduce their dimensions and weight, and to improve their efficiency. Therefore, substantially smaller and lighter transponders were produced by developing technologies that made it possible to miniaturize TWTA,³ to use ICs for general-purpose circuits, to introduce LSI with enhanced radiation-resistivity and MMIC receivers,⁴ to convert the power source switching frequency to a high frequency,⁵ and to use containers made of magnesium alloy. A comparison of the weight of existing and newly developed transponders is shown in Figure 3.

4. Satellite Switch

Since the dimensions of switches for use on a large-capacity communications satellite increase as the number of input-output beams increases, it is important to miniaturize them. Thus, an MMIC switch that is able to switch rapidly in an IF (1 GHz) band has been developed. By using this MMIC switch, a 16 x 12 matrix switch that has only about one-third the weight of existing switches has been produced.⁶

5. Function of Fixed Satellite Communications Transponder⁷

(1) SS-TDMA

It rapidly interconnects as required a number of up-link and down-link beams (below number + nsec) by IF-SW in terms of time division.

(2) Connection of Different Frequency Bands and Connection of Single Beam With Multibeam

The transponder is structured so that it can temporarily convert signals from beams with different frequencies into the 1F band of the same frequency and input to the IF-SW, as shown in Figure 2, in order to make it possible to connect beams and crossbands. Therefore, crossband diversity, one-step

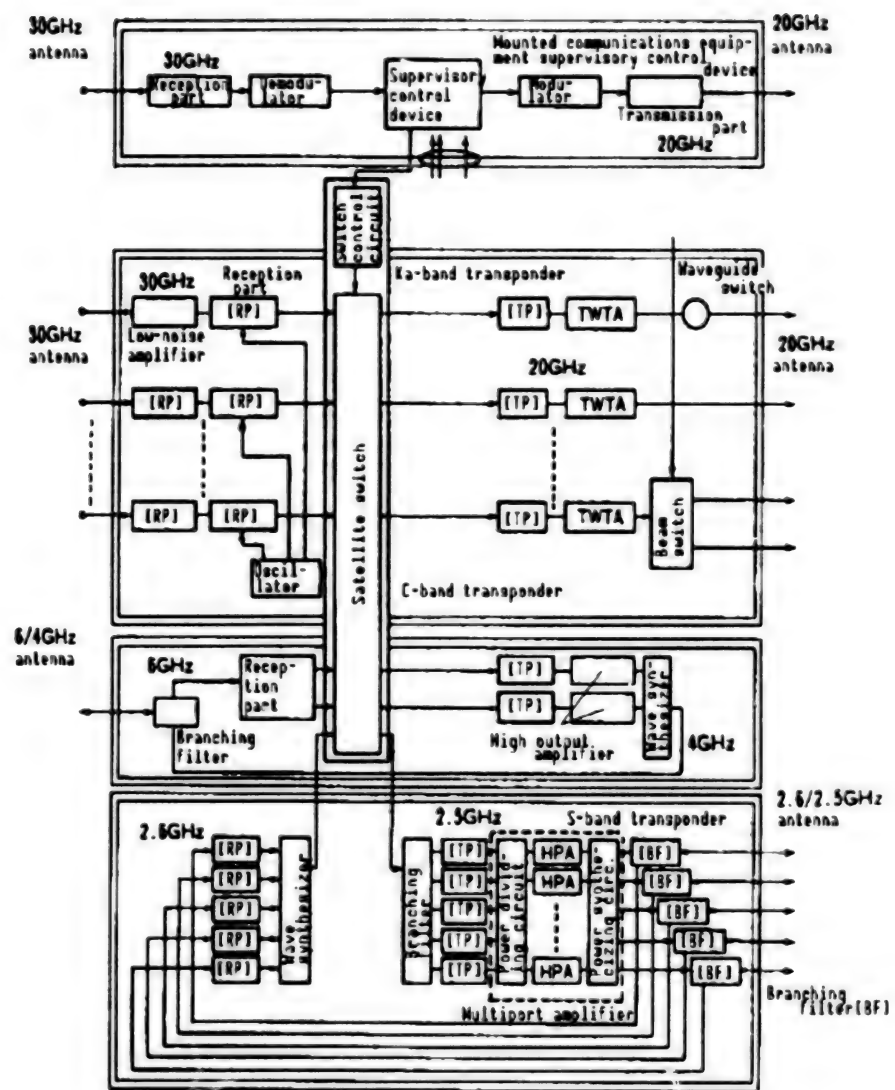


Figure 2. Structure of Transponder for ETS-VI

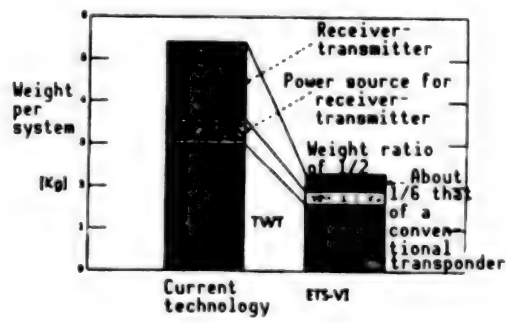


Figure 3. Comparison of Weight of Transponders

connection between the multibeam (30 GHz) and the single beam (6/4 GHz), and a redundant structure using different frequency bands becomes possible.

(3) Band Dividing Connection

The receiving circuit, which consists of a filter covering all bands and a filter dividing a band into two, is placed ahead of the IF-SW to make it possible to transmit high bit-rate signals or two-wave low bit-rate signals. The low bit-rate signals can be connected independently between beams, so the transponder can be operated efficiently.

(4) High-Speed Beam Switching

A high-output high-speed (10 W, 100 nsec) switch was developed⁶ and placed after the TWT. It is possible for low traffic beams to share a transponder in terms of time division due to the function of that switch, thereby enhancing the utility factor of the transponder.

(5) 1:N Connection

Providing the IF-SW with a distribution connection function made it possible to connect signals from specific beams to a number of different beams and to transmit them simultaneously.

(6) SCPC Signal Transmission

Transponders that operate in the 30/20 GHz and 6/4 GHz bands are variable in gain and can transmit TDMA signals as well as SCPC signals. They can also be used as a mobile satellite communications feeder link.

6. Structure and Characteristics of Satellite Mobile Communications Transponder

It is important for satellite mobile communications that transponder output be increased in order to miniaturize the mobile machine. The traffic carried by each beam is not the same. A multiport amplifier for the S-band with about 100 W was specifically developed as a power amplifier for mobile communications.⁸ Since this amplifier amplifies signals from a number of beams with a number of amplifiers jointly, a specific transmission capacity can be secured regardless of the traffic distribution between beams. Furthermore, it has an excellent characteristic in that, unlike conventional systems which individually adapt a beam to an amplifier, in this scheme the failure of some amplifiers will not cause any specific beam to fail entirely. Figure 4 shows the theory of the mobile communications transponder adopting the MPA.

7. Conclusion

The manufacture, environmental testing of the components, and the assembling of the transponder have been completed. The performance evaluation test of the overall system is being carried out in preparation for launching the ETS-VI.

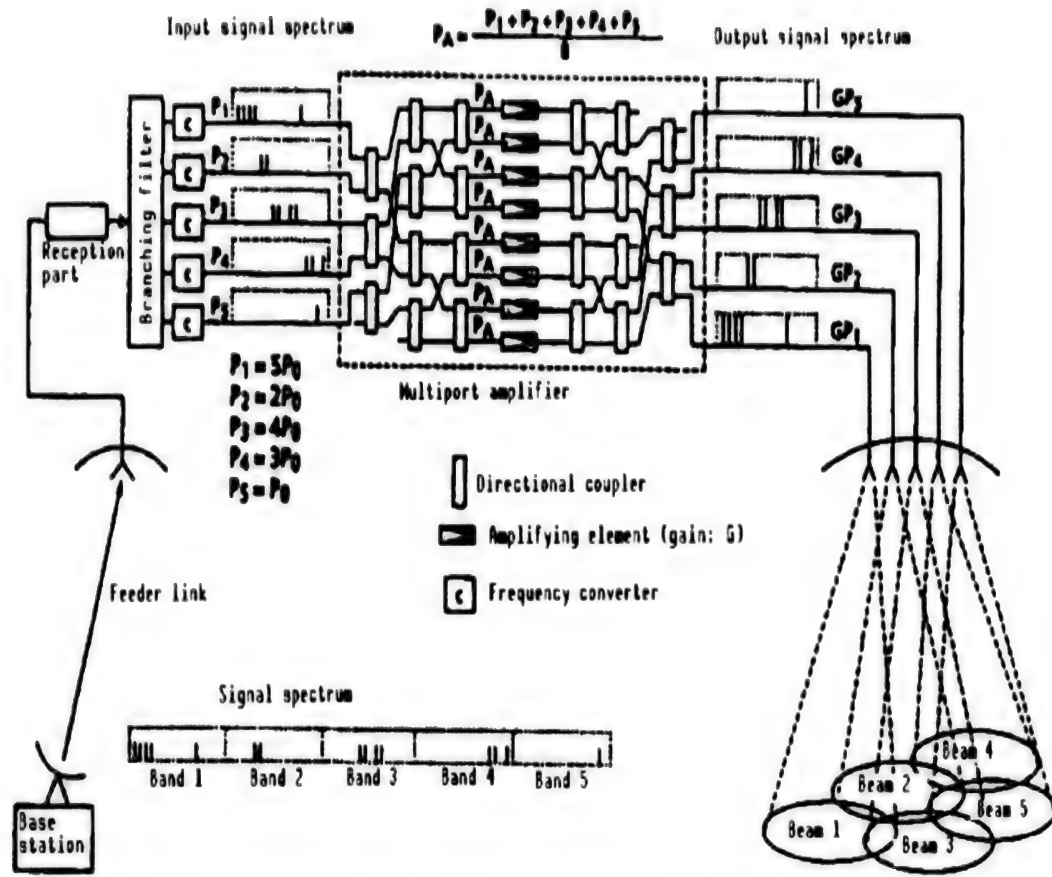


Figure 4. Theory for Mobile Communications Transponder
Adopting a Multipoint Amplifier

References

1. Tanaka, M., et al., "Experimental Fixed and Mobile Multibeam Satellite Communications," ICC'89, pp 1587-1594.
2. Izumisawa, et al., "ETS-VI Communications Equipment Supervisory Control System," UKAGIREN, 19889.
3. Makishima, et al., "ETS-VI Traveling Wave Tube Amplifier," Ibid.
4. Kato, et al., "Satellite-Mounted 30 GHz MMIC Receiver," TSUKEN JIPPO, Vol 38 No 3, 1989.
5. Yamamoto, et al., "Weight Reducing Technology for Satellite Power Source," SHINGAKU GIHO, PE-89.
6. Araki, et al., "Structure and Characteristics of ETS-VI Satellite Switch," UKAGIREN, 1989.
7. Tanaka, et al., "ETS-VI High-Function Multibeam Transponder," SHINGAKU SOZENDAI, B-241, 1989.
8. Yamamoto, et al., "ETS-VI Multipoint Amplifier," UKAGIREN, 1989.

Satellite Switch for ETS-VI

906C3836 Tokyo DAI33KAI UCHU KAGAKU GIJUTSU RENGO KOENKAI KOENSHU in Japanese
31 Oct-2 Nov 89 pp 486-487

[Article by Katsuhiko Araki, et al., Radio System Laboratories, NTT]

[Text] 1. Introduction

The NTT Radio Research Institute has recently manufactured a transponder for multibeam satellite communications¹ to be mounted on ETS-VI, which had been under development for some time. Since a multibeam satellite connects signals between different beams, it must be equipped with a connection switch (satellite switch). A number of satellite switches have been developed for the ETS-VI. These include a 16 x 12 IF-band switch matrix (IF switch) that uses monolithic IC technology, an RF-band changeover switch (RF switch) that is able to rapidly change over 20 GHz, 10 W signals in two directions, and a switch control device (SSC) for controlling these switches. This article will describe the structures, functions, and characteristics of the devices comprising the satellite switches.

2. Structures, Functions, and Characteristics of Satellite Switches

A conceptual diagram of the transponder is shown in Figure 1. The signals received by the transponders in the Ka-, C-, and S-bands are converted in the IF band (1 GHz) and are passed through the IF switch, thus making crossband connection possible. The RF switch connects one TWTA output (20 GHz, 100 W) signal to two beams in terms of time division. The connection to low traffic beams makes it possible to improve the utility factor of the transponders. The IF switch and the RF switch are centrally controlled and changeover is synchronized.

2.1 IF Switch

By using a 2 x 2 monolithic IC switch,² which was developed as a switch element for the IF switch, a 16 x 12 matrix has been produced. The switch part adopts a crosspoint stand-by structure³ and the power source features a complete stand-by structure to ensure reliability. The IF switch functions in three operational modes: 1) connecting one specific input terminal with one specific

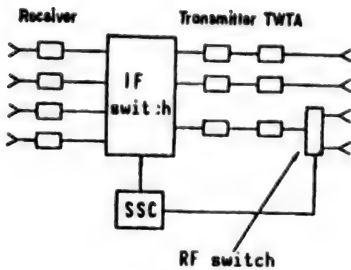


Figure 1. Conceptual Diagram of Transponder

output terminal; 2) outputting one specific input terminal's signals to a number of output terminals (distribution mode); and 3) synthesizing signals from two specific input terminals and outputting to one specific output terminal (intensive mode). The second function, item 2), corresponds to a broadcasting connection while 3) corresponds to a band division transmission system⁴ that performs multicarrier transmission by sharing one transponder with a number of radiowaves after carrying out frequency multiplication inside the IF switch. Figure 2 [not reproduced] is a photograph of the IF switch. The IF switch achieved an isolation of more than 54 dB and a switching time of less than 16 nsec for all routes in a band with a central frequency of ± 100 MHz. It weighs 6.8 kg.⁵ The introduction of a monolithic IC as a switch element made it possible to reduce the size of the IF switch by one-half and its weight by one-third, as compared to the case when a hybrid IC is used.

2.2 RF Switch

This is a one-input two-output switch using a PIN diode phase shifter.⁶ Figure 3 shows its circuit diagram. The signal input to the input terminal (a) is output to the output terminal (b) or (c) by changing the phase of the phase shifter. The PIN diode phase shifter has a redundant structure to ensure reliability. Figure 4 [not reproduced] is a photograph of the RF switch. Its switching time is 100 nsec and it weighs 420 g.

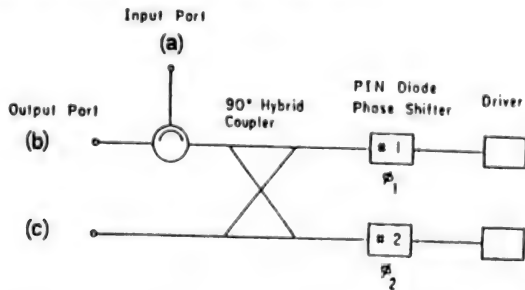


Figure 3. Circuit Configuration of RF Switch

2.3 SSC

The function of the SSC is to store the switching pattern data sent from the ground through the supervisory control circuit in its memory, read out the contents of the memory, send the information to the IF switch and the RF

switch, and refresh the switch pattern every 8 μ sec. To account for soft errors by the memory due to cosmic rays, the memory unit of the CPU executes one-error correction and two-error detection. Additionally, the SSC has a three-system CPU memory with the same function, which makes majority decision judgment on its output data to ensure reliability. Figure 5 [not reproduced] is a photograph of the SSC. It weighs 5 kg. The SSC is only one-fourth the size and consumes only one-tenth of conventional individual ICs. These reductions were accomplished by introducing CMOS LSI with enhanced radiation-resistivity⁷ in the internal circuits.

3. Conclusion

Two satellite switches have been developed for use on the ETS-VI. These are a large, 16 x 12 IF switch and a high-speed highly power-resistant RF switch. An SSC to control these switches has also been developed. It has been confirmed that their performance will meet the specified levels. Testing and evaluation of the complete transponder system will be conducted in the future. Finally, thanks are due to Director Yamamoto of the Radio Research Institute, and Manager Morita and Manager Samejima for their unflagging guidance.

References

1. Tanaka, et al., "ETS-VI Multibeam Transponder," to be presented in this lecture meeting.
2. Araki, et al., "SHINGAKU SOZENDAI, 1987, p 756.
3. Araki and Tanakaga, SHINGAKU SHUKI ZENDAI, B-269, 1988.
4. Mori, et al., SHINGAKU GIHO, SAT86-41.
5. Araki, et al., SHINGAKU SHUKI ZENDAI, B-111, 1989.
6. Ibid., ELECTRONICS LETTERS, Vol 21 No 11, pp 474-475.
7. Ono and Mori, SHINGAKU SHUKI ZENDAI, B-110, 1989.

Development of Antenna Expansion Mechanism for S-Band Intersatellite Communications

906C3836 Tokyo DAI33KAI UCHU KAGAKU GIJUTSU RENGO KOENKAI KOENSHU in Japanese
31 Oct-2 Nov 89 pp 488-489

[Article by Masato Tanaka, National Space Development Agency; Shigeru Kimura, et al., Communications Research Laboratory, Ministry of Posts and Telecommunications; and Hitoshi Ishikawa, et al., Mitsubishi Electric Corp.]

[Text] 1. Introduction

The S-band intersatellite communications antenna to be mounted on Engineering Test Satellite VI (ETS-VI) consists of an array antenna with 19 elements. It is connected with apparatuses inside the satellite by 19 RF cables. The antenna, which is in a stored configuration during launch, is unfolded in orbit by a lift-expansion mechanism. This article will describe this mechanism.

2. Outline of Lift-Expansion Mechanism

The S-band communications antenna that must be deployed in orbit after being launched in a housed configuration has 19 large coaxial cables. Therefore, a power hinge expansion mechanism that uses a stepping motor to alleviate the effect of resistance torque was selected.

The lift-expansion mechanism is attached to the ends of two support arms of an antenna supporter. It interfaces with the satellite tower and deploys the antenna to a specific angle. One unit of the lift-expansion mechanism comprises two such machines. Only one hinging mechanism is attached to the support arm on the +x side of the antenna supporter while another hinging mechanism and a driving mechanism are attached to the support arm on the -x side. The configuration (expanded state) of a thermal structural model of the lift-expansion mechanism is shown in Figure 1. As shown in the figure, the hinging mechanism is common to the +x side and the -x side. Thus, it offers a load path from the antenna supporter and holds the center of expansion and rotation of the antenna.

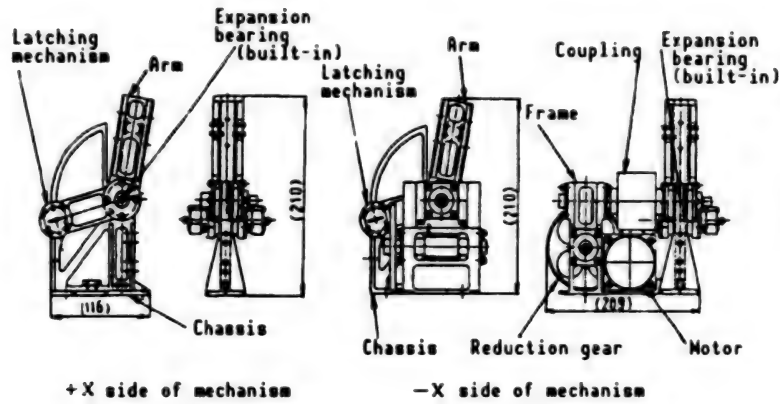


**Figure 1. Configuration of Lift-Expansion Mechanism
(Expanded state)**

The driving mechanism generates power for antenna expansion and transmits the motor's rotating power to the antenna's expansion-rotation shaft via the reduction gear.

3. Design of Mechanisms

(1) Hinging mechanism

The hinging mechanism basically consists of an arm, an expansion bearing, a latching mechanism, and a chassis. The arm interfaces with the support arm of the antenna supporter and the chassis with the antenna tower. Both the arm and chassis are linked by the expansion bearing, which ensures free rotation, and latched by the latching mechanism when the antenna expands to a specific angle.

(2) Driving mechanism

The driving mechanism increases the motor's rotation torque by the reduction gear and transmits antenna expansion torque to the hinging mechanism's expansion-rotation shaft via the coupling. A diagram of the driving mechanism is shown in Figure 2. In this mechanism, motors, spur gears (small and large), worms, a worm wheel and bearings to support them are mounted on the frame, and a coupling is attached to the end of the worm wheel shaft.

4. Performance Characteristics

The principal performance characteristics of the lift-expansion mechanism are shown in Table 1.

5. Conclusion

The validity of the design of the lift-expansion mechanism has been confirmed through the manufacture and development testing of a thermal structural model. Based on these results, the next step is to develop an actual device.

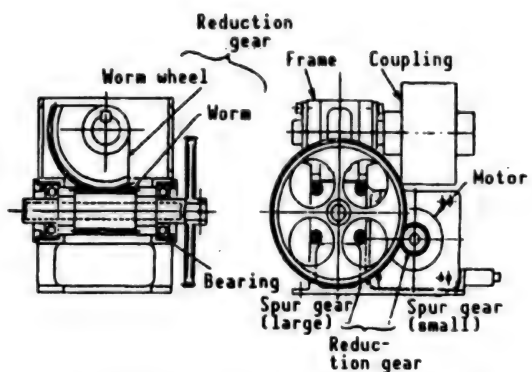


Figure 2. Driving Mechanism

Table 1. Performance Characteristics of Lift-Expansion Mechanism

Item	Performance	Remarks
Expanding angle	90°	Nominal value
Time required for expansion	More than 90°	Nominal value
Rigidity after expansion	More than 1.3×10^3 kgf·m/rad	
Reproduction error	Less than $\pm 0.1^\circ$	
Thermal deformation error	Less than $\pm 0.25^\circ$	
Mass	Less than 5 kg	One unit comprises two machines

On-Orbit Calibration of Optical Sensors

906C3836 Tokyo DAI33KAI UCHU KAGAKU GIJUTSU RENGO KOENKAI KOENSHU in Japanese
31 Oct-2 Nov 89 pp 502-503

[Article by Hideo Hino, Mitsuru Takei, and Hiroki Ono, Resources Prospecting Observation System Research and Development Organization; and Riichi Nagura, Shinzo Koo, Yoshito Narimatsu, Yasuhisa Nakamura, and Naoshi Suzuki, NEC Corp.]

[Text] 1. Introduction

For the advanced optical sensors used for remote sensing from satellites, on-orbit sensitivity calibration, in addition to calibration on the ground, is important in the use of picture data. LANDSAT-TM and the SPOT-HRV satellites perform on-orbit optical calibration through the use of a lamp. Japan is currently developing a special calibration device for on-orbit optical calibration that will be incorporated in the advanced optical sensor (OPS) to be carried by the Earth Resources Satellite 1 (ERS-1). On the basis of test data, we predict that this device will provide stable on-orbit optical calibration of this ERS-1 OPS.

2. Outline

The principal performance characteristics of the ERS-1 OPS are shown in Table 1. The OPS has two radiometer sections: one for visible near-infrared radiometer use and the other for shortwave infrared use. Each section has an independent optical calibrating device. The outgoing beam formula for luminous energy, which is the standard of optical calibration, is basically common. A functional system chart of the calibration device is shown in Figure 1. The composition of the standard light source section for shortwave infrared use is shown in Figure 2. The main purpose of the OPS is to perform optical calibration for all picture elements in all bands and to confirm changes of sensitivity while in orbit. Table 2 summarizes the performance of the optical calibration system.

3. Test Results

The OPS optical calibrating system was tested, using an engineering model (EM) and an evaluation model to evaluate resistance to various environments.

Table 1. Principal Performance Characteristics of Optical Sensor System

Item	Performance characteristics		
	Band	Central wavelength (μm)	Bandwidth (μm)
Observation wavelength area	1	0.56	0.08
	2	0.66	0.06
	3	.81	0.10
	4 (stereoscopic vision)	0.81	0.10
	5	1.655	0.11
	6	2.065	0.11
	7	2.19	0.12
	8	2.335	0.13
Surface resolution	19.3 m x 24.2 m		
Scanning width	75 km		
Picture elements/scanning width	4,096/band		
Angle of stereoscopic vision	15.3° (B/H=0.3: front and traverse)		
Number of quantified bits	6 bits		
Output data rate	30 Mb/s x 2		

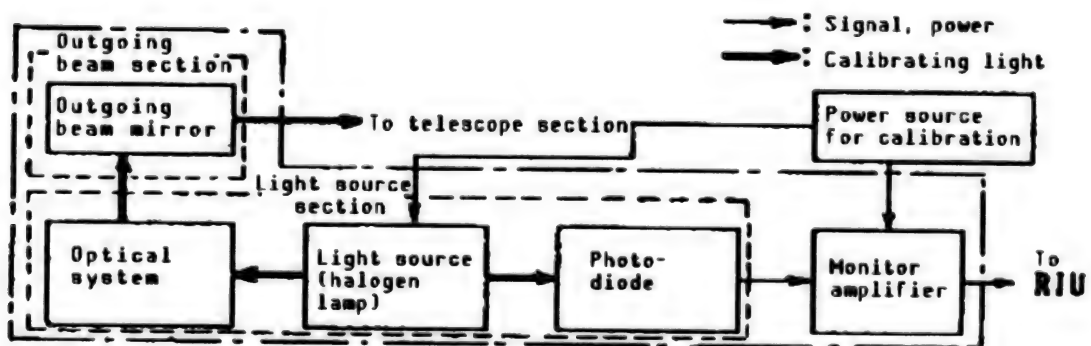


Figure 1. Functional System Chart of OPS Optical Calibration Section

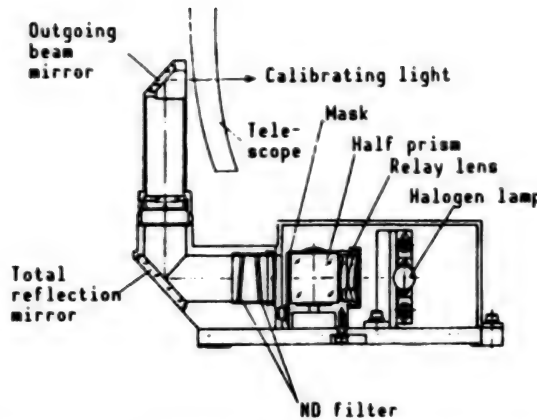


Figure 2. Composition of Standard Light Source Section for Shortwave Infrared Use

Table 2. Performance of Optical Calibrating System

Item	Performance
Calibrating light wavelength area	Observation wavelength area of OPS radiometer
Luminous energy distribution on surface of detector	(End/center) luminous energy ratio: 50 percent or more
Luminous energy stability	Less than ± 2.2 percent

Also, the lamp itself was tested for life and resistance to different environments. With regard to the test results for the optical system, we report here only about the shortwave infrared radiometer section (SWIR), but similar results were obtained for the visible near-infrared radiometer.

Table 3 shows the characteristics of the light source voltage of the telemetry output which monitors lamp luminous energy. The rate of change for the telemetry output corresponds to the rate of change for the lamp luminous energy. Table 4 shows the results of tests on resistance to various environments on the rate of change for the lamp luminous energy of the optical calibration system.

Table 3. Output Characteristics of Lamp Luminous Energy

Type of lamp presently used/redundant	Power source voltage variation characteristics of telemetry output		Telemetry output rate of change for assumed power source voltage of $9.5 \text{ V} \pm 0.2$ percent
	Voltage (8.5 V)	Voltage (9.6 V)	
LAMP A	3.726 V	5.173 V	$0.51\% < 0.6\%$
LAMP B	1.264 V	1.780 V	$0.53\% < 0.6\%$

4. Evaluation and Discussion

Optical calibration using a lamp anticipates confirmation of the secular change after launching. Items that should be considered as factors that cause changes in the luminous energy of the lamp include on-orbit variation factors, which correspond to the test categories listed in Table 4, and changes in the power supply. The power source voltage variation is less than 0.2 percent. The corresponding change in the luminous energy of the lamp is less than 0.6 percent (nominal value of telemetry ((change ratio of TLM output/lamp voltage)) /amount of change of power source). Therefore, on-orbit luminous energy stability is 2.2 percent. This is the combined total of the RSS values of 2.04 percent and 0.6 percent. The data cited here for the lamp itself are the worst values for each test. The evaluation model shows a smaller change than the lamp itself, as indicated in Table 4, even if it includes elements (circuit system, etc.) other than the lamp itself. Thus, for a number of reasons it can be presumed that the stability of the optical calibrating system is significantly smaller than 2.2 percent. (The case of the heat vacuum test is exceptional but this is due to the effect of factors other than the lamp itself.)

Table 4. Results of Tests on Resistance to Various Environments

Item for evaluation	Model	Evaluation model (SWIR) (percent)	Lamp itself (percent)
Test items corresponding to on-orbit variation factors	Flash life test	—	1.58
	Heat vacuum test	0.73	0.34
	Temperature cycle test	—	0.70
	Radiation test	—	1.04
	RSS value	—	2.04
Test items corresponding to launch environment	Impact test	0.18	0.88
	Random test	0.12	0.70
	Sine wave vibration	0.26	1.38
RSS value			

5. Conclusion

Our recent study has disclosed that the on-orbit stability of the optical calibration system is less than 2.2 percent. This result fully satisfies the required specification of 3.5 percent. We are scheduled to evaluate future PFM products using test data.

6. Acknowledgement

Our grateful thanks are due to the personnel of the Space Industry Section, Agency of Industrial Science and Technology, Ministry of International Trade and Industry; the Resources Prospecting Observation System Research and Development Organization; and the NEC Corp. who helped us in developing the ERS-1 OPS.

Performance of Radiometer for ERS-1 Optical Sensor

906C3836 Tokyo DAI33KAI UCHU KAGAKU GIJUTSU RENGO KOENKAI KOENSHU in Japanese
31 Oct-2 Nov 89 pp 504-505

[Article by Hideo Hino, Mitsuru Takei, and Hiroki Ono, Resources Prospecting Observation System Research and Development Organization; and Riichi Nagura, Shinzo Koo, Yoshito Narimatsu, Yu Hiramatsu, and Hisashi Harada, NEC Corp.; Note: This study was conducted as part of a program known as the "Research and Development of a Resources Prospecting Observation System," which is a major project sponsored by the Agency of Industrial Science and Technology, Ministry of International Trade and Industry]

[Text] Introduction

The optical sensor system that will be carried by the Earth Resources Satellite No. 1 (ERS-1) will be capable of taking high-resolution pictures in eight different bands ranging from visible light to the shortwave infrared area. It will have four wavelength bands in the shortwave infrared area, which will enable it not only to perform multiband observation but also to perform high-resolution stereoscopic observation in the visible near infrared area. We have recently conducted a test using an engineering model (EM) as part of the development effort and have evaluated the functions and performance of the optical sensor. This report describes the ERS-1 optical sensor system.

Configuration of Optical Sensor System

As indicated in Figure 1, the optical sensor system (OPS) comprises two subsystems: a radiometer section and an electronic circuit section. The radiometer section, in turn, consists of two radiometers, one for visible near-infrared use and one for shortwave infrared use. High-resolution picture signals from each radiometer are digitalized in the electronic circuit section and undergo signal processing before being fed to the mission transmitter. This report shows the results obtained from the EM, focusing primarily on the visible near-infrared radiometer section and the shortwave infrared radiometer section. Both of these sections incorporate many new techniques including an aspherical optical system with a wide angle of view and high resolution, and a CCD with 4,096 elements.

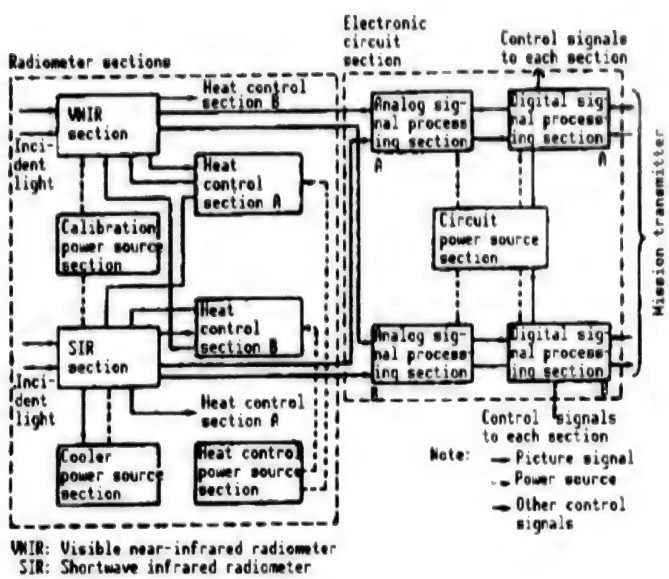


Figure 1. Functional System Chart of OPS

Visible Near-Infrared Radiometer Section

Figure 2 [not reproduced] shows the external appearance of the visible near-infrared radiometer section of the EM. It represents a considerable reduction in size and weight. Its total weight is 29.6 kg, compared with 28 kg for the optical system of the Momo No. 1 MESSR satellite, but has more than double the latter's resolution. It can observe three bands; Bands 1-3, from the same point. Band 4 is a band for acquiring stereoscopic pictures with the same wavelength and the same point as Band 3. The wavelength characteristics and signal to noise ratio (S/N) of Bands 1-3 are shown in Tables 1 and 2. As indicated by these data, high S/N multiband and stereoscopic pictures can be obtained. This adequately satisfies the required specifications.

The results obtained for MTF characteristics by which resolution is evaluated are shown in Table 2. The MTF values shown satisfy the specifications for pictures with a ground resolution of 18.3 m.

The OPS can perform optical calibration using an internal light source. This is done by causing incidence of the calibrating light from the front of the optical system and measuring picture signals. Optical calibration date for Band 1 are shown in Figure 3 as an example of measurement from the EM. The secular change of the optical system and the CCD sensor can be confirmed on orbit by optical calibration.

Shortwave Infrared Radiometer Section

The external appearance of the shortwave infrared radiometer section of the EM is shown in Figure 4 [not reproduced]. It weighs 56.8 kg but this represents a considerable reduction of size and weight, especially since this includes a cooler and other heavy objects.

Table 1. Observation Wavelength Area for Visible Near-Infrared Radiometer Section

Band	Central wavelength (μm)		Bandwidth (μm)	
	Specification	EM	Specification	EM
1	0.56 ± 0.01	0.564	0.08 ± 0.02	0.081
2	0.68 ± 0.01	0.661	0.06 ± 0.02	0.055
3	0.81 ± 0.01	0.804	0.10 ± 0.02	0.110
4	0.81 ± 0.01	0.804	0.10 ± 0.02	0.105

Table 2. S/N and MTF for Bands 1-4

Band	S/N (dB)		MTF (percent)	
	Specification	EM	Specification	EM
1	36	42	15	18
2	35	44	10	16
3	36	42	10	12
4	36	43	10	10

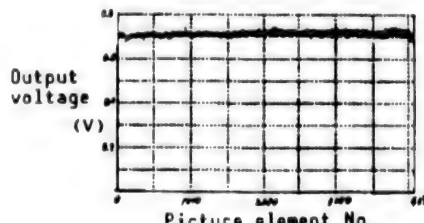


Figure 3. Optical Calibration for Band 1

The shortwave infrared radiometer section has four bands in the medium infrared wavelength area. These are Bands 5-8. Its wavelength characteristics are shown in Table 3. These characteristics depend primarily on the optical filter on the surface of the detector supplied by the manufacturer in charge. It uses bands that have been identified as corresponding to characteristic absorption spectra found in altered rocks, etc. Thus, it is expected that this system will be able to furnish enough information to make it possible to distinguish rocks.

The optical calibration data for Band 5 are shown in Figure 4. Secular change, etc., can be confirmed from it, as in the case of the visible near-infrared radiometer section.

Table 3. Observation Wavelength Areas of Bands 5-8

Band	Central wavelength (μm)		Bandwidth (μm)	
	Specification	EM	Specification	EM
5	$1.655^{+0.016}_{-0.015}$	1.663	0.11 ± 0.02	0.078
6	$2.065^{+0.015}_{-0.017}$	2.068	0.11 ± 0.02	0.114
7	$2.19^{+0.015}_{-0.019}$	2.194	$0.12^{+0.02}_{-0.023}$	0.114
8	$2.335^{+0.015}_{-0.020}$	2.350	$0.13^{+0.022}_{-0.024}$	0.120

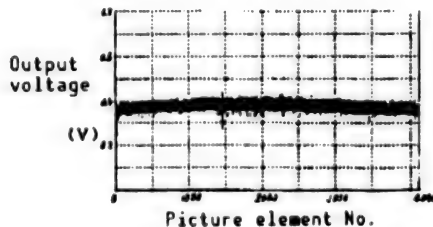


Figure 5. Optical Calibration for Band 5

We are now designing an OPS based on the results obtained with the EM, etc., and are incorporating waveform and MTF improvements. We are also developing a prototype flight model (PFM) that actually will be launched.

Acknowledgement

Our grateful thanks are due to the personnel of the Space Industry Section, Agency of Industrial Science and Technology, Ministry of International Trade and Industry, Resources Prospecting Observation System Research, and Development Organization who have helped us with the optical sensor study.

Countermeasures Against Disturbances Caused by Optical Sensor Cooler

906C3836 Tokyo DAI33KAI UCHU KAGAKU GIJUTSU RENGO KOENKAI KOENSHU in Japanese
31 Oct-2 Nov 89 pp 506, 509

[Article by Hideo Hino, Mitsuru Takei, and Hiroki Ono, Resources Prospecting Observation System Research and Development Organization; and Riichi Nagura, Shinzo Koo, Yoshito Narimatsu, Yoshihide Kato, and Naoki Takizawa, NEC Corp.]

[Text] 1. Introduction

The shortwave infrared radiometer for the ERS-1 optical sensor will be the first Japanese radiometer of its kind to feature a circulating cooler to maintain a detector temperature of about 80 K. This cooler vibrates when it starts. This creates a number of problems requiring technical solution, such as how to prevent the detector from vibrating, to ensure highly accurate optical performance. This report describes the mechanical system design process that was undertaken to solve these problems and presents the results of tests conducted with an engineering model (EM).

2. Technical Problems

The technical problems involved in installing the on-board circulating cooler are as follows:

- Occurrence of force and torque (mechanical disturbance characteristics) attendant to intracooler piston action
- Effect of cooler vibration on sensor → Sensor vibration countermeasures
- Effect on satellite attitude control system → Adjustment of interface (I/F) with satellite system

3. Design Process and Evaluation Results

The method of I/F adjustment, the study carried out to solve the second problem listed above and the process of evaluation are shown in Figure 1.

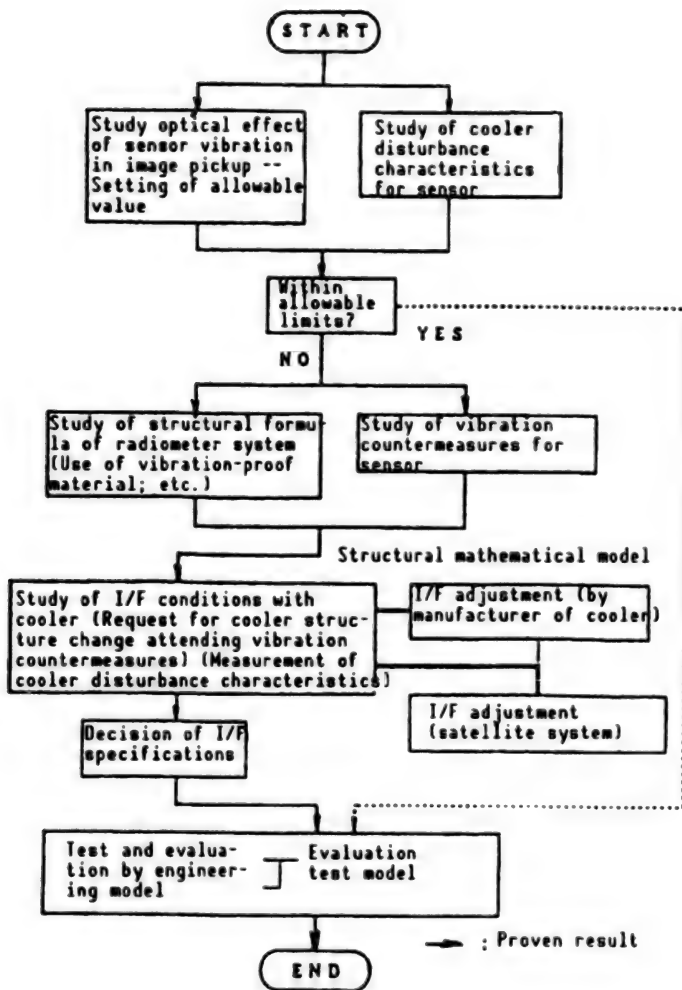


Figure 1. Process of Mechanical System Design for Installation of On-Board Cooler

(1) Effect of Cooler Vibration

It became clear that in the initial structure the sensor vibration exceeded the allowable vibration limit required to satisfy optical performance. This was because, as indicated in Figure 2, cooler-generated disturbance was transmitted directly to the sensor via the diffuser. We confirmed that in order to solve this problem it was necessary to adopt a flexible form of linkage between the sensor and the diffuser, have the cooler manufacturer make an I/F adjustment, decide on the specifications and, finally, demonstrate the initial performance capability of the radiometer section through a test.

(a) Specification of spring constant with six degrees of freedom

As the result of the increased flexibility between the cooler and the sensor, only a very small part of the cooler-generated disturbance is directly inputted into the sensor. The path for transmitting the remaining vibration

energy is, as indicated in the schematic diagram in Figure 3, comprises the cooler attachment and base plate, and the portion routed through the optical system. If these components were to exceed their allowable values, it would be necessary to consider, say, using a damping material for the base plate. However, we refrained from using a damping material because we thought we could satisfy the allowable value for sensor vibration by reinforcing the base plate. To do so, we incorporated a structural mathematical model reflecting the spring constant of cooler flexibility and conducted an analytical simulation. The allowable values for sensor vibration and the results of the analytical simulation are shown in Table 1.

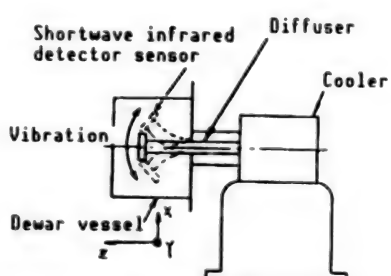


Figure 2.

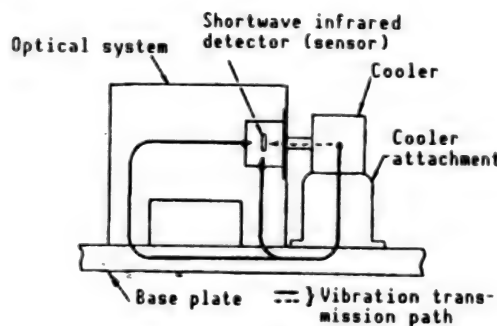


Figure 3.

Table 1. Sensor Vibration During Cooler Operation

Axial direction	Allowable extent of sensor vibration (μm)	Analytical simulation (μm)
X	Less than ± 1.5	± 0.014
Y	Less than ± 1.5	± 0.080
Z	Less than ± 1.0	± 0.038

Y: Direction of line of sensor picture elements

Z: Direction of optical axis

--Test Results--

An optical test in the shortwave infrared radiometer confirmed that it satisfied its required performance

(b) Extent of motion between sensor and diffuser

The use of a flexible linkage made the distance between the sensor and the cooler subject to change, but the amount of allowable motion had to be limited because of structural restrictions. If, therefore, as a secondary problem, the amplitude between the sensor and the cooler were to exceed the real value for allowable motion during launch or in a vibration test, breakage could occur.

In addressing this problem, we predicted the relative displacement in a simulated mechanical environment test that incorporated a structural mathematical model and determined the specifications for the allowable motion between the sensor and the diffuser.

--Test Results--

We conducted a vibration test on a shortwave infrared radiometer, which confirmed that there was no problem with regard to its functions and performance. We also measured the relative variation, respectively, of the sensor and the cooler by monitoring the vicinity of the sensor and the acceleration of the cooler and used it as a means to assure I/F conditions. The real values for the cooler, the results of the analytical simulation and the results of the vibration test are shown in Table 2.

Table 2. Extent of Mobility in Flexible Section

Axial direction	Real value (mm)	Analysis simulation (mm)	Measured value at time of vibration test (mm)
X	± 1.0	± 0.74 Maximum	± 0.3
Y	± 2.0	± 0.79 Maximum	--
Z	± 2.0	± 0.78 Maximum	--

(2) Effect on Attitude Control System of Satellite

Cooler-generated disturbance represents a source of external disturbance to the attitude control system of the satellite and may eventually effect the performance of different on-board missions, including the optical sensor. Thus, we made an I/F adjustment to compensate for two factors according to the measured disturbance data of the cooler and confirmed that cooler-generated disturbance did not affect the performance of ERS-1. The two factors compensated for in the I/F adjustment were:

- Cooler-generated force and generated torque
- Cooler angular momentum

4. Summary

As the result of the process described above, it proved possible to install an on-board circulating cooler for the shortwave infrared radiometer of the ERS-1 optical sensor. This is the first time such an approach has been adopted in Japan. Our grateful thanks are due to personnel of Fujitsu, Ltd., who were in charge of the cooler, and those of Mitsubishi Electric Corp., who were in charge of the ERS-1 satellite, for helping us with these achievements.

Development of Focusing Mechanism for ERS-1 Optical Sensor

906C3836 Tokyo DAI33KAI UCHU KAGAKU GIJUTSU RENGO KOENKAI KOENSHU in Japanese
31 Oct-2 Nov 89 pp 508, 507

[Article by Mitsuru Takei and Hiroki Ono, Resources Prospecting Observation System Research and Development Organization; and Riichi Nagura, Shinzo Koo, Yoshito Narimatsu, Yoshihide Kato, and Naoki Takizawa, NEC Corp.]

[Text] 1. Introduction

We have developed and evaluated a mechanism for adjusting the on-board focal point position in order to assure highly accurate optical performance during on-orbit use of the optical sensor to be carried by the earth resources satellite No. 1 (ERS-1). This report describes the structure and functions of this focusing mechanism.

2. Background

The ERS-1 optical sensor has two radiometer sections: a visible near-infrared radiometer section and a shortwave infrared radiometer section. To ensure the highly accurate optical performance of each section, it is necessary to compensate for any deviation in focal point position due to the thermal strain of the telescope. In the optical sensor, therefore, heat input and output between the sensor and the satellite itself are interrupted and a highly accurate, independent heat control mechanism for maintaining temperature variation within a range of $\pm 2\text{--}3^\circ\text{C}$ has been incorporated. But to compensate for the effect of extended period temperature offset for such reasons as temperature differences between the time of on-the-ground sensor position decisions and the time of operation or seasonal changes, it became necessary to devise a means for the on-board adjustment of the focal point position.

3. Functions/Performance

The performance specifications for this adjusting mechanism are shown in Table 1.

Table 1. Performance Specifications

Division	Item	Specification	Design value
Focusing mechanism for visible near-infrared radiometer (VFAM)	Focusing range	$\pm 75 \mu\text{m}$ or more	$\pm 83 \mu\text{m}$
	Focusing step	Less than $4 \mu\text{m}$	$3.35 \mu\text{m}$
Focusing mechanism for shortwave infrared radiometer (SFAM)	Focusing range	$\pm 150 \mu\text{m}$ or more	$\pm 162 \mu\text{m}$
	Focusing step	Less than $4 \mu\text{m}$	$3.24 \mu\text{m}$

To satisfy these specifications during the design process, we devised a means for adjusting focal distance by placing two sheets of wedge-shaped glass face to face in the optical path of the optical system and by moving one of the sheets parallel to the aperture to change the thickness of the glass to be penetrated by the beam of light. The wedge-shaped glass sheet is moved by a lead screw device, which uses a stepper motor as a drive. It also serves to monitor the position of the glass by an encoder. An MoS₂ solid lubricant is used to lubricate all sliding parts.

A diagram of this arrangement is given in Figure 1, which its external appearance is shown in Photographs 1 and 2 [not reproduced].

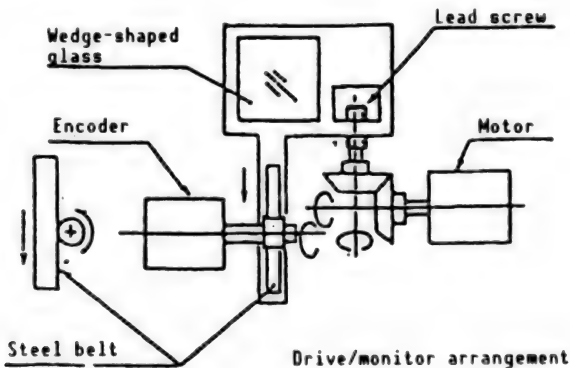


Figure 1. Conceptual Diagram of Focusing Mechanism

4. Evaluation Tests

In the process of development, we manufactured and evaluated a model focusing mechanism assembly before incorporating it into the optical sensor.

The details of each test and the summary of test results are shown below:

(1) Performance test

We measured the output of the encoder for the drive command of the motor and the position of the glass wedge. As indicated in Figure 2 (example of VFAM data), the results showed satisfactory degree of linearity.

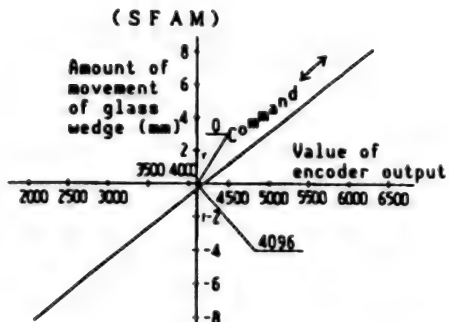


Figure 2. Example of Performance Test Data (VFAM)

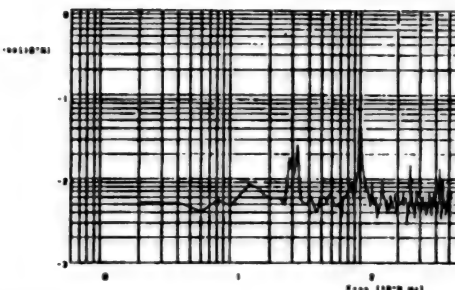


Figure 3. Example of Measurement of Disturbance Characteristics (SFAM)

There was no change before or after the mechanism environment test and the life test.

(2) Vibration test

We tested for the effects of sine wave vibration and random vibration separately by VFAM and SFAM, and confirmed that there were no problems.

(3) Life expectancy test

We conducted a 55-hour continuous action test in a vacuum chamber (less than 10^{-5} torr) and confirmed that it fully satisfied the specifications for operational life.

(4) Mechanical disturbance characteristics measurement test

We measured the force and torque generated when driving the focusing mechanism using a six-axis sensor. It was clear from these data that, in terms of mechanical disturbance, there were no problems in controlling satellite attitudes. Examples of the measured data (SFAM data) are shown in Figure 3.

5. Summary

We have developed an optical sensor mechanism to adjust focal point position on-board the ERS-1 and have confirmed by tests that it has been designed appropriately.

We wish to make effective use of our recent results to develop more complex mechanisms, including a mechanism to make on-board six-axis adjustment of sensor positions, so that we can meet mission requirements, which will become more precise than ever.

Finally, we express our gratitude and thanks to personnel of Fujitsu Ltd. and Mitsubishi Electric Corp. who helped us achieve these results as part of the ERS-1 project.

Conceptual Design for Advanced Microwave Radiometer

906C3836 Tokyo DAI33KAI UCHU KAGAKU GIJUTSU RENGO KOENKAI KOENSHU in Japanese
31 Oct-2 Nov 89 pp 510-511

[Article by Akimichi Nitta, Yasuyuki Ito, and Yuji Seto, Tsukuba Space Center, National Space Development Agency of Japan; and Toshio Imatani, Masaharu Miura, Hiroshi Harada, Hiroyuki Inhabata, and Hiroaki Nakaguro, Kamakura Works, Mitsubishi Electric Corp.]

[Text] 1. Background

The advanced microwave scanning radiometer (AMSR) to be carried by the future polar-orbit platform is an electronic scanning radiometer designed to observe physical phenomena, such as sea surface temperature, sea wind, cloud water content, and the amount of water vapor in the atmosphere. This is done by measuring microwave-band noise waves radiated from the sea surface or the atmosphere.

This report presents the principal parameters, system composition, design characteristics, and predicted performance of the AMSR based on the results of the conceptual design study.

2. Principal System Parameters

The principal parameters for the AMSR are shown in Table 2.1.

3. System Configuration

The system configuration of the AMSR is shown in Figure 3.1. In this system, the primary radiator array, which comprises 36 elements for the low-frequency bands (6 G and 10 G) and 72 elements for the high-frequency bands (18 G, 23 G, and 36 G), is installed opposite a trussed reflecting mirror and each primary radiator is connected to a tournament-form switch matrix via a polarization coupler.

The output of the switch is connected via the calibration section to the receiving section, which consists of one element for each low-frequency band and four elements for each high-frequency band. The calibration section is composed of a sky monitor, which is a low-temperature calibration source; a

Table 2.1 Primary Parameters for AMSR

Parameter	Value
Satellite altitude	708 km
Orbit condition	Sun synchronous orbit
Observation frequencies	6.6 GHz, 10.65 GHz, 18.7 GHz, 23.8 GHz, 36.5 GHz
Polarization	Vertical and horizontal
Absolute precision	Less than 1.5 K
Dynamic range	30-350 K
Angle of incidence	About 55°
Scanning shape	Conical scanning
Observation width	935 km
Receiving formula	Dickey comparative noise source
Antenna size	6 m x 2.7 m
Weight	Less than 400 kg
Power consumption	Less than 360 W

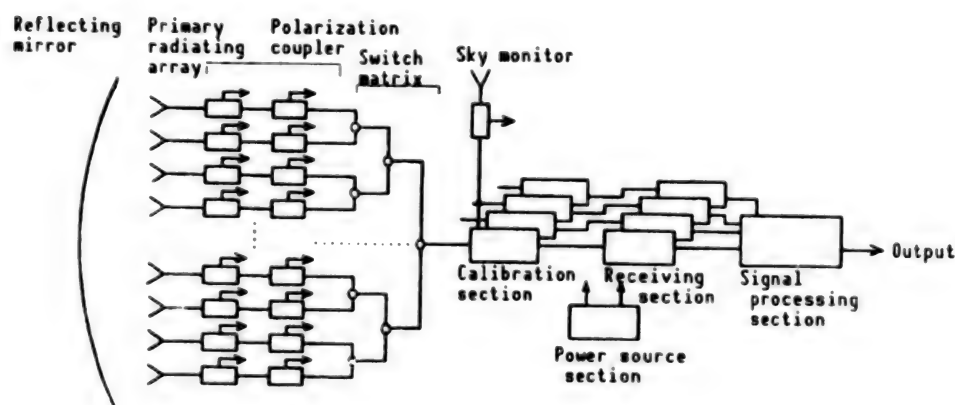


Figure 3.1 Block Diagram of AMSR System

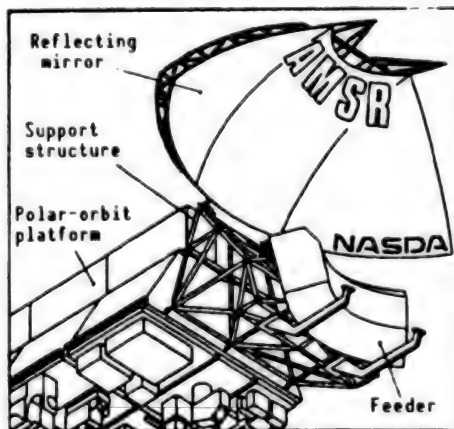


Figure 3.2 Schematic Diagram of AMSR

cold dummy, which is a high-temperature calibration source; and a Dickey comparative noise source. The receiving section handles frequency conversion and IF amplification and detection. Input is provided by the HEMT low-noise amplifier, which amplifies noise waves. Detection voltage is integrated and A/D converted in the signal processing section and then formatted and output as serial signals. A schematic diagram of the AMSR is presented in Figure 3.2. As Figure 3.2 shows, the AMSR consists of a reflecting mirror, a feeder, and a support structure.

4. Design Characteristics

The design characteristics of the AMSR include the following:

- (1) Operation of the AMSR does not affect the attitude of the satellite because it scans the ground with an electronically steered array.
- (2) It can effect conical scanning for a given angle of incidence to the ground surface by combining a torus reflecting mirror and the electronically steered array.
- (3) It has improved temperature resolution capability achieved through the use of a plural number of receivers and by multibeam scanning of the ground.
- (4) It has optimum beam propagation arrangement such that the ground footprints are homogeneous and in close proximity and that the high-frequency bands and the low-frequency bands can form matched beams.
- (5) It has a high distance resolution realized by using a large antenna.
- (6) It has improved temperature resolution achieved by using a HEMT amplifier at the RF front end.

5. Predicting Performance

The predicted performance of the AMSR is shown in Table 5.1. It fully satisfies the main performance requirements as its temperature resolution is always less than 0.6 and its beam efficiency is 80 percent or more.

6. Conclusion

We have reported on the AMSR. We are scheduled to carry out a more detailed design study of the system and eventually to build it.

Table 5.1 Predicted Performance of AMSR

Parameter	Predicted performance					Remarks
Observation frequency (GHz)	6.6	10.65	18.7	23.8	36.5	
Bandwidth (MHz)	400	100	200	400	1,000	
Temperature resolution (K)	0.23	0.51	0.55	0.45	0.41	15 300 K 1σ
Integral time (msec)	90	90	90	90	90	
Number of receivers (per polarized wave)	1	1	4	4	4	
Distance resolution (3 dB beamwidth) (km)	50.0 x 22.6	44.5 x 18.5	16.7 x 10.0	13.5 x 8.9	8.9 x 7.6	V polarized wave (example)
Beam efficiency (percent)	83.9	88.6	83.9	85.4	83.2	Same as above
Beam interval (km)	26		13 km			

System Parameters for Satellite-Mounted AVNIR

906C3836 Tokyo DAI33KAI UCHU KAGAKU GIJUTSU RENGO KOENKAI KOENSHU in Japanese
31 Oct-2 Nov 89 pp 512-513

[Article by Go Masuda, Kiyotaka Yashiro, Yoshio Tange, and Yuji Miyaji, National Space Development Agency of Japan; and Makoto Ono, Hirokazu Tanaka, Kyoko Osaki, and Akira Akazaka, Mitsubishi Electric Corp.]

[Text] 1. Introduction

An advanced visible near-infrared radiometer (AVNIR) is being designed for the earth observation platform technical satellite, which is scheduled to be launched by an H-II rocket in FY 1994. The BBM for the AVNIR is currently under development, but this report focuses on the system parameters of the AVNIR.

2. System Trade-Off

The AVNIR system consists of two major components. These are the optical system and the CCD.

The basic performance parameters of the AVNIR optical system include caliber, F number, focal distance, angle of visibility, instantaneous geometric field of view, and aberration. In addition, in studying the feasibility of the AVNIR optical system—presupposing the installation on the ADEOS—such physical characteristics as overall size, weight, thermal strain, resistance to radiation in outer space and the relative ease of manufacture must be considered in addition to its basic performance parameters. The large-caliber Schmidt refraction system has been selected as the AVNIR optical system as it can best satisfy performance requirements and is the most feasible after a trade-off involving several image-forming optical systems with consideration given to the various other factors. Also, a truss structure using CFRP pipes with a low coefficient of linear expansion for the lens barrel has been adopted to ensure that the AVNIR optical system will provide high-resolution images.

The conditions required of the CCD in converting light signals obtained by the AVNIR optical system into electric signals include sensitivity, registration between bands, blooming, resistance to radiation, and ease of manufacture.

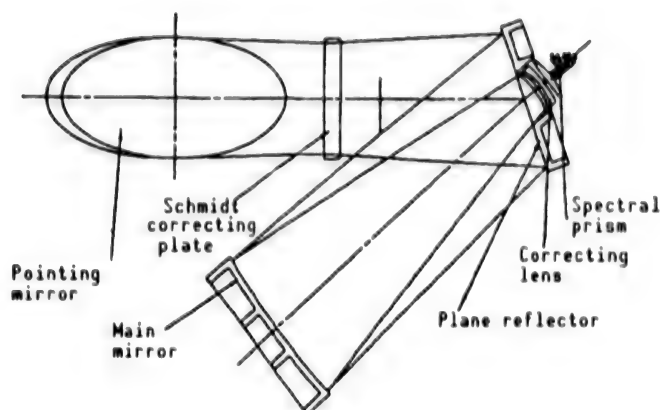


Figure 1. Arrangement of AVNIR Optical System

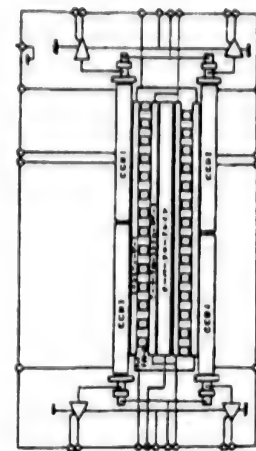


Figure 2. CCD Configuration

Based on these requirements, a staggered CCD with 5,000 picture elements for the multiband and 10,000 picture elements for the panchromatic band has been selected for the AVNIR. The CCD is provided with an electronic shuttering function for adjusting exposure to give the system the ability to handle a wide range of brightness levels caused by changes in latitude and seasonal variations.

3. System Parameters

The arrangement of the AVNIR optical system and the composition of the CCD derived from the system design study are shown in Figure 1 and Figure 2, respectively. Table 1 lists the projected performance levels for the AVNIR.

Table 1. Primary System Parameters for AVNIR

Band	Wave-length (μm)	Focal dis-tance (F num- ber)	Resolution		MTF		S/N (dB)	Input bright- ness (W/ m^2 / $\text{sr}/\mu\text{m}$)
			Dis-tance (m)	Radio-metric	Cross track	Along track		
Mul	.40-.50		16	8bit	.38 or more	.36 or more	46 or more	357
Mu2	.52-.62	f=800 mm	16	8bit	.36 or more	.25 or more	46 or more	346
Mu3	.62-.72		16	8bit	.35 or more	.25 or more	46 or more	296
Mu4	.82-.92	F/3.3	16	8bit	.27 or more	.25 or more	46 or more	192
Pan	.52-.72		8	8bit	.27 or more	.29 or more	39 or more	323

4. Conclusion

This report concerns only the primary parameters of the AVNIR but we are now proceeding with a detailed design of the BBM. We will make a separate detailed report when our tentative manufacture and test of the BBM is completed.

References

1. Masuda, et al., "Outline of Advanced Visible Near-Infrared Radiometer (AVNIR) To Be Carried by Earth Observation Platform Technical Satellite," in this collection of papers.

Examination of Mechanical System for AVNIR

906C3836 Tokyo DAI33KAI UCHU KAGAKU GIJUTSU RENGO KOENKAI KOENSHU in Japanese
31 Oct-2 Nov 89 pp 514-515

[Article by Go Masuda, Kiyotaka Yashiro, Yoshio Tange, and Yuji Miyaji, National Space Development Agency of Japan; and Hisayuki Mukae, Hideji Nishide, Eiichi Michioka, Hiromitsu Masumoto, Tetsu Iwamura, and Yasushi Takenouchi, Mitsubishi Electric Corp.]

[Text] 1. Introduction

The advanced visible near-infrared radiometer (AVNIR) to be carried by the Advanced Earth Observation Satellite (ADEOS) is an earth observation optical sensor equipped with a sophisticated Schmidt refraction system. This optical sensor must ensure a highly accurate relative positional arrangement among the optical system components to achieve an optical resolution of 8 m. The lens barrel must be designed not only with high dimensional accuracy but also high dimensional stability. This report describes the concepts underlying the structural and thermal design, focusing particularly on the design of the lens barrel.

2. Design Policy Aimed at Achieving Optical Performance Requirements

As indicated in the functional block diagram of the AVNIR optical system shown in Figure 1, light from the observed target reaches the light condensation/spectral diffraction section via the pointing mechanism. It is then converted in the photoelectric transfer section into electric signals that are then subjected to picture signal processing by the electric circuit unit. The light condensation/spectral diffraction section, which forms an important part of the optical system, is composed of three major optical elements: a Schmidt correction plate, a plane mirror, and a main mirror plus a group of correcting lenses. It acts to focus light on the detector by interfacing with the photoelectric transfer section.

In designing the main mirror and the focal plane that forms the focus in this optical system, it is necessary not only to assure absolute dimensions that are optically optimum for a nominal distance of about 800 mm but also to suppress dimensional change within several microns. We have adopted the

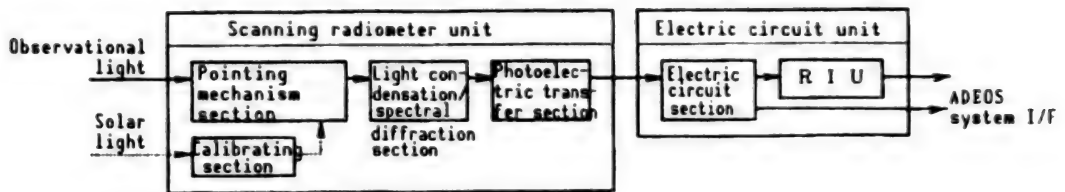


Figure 1. Functional Block Diagram of AVNIR

following design policy to enable the lens barrel to meet the requirements for absolute dimensions and dimensional stability:

- (1) Setting of absolute dimensions by optical adjustment during assembly.
- (2) Realization of lens barrel structure that is largely free from thermal deformation (development of materials with minimal coefficients of linear expansion).
- (3) Suppression of thermal deformation by high-stability heat control of the lens barrel section.
- (4) Adoption of lens barrel supporting structure that prevents external deformation from contributing to lens barrel deformation.

A proposed structure for the scanning radiometer unit is shown in Figure 2 and concepts for structural and thermal design, notably how to achieve the required level of dimensional stability, are described below.

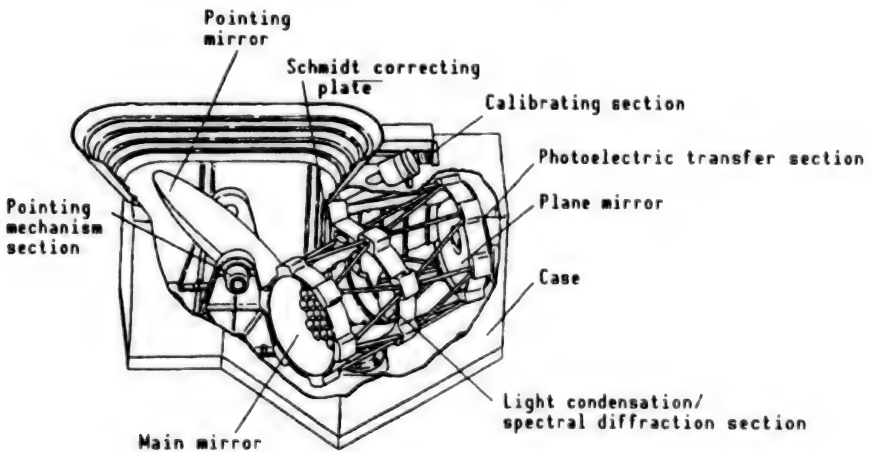


Figure 2. Structure of Scanning Radiometer Unit (Proposed)

3. Structural Design

In view of the level of dimensional stability necessary for optical performance, ordinary space-use structural materials must be carefully selected because of the magnitude of their coefficients of linear expansion. Thus, a lens barrel that is light in weight and that has a minimal coefficient of

linear expansion can be designed by using a CFRP with a low coefficient of linear expansion as the main structural material for the lens-barrel and forming a supporting truss structure. A highly elastic fiber will be used for the projected CFRP truss material. Its orientation is to be set so that its coefficient of longitudinal linear expansion will be negative and its design will be such that its overall coefficient of linear expansion, including the joint, will be $0 \pm 0.5 \times 10^{-6}/^{\circ}\text{C}$ when assembled. This scheme takes advantage of the fact that the coefficient of linear expansion of the carbon fibers that compose the CFRP is negative. We also hope to achieve a lens barrel structure that affords high dimensional stability against temperature change by selecting low-expansion metal materials, such as super amber, taking into consideration the fact that the coefficient of linear expansion of parts with complex worked shapes, such as the optical component support, is much the same as that of the truss material.

Meanwhile, if the lens barrel is subjected to an external force via the support structure as it is affected by an external deformation, the optical components are also deformed and the relative position changes, thus reducing optical performance. For this reason, the support structure is designed so that the lens barrel itself will not be affected by any external deformation. This is accomplished by adopting a structure for the lens barrel support that will be subject to deformation only in a certain direction. We have also taken care to prevent an internal force from affecting the optical components by adopting a mechanism with a flat spring for the optical component support.

4. Thermal Design

Basically, independent heat control is the principle for the AVNIR and, for its scanning radiometer unit in particular, the internal temperature must be stabilized to suppress the effect of thermal deformation. To accomplish this, the exothermic apparatus is located in a separate unit insofar as possible and the scanning radiometer unit thus thermally separated is singly subjected to heat control so that the internal temperature may be stabilized. Further, we believe that for those sections that have strict requirements for maintaining temperature within a narrow range, not only negative heat control by multi-layer insulation or other means should be used but also positive heat control using a heater should be applied so that temperature can be held within a range of 5°C .

5. Summary

We have described our concept for structure and thermal design, especially lens barrel design, which are important to the achievement of optical performance. Our work represents a part of the study of the AVNIR mechanical system, which is now at the BBM design stage.

Deployment Mechanism for Advanced Microwave Scanning Radiometer

906C3836 Tokyo DAI33KAI UCHU KAGAKU GIJUTSU RENGO KOENKAI KOENSHU in Japanese
31 Oct-2 Nov 89 pp 518-519

[Article by Akimichi Nitta, Yasuyuki Ito, Yuji Sato, Hidehiko Mitsuma, and Eiichi Endo, National Space Development Agency of Japan; and Ken Oishi, Eiichi Michioka, Yasushi Takenouchi, and Toshio Imatani, Mitsubishi Electric Corp.]

[Text] 1. Introduction

The advanced microwave scanning radiometer (AMSR) to be carried by the polar-orbit platform (POP) is a trussed reflecting mirror sensor measuring about 6 m x 3 m. It is equipped with a positioning mechanism and an unfolding mechanism. The mirror is housed during launching. When in orbit, the spring unfolds, and is then pushed by the positioning mechanism into position. The AMSR deployment mechanism is larger and heavier than conventional mechanisms. It cannot easily meet its weight requirement because the inertia of the AMSR reflection mirror is large and the requirements for positioning the mirror are strict. We have studied the problem of developing highly accurate spring and unfolding mechanisms capable of displacing objects with large initial inertia under the requirement of minimizing weight. This report describes the results of our efforts.

2. Purpose and Composition of Mechanisms

(1) Purpose

The positioning mechanism positions the reflecting mirror by causing the entire mirror to rotate around its connection to the POP (Figure 1).

The unfolding mechanism turns around the vicinity of the rift in the mirror and unfolds the mirror, which is divided into three parts, to form a single whole. (Figure 2 shows the unfolding action as viewed from position A in Figure 1.)

(2) Composition

In general, both the positioning mechanism and the unfolding mechanism consist of 1) a latch section, 2) a drive section, and 3) a structural section.

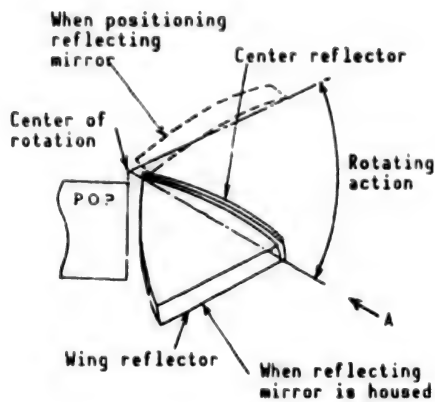


Figure 1. Conceptual Diagram of Positioning Mechanism

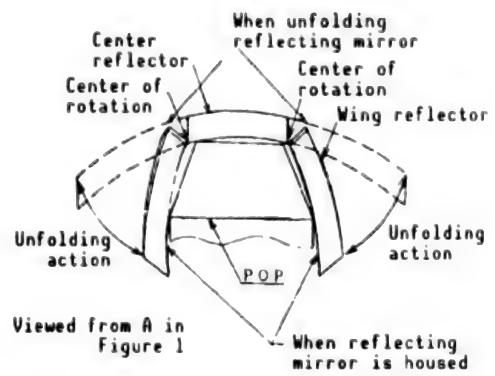


Figure 2. Conceptual Diagram of Unfolding Mechanism

The latch section fixes the mechanism by pushing the latch pin into the taper hole when the mechanism has completed its action. The drive section is composed of a coiled spring that serves as a drive source, a motor, and its accessories.

The structural section comprises the remaining elements. Its sliding parts are provided with vacuum lubrication by a solid lubricant.

3. Summary and Results of Study

Our study of the positioning and unfolding mechanisms included an examination of latch impact, accuracy, and rigidity. The following is a summary of the

Table 1. Target Design Values

Item	Conditions required for positioning mechanism	Conditions required for unfolding mechanism
Drive angle	0.873 rad	1.05 rad
Inertia of driven object	452 kg/m ²	18 kg/m ²
Mass of driven object	120 kg	30 kg
Positioning and unfolding accuracy	±0.025°	±0.025°
Positioning and unfolding time	Less than 5 minutes	Less than 5 minutes
Upper limit of speed at latch time	0.00434 rad/s	0.3 rad/s
Rigidity (Translation) after latching (Rotation)	3.8×10^7 N/m or more 5.3×10^5 Nm/rad or more	3×10^6 N/m or more 2×10^4 Nm/rad or more
Weight	Less than 10 kg/set	Less than 8 kg/set

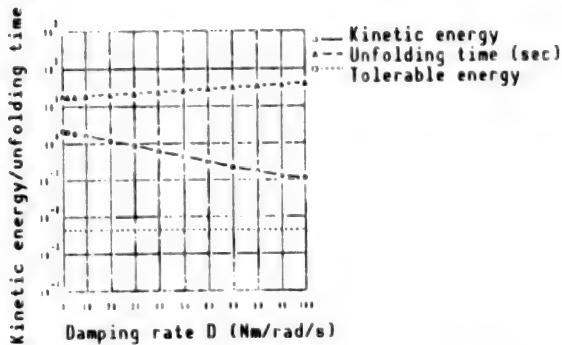


Figure 3. Study of Latch Impact

results of our study, presented item by item. Target design values are given in Table 1.

(1) **Latch impact:** We designed the mechanism so that the kinetic energy impact caused by latching would be less than what is structurally tolerable. We studied both the motor and the spring that are used as drive sources. For the spring, we added a damper to ease impact. We were able to derive a driving formula in which the latch impact was smaller than what is structurally tolerable by studying latch kinetic energy while using the damping rate of the damper as a parameter (Figure 3 is an example).

(2) **Accuracy:** This can be divided into the factors of reproducibility and thermal deformation. For reproducibility, we set an optimum value for clearance in the hinge section, taking clearance decrease due to temperature differences into consideration. As for thermal deformation, we optimized it for mechanical form and temperature distribution.

(3) **Rigidity:** We improved the rigidity of such components as the hinge section and the pin section of the latch mechanism, and produced an optimum design taking into consideration the weight increase required for this improvement.

Our study of latch impact was disclosed that a motor drive is best for the positioning mechanism which has to overcome great inertia. It has also indicated that a formula involving a damper along with a spring drive is best for the unfolding mechanism.

Accuracy: Both mechanisms satisfied the requirement for a value less than 0.025° as the total of reproducibility and thermal deformation.

Rigidity: We met the design requirement for the latch mechanism portion at a weight of about 3 kg for both mechanisms by improving hinge rigidity and latch pin rigidity at the level of rigidity required of the mechanisms.

We learned from this that the positioning mechanism and the unfolding mechanism can be designed at the target weights of less than 10 kg and 8 kg, respectively.

4. Summary

We made a conceptual study of the positioning and unfolding mechanisms for the AMSR. As a result, we were able to prepare designs that met the target values for driving very heavy objects with a high degree of accuracy under the strict weight limitations required for both the positioning and unfolding mechanisms.

In the future, we will proceed with detailed designs incorporating I/F conditions and environmental conditions.

Ion Engine System for ETS-VI

906C3836 Tokyo DAI33KAI UCHU KAGAKU GIJUTSU RENGO KOENKAI KOENSHU in Japanese
31 Oct-2 Nov 89 pp 526-527

[Article by Kenichi Kajiwara, National Space Development Agency; and Kazuo Sato, Sadanori Shimada, Harutaka Takegahara, and Sachifumi Goto, Mitsubishi Electric Corp.]

[Text] 1. Introduction

In the course of developing the ion engine system (IES), which is scheduled to be mounted on the Engineering Test Satellite VI (ETS-VI), performance tests and various environmental tests were performed on an engineering model (EM). These tests confirmed that there were no problems in terms of performance and environmental durability. This article reports on the results of these tests.

2. Tests and Test Results

In the tests conducted using the EM, performance and environmental durability were first evaluated at the component level. Next, tests were conducted at the subsystem level to assess performance and environmental durability. Figure 1 shows a block diagram of the IES.

• Component tests

The environmental durability tests (QT level), confirmed that performance was satisfactory. Environmental durability tests—consisting of a thermal vacuum test, a sine wave vibration test, a random vibration test, and an impact test—were performed for each individual component. The results of these tests demonstrated that the components developed for the EM have satisfactory environmental durability to meet the design standards for the ETS-VI.

• Subsystem tests

Figure 2 shows the test configuration at the subsystem level. It was confirmed that the IES enters the beam jet mode (thrust generation) 5 minutes after receiving the "IES START" command and that there are no problems in terms of the interface between individual components. Table 1 shows performance levels at representative operation points.

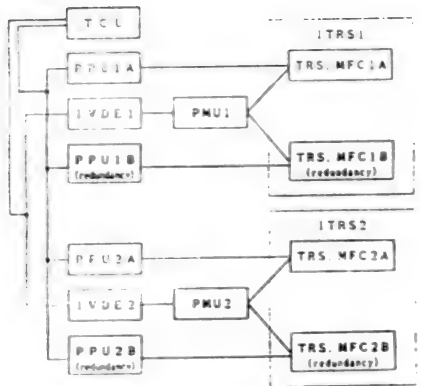


Figure 1. Block Diagram of IES System

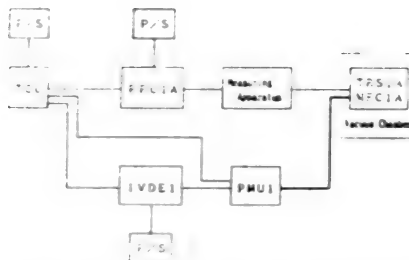


Figure 2. Test Configuration

Table 1. Overall Performance

Operating parameter	Value
Beam voltage/current	1000 V/481 mA
Accelerator voltage/current	-46 V/-2.2 mA
Discharge voltage/current	37.0 V/3.39 A
Cathode keeper voltage/current	3.9 V/0.50 A
Neutralizer keeper voltage/current	20.6 V/0.50 A
Total power per TRS	619.8 W
TRS efficiency	77.6%
Total power per MFC	1.5 W
Total power per PPU	721.2 W
PPU efficiency	85.9%
Total efficiency	66.7%
Mass flow rate	
Main hollow cathode	2.4 SCCM
Main propellant feed	5.5 SCCM
Neutralizer hollow cathode	0.4 SCCM
Thrust (individual thruster)	25.1 mN*
Specific impulse (individual thruster)	3142 s*
Ion production cost	264.8 eV/ion
Propellant utilization efficiency	808.8%
TCU power	7.3 W
IVDE power	1.0 W
PMU power	1.4 W

*: Excluding beam divergence and doubly charged ion losses

Electric- and magnetic-field radiation noises from the thruster were also measured with the EMC test. Figure 3 shows the results of the test. Electric-field radiation noises that were not within the specification limits were observed in a frequency range of 1-200 MHz. It was ascertained, however, that these noises were caused by power supply switching and by the electron cyclotron motion in the discharge chamber, and that they did not effect the satellite system because the frequencies used were different. For the ITRS and the PMU, which are installed outside the satellite, vibration resistance

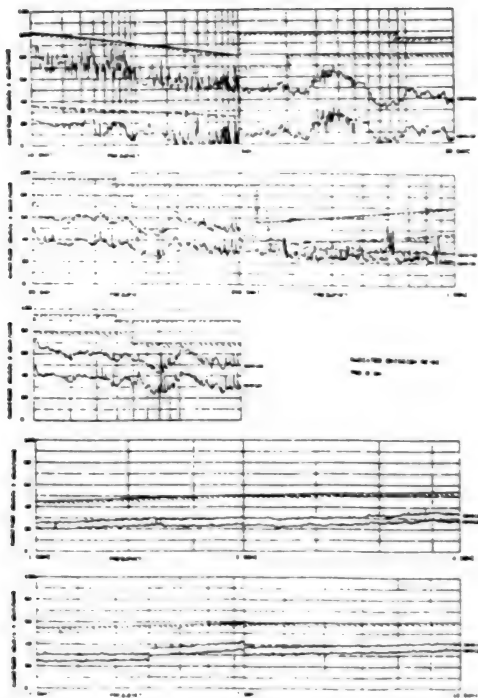


Figure 3. Results of EMC Test

was confirmed by performing acoustic tests in a state where these devices were integrated on the IES panel (Figure 4 [not reproduced]).

3. Summary

Our tests confirmed the performance and environmental durability of each component and demonstrated that the interface between components poses no problems.

The overall performance of the IES meets the required values. The information gained from these tests will be reflected in future designs and will be fully used in developing the prototype flight model which then becomes a mission-capable device.

References

1. Shimada, S., "25th Joint Propulsion Conference," AIAA-89-2267.
2. Takegahara, et al., "32nd Space Sciences & Technology Conference," 2G9, 1988.

Development of Power Supply for ETS-VI Ion Engine

906C3836 Tokyo DAI33KAI UCHU KAGAKU GIJUTSU RENGO KOENKAI KOENSHU in Japanese
31 Oct-2 Nov 89 pp 528-529

[Article by Kenichi Kajiwara, National Space Development Agency; and Kazuo Iwanami, Hiromichi Kouchi, and Yasuhiko Onuma, Komukai Factory, Toshiba Corp.]

[Text] 1. Introduction

The total output of the power production unit (PPU) of the ion engine (level of thrust = 20 mN) for north south orbital control of the Engineering Test Satellite VI (ETS-VI) is 787 W. The PPU is a nine-output, multisystem power supply that can provide as much as 1,200 V. In this country, it is the largest unit of its kind that has been developed for satellite use. In particular, development of the PPU has focused on the high voltage power supply (beam/acceleration power supply) which accounts for about 80 percent of the total output. In this context, consideration effort was devoted to securing greater efficiency, a reduction of weight and increased reliability. To meet these objects, the PPU features a voltage-doubled rectifying circuit, a current-resonance invertor and a current-feedback drive circuit. At present, development tests have been completed on a single engineering model (EM).

2. Outline of Power Supply

The PPU is one of the components of the ion engine system. It receives a bus power supply (about 50 VDC) from the satellite. It receives control signals from the thruster control unit (TCU) and supplies the power necessary for the ion thruster. The power supply output to the ion thruster consists of a nine-output seven-system power supply part. In addition, the PPU is also provided with an auxiliary power supply to control these power sources and a telemetry monitor conversion circuit for output of the monitor and telemetry signals related to the ion thruster.

Figure 1 shows a block diagram of this power supply. Figure 2 [not reproduced] is a photograph of the PPU.

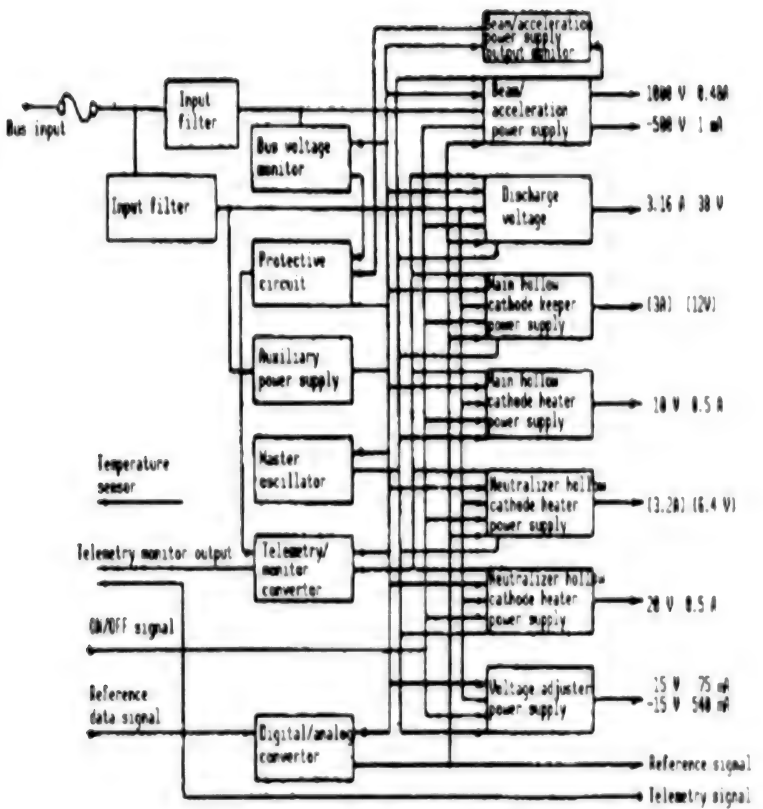


Figure 1. Block Diagram of PPU

3. Characteristics

The beam/acceleration power supply unit consists primarily of a voltage-doubled rectifier, a current-resonance inverter, a boosting chopper regulator, and a drive control circuit. Figure 3 is a block diagram of this unit. The voltage-doubled rectifying circuit adopted here has many functions that are not found in conventional voltage-boosting circuits. The purposes of using these circuits are:

- (1) Two kinds of voltage can be output with one converter transfer winding.
- (2) High-frequency AC voltage, which is regarded as a cause of corona discharge continuation, can be lowered.
- (3) Compared with the number of boosting steps, the voltage drop by load current is very small.

In the actual deterioration of the number of boosting steps, a condenser for higher voltage became necessary as the number of steps increased. Therefore, the number of boosting steps was determined based on a trade-off for a drop in the AC voltage of the inverter.

The current-resonance inverter has an inductor inserted in the DC line of the primary-side center tap of the transformer and performs current-resonance operations with the equivalent composite capacity of the inductor and the rectifying circuit. This eliminates the intersecting part of the voltage and

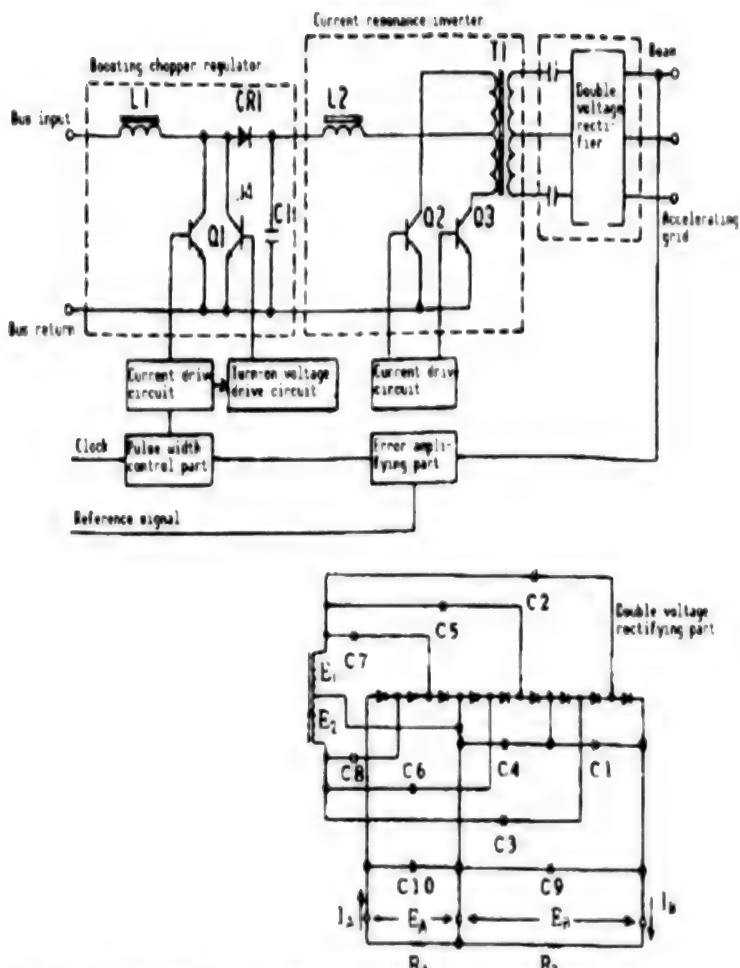


Figure 3. Block Diagram of Beam/
Acceleration Power Supply

current of the switching element, reduces switching loss and is aimed at higher efficiency. Figure 4 shows the operational state of the switching transistor.

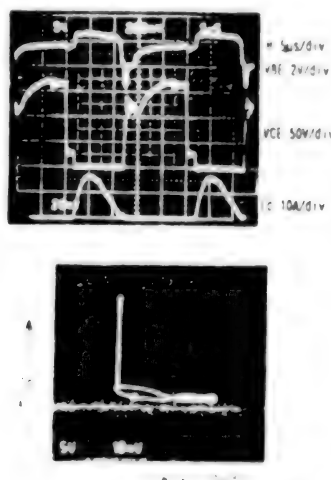


Figure 4. Switching Waveform of Current Resonance Invertor

Since the boosting chopper regulator part has an inductor inserted in series on the input side, it has the advantage of continuous input current and of being capable of reducing the ripple current to the input side.

The drive control circuit has an externally applied trigger for use only at the time of turning on and off by adopting a current feedback drive circuit using a current transformer. At the time of actual turning on by the transistor, even a considerable overdrive cannot reduce loss at the time of turning on because of the transition frequency limit (f_t : frequency at which the current amplifying factor becomes 1) of the switching transistor. This f_t limit value depends on the collector current of the transistor and the f_t limit value deteriorates and increases loss as the current increases. In the drive circuit described here, a transistor is connected in parallel to prevent current feedback by external turning on of current feedback to improve the f_t limit value and to reduce switching loss at the time of turning on by distributively allowing the current to flow across the small transistor connected in parallel.

4. Conclusion

The authors have completed development tests on the EM, confirmed its functions and performance levels, and attained the expected targets, for example, an overall efficiency of 85~87 percent and a weight of 9.9 kg.

The authors are scheduled to perform combined tests at the satellite system level including extended operation tests with the ion thruster. These tests are aimed at optimizing the design of mission-capable units.

Development of Ion Engine Thruster Control Units

906C3836 Tokyo DAI33KAI UCHU KAGAKU GIJUTSU RENGO KOENKAI KOENSHU in Japanese
31 Oct-2 Nov 89 pp 530-531

[Article by Kenichi Kajiwara, National Space Development Agency; and Kazuo Iwanami, Hiromichi Kouchi, Kiyoshi Murasawa, and Hideaki Ando, Komukai Factory, Toshiba Corp.]

[Text] 1. Introduction

This article reports on the manufacture of development tests performed on an ion engine thruster control unit (TCU) and an engineering model (EM) of the Engineering Test Satellite VI (ETS-VI).

2. Outline of TCU

The TCU is a component of the ion engine system (IES). It controls the ion engine power production unit (PPU), the ion engine valve drive circuit (IEVD), and the ion engine propellant storage and supply unit (PMU) with commands from the remote interface unit (RIU). It returns telemetry control results from these devices to the RIU in a digital format. Photograph 1 [not reproduced] shows the appearance of the TCU.

3. Configuration

The principal components of the TCU are as follows. Figure 1 is a functional block diagram of the TCU.

(1) CPU unit	Central processing unit (8-bit MPU mounted)
(2) Memory unit	Memory (ion engine control flight software (ICFS) mounted)
(3) Clock timing unit	Internal timing generation
(4) Magnitude command unit	Processes magnitude command
(5) Serial telemetry unit	Processes serial telemetry
(6) Digital input unit	Digital input processing
(7) Analog conversion unit	Analog/digital conversion
(8) Digital output unit	Digital output processing
(9) Analog input/digital output register unit	Analog input signal selection/digital output data/serial-parallel conversion

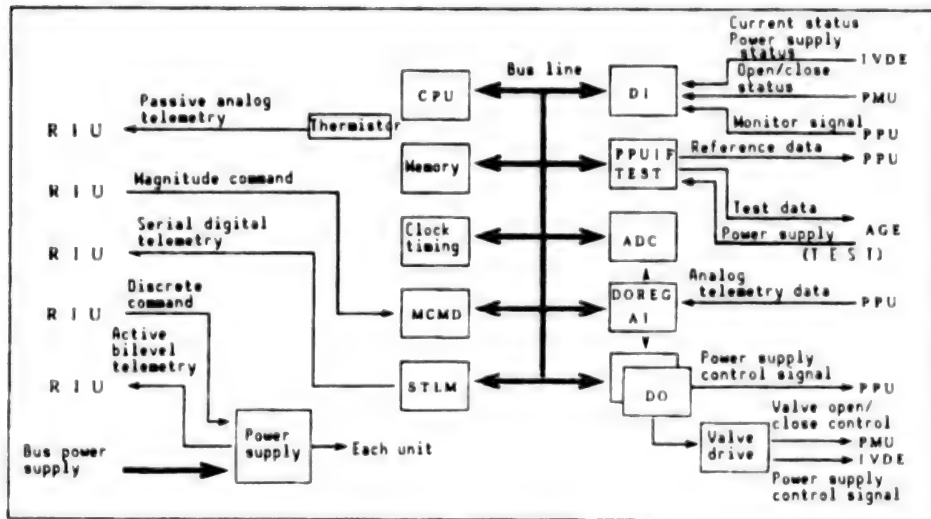


Figure 1. Functional Block Diagram of TCU

- | | |
|------------------------------|--|
| (10) Valve drive unit | Drives IEVD and PMU |
| (11) PPU interface/TEST unit | PPF reference data interface/ground assistance equipment (GAE) interface |
| (12) Power supply part | DC/DC power supply |

4. Characteristics

The TCU has the following characteristics:

- (1) Control rules are easy to change because of the stored program control system.
- (2) A serial interface system, which has a significant weight advantage, is used for the internal bus.
- (3) Power consumption has been significantly reduced by adopting CMOS devices and a ROM power strobe system.

5. Principal Features

Table 1 shows the principal features of the TCU.

6. Development Tests

The following development tests were performed on the TCU to confirm the appropriateness of its electric, mechanical, and installation designs, and the manufacturing process.

- (1) Mechanical inspection
Dimensions, weight, and center of gravity.
- (2) Electric performance tests
Commands, telemetry, input-output, and control modes.

Table 1. Principal Features

Item	Explanation	Value
Control system	Stored program system	
Control mode	Thruster control Valve control	5 kinds 2 kinds
Command	Discrete Magnitude	5 kinds 14 kinds
Telemetry	Analog bilevel Passive analog Serial digital	1 kind 1 kind 77 kinds
Input-output	Digital input Digital output Analog input Serial digital output Test data output	48 CHs 64 CHs 64 CHs 4 CHs 1 CH
MPU	8-bit MPU	
Memory	ROM RAM	8K bytes 8K bytes
Power consumption	7.01 W (maximum)	
Dimensions	287.6 x 298.0 x 157.2	
Weight	7.75 kg	

(3) Electromagnetic appropriateness tests

Magnetic-field radiation noise limit (RE01)
 Electric-field radiation noise limit (RE02)
 Power supply line conduction noise limit (CE01, 03)

(4) Thermal vacuum tests (-15°C~+88°C)

Exposure to low temperature, exposure to high temperature, immersion in low temperature, and immersion in high temperature.

(5) Vibration tests

Application of sine wave vibration and random vibration in three axis directions in the conducting stage.

(6) Impact test

Application of impact in three axis directions in the conducting state.

7. Conclusion

The appropriateness of the design of the TCU has been confirmed through development tests on the engineering model (EM).

Hereafter, the prototype flight model (PFM) will be manufactured and tested on the basis of an evaluation of the performance of an electric system model of the ETS-VI.

References

1. Umemoto, et al., "Manufacturing Ion Engine Thruster Control Device," 30th Space Sciences & Technology Conference, 2D17.
2. Kajiwara, et al., "Test Manufacturing and Testing of Thruster Control Device for ETS-VI Ion Engine," 32nd Space Sciences & Technology Conference, 2G12.

Propulsion Performance of Hall-Type Ion Thruster

906C3836 Tokyo DAI33KAI UCHU KAGAKU GIJUTSU RENGO KOENKAI KOENSHU in Japanese
31 Oct-2 Nov 89 pp 532-533

[Article by Kimiya Komurasaki, Satoshi Ichikawa, Tsuruo Kobayashi, and Yoshihiro Arakawa, Faculty of Engineering, University of Tokyo]

[Text] 1. Introduction

The authors have been involved in research on the Hall-type ion thruster and, in a recent experiment, measured thrust using a pendulum-type thrust stand. The authors further investigated the propulsion performance of the Hall-type ion thruster by measuring the energy distribution of the ion beams using a multi-grid energy analyzer. They also measured beam quantity with an ion collector.

2. Experiment

Figure 1 is a diagram of the Hall-type ion thruster used in this experiment. The accelerating part is designed to be short to reduce ion loss from the wall. In this experiment, the subdischarge of the plasma generation part is used only to ignite the main discharge and measurements were taken after the subdischarge had stopped following the start of steady operation. Xenon and argon were used as the propellant. Figure 2 shows the thrust measuring system. The thruster was mounted on a thruster stand supported by two bearings and vacuum bellows, and the stand displacement that occurred in proportion to thruster thrust was measured.

Further, an energy analyzer with three grids was used to measure the energy distribution of the ion beams.

Propulsion efficiency is defined as:

$$\eta_T = \frac{T^2}{2mV_a I_a} \quad (1)$$

where V_a : accelerating voltage

I_a : accelerating current

m : propellant flow rate

T : thrust

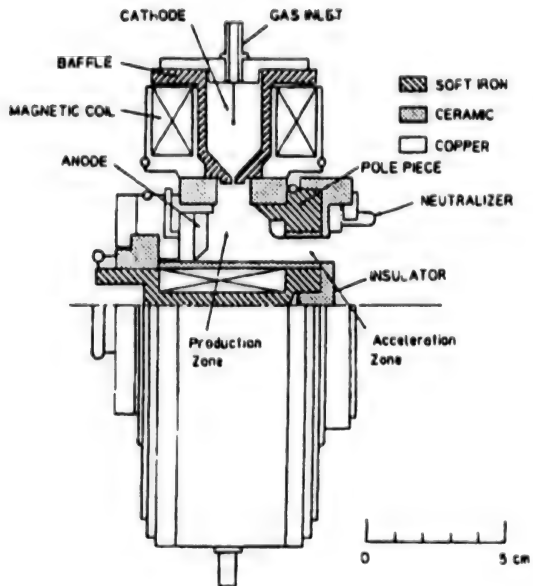


Figure 1. Hall-Type Ion Thruster

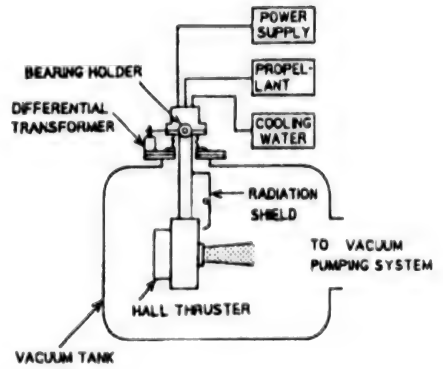


Figure 2. Thrust Measuring System

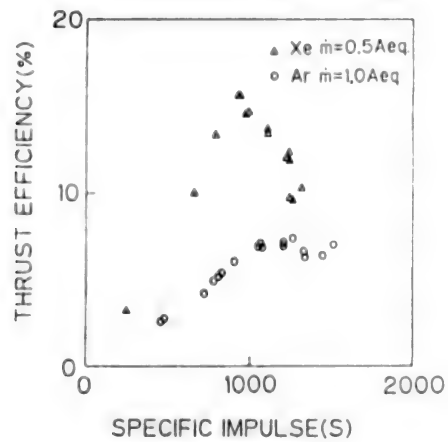


Figure 3. Thrust Performance

Figure 3 shows the propulsion performance of this thruster. For a mathematical expression, let ion beam quantity be I_b and its average energy be \bar{V} . Thus, propellant use efficiency, η_u , acceleration efficiency, η_a , and the ratio of the average energy of beams to accelerating voltage, η_E , can be represented as shown below.

$$\eta_u = \frac{I_b}{\dot{m}}, \quad \eta_a = \frac{I_b}{I_s}, \quad \eta_E = \frac{\bar{V}}{V_s} \quad (2)$$

Therefore, propulsion efficiency can be represented by the above three efficiency factors as shown below.

$$\eta_T^* = \eta_E \eta_s \eta_x \quad (3)$$

Measurements of the energy distribution of ion beams showed that η_E changed with the acceleration parameter. Table 1 compares the propulsion efficiency η_T^* , which is calculated from expression (3) in the case where $\eta_E = 60$ percent and the propulsion efficiency η_T , which is obtained by measuring the thrust.

Table 1. Thrust Efficiency for Each Operational Parameter

m (Aeq.)	V_a (V)	I_a (A)	I_b (A)	T(g)	η_a (%)	η_s (%)	η_T^* (%)	η_T (%)
Ar 1.25	200	1.85	0.50	0.53	40	27	6.5	7.0
Ar 1.50	200	2.52	0.73	0.76	49	29	8.5	9.0
Ar 1.75	200	3.08	0.92	1.01	52	30	9.3	11.2
Xe 0.50	150	1.45	0.40	0.67	80	28	13.2	14.5
Xe 0.50	180	1.72	0.47	0.76	94	27	15.4	13.4

References

1. Komurasaki and Arakawa, "32nd Space Sciences and Technology Conference," 1988 pp 758-759.

Basic Experiments on Microwave Discharge Ion Thruster

906C3836 Tokyo DAI33KAI UCHU KAGAKU GIJUTSU RENGO KOENKAI KOENSHU in Japanese
31 Oct-2 Nov 89 pp 534-535

[Article by Toshiaki Yasui, Hirokazu Tawara, Kenichi Onoue, and Takao Yoshikawa, Faculty of Basic Engineering, Osaka University]

[Text] 1. Introduction

A microwave discharge ion thruster generates plasma through microwave discharge in the place of dc glow discharge as in conventional electron impact ion thrusters. Since microwave discharge is electrodeless discharge, it prevents reduced operational life due to electrode loss, which has been a problem. In addition, it can generate clean plasma. Other advantages include a uniform plasma that can be generated in a discharge chamber, a wide operational range, and a simple physical structure. Making full use of these characteristics, microwave discharge is being actively applied in industry as the plasma source for semiconductor manufacturing.

This article reports on an ion source that has been test manufactured to clarify the basic operational characteristics of the microwave discharge ion thruster and presents the results of operational experiments performed on the thruster.

2. Experimental Device

Figure 1 shows a cross section of the microwave discharge ion thruster used in this experiment. The thruster consists principally of a cavity resonator that makes microwaves resonate, a discharge tube to confine the plasma, and the electrode, which pulls out ions.

The cavity resonator is a bronze cylinder with an internal diameter of 120 mm. It has a discharge tube on one surface and a wall movable in the axis direction inserted from the other surface. Moving this wall generates stationary microwaves in the resonance chamber. This resonator generates TM_{011} -mode or TM_{211} -mode stationary waves. The discharge tube is a quartz glass tube with one end sealed. It has an internal diameter of 80 mm. By moving the movable electrode part in the discharge tube, an arbitrary discharge chamber volume is obtained. The electrode plate is made of stainless steel. It is a multihole

plate that has 55 holes 6 mm in diameter. A neutralizer that has a stretched wire is located inside this electrode plate. The propellant is introduced into the discharge chamber from two directions along the inner wall from the electrode side (vacuum tank side) in the discharge tube. Ions in the discharge chamber are pulled out by the electric field and are exhausted after being electrically neutralized by the neutralizer.

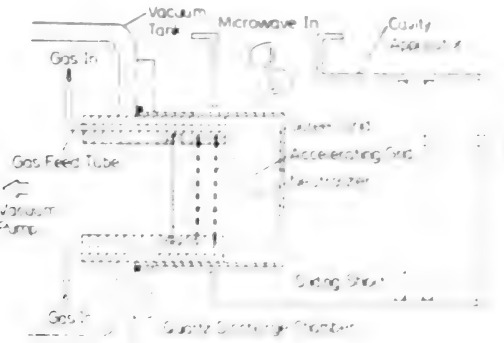


Figure 1. Thruster

3. Operational Experiments

In the operational experiments performed on the thruster, Ar gas was used as the propellant. Figure 2 shows the introduction paths for the microwaves and gas together with a layout of the power supply for the movable electrode. The 2.45 GHz microwaves generated by the magnetron are introduced into the resonator after undergoing impedance matching by a stub tuner. At this time, the supplied power is measured by the power monitor, which is equipped with a directivity coupler. Operational characteristics are investigated by measuring the ion beam quantity exhausted from the thruster, using propellant flow rate, acceleration voltage, and discharge chamber volume as parameters. The ion beam quantity is estimated by measuring I_n or I_a and I_s , as shown in Figure 2.

3. Conclusion

This experiment involved plasma generation by resonance heating using a cavity resonator. At present, microwaves are introduced into the cavity resonator with a rectangular waveguide, but an introduction method using a probe coupling is also possible. An alternate method scheduled to be tried in an effort to improve the efficiency of plasma generation involves arranging a Kapp's magnetic field around the resonator. Heating is also possible for a microwave source that does not use a resonator and where the ECR resonance is produced by a magnetic field (Figure 3). Experiments are scheduled to be made on such plasma generation methods after further investigation.

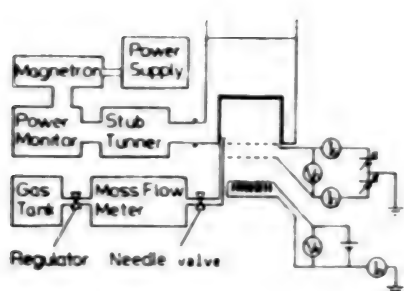


Figure 2. Experimental System

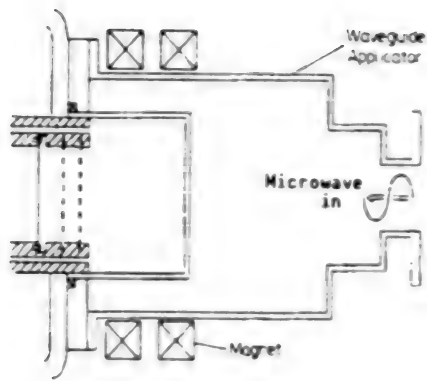


Figure 3. ECR Resonance Thruster

Microwave Discharge Ion Engine

906C3836 Tokyo DAI33KAI UCHU KAGAKU GIJUTSU RENGO KOENKAI KOENSHU in Japanese
31 Oct-2 Nov 89 pp 536-537

[Article by Yasuo Horiuchi, Arata Sashima, and Hiroaki Miyoshi, University of Tokyo Graduate School; and Hitoshi Kuninaka and Kyoichi Kuriki, National Space Development Agency]

[Text] 1. Introduction

This article reports the results of measurements of the propulsion performance, the operational characteristics of the plasma source, and the microwave resonance characteristics of a non-ECR microwave discharge ion engine that the authors manufactured. A principal characteristic of this thruster is that plasma is generated in the two discharge chambers for acceleration and a neutralizer, respectively, with one microwave power supply. The advantages of this thruster are as follows:

- 1) The discharge is electrodeless, thereby avoiding such problems as electrode loss and heat loss.
- 2) No hollow cathode is used and the structure is simple.
- 3) There is a possibility that the number of power supplies can be sharply reduced as compared to the conventional type.

2. Outline of Thruster

Figure 1 shows a cross section of the thruster and Table 1 presents the basic specifications. Argon is used as the propellant. The 2.45 GHz microwaves generated by the magnetron pass through the waveguide, enter the resonance (cavity), and generate a stationary wave there. Microwave matching is performed by changing three variables: the inductive iris (aperture), which is put halfway into the waveguide; the length of the resonance, which changes with the movable bottom (plunger); and the size of the reflection ring. In the experiment, the TM011 mode was used and up to 95 percent or more efficiency was obtained.

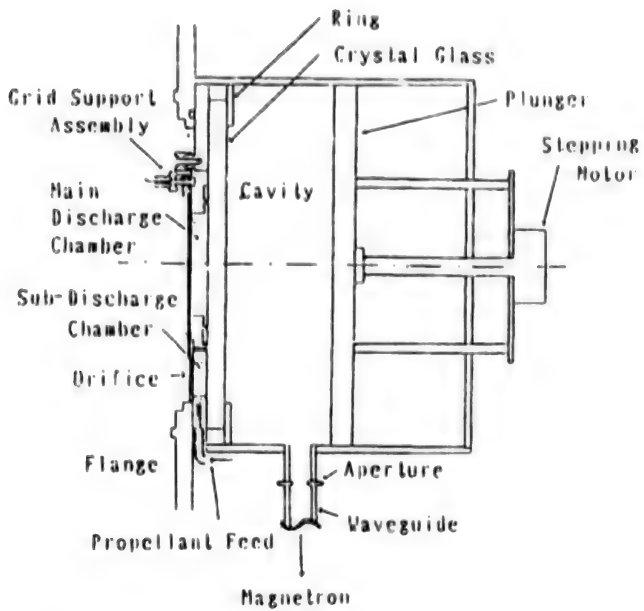


Figure 1. Thruster Cross Section

Table 1.

Parameter	Value
Diameter of main discharge chamber	6.0 cm
Diameter of auxiliary discharge chamber	2.6 cm
Length of discharge chamber	1.1 cm
Grid material	Stainless steel
Thickness	0.5 mm
Hole diameter	2.0 mm
Aperture	0.27
Microwave supply power	150 W
Propellant	Ar
Operating current	0.7 eqA
Ion beam current	180 mA
Total accelerating voltage	2.0 kV
Effective accelerating current	1.6 kV
Propellant use efficiency	0.26
Thrust	4.3 mN
Specific thrust	2400 sec
Ion cost	833 eV

The power stored in the cavity enters the discharge chamber via the quartz glass and generates a plasma with a density of $10^{11}\text{--}10^{12}\text{cm}^{-3}$. However, since this density exceeds the cutoff level for microwave density, the microwave power is absorbed by the microwave absorbing layer (thickness: about 1 mm) near the quartz glass surface.

The discharge chamber (length; 11 mm) is divided into two electrically insulated parts. One is the main discharge chamber (internal diameter: 6 cm) for the ion engine and the other is the auxiliary discharge chamber (internal diameter: 2.6 cm) for the neutralizer.

The acceleration system consists of two grids, a screen and an acceleration grid, and is made of stainless steel.

3. Experimental Results

Figure 2 shows microwave resonance characteristics. This figure shows large resonance peaks at three places.

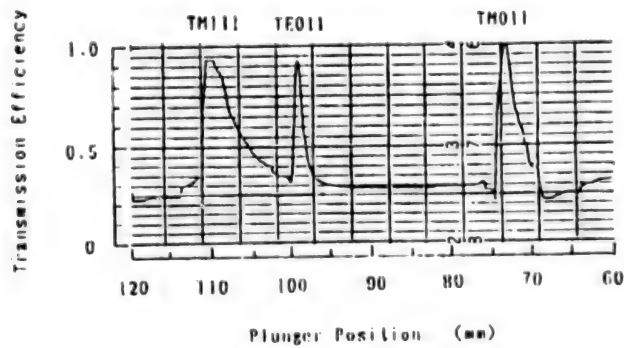


Figure 2.

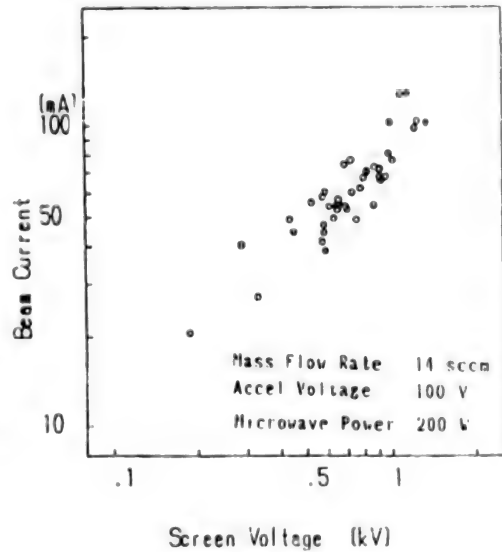


Figure 3.

These are thought to be TM011, TE011, and TM111 modes, based on the positions of the resonance points. The positions of the resonance points shift with changes in the propellant flow rate and the power supplied to the microwave generator, but the magnitude of such shifts is very small in the thruster operation range, and the thruster can be operated in the state where matching parameters could be assumed to be constant. The presence of the plasma in the auxiliary discharge chamber has virtually no influence on the positions of the resonance points, but a change in plasma brightness is observed as the ratio of the propellant flow rates in the main and auxiliary discharge chambers varies. This is thought to reflect a change in the power distribution ratio. In the future, it will be important not only to clarify the change in this power distribution ratio but also to establish a method for controlling the distribution ratio.

Figure 3 shows the current-voltage characteristics of the thruster. Propulsion performance at this time is as follows: The extracted ion current is 120 mA when the total acceleration voltage is 1.2 kV and the effective acceleration voltage is 1.1 kV.

Propellant for 150 mN Ion Thruster

906C3836 Tokyo DAI33KAI UCHU KAGAKU GIJUTSU RENGO KOENKAI KOENSHU in Japanese
31 Oct-2 Nov 89 pp 538-539

[Article by Hideki Yoshida, Hiromichi Kouchi, and Kiyoshi Hashimoto, Toshiba Corp.; and Hiroshi Miyauma, and Kenichi Kajiwara, National Space Development Agency]

[Text] 1. Introduction

Xenon (Xe) is currently used as the propellant for ion thrusters. However, Xe will be in short supply¹ in the space mass transportation age, which will begin around the year 2000. This article, therefore, investigates the possibility of using inactive gases (He, Ne, Ar, Kr) as substitutes. The ion thruster used for this study is an electron impact thruster that generates 150 mN of thrust (Figure 1). Toshiba Corp. is currently exploring such a thruster in cooperation with the National Space Development Agency.

2. Method of Investigation

The investigation was performed simply by changing the physical property values of Xe in the analytical model that was used in the basic design of the thruster shown in Figure 1. This analytical model has so far performed satisfactorily in experiments and is thought to be sufficiently reliable. The collision process is supposed to consist only of monovalent and bivalent ion generation processes and radiation processes. The ionization cross section is the experiment data represented by Drawin's formula and the cascade excitation cross section is the second-level model. Electron energy distribution is supposed to be a two-temperature model, and the magnetic field confinement of plasma is supposed to be performed by a five-ring cusp magnetic field (Sm-Co magnet). The electrode structure has the following parameters: beam voltage: 1 kV; acceleration voltage: -500 V; screen grid thickness: 0.3 mm; hole diameter: 2.2 mm; aperture: 73.1 percent; acceleration grid thickness: 0.5 mm; hole thickness: 1.3 mm; aperture: 25.5 percent; grid interval: 0.8 mm; and plasma diameter: 30 cm.

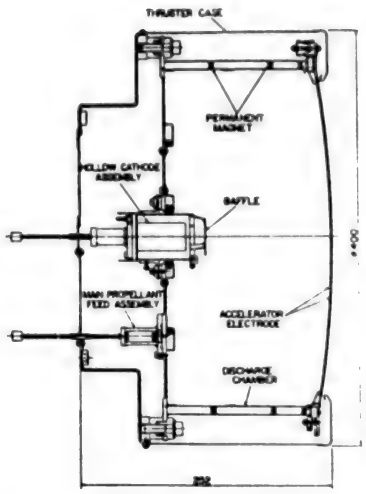


Figure 1. Ion Thruster

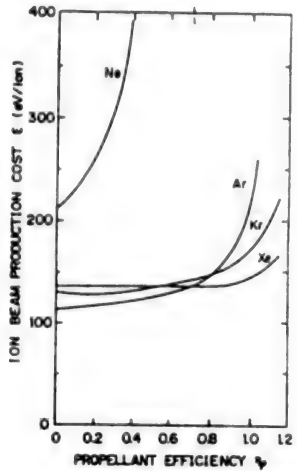


Figure 2. Ion Generation Cost

Since the thrust level of 150 mN is independent of the kind of propellant, the solutions to be obtained involve whether or not a propellant use efficiency of 90 percent is attainable and, if attainable, what is the cost of ion generation and what is the rate of power consumption.

3. Results

Figures 2 to 5 show the relationship of ion generation cost, the temperature of high-speed electrons, and the densities of monovalent and bivalent ions to propellant use efficiency. Table 1 shows the thruster performance for each propellant. The following conclusions can be drawn from the data presented in the table.

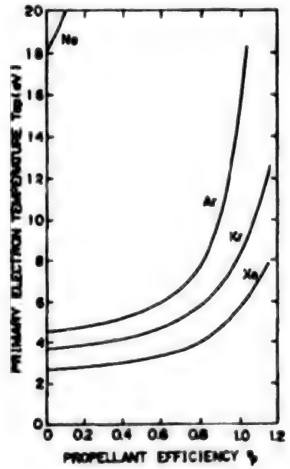


Figure 3. Temperature of High-Speed Ions

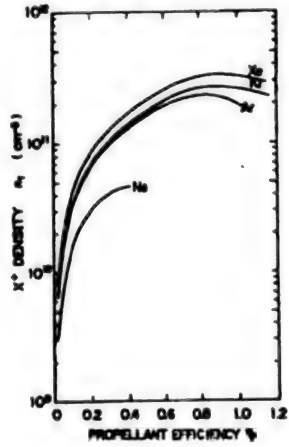


Figure 4. Density of Monovalent Ions

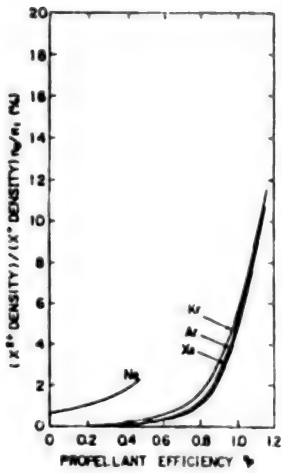


Figure 5. Proportion of Bivalent Ions

(1) When Kr is used, the ion generation cost is 1.13 times that when Xe is used, the discharge power is 1.42 times that when Xe is used, and the power consumption is 1.27 times that when Xe is used. However, since the same hollow cathode can be used, Kr is satisfactory for use in the thruster during the current developmental stages.

(2) When Ar is used, the ion generation cost is 1.22 times that when Xe is used, the discharge voltage is 2.22 times that when Xe is used, and the power consumption is 1.86 times that when Xe is used. Since the same hollow cathode can be used, Ar also can be used in the thruster during the current developmental stages if the cooling method is strengthened.

(3) He and Ne are for use in high-output thrusters and are not suitable for use in the thruster during the current developmental stages.

Table 1. Thruster Performance for Each Propellant

Parameter	Symbol	He	Ne	Ar	Kr	Xe
Atomic number		2	10	18	36	54
Atomic weight	A	4.00260	20.179	39.948	83.80	131.50
Ion enthalpy (eV)	E_{10}	24.588	21.565	15.760	14.000	12.130
	E_{21}	54.418	40.964	27.62	24.56	21.21
Strongest radiation beam (eV)	E_{EX}	21.218 (584.33 Å)	16.848 (735.89 Å)	11.828 (1048.22 Å)	10.033 (1235.82 Å)	8.437 (1469.62 Å)
Thrust (mN)	F	150	150	150	150	150

[continued]

[Continuation of Table 1]

Parameter	Symbol	He	Ne	Ar	Kr	Xe
Specific thrust (sec)	S.P.	20148	8974	6381	4403	3523
Beam voltage (kV)	V_B	1.0	1.0	1.0	1.0	1.0
Beam current (mA)	I_B	16.5	7.33	5.21	3.60	2.88
Accelerating voltage (V)	V_A	-500	-500	-500	-500	-500
Accelerating current (mA)	I_A	165	73.3	52.1	36	28.8
Propellant use efficiency	η_p	0.9	0.9	0.9	0.9	0.9
Flow rate of propellant (A)	\dot{m}	18.3	8.15	5.79	4.00	3.19
Ion current density/beamlet (mA/cm^2)	J	31.87	14.19	10.09	6.97	5.56
Beam diameter (cm)	D_p	30	30	30	30	30
Beamlet divergence angle (deg)	$\theta_{1/e}$	6.2	5.8	5.7	5.5	5.5
Transmission factor	T_T	1.10	1.10	1.10	1.09	1.09
Elec- tron temp. (eV)	T_{et}	>50	>18.2	4.5~10.2	3.7~6.8	2.7~4.7
High- speed	T_{ep}	>50	>50	10.2	6.8	4.7
X density (cm^{-3})	n_g	*	*	1.7×10^{12}	1.8×10^{12}	1.7×10^{12}
X ⁺ density (cm^{-3})	n_1	*	*	2.2×10^{11}	2.7×10^{11}	3.3×10^{11}
Proportion of X ⁺² ion	n_2/n_1	*	*	0.026	0.032	0.023

[continued]

[Continuation of Table 1]

Parameter	Symbol	He	Ne	Ar	Kr	Xe
Ion generation cost (eV/ion)	ϵ	*	*	169	156	138
Discharge power (W)	P_D	*	*	880	562	397
Discharge voltage (V)	V_D	*	*	-65	-45	-30
Discharge current (A)	I_D	*	*	-13.5	-12.5	-13.2
Power consumption (kW)	P_T	*	*	6.12	4.18	3.29
Remarks		Inadequate	Inadequate	Adequate	Adequate	Adequate

- Notes:
1. The relation $I_A \approx 0.01 \cdot I_S$ is assumed.
 2. For power consumption, P_T , keeper power and neutralizer power is ignored and the relation $P_T = V_B \cdot I_B + |V_A| \cdot I_A + P_D$ is assumed.
 3. Symbol * indicates areas which cannot be calculated with the two-electron temperature model.

References

1. Nakamura and Kitamura, DAI32KAI UCHU KAGAKU RENGO KOENKAI YOKOSHU, p 30.

Characteristics Test on 150 mN Ion Thruster

906C3836 Tokyo DAI33KAI UCHU KAGAKU GIJUTSU RENGO KOENKAI KOENSHU in Japanese
31 Oct-2 Nov 89 pp 540-541

[Article by Hideki Yoshida, Hiromichi Kouchi, Daisuke Miyazaki, Toshiharu Higuchi, and Kiyoshi Hashimoto, Toshiba Corp.; and Katsuhiro Miyazaki, Yoshihiro Nakamura, and Masaharu Kitamura, National Space Development Agency]

[Text] 1. Introduction

The authors have been engaged since FY 1986 in basic research on a large ion thruster (Figure 1) that will be suitable for the main thruster of an inter-orbit transport plane and for maintaining the south/north position of a stationary space platform. At present, the authors have completed three sets of characteristics tests and have succeeded in obtaining a steady operation of rated thrust at 150 mN. This article reports on the results obtained from a series of characteristics tests and from a thermal analysis.

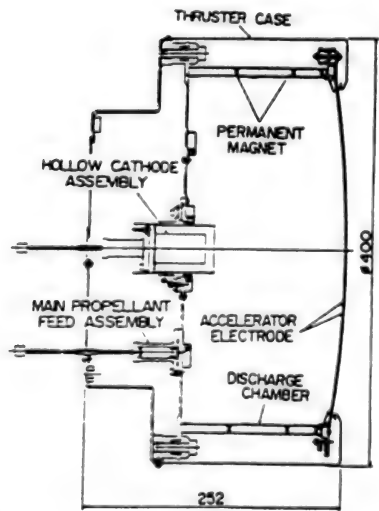


Figure 1. Ion Thruster

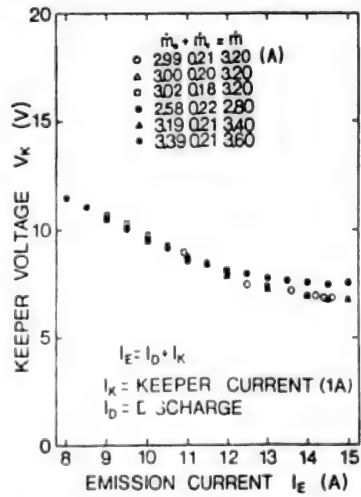


Figure 2. Emission Characteristics

2. Test Results

The main characteristics of the acceleration electrode at the time when we succeeded in obtaining steady operation at the rated thrust include the installation of leaf springs—which are flexible in the radial direction and rigid in the axial direction—on the peripheral part of the electrode plate, and small changes to the curvatures of the individual grids during fabrication (screen grid: 1.1 m; acceleration grid: 1 m). The purpose of the leaf springs is to absorb the thermal expansion of the grid during the stabilization period of temperature distribution and the different curvatures are to absorb the deformation caused by the nonuniformity of temperature distribution that occurs in a transition period on the grids.

Figure 2 shows the relationship between the emission current and the keeper voltage and Figures 3 to 5 show the dependency of ion generation cost, acceleration current, and discharge voltage on propellant use efficiency. In these figures, \dot{m} represents Xe gas flow rate, \dot{m}_i is the Xe gas flow rate from the inlet on the upper lid of the discharge chamber, and \dot{m}_c is the Xe gas flow rate from the inlet of the hollow cathode. Figure 3 shows that the ion generation cost is 178 eV/ion at a propellant use efficiency of 90 percent. This value does not satisfy the design value (solid line in Figure 3) and the reason is that the difference between the grid curvatures is too large. This needs to be improved. The discharge voltage is near the upper limit of the designed range (between curves I and II in Figure 5) and enlargement of the orifice diameter of the hollow cathode may be necessary. According to Figure 4, the acceleration current is 13 to 21 mA and some beam collision to the acceleration grid is noticeable.

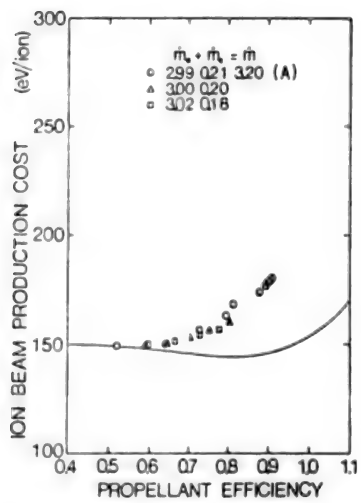


Figure 3. Ion Generation Cost

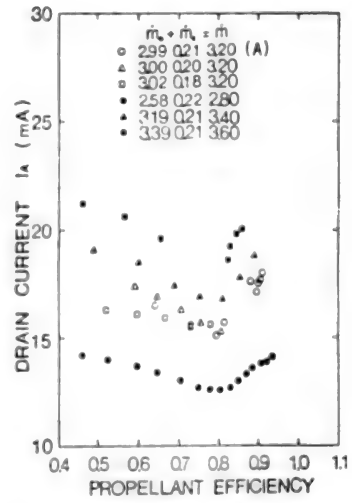


Figure 4. Accelerating Current

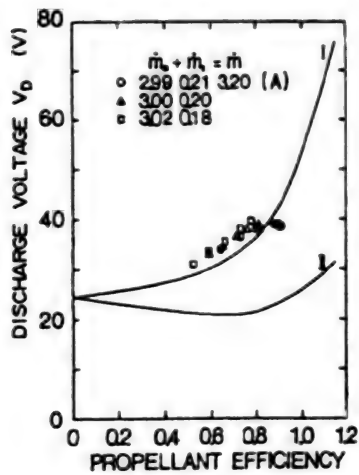


Figure 5. Discharge Voltage

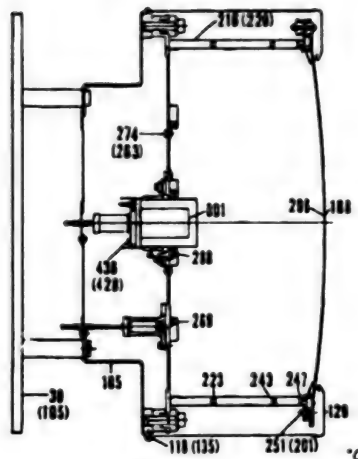


Figure 6. Temperature Distribution Calculation (Measured value)

3. Thermal Analysis

Figure 6 shows the results of a thermal analysis at the rated operation (designed discharge power: 414 W; keeper power: 10 W). The flow path distribution of the discharge power has been calculated on the basis of the free drop model (the plasma analysis model from which the design values were obtained). The values in parentheses in Figure 6 are measured temperature values when discharge power is 428 W and keeper power is 7.3 W. These values were obtained 80 minutes or more after the start of thruster operation, when the temperature had stabilized. The results of this analysis satisfactorily explain the results of our experiments, with the exception of those involving the electrode support element. The temperature of the electrode support element is a topic for future study since the leaf spring structure is not yet well understood. The results of the analysis shown in Figure 6 indicate that it is necessary to improve the cooling method, because the magnet temperature is still high (the target is 250°C or less). A grid temperature difference of 108°C agrees with the temperature difference that was calculated based on the extent of bending of the electrode. An imprecathode operation temperature of 801°C also does not contradict the results of single-body testing (8 W is supplied from the discharge power).

Basic Experiments With High-Powered Stationary Plasma Jet

906C3836 Tokyo DAI33KAI UCHU KAGAKU GIJUTSU RENGO KOENKAI KOENSHU in Japanese
31 Oct-2 Nov 89 pp 540-541

[Article by Takahisa Sakakibara, Hirokazu Tahara, Kenichi Onoue, and Takaо Yoshikawa, Faculty of Basic Engineering, Osaka University]

[Text] 1. Introduction

The high-power plasma jet has recently begun to be regarded as a promising technology for the transportation of materials to be used for the construction of large space structures (space stations and solar generation satellites), orbit transition, and the main thrust rockets of deep space probes. However, many subjects remain to be settled, including degradation of thruster performance and restricted operational life because of cathode wear.¹ A number of measures, such as the application of external magnetic fields, have been tried in an effort to reduce the extent of cathode wear,² but the reasons for cathode wear are not understood sufficiently. This experiment was aimed at clarifying the cathode discharge mechanism and the properties of the near-cathode plasma by directly observing and optically measuring the near-cathode phenomena of the shape in a manner approximating that of an actual device.

2. Experimental Device

Figure 1 is a rough drawing of the main body of the thruster. The anode and cathode of the thruster are water cooled. The anode is made of copper, the constrictor and the nozzle are insulated, and the current that flows through each of these sections can be measured.

To observe the near-cathode phenomena, the side surfaces of the plenum room are made of water-cooled quartz glass tubes. The cathode is made of Th-W and its tip has a conical shape with a vertical angle of 60 degrees. It can be exchanged for a solid one for purposes of comparison with a hollow cathode. The cathode can be removed to measure the extent of wear. The thrust gas can be supplied from a point near the cathode base as a turning flow. When a hollow cathode has been mounted, the thrust gas can also be supplied from its tip. The distance between the cathode and constrictor can be altered by as much as 15 nm by moving the cathode part relative to the main body.

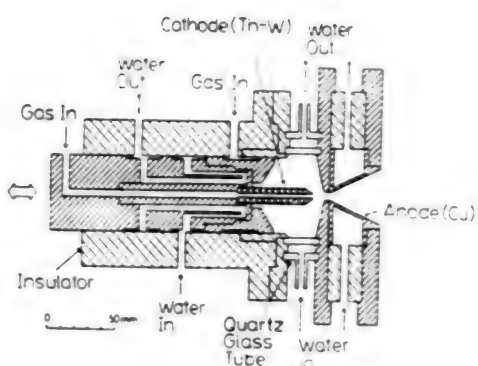


Figure 1. Rough Drawing of Main Body of Thruster

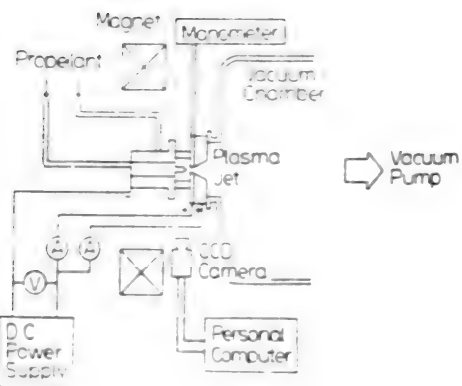


Figure 2. Configuration of Experimental Device

Figure 2 shows the entire configuration of the experimental device. As can be seen in the figure, the thruster is connected to a vacuum tank. The internal pressure of the vacuum tank is kept at 0.1 torr or less. Optical measuring devices (CCD camera, spectroscopic measuring device, and infrared radiation thermometer) are laid out on both sides of the thruster to observe and analyze the cathode and nearby plasma. The solenoid coil for applying the external magnetic field is provided at the back part of the thruster.

3. Method of Experiment

Table 1 shows the operating conditions. The kind and flow rate of the thrust gas were set so that experiments could be simulated on the existing high-powered arc jet. The strength of the external magnetic field can be varied to up to about 1,600 gauss. The experiments measure discharge voltage, the pressure in the plenum room and the extent of cathode wear using discharge current, the kind of gas used, flow rate, and the strength of the external magnetic field as variables. Also, the discharge plasma state near the cathode was observed with the CCD camera, the temperature distribution on the cathode surface was measured with the infrared radiation thermometer, and the current distribution on the anode surface was measured using the split anode. The size and movement of the cathode spot were observed since the spot is closely associated with cathode wear.

Table 1. Operating Conditions

Input power	(kW)	10-30
Arc current	(A)	100-300
Propellant		$N_2 + 2H_2, NH_3, Ar$
Flow rate	(g/s)	0.2-0.3
Applied magnetic field	(G)	0-1,600

4. Conclusion

This experiment was aimed at determining the operating conditions that minimize cathode wear and at finding a method for reducing cathode wear by clarifying the causes of wear. Experiments will also be performed to see if the oozing cooling method, which uses porous cathodes, can serve as a method for reducing cathode wear. How to extend thruster life will be examined in conjunction with thrust performance by measuring the thrust.

References

1. Pivirotto, T.J., King, D.Q., and Deininger, W.D., "Long Duration Test of a 30 kW Class Thermal Arc Jet Engine," AIAA 87-1083, 19th IEPC, 1987.
2. Tahara, H., Kagaya, Y., and Yoshikawa, T., "Quasisteady Magnetoplasma-dynamic Thruster With Applied Magnetic Field for Near-Earth Missions," J. PROPULSION AND POWER, September-October, 1989.

Performance, Electromagnetic Field Distribution of Microwave-Heating Plasma Jet

906C3836 Tokyo DAI33KAI UCHU KAGAKU GIJUTSU RENGO KOENKAI KOENSHU in Japanese
31 Oct-2 Nov 89 pp 544-545

[Article by Masao Yasufuku, Hirokazu Tahara, Kenichi Onoue, and Takao Yoshikawa, Faculty of Basic Engineering, Osaka University]

[Text] 1. Introduction

An electrically heated thruster that uses microwaves has a number of advantages, including the fact that it needs no electrode, has a simple structure, and is easy to ignite. In our last report we examined the influence exerted on the performance and discharge characteristics of the thruster by a microwave transmission system and different methods for supplying the cavity resonator with microwaves. We have since improved the thruster in order to attain a performance level equal to or greater than those of other electrically heated thrusters (specific thrust: 500 s; thrust efficiency 20 percent). We measured not only the thrust performance of this thruster but also the distribution of stationary waves in the microwave electromagnetic field of the resonator. From the obtained electromagnetic field distribution, we evaluated how stationary wave distribution differs depending on differences in the method of supplying the resonance chamber with microwaves, the amount of energy absorbed by the plasma, and the amount of energy lost to the resonator wall. Our efforts are aimed at enhancing the thrust efficiency of the thruster.

2. Structure of Microwave-Heated Thruster Using a Cavity Resonator

Figure 1 shows a cross section of the thruster. The thruster consists of a discharge tube (quartz glass), a nozzle (copper), and a cavity resonator (brass) to resonate microwaves. The cavity resonator is capable of varying the effective length by moving the back wall in the axis direction.

The thruster has been improved in the following ways:

- (1) The diameter of the constrictor has been reduced from $\phi 2.0$ mm to $\phi 1.0$ mm and then to $\phi 0.6$ mm. This causes a high-pressure plasma in the discharge tube. In the preparatory experiment, discharge could be maintained in He gas up to about 1 atm of the pressure in the discharge tube.

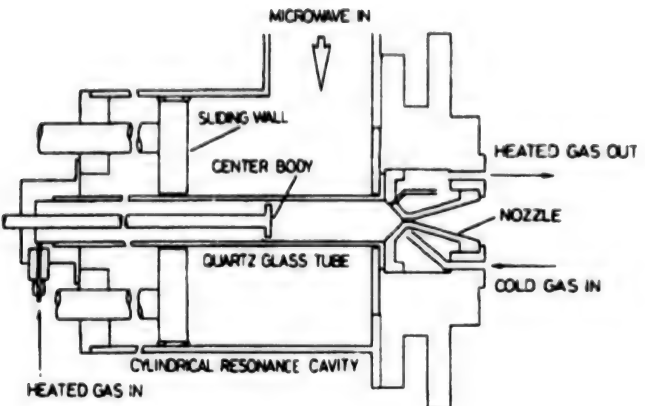


Figure 1. Structure of Microwave-Heated Thruster

- (2) To suppress heat loss caused by the discharge tube wall, the distance between the heating part and the nozzle has been reduced.
- (3) The nozzle has been made replaceable and has been given a shape that allows reproduction cooling of the propellant.
- (4) To prevent uneven heating of the propellant (propellant near to the tube wall is heated) by the skin effect of the microwaves, a center body (quartz glass) has been inserted to stir the flow in the discharge tube. The propellant is preheated by cooling the nozzle and it enters into the discharge tube from the left end. It becomes a high enthalpy plasma because of the energy received from the microwave electric field in the resonance chamber, and undergoes supersonic expansion at the nozzle. He, H₂, and N₂+H₂ are used as propellants. Two methods are used to supply microwaves. One directly supplies microwaves from a wave guide, and the other converts microwaves into the coaxial mode and supplies the converted microwaves via a probe. The target method is used to measure thrust.

3. Measurements of Microwave Electric Field

The microwave electric field causes a stationary wave in the resonator. Figure 2 shows the configuration of the stationary wave measuring device. Eight to 10 holes are provided on the side surface of the resonator and high-frequency signals are detected by inserting a probe. The detected signals are attenuated with an attenuator and the signals in higher modes are removed with a low-pass filter. The resulting signals are further reviewed with a crystal detector and output signals are displayed on an oscilloscope. The resultant detection current is proportional to the square of the electric field.

Another method of measuring electric field distribution that involves the use of liquid crystal, whose density varies depending on the temperature, will also be used. A thin liquid crystal plate on which a dielectric has been applied is inserted into the resonator and the relative distribution of field strength is obtained after the resultant electric field distribution pattern undergoes image processing.

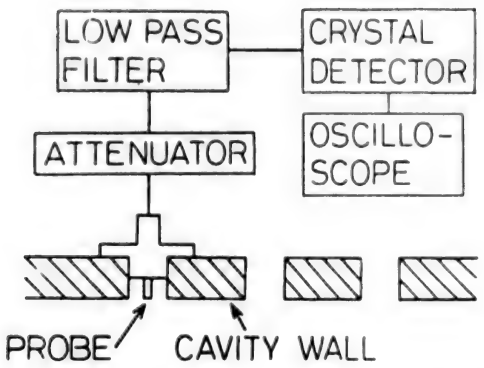


Figure 2. Configuration of Electric Field Measuring Device

4. Conclusion

We are currently involved in carrying out thrust measurement experiments. We have confirmed that the microwave electric field process described above operates stably with a constrictor diameter of $\phi 1.0$ mm and a pressure in the discharge tube of 1 atm. Hereafter, electric field experiments are scheduled to be performed.

References

1. Tanaka, Y., Yasufuku, M., Tahara, H., Onoue, K., and Yoshikawa, T., "Performance and Discharge State of Microwave Resonance Heating Thruster," DAI32KAI UCHU KAGAKU RENGO KOENKAI KOENSHU, October 1988, pp 762-763.
2. Tahara, H., Tanaka, Y., Ono, K., and Yoshikawa, Y., "Electrothermal Thrusters Utilizing Electrodeless Discharge," 20th IEPC, 1988, pp 80-103.

Discharge Mechanism of Semistationary MPD Thruster

906C3836 Tokyo DAI33KAI UCHU KAGAKU GIJUTSU RENGO KOENKAI KOENSHU in Japanese
31 Oct-2 Nov 89 pp 546-547

[Article by Masanori Sasaki, Hirokazu Tahara, Yoichi Kagaya, and Takao Yashikawa, Faculty of Basic Engineering, Osaka University]

[Text] 1. Introduction

For several years we have been researching the thrust characteristics of a semistationary MPD thruster, which has an external magnetic field. We have clarified experimentally the optimum external magnetic field shape that enhances both thrust and thrust efficiency. This was accomplished by performing the operation in the neighborhood of the theoretical critical current where electromagnetic acceleration is dominant.¹

In this experiment, physical quantities were measured inside the discharge chamber to assess the influence exerted on the discharge and acceleration mechanism by the external magnetic field. This article describes the pumping force, which is one of the electromagnetic acceleration components; shows how the external magnetic field influences the pressure of the plasma at the electrode tip; and discusses the acceleration mechanism of the MPD thruster.

2. Experimental Method

The MPD thruster used in this experiment is an improved version of the conventional type.¹ Its cathode and anode are each provided with a $\phi 3$ mm pressure tap (Figure 1). For pressure measurement, a piezoelectric pressure sensor with a 10 kHz frequency characteristic (TOYODA PMS-5 5H) was used. The pressure sensor is fitted with a holder containing a quartz glass tube with an external diameter of 2.9 mm and an internal diameter of 1.7 mm (length = 93 mm for cathode and 31 mm for anode). The sensor is inserted into the pressure tap of the thruster after silicon oil (SH-200) is sealed into the glass tube.

Figure 2 shows the shape of the external magnetic field used in the experiment (C1L type with one-turn coil and highest thrust performance). The coil for applying the external magnetic field is connected in series with the discharge circuit for reasons of practicality and the magnetic force is proportional to the discharge current.

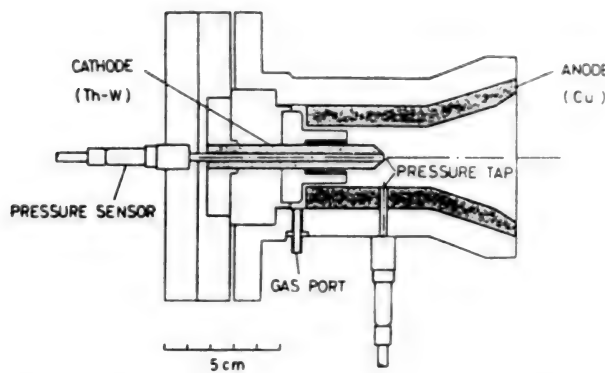
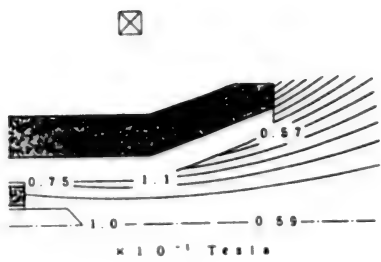


Figure 1. MPD Thruster



C1L type: cold diameter, 57 mm

Figure 2. Shape of External Magnetic Field

The numbers in the figure represent magnetic power when the discharge current is 10 kA. The C2L type is a 2-turn coil. Its magnetic field shape is the same as that of the C1L type and its magnetic force is twice that of the C1L type.

3. Results and Assessment of the Experiment

Figure 3 shows the electrode tip pressure-discharge current characteristic when the thrust gas is H₂ and the flow rate is 0.4 g/sec (the theoretical critical current is about 11 kA). In the figure, the straight line represents the theoretical electrode tip pressure and SELF indicates the case where no external magnetic field exists. Compared to the case where no external magnetic field exists, it was found that the plasma pressure at the electrode tip becomes smaller as the external magnetic field becomes larger. When the flow rate of the thrust gas was increased, the pressure reduction rate caused by application of the external field became smaller.

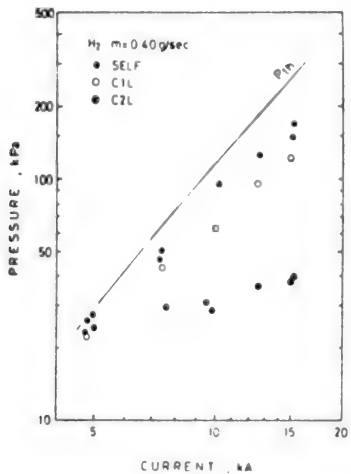


Figure 3. Characteristics of Cathode Tip Pressure-Discharge Current

The following two factors are thought to be the cause of pumping power reduction.

- 1) A circumferential current, $j\theta$, caused by reverse electromotive force ($j\theta = -\sigma U_r B_z$, where $U_r < 0$) and an electromagnetic force that occurs outwardly in the radius direction because of the external magnetic field B_z .² (The Hall parameter is expected to be small ($\omega_e r_e < 1$).)
- 2) A reduction of the current that flows into the conical part of the electrode.

4. Conclusion

A further detailed examination will be carried out to identify the reasons for the increase in thrust and the decrease in pumping power, caused by the application of an external magnetic field, based on the results of measuring discharge current density distribution.

References

1. Tahara, Sasaki, et al., "High Specific Thrust Operation Characteristics of Semistationary MPD Thruster With External Magnetic Field," UCHU YUSOSHIMPOJIUMU, Space Science Laboratory, December 1988, pp 208-213.
2. Walliaris, A.C., "Phenomena in the Cathode Region of an MPD Accelerator," AIAA JOURNAL, Vol 5, 1967, pp 1325-1328.

Characteristics of Electromagnetic Acceleration Using External Magnetic Field

906C3836 Tokyo DAI33KAI UCHU KAGAKU GIJUTSU RENGO KOENKAI KOENSHU in Japanese
31 Oct-2 Nov 89 pp 548-549

[Article by Akihiro Samune, Faculty of Engineering, Nagoya University; and Yoshihiro Arakawa, Faculty of Engineering, University of Tokyo]

[Text] 1. Introduction

An MPD arc jet is an electromagnetic acceleration thruster that uses electric propulsion. One kind of MPD arc jet, those which use a self-induced magnetic field as the means to obtain electromagnetic thrust, is already entering the stage of practical use.¹ However, a number of studies have reported that propulsion performance effectively can be raised by using an external magnetic field.^{2,3} This study reports on analysis and experiments aimed at clarifying the characteristics of acceleration caused by an external magnetic field.⁴

2. Analysis

First, consider an axially symmetric cylindrical acceleration area (of radius R) where j , B , u , E , and p_e represent current density, magnetic flux density, plasma flow rate, electric field, and electron pressure gradient, respectively, and where $\alpha = B_r/B_z$. Next, select the position where $r = R/2$ as the representative point of the acceleration area and attach to the physical quantities at that position. In the generalized ohm's formula, j_θ and j_r are related as shown below by neglecting E_z , dp_e/dz , u_θ , u_r , and B_θ , and assuming the conditions $j_r \ll j_\theta$ and $B_r \ll B_z$. \bar{j}_θ , \bar{j}_r are related as shown below.

$$\bar{j}_\theta = (\omega_\theta \tau_\theta) \bar{j}_r + \bar{\sigma}_\theta u_z \bar{B}_r \quad (1)$$

where, $\bar{\omega}_\theta \bar{\tau}_\theta = \bar{\sigma}_\theta \bar{B} (B - B_z)$. The electromagnetic thrust, F , can be represented as shown below, using the equivalent volume V .

$$F = \dot{m} u_z = \int_0^R (-j_\theta) B_r 2\pi r L dr + \int_0^R 2\pi r \int_r^R (-j_\theta) B_z dr' dr = V(-\bar{j}_\theta) B \quad (2)$$

From (1) and (2), j_θ and I_{sp} ($= F/\dot{m}g$: specific thrust) can be shown as follows:

$$\bar{J}_\theta = \frac{[(B^2/\dot{m})_c B^2/\dot{m}]^{1/2}}{B^2/\dot{m} + (B^2/\dot{m})_c} \bar{J}_\theta, c,$$

$$\bar{J}_\theta, c = \left(\frac{\sigma_\theta \dot{m}}{\alpha V} \right)^{1/2} \bar{P} \bar{J}_r = (\omega_e \tau_e)_c \bar{J}_r$$
(3)

$$I_{sp} = \frac{B^2/\dot{m}}{B^2/\dot{m} + (B^2/\dot{m})_c} I_{sp, max},$$

$$I_{sp, max} = \frac{\bar{P} (-\bar{J}_r)}{\bar{a} g}$$
(4)

From expressions (3) and (4), \bar{J}_θ and I_{sp} are found to have the characteristic quantity B^2/\dot{m} . According to expression (3), \bar{J}_θ rises with B^2/\dot{m} when the latter is small, but, conversely, drops when the characteristic quantity exceeds B^2/\dot{m} . This is because of the influence of the reverse electromotive force caused by the interference between the plasma flow rate and the external magnetic field. Further, with this variation of \bar{J}_θ , the rise of I_{sp} hits its highest point in the range where the characteristic quantity is large.

3. Experiment

Measurements of j_θ on the test-manufactured MPD arc jet with a Hall sensor confirmed the existence of j_θ in the downstream of the thruster exit when H_2 or He was used as the propellant. In the neighborhood of the thruster exit, j_θ becomes maximal independently of the operating conditions at the point where the radius is about 4 mm. Figure 1 shows the relationship between B^2/\dot{m} and the maximal value of j_θ , measured near the thruster exit ($z = 8$ mm; z is the position in the axial direction when the thruster exit is assumed to be 0). In the same way as the analysis, the experiment also showed the existence of the B^2/\dot{m} , which fully maximizes j_θ, max . Figure 2 shows the relationship between the measured I_{sp} and B^2/\dot{m} . The results of the analysis also explain the operation of the actual thruster well.

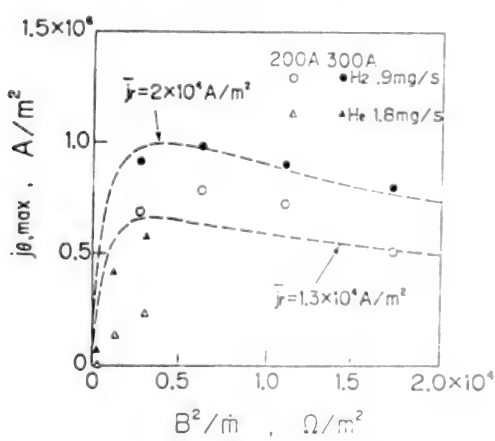


Figure 1. Relationship Between j_θ, max and B^2/\dot{m}

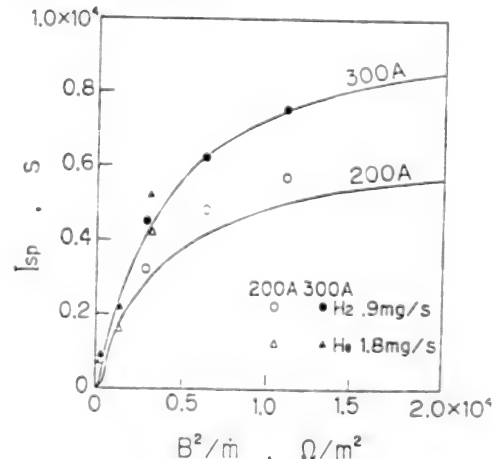


Figure 2. Relationship Between I_{sp} and B^2/\dot{m}

4. Summary

This report shows that the characteristics of electromagnetic acceleration using an external magnetic field can be represented with the characteristic quantity B^2/\dot{m} . This indicates that when the propellant flow rate is increased, for example, the external magnetic field needs to be strengthened to obtain the same performance level.

References

1. Kuriki, K. and Nakamura, Y., IEPC 84-003, 1984.
2. Nelheim, N.M. and Kelly, A.J., NASA THE 32-1196, 1968.
3. Tahara, H., et al., AIAA paper 87-1001, 1987.
4. Samune, A., TOKYO DAIGAKU DAIGAKUIN HAKUSHI RONBUN, 1989.

Ignition Characteristics of MPD Arc Jet Thruster

906C3836 Tokyo DAI33KAI UCHU KAGAKU GIJUTSU RENGO KOENKAI KOENSHU in Japanese
31 Oct-2 Nov 89 pp 550-551

[Article by Kenko Otsuka, Kazuo Uematsu, and Hiromi Yamaguchi, Ishikawajima-Harima Heavy Industries Co., Ltd.; and Kyoichi Kurihara, Space Science Laboratory]

[Text] 1. Introduction

Reliable ignition is very important to the operation of a semistationary MPD arc jet. Before launch, the MPD arc jet is in a storage configuration. After launch, however, the operating environment changes from the initial high-vacuum superlow-temperature state to a high-temperature state during continuous discharge. Sufficient ignition performance needs to be guaranteed for each stage. We have adopted an ignition method based on trigger discharge using an auxiliary electrode in the MPD arc jet to be mounted on the SFU, whose development is currently under way. Ignition failure and discrepancy of ignition timing (ignition delay and self-discharge) are classified as abnormal ignition modes. The former tends to occur at starting when the temperature of the electrode is low, while the latter occurs during continuous operation when the electrode temperature becomes high.

This study not only confirms the influence exerted on ignition performance by changes in the operating environment but also investigates and reports on ignition performance under discharge conditions, which deviate from the designed point of this arc jet, to obtain a guideline for design.

2. Experimental Device

Figure 1 [not reproduced] is a photograph of the arc jet device used in the experiment. This device is equivalent to the testing machine used in the system test performed in the Space Science laboratory from December 1987 to February 1988.^{1,2} The anode and power supply are divided into 18 parts and there are three trigger electrodes. Figure 2 shows a cross section of the device.

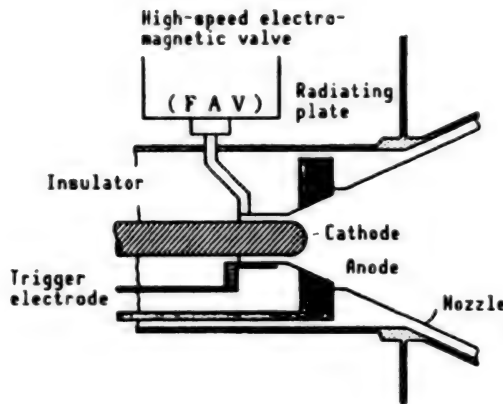


Figure 2. Cross Section of Discharge Chamber

Table 1. Parameters of Experiment and Set Values
(Underlined numbers are those which become reference values.)

Parameters of experiment	Set values in experiment (range of fluctuation)
Cathode tip temperature (°C)	<u>Room temperature</u> -200 (start time), <u>800</u> (1 Hz), <u>1,000</u> ~ (2 Hz)
Propellant mixing ratio (N ₂ :H ₂ :NH ₃ (mole percent))	33:67:0, <u>28:56:16</u> , 17:33:50
Flow rate (mg/shot)	3, <u>5</u> , 8
Charging voltage (V)	200, <u>350</u> , 450
Trigger energy (J)	0.5, <u>0.8</u> , 1.0

3. Experimental Conditions

The experimental parameters included the discharge frequency and cathode tip temperature (which is influenced by the discharge frequency), the mixing ratio and flow rate of the propellant, the charging voltage of the main discharge power supply condenser and trigger discharge energy. Table 1 shows the set values of these parameters. In this system test, the cathode tip temperature at the time of stationary discharge was about 1,000°C, and heating with an infrared lamp was adopted so that this state could be quickly attained. The low temperature side was repeatedly operated (100 times) to cause the temperature to rise from room temperature to about 200°C. A mixed gas consisting of N₂, H₂, and NH₃ (the designed values 30:55:15 in mole percent were used as the propellant in this experiment. Based on a mixture whose mixing ratio is near to the designed value, ammonia-free mixtures were compared with mixtures containing excess ammonia. The designed value for the flow rate of the

propellant was about 5 mg/shot. The secured degree of vacuum was not more than 3×10^{-4} torr (0.04 Pa) at the initiation of discharge and not more than 1×10^{-3} torr (0.13 Pa) even in continuous operation. The designed value for the trigger discharge energy was 0.8 J, the charging voltage of the main discharge power supply condenser was 350 V, and the discharge frequency was 1-2 Hz. It is well known that the ignition characteristics of the arc jet depend to a great extent on the physical and chemical properties of the surface of the cathode material. The optimum operating temperature for BaO-W, which was used in this experiment, is about 900°C. Complex thermochemical reactions occur at this temperature. The surface property after discharge will differ from that at the time of retesting because of the chemical reaction in the atmosphere. An experimental procedure is determined only after carrying out a thorough investigation of the thermochemical characteristics of the BaO-W cathode.

4. Test Plan

Ignition performance is evaluated in the following manner: The FAV operation signal and the discharge current are monitored. A normal ignition state is determined if the discharge current rises within a fixed time of the FAV operation current. Since ignition time is thought to vary depending on operating conditions—such as the condition of the electrode surface, the propellant, and the charging voltage—this discriminating time was assumed to be 10 μ s. If the delay time is within 10 μ s of the normal operation time, any drop in propulsion performance will be negligible.

References

1. Suzuki, H., et al., "3 Million Shots Endurance Test of 1 kW-Class MPD Arc Jet Thruster," IEPC 88-014, October 1988.
2. Suzuki, Uematsu, Shiina, Miyakogi, Shimizu, and Kuriki, "Development of MPD Thruster and Propellant Supply System for Mounting on SFU," Space Transportation Symposium, FY 1988

EM Development of MPD Thruster, Propellant Supply System for Mounting on SFU

906C3836 Tokyo DAI33KAI UCHU KAGAKU GIJUTSU RENGO KOENKAI KOENSHU in Japanese
31 Oct-2 Nov 89 pp 552-553

[Article by Kyoichiro Suzuki, Space Science Laboratory; and Hirokazu Suzuki, Shinji Morimoto, Hiroshi Suzuki, Kazuo Uematsu, and Kotaro Shiina, Ishikawajima-Harima Heavy Industries Co., Ltd.]

[Text] 1. Introduction

The authors are currently engaged in EM development of an MPD thruster and a propellant supply system for the Electric Propulsion Experiment (EPEX). This experimental device is a candidate for mounting on SFU No 1, which is scheduled to be launched in FY 1993. This report describes the present status of development.

Figure 1 presents the development schedule.

2. EM Development of Thruster

Development of the MPD thruster involved a number of subsidiary goals. These include: 1) enhancement of propulsion performance; 2) enhancement of the process of heat exhaustion; and 3) weight reduction. The results of our investigation, as well as the fruits of BBM development, were reflected in the EM design. Table 1 summarizes the principal design changes that led from the BBM to the EM.

Since the resource (weight distribution) requirement from the overall system is severe, we attached special importance to the problem of weight reduction in designing the EM. Weight reduction was accomplished by 1) reducing the number of parts; 2) reducing the thickness of the wall; and 3) the use of lighter materials. As a result, it appears that it will be possible to satisfy the target requirement for weight.

3. EM Development of Propellant Supply System

EM development of the propellant supply system is currently under way, with particular attention being devoted to the following problems.

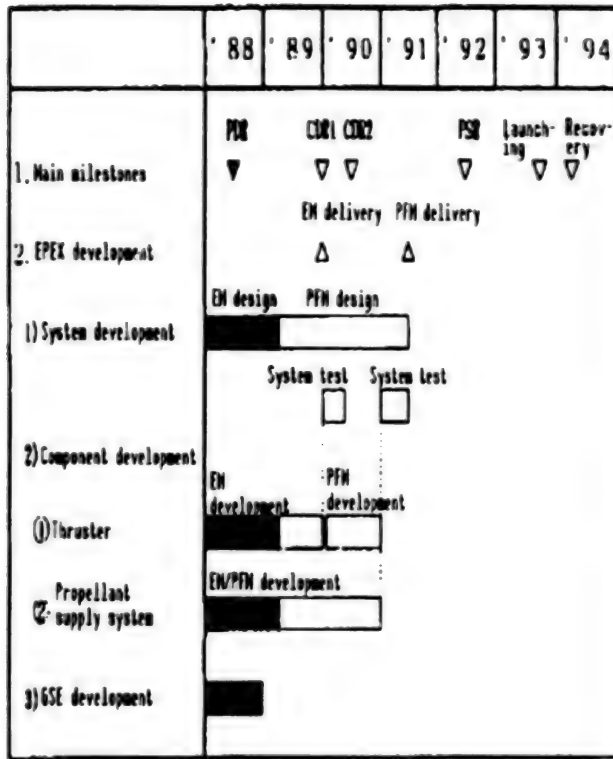


Figure 1. Development Schedule

Table 1. EM Thruster Design

Item	BBM	EM
Weight	10 kg	6.8 kg (target)
Cooling system	High temperature part: heat radiation plates Low temperature part: water cooling pipes	Heat radiation plates Heat pipe
Alignment	Fixed	±1° adjustment included
FAV drive power	47J/shot (2-pulse drive)	21J/shot (target) (1 pulse drive)

Propellant processing

Hydrazine is used as the propellant for the MPD thruster. Thus, strict safety requirements are necessary, particularly when hydrazine is being returned on a space shuttle.

Table 2 shows the effects of tradeoffs related to propellant processing.

Table 2. Trade-Off in Propellant Processing Method

Processing method	Characteristics	Problems	Judg- ment
1) Retention	•Recovery of propellant •No contamination	•Heat control necessary to prevent propellant from freezing •Safety requirement severe	x
2) Neutralizing and absorbing processing	•Neutralization with acid and absorption •No contamination	•Neutralizer necessary, weight increase (TBD kg)	x
3) Decomposition by heating	•Decomposition by heater •Complete decomposition possible, little contamination	•Resource (power) necessary •Redundant system necessary, weight increase (TBD kg)	x
4) Nonheating decomposition	•Decomposition by catalyzer •High reliability	•Possible contamination because of ammonia generation •Decomposition heat generated	o
5) Direct exhaustion	•Exhaustion of propellant in liquid state •No device needed other than exhaust valve	•Possible contamination	Δ

Retaining the propellant or neutralization and absorption processing using an acid are possibly viable methods that do not require the propellant to be exhausted. However, if the thruster is to be returned on the shuttle with its propellant still inside, there will be increased demands for resources (power and weight) and an adjustment of the arrangement with NASA will be necessary to ensure an adequate safety design to prevent propellant leakage. To neutralize and absorb propellant with acid, a neutralizer such as a porous agent impregnated with sulfuric acid is necessary, and this requires a weight increase.

To decompose an exhaust propellant in a gaseous state, several processing methods, grouped into the categories of heating decomposition and nonheating decomposition, are available. Heating decomposition methods include a method whereby the propellant is heated until it begins to decompose by itself, one where decomposition of the propellant is accomplished by activating the catalytic function of platinum by a heater and a third that uses photochemical reaction. All of these methods, however, increase resource (power and weight) requirements.

Nonheating decomposition methods include a method for decomposing the propellant by the action of a catalytic layer and a second that involves decomposing the propellant through a reaction with nitrogen tetroxide. The latter requires an oxidizing agent supply system, which again increases the weight. Since the former makes use of conventional gas jet techniques, enjoys a high degree of reliability, and does not increase resource requirements, it is thought of as the most promising system. However, there is a possibility of contamination by the ammonia gas contained in the decomposition gas.

Since the method of directly exhausting the propellant in a liquid state needs no excess devices other than valves, the increase in resource requirements is small, but there is a possibility of contamination. Therefore, the method currently being investigated for adoption as a redundant system is that of decomposition using a catalytic layer.

Heat control

The objects of heat control are 1) to keep the propellant at the correct temperature; 2) to keep the device itself at the correct temperature; and 3) to exhaust heat caused by propellant decomposition. The propellant (hydrazine) needs to be kept at a temperature of 10°C or above to prevent it from freezing. For this purpose, the system is equipped with a heater for freeze prevention. Since this heater concurrently plays the role of heat control for the entire PLU, a thermal analysis of the entire system including the PLU and other mounted devices is needed to optimize heater power and device layout.

At the same time of thruster operation and propellant exhaustion, decomposition heat is produced and the temperature of the gas generator rises considerably, because hydrazine is decomposed by the gas generator. Therefore, the operation mode needs to be optimized for effective heat insulation between the gas generator and the panel and for the suppression of calorific values.

Contamination

For contamination, which poses a problem at the time of propellant exhaustion, a design investigation including a bloom thruster analysis is required.

4. Conclusion

The authors are moving forward with EM development of the MPD thruster for EPEX and of the propellant supply system. For propellant processing in orbit, a principal development theme, the authors plan to use catalytic gasification and exhaustion, and will move forward with a design investigation including an analysis of contamination.

References

1. Kuriki, Mako, et al., "EM Development of an MPD Thruster and Propellant Supply System for Mounting on SFU," DAI32KAI UCHU KAGAKU GIJUTSU KOENKAI KOENSHU, 1988.

Correlation Between MPD Propulsion Characteristics, Flow Field

906C3836 Tokyo DAI33KAI UCHU KAGAKU GIJUTSU RENGO KOENKAI KOENSHU in Japanese
31 Oct-2 Nov 89 pp 554-555

[Article by Takayuki Nakayama and Tatsuya Yoshida, University of Tokyo Graduate School; and Kyoichiro Miyakogi and Kyoichi Kuriki, Space Science Laboratory]

[Text] 1. Introduction

The study reported in this article is aimed at creating a numerical analysis model that appropriately simulates the MPD flow field. This model, together with experiments and numerical analysis, will help to establish a design guideline for the MPD thruster. The experiments measure the flow field in the two-dimensional MPD arc jet, primarily through optical techniques, to obtain the correlation between propulsion characteristics and flow field.

From the measurement results on plasma characteristics obtained so far, the following correlations between propulsion characteristics and flow field have been obtained.^{1,2}

- 1) The differences in propulsion characteristics caused by different thruster shapes depend on differences in current path.
- 2) Variations in propulsion efficiency caused by operating conditions (dependency of propellant on flow rate and N-shape transition) depend on the difference between the accelerating processes for ions and for neutral particles.
- 3) Hydrogen-based propellant performs well because of the formation of a cathode jet.

2. Flow Rate Measurement by Laser Fluorescence Method

To confirm the direct correlation between propulsion performance and flow field, we investigated the accelerating processes for ions and for neutral particles. Flow rate distribution measurement based on the laser fluorescence method (LIF) is capable of measuring the two-dimensional distribution of flow rate vectors for ions and neutral particles. As shown in Figure 1, sheet-like beams are made incident into the discharge chamber and the fluorescence

emitted by the ions or neutral particles that absorbed the laser is measured from a direction at right angles to the laser. The fluorescence provides information about the Doppler shift of the absorption spectrum for each particle. The positions indicated by the vertical lines in Figure 2 represent the frequencies of actually incident lasers and the absorption spectrum for a particular particle can be determined by using laser beams at different frequencies and then interpolating the intensity of the fluorescence.

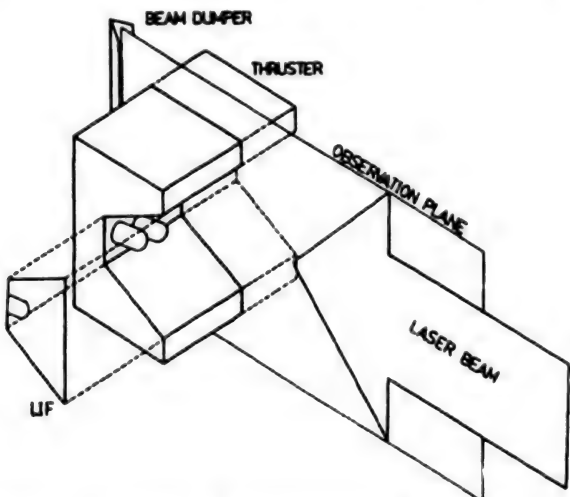


Figure 1. Laser Fluorescence Method (LIF)

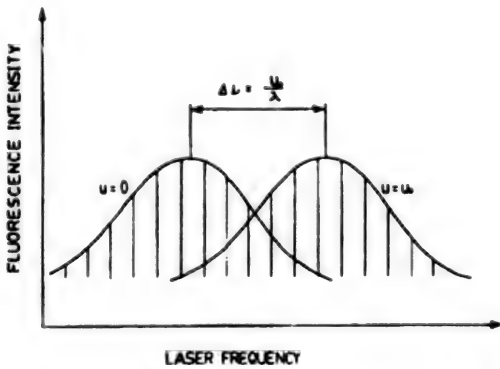


Figure 2. Doppler Shift of Absorption Spectrum
(For a particle which has a speed u_0 , the laser beam is seen as blue-shifted by $\Delta\nu$)

The fluorescence peak for an incident laser frequency shifts depending on speed. Using this phenomenon, the flow rate distribution of ions and neutral particles can be measured on a two-dimensional plane.

3. Experimental Device

Figure 3 shows the experimental device. A pulse coloring matter laser is currently being manufactured. At present, laser conversion efficiency is 6 percent, line width is 45 GHz, and pulse width is 1 ns for a nitrogen laser whose peak output is 1 MW (when Rhodamine 6 G is used). To measure Doppler shift, as shown in Figure 2, the laser line width must be sufficiently smaller

than the line width of the absorption spectrum of the particle (about 10 GHz). Finally, a line width 0.66 GHz is sought for by inserting etalone. The laser beams are formed into an approximate sheet and are made incident on an MPD arc jet at an angle difference of 45 degrees. A CCD camera with an interference filter is used to measure fluorescence. The flow rate vector of each pixel of the CCD is obtained by image processing with a computer.

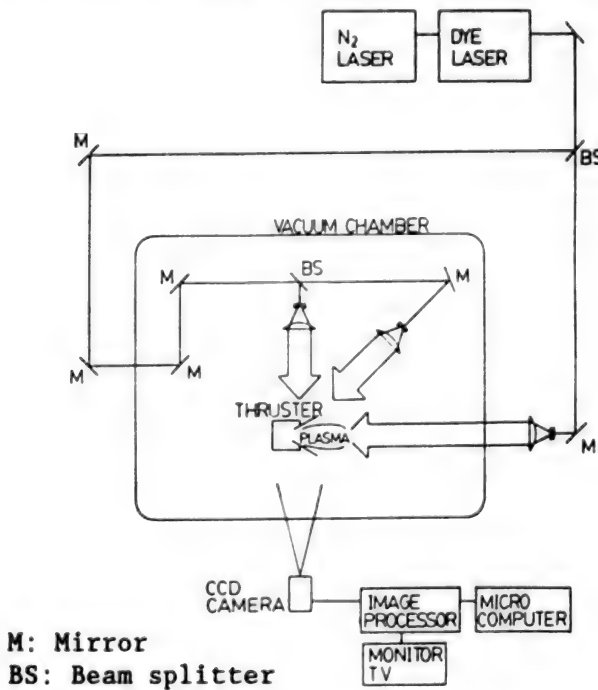


Figure 3. Flow Rate Distribution Measurement Experimental Device Using Laser Fluorescence Method

4. Determination of Laser Wave Length

The incident laser beam must coincide with the absorption line of each particle; thus a particle at low level of excitation is made to absorb laser beams for argon, the propellant.

In selecting the absorption line, the following conditions were taken into consideration:

- 1) To obtain high fluorescence intensity, the particle density at the level to be excited should be high.
- 2) To raise the signal to noise (S/N) ratio, excitation should occur at a level that does not exist in MPD discharge.

Figure 4 shows examples that satisfy such conditions.

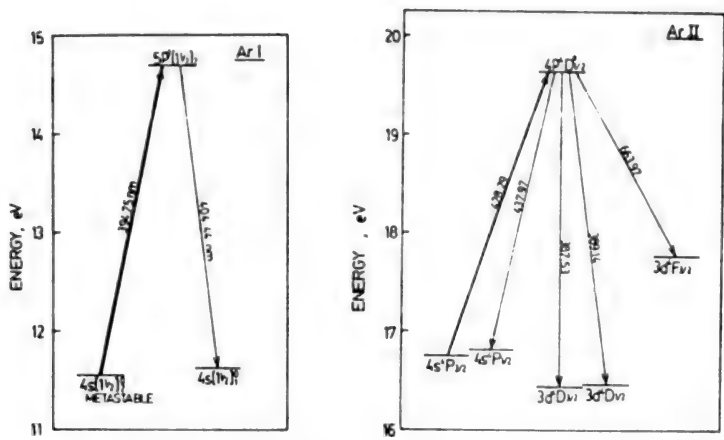


Figure 4. Energy Diagrams of Ar I and Ar II

References

1. Miyakogi, et al., DAI31KAI UCHU KAGAKU GIJUTSU RENGO KOENKAI YOKOSHU, No 2D3, 1987, pp 426-427.
2. Nakayama, et al., DAI32KAI UCHU KAGAKU GIJUTSU RENGO KOENKAI YOKOSHU, No 2G3, 1988, pp 470-471.

Numerical Analysis of Axially Symmetric Flow in MPD Thruster

906C3836 Tokyo DAI33KAI UCHU KAGAKU GIJUTSU RENGO KOENKAI KOENSHU in Japanese
31 Oct-2 Nov 89 pp 556-557

[Article by Osamu Kimura and Toshitaka Fujiwara, Aeronautics Department,
Faculty of Engineering, Nagoya University]

[Text] 1. Introduction

Since Robert H. Goddard first advocated a concept for the acceleration of propellant using electromagnetism, the idea of electric thrusters has been actively explored. One such thruster is the magnetoplasmadynamic (MPD) thruster. This thruster has a number of characteristics—such as high specific thrust, high thrust density, a simple structure, capability of low voltage operation, and ease of thrust control—that suggest it may find extensive application in a variety of fields, such as the main thrusters for planet probes, AOTV, and thrusters for the interorbit transportation of large space structures.

Much experimental research has been conducted on the MPD thruster. One technique used in this research is numerical simulation by computer, which is an effective tool for analyzing the characteristics of the flow field in a thruster. Our experiment used two analytical techniques—the TVD-UPWIND scheme for a nonstationary, nonviscous, compressible, and axially symmetric flow, and the one-fluid-approximating electromagnetic fluid equation system—to provide a clearer picture of the state of plasma flow in a thruster.

2. Governing Equations

The following conditions were assumed before a numerical analysis of the plasma flow in an MPD thruster was carried out.

- Argon is used as the propellant and is supposed to be completely ionized at the entrance of the thruster.
- Plasma is electrically neutral on a macroscopic level and is regarded as a single fluid, though it actually consists of electrons and positive ions.

- Plasma follows the mathematical equation for an ideal gas and is treated as a perfect gas whose constant pressure and constant volume specific heats are constant.
- Transportation phenomena such as heat conduction and the scattering of energy by viscosity are not considered.
- Magnetic field is only that caused by self-inductance and its component is only in the circumferential direction.
- The Hall effect is taken into consideration but the ion slip effect is not.

The nonviscous compressive Euler equation is applied as the basic equation. In a nonstationary, semipreserving, and axially symmetric environment it can be expressed as follows:

$$U = \begin{bmatrix} \rho \\ \rho u \\ \rho v \\ e+B^2 \\ B \end{bmatrix}, F = \begin{bmatrix} \rho u \\ \rho u^2+p+B^2 \\ \rho uv \\ (\epsilon+p)u-2BE_r \\ -E_z \end{bmatrix}, G = \begin{bmatrix} \rho v \\ \rho uv \\ \rho v^2+p+B^2 \\ (\epsilon+p)v+2BE_r \\ E_r \end{bmatrix}, H = \begin{bmatrix} \rho u/r \\ (\rho u^2+2B^2)/r \\ \rho uv/r \\ (\epsilon+p)u/r \\ 0 \end{bmatrix}$$

$$e = \frac{1}{2}\rho(u^2+v^2) + \frac{1}{\gamma-1}\rho T$$

$$\begin{bmatrix} E_r \\ E_z \end{bmatrix} = \frac{1}{R_m \sigma} \begin{bmatrix} 1 & -h_\sigma B \\ h_\sigma B & 1 \end{bmatrix} \begin{bmatrix} -\frac{\partial B}{\partial z} \\ \frac{1}{r} \frac{\partial}{\partial r} (rB) \end{bmatrix} + \begin{bmatrix} vB \\ -uB \end{bmatrix}$$

$$h_\sigma = \mu_\sigma B = \frac{m_i}{e} \frac{\sigma}{\rho} B, R_m = \mu_0 \sigma V_m R_c$$

where, ρ is mass density; u and v are speed components in the radial and axial directions, respectively; p is pressure; B is magnetic flux density; and E is the electric field. These are all dimensionless quantities; h_σ is the hole parameter and R_m is the magnetic Reynolds number.

3. Numerical Analysis Method

As the difference scheme, the secondary-precision TVD-UPWIND scheme is used. Figure 1 shows the thruster shape and coordinate system. The thruster is a hollow cylinder that coaxially lays out an anode with a right-angle aperture and a cathode that combines a cone and a cylinder. An axially symmetric flow field is considered. The calculation lattice is positioned in parallel with the axis of symmetry. The principle of mirror image, conditions of symmetry and regularity, and conditions of extrapolation are given as boundary conditions on the electrode wall surface, the axis of symmetry, and the external free boundaries, respectively.

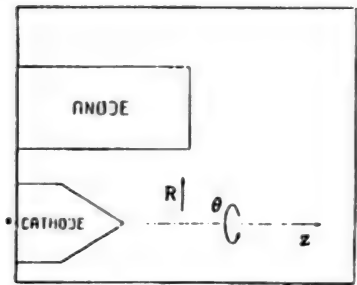


Figure 1. Thruster Geometry and Coordinate System

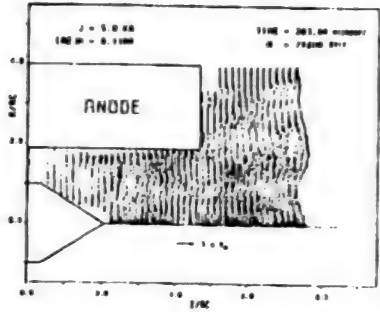


Figure 2. Velocity Distribution

4. Example of Numerical Calculation

Figure 2 shows a speed vector diagram calculated using the McCormick-FCT method as an example of calculation. Since plasma density becomes higher near the central axis because of the pumping force, speed is somewhat reduced around this part.

5. Conclusion

The McCormick-FCT method, which we have used before, requires more calculation time and is inferior to TVD in terms of stability. Therefore, this study forecasts various characteristics of the flow in an MPD thruster through a numerical analysis using a technique known as the TVD-UPWIND method.

References

1. Yamada, H. and Fujiwara, T., "Computational Fluid Dynamics Study of an MPD Thruster," MEMOIRS OF FACULTY OF ENGINEERING, Nagoya University, Vol 38, 1986.
2. Yee, H.C., "Upwind and Symmetric Shock Capturing Schemes," NASA TM-89464, 1987.

Specified Thrust Characteristics of 1 kW DC Arc Jet

906C3836 Tokyo DAI33KAI UCHU KAGAKU GIJUTSU RENGO KOENKAI KOENSHU in Japanese
31 Oct-2 Nov 89 pp 558-559

[Article by Tetsuya Yamada, University of Tokyo Graduate School; and Kyoichito Miyakogi and Kyoichi Kuriki, Space Science Laboratory]

[Text] 1. Introduction

The DC arc jet is an electric thruster that belongs in the general category of thermal electron accelerating thrusters. The authors have conducted a thermal analysis using the finite element method and have designed and manufactured a new 1 kW thruster (SAGAMI-I). SAGAMI-I, which uses heat-resistant materials and whose thermal characteristics have been carefully studied, has a greatly enhanced propulsion performance compared with conventional thrusters.

2. Experimental Device

(Thruster) (Figure 1) The reproduction cooling effect enhances the specific thrust because of the rise in temperature at the nozzle entrance. With SAGAMI-I, contact heat resistance is reduced by making the anode part (constrictor diameter: 0.6 mm) and the structural body closely adhere to each other using a taper. We attempted to increase the reproduction cooling effect by making the thruster smaller using a high-melting-point material (Mo) in the structural body itself. The shape of the propellant flow path was taken into consideration and optimized from the viewpoint of heating temperature and pressure loss. The temperature of the cathode tip was increased by reducing its heat capacity and by making the cathode as thin as $\phi 2.4$ mm to increase its thermal electron emitting capability.

(Experimental Device) (Figure 2) Thrust was measured by converting the displacement of the pendulum-type thrust stand into voltage by a differential transformer. To prevent the device from receiving radiation heat from the thruster, a water-cooled panel was provided in the vacuum chamber. The propellant is hydrazine decomposition imitation gas, which mixes nitrogen and hydrogen 1 to 2 in mole ratio and was controlled by a flow rate controller in units of 0.1 mg/s. Discharge causes insulation destruction at the initially applied voltage of 450 V-20 A with argon as the propellant and then moves to the stationary state with the argon propellant replaced by hydrazine

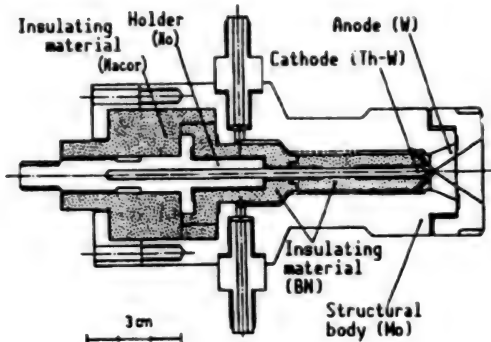


Figure 1. SAGAMI-I

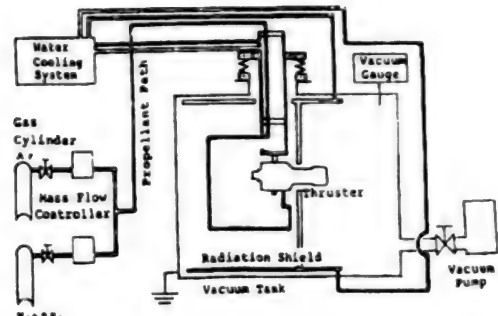


Figure 2. Complete Diagram of Experimental Device

decomposition imitation gas. During the experiment, the back pressure in the vacuum chamber was held at 0.1 torr or less.

3. Results of Experiment

Experimental data was acquired beginning about 10 minutes after the thruster entered stationary operation and thrust and after pressure reached an equilibrium.

Figure 3 shows the applied power-specific thrust characteristics obtained in the experiment. If applied power is constant, specific thrust increases as the applied power becomes smaller. Specific thrust increases linearly as applied power increases. The case where the gap (distance between the constrictor entrance and cathode tip) between the electrodes was 0.0 mm was compared with the case where the gap is 0.5 mm. The latter proved more difficult to ignite but no difference was found in performance.

Figure 4 shows the discharge current-discharge voltage characteristic. The voltage is higher by about 10 percent as a whole when the gap between the electrode is 0.5 mm as opposed to when the gap is 0.0 mm. When compared to the characteristics of conventional thrusters, the discharge voltage of SAGAMI-I is higher about 20 V, even if all conditions are the same. If it is taken into consideration that the voltage characteristic of the positive column is flat in a comparatively wide pressure range,² this is thought to be due not only to the difference in constrictor diameter but also due to the difference in electrode sheath area.

Figure 5 was produced by plotting the results of the temperature measurement, obtained by a radiation thermometer, on the thruster temperature distribution. This latter variable was obtained by the finite element method and was used in heat design. It is understood that heat radiation from the bloom exerts more influence than the steepness of the temperature gradient actually measured at the nozzle exit.

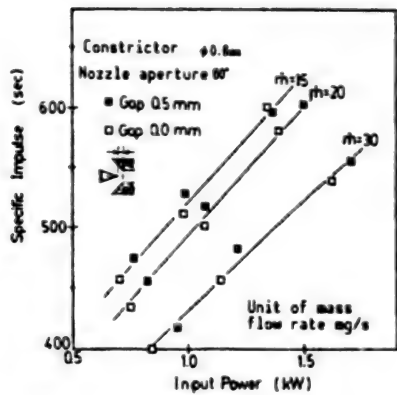


Figure 3. Supplied Power-Specific Thrust Characteristics

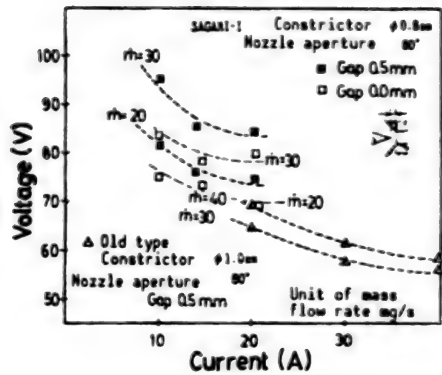


Figure 4. Discharge Current-Discharge Voltage Characteristics

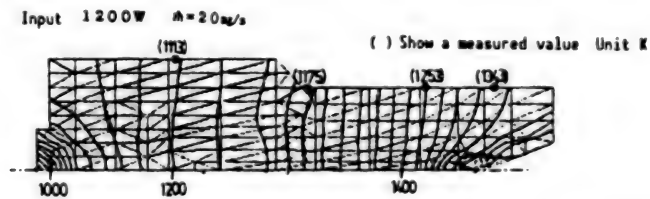


Figure 5. Thruster Temperature Distribution

4. Summary

The performance of the new DC arc jet SAGAMI-I depends on the operational parameters in a comparatively simple manner. This means that discharge is stable for changes in operating conditions and consequently a high degree of specific thrust was obtained. Based on this finding, the authors will grapple with the problems of electrode wear, understanding the internal discharge state and, further, enhancing thrust performance.

References

1. Amakata, R., et al., DAI3IKAI UCHU KAGAKU RENGO KOENKAI YOKOSHU, 2D13.
2. Hoyaux, Max F., "Arc Physics," Springer-Verlag, New York.

Experimental Research on Low-Power Arc Jet Thruster

906C3836 Tokyo DAI33KAI UCHU KAGAKU GIJUTSU RENGO KOENKAI KOENSHU in Japanese
31 Oct-2 Nov 89 pp 560-561

[Article by Yasuo Kawai and Osamu Kimura, Nagoya University Graduate School;
Toshitaka Fujiwara, Nagoya University; and Masao Aoki, Daido Technical
College]

[Text] 1. Introduction

Our research group has focused its attention on the shape of the anode for an arc jet thruster and has conducted a number of experiments over the past several years. These experiments have demonstrated that an anode featuring a two-stage narrow throat¹ produces a high level of specific thrust with a high degree efficiency. The group has also started research on hollow cathodes aiming at the development of cathode cooling techniques. This article reports on these two experimental research efforts.

2. Two-Stage Narrow Throat Anode

In our experiments, the two-stage narrow throat thruster (constrictor diameter: 3 mm) shown in Figure 1(a) is supported from below by a duralumin plate in a low-density wind tunnel. The thruster is externally supplied with Ar gas (the propellant), high voltage for destroying the insulation power for arc jet formation and cooling water. Thrust at the time of arc jet formation is recorded on an open recorder after measuring the strain of the duralumin plate with a load cell and amplifying the results with an amplifier. Figure 2 shows the results of the experiments. This two-stage narrow throat anode yields a maximum performance efficiency of 74 percent and a maximum specific thrust of 1,200. This makes it possible to operate at a low level of power. We believe there are three reasons for this enhanced performance. The first is that attaching a throat to the constrictor reduces the distance between the cathode and the anode, lowers the voltage required for arc column formation. Second, the optimum heat quantity (for small heat loss) is consistent with the requirement for heating the Ar gas at the discharge part. And third, shock wave reflection in the constrictor is held to a minimum by the short throat and thus the drop of gas speed due to the effect of the shock wave is reduced.

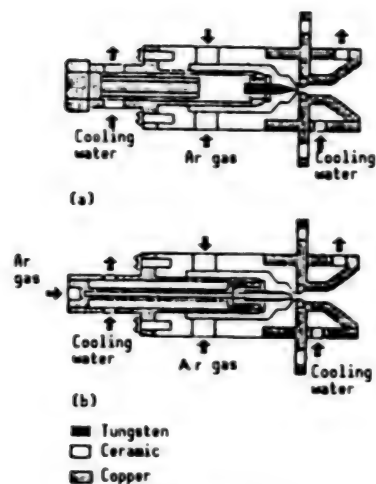


Figure 1.

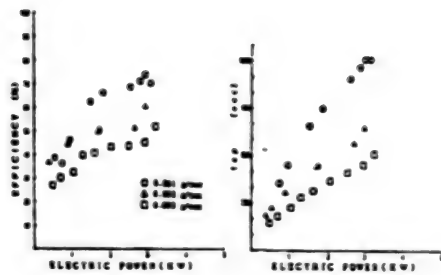


Figure 2.

3. Arc Jet Thruster Using Hollow Cathode

To date, most of our attention has been focused on the anode, but we have tentatively shifted to the cathode. The authors performed a series of experiments using the two-stage narrow throat resonance and an auxiliary system using a hollow cathode (cathode diameter: 5 mm, internal diameter of hole: 2 mm). The purpose of the experiment was to cool the cathode with the propellant and to change the flow rate of the Ar gas around the hollow cathode and the central part. Figure 3 shows the results of these experiments. The results indicate that the flow rate around the central part of the cathode needs to be increased to obtain a high level of efficiency.

4. Numerical Analysis

To compare the results of the experiments, a simple numerical analysis was performed based on the assumption that the flow inside the thruster is a one-dimensional semistationary flow.

Equation of continuation:

$$\rho u A = \dot{m}$$

Equation of energy:

$$h_0 + u_0^2/2 + Q(x) = h + u^2/2$$

Equation of state:

$$P = \rho RT$$

Equation of momentum:

$$dP = -\rho u du$$

The Mach number at the constrictor entrance is obtained by a calculation based on the hypothesis that the flow clogs at the constrictor exit, that is, there is a C-J-Deflagration condition. First, dimensionless simultaneous ordinary differential equations for the pressure in the plenum chamber and the pressure at the central part are obtained as initial values. These differential equations are then solved for the constrictor entrance using the Runge-Kutta method. Since the initial pressure that makes the obtained Mach number equal to that calculated by the Runge-Kutta method shows the correct flow field, this pressure is obtained by repetition. If the downstream of the constrictor exit is solved as an equientropy stream, all the physical quantities at the nozzle exit can be obtained. Figure 4 shows the results of calculating energy efficiency for the case where the flow rates in the central part and in the neighborhood of the cathode are changed. These results show that energy

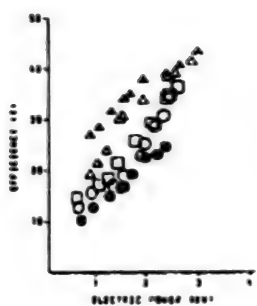


Figure 3.

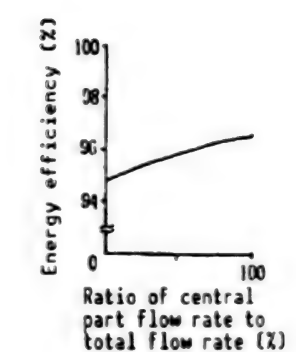
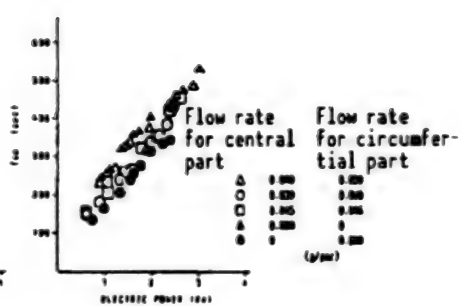


Figure 4.

efficiency is higher when the flow rate in the central part of the cathode is increased. The calculated value agrees with the experimental data.

5. Conclusion

Hereafter, we plan to conduct experimental research on the shape of the hollow cathode and the main body of the cathode, which uses radiation cooling.

References

1. Kawai, Y., Fujikawa, H., Aoki, M., and Fujiwara, T., "Enhancement of Arc Jet Thruster Efficiency," OUCHU YUSO SHIMPOJIUMU PY 1988, 1988, pp 257-259.

Extended Operational Characteristics of Low-Input Arc Jet Thruster

906C3836 Tokyo DAI33KAI UCHU KAGAKU GIJUTSU RENGO KOENKAI KOENSHU in Japanese
31 Oct-2 Nov 89 pp 562-563

[Article by Yuzuru Yasuda, Kenichi Onoue, and Takao Yoshikawa, Faculty of Basic Engineering, Osaka University; and Masahiro Ishii and Kazuo Uematsu, Ishikawajima-Harima Heavy Industries Co., Ltd.]

[Text] 1. Introduction

Development is currently under way on a low-input arc jet thruster that can be used for position control of artificial satellites or a space station. Another factor behind our research over the past several years has been the assumption that a low-input arc jet thruster will be used for north/south control of a 1-ton stationary satellite. As the result of our research up to last year, we were able to meet the targets for performance, specific thrust (500 s) and propulsion efficiency (30 percent) with a power input of about 600 W using $N_2 + 2H_2$ as the propellant. For practical purposes, there are two basic operational modes. Total operating time becomes about 690 hours when the input of the thruster is 500 W, the specific thrust is 500 s, and the ratio of thrust to input is 200 mN/kW for mission life of 10 years. The two operational modes are:

- 1 hour ON/127 hours OFF x 690 times
- 11.4 minutes ON/24 hours OFF x 3,650 times

Therefore, about 700 hours of durability is required if a low-input arc jet thruster is to be used for the purpose noted above. In this study, therefore, we test manufactured a new arc jet thruster to assess the characteristics of arc jet thrusters during periods of extended use and to perform a continuous operation experiment of about 50 hours to investigate cathode wear, expansion of constrictor diameter, the drop in propulsion performance caused by electrode wear and variations in the temperature of each part of the thruster over time.

2. Thruster for Extended Operation Experiment

Figure 1 shows the new radiation-cooling arc jet thruster (RAT-V) that we designed and manufactured. The cathode is made of tungsten mixed with thorium

and has a bar diameter of 2 mm. The vertex angle of the conical tip is 60 degrees. The anode is of tungsten. Its constrictor diameter and length are both 0.6 mm, its nozzle aperture is 60 degrees, and its aperture ratio is 400. The body and cathode holder are of molybdenum and the insulating materials are boron nitride and macor. Compared to the RAT-III, the RAT-V features two important improvements.

- 1) It is smaller and lighter than the RAT-III and has a better heat capacity.
- 2) The center lines of the cathode and anode coincide exactly.

Regarding the first point, the weight and heat capacity are both about one-half that of the RAT-III, as shown in Table 1. Therefore, the time from thruster ignition to the time of operational equilibrium can be reduced. Further, it should be possible to enhance arc efficiency due to the rise of thruster temperature. With regard to external dimensions, the diameter of the front part of the body has been reduced from 40 mm to 30 mm. As for the second point, anode/cathode alignment makes it possible to achieve a stable discharge state and constrictor wear due to arc deviation can be prevented.

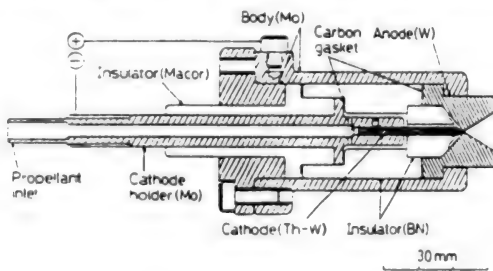


Figure 1. RAT-V

Table 1. Mass and Heat Capacity of Thruster (Metallic parts only)

	RAT-III		RAT-V	
	Mass (g)	Heat capacity (J/K)	Mass (g)	Heat capacity (J/K)
Anode	243.2	34.0	112.3	15.7
Cathode	7.2	1.0	1.8	0.3
Cathode holder	78.1	23.4	47.1	14.1
Body (F)	512.8	153.8	236.4	70.9
Body (R)	251.3	75.4	153.9	46.2
Total	1092.6	287.6	551.5	147.2

3. Extended Continuous Operation Experiment

Figure 2 shows the experimental device. The arc jet thruster is installed in a vacuum wind tunnel ($\phi 1.2 \text{ m} \times 2.0 \text{ m}$) and the power and the propellant are supplied externally. The thrust measuring device uses a pendulum and measures

thrust with a load cell. To prevent output temperature drift, the load cell is attached to a water-cooled container. The temperature of the thruster surface is measured with a thermocouple. The experimental conditions were set up as shown in Table 2, which contains experimental data from RAT-III obtained during the last fiscal year.

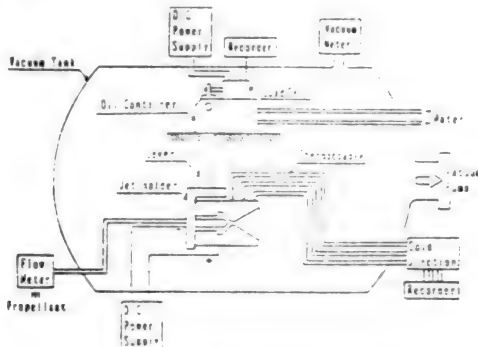


Figure 2. Experimental Device

Table 2. Experimental Conditions

Propellant	$N_2 + 2H_2$
Mass flow rate	15-30 mg/s
Discharge current	8-12 A
Input power	500-600 W
Specific impulse	500 sec
Thrust efficiency	30 %
Thrust-power ratio	200 mN/kW

Argon is used during thruster ignition, after which a switch is made to $N_2 + 2H_2$. Discharge voltage, input, thrust, and thruster surface temperature are continuously measured until the thruster reaches a stable operational state. The mass of the electrode is measured before and after an experiment, and the cathode tip surface and the anode constrictor part were photographed to measure the extent of electrode wear and to observe changes in electrode shape.

4. Conclusion

The schedule for the future is to conduct about 1,000 experiments using $N_2 + 2H_2$ as the starting gas, to measure the extent of electrode wear to observe changes in electrode shape, and to compare and investigate these data with data obtained during the period of stable operation.

Vibration Characteristics of 3.5 m ϕ Antenna for ETS-VI

906C3836 Tokyo DAI33KAI UCHU KAGAKU GIJUTSU RENGO KOENKAI KOENSHU in Japanese
31 Oct-2 Nov 89 pp 676-677

[Article by Shokichi Misawa, Akira Meguro, and Yasuo Ayatsuka, Radio System Laboratory, Nippon Telegraph and Telephone]

[Text] 1. Introduction

One mission of the Engineering Test Satellite VI (ETS-VI) is to conduct experiments on point-to-point communications and mobile communications. An antenna with a 3.5 m aperture is used for such purposes. One problem involved in developing such a large antenna is understanding and evaluating its vibration characteristics. To date, we have reported on this problem from the standpoint of evaluation and the evaluation procedure,¹ and the effects of the antenna components and the atmosphere on its vibration characteristics.^{2,3} In this paper, we report on the results of our studies on the vibration characteristics of a 3.5 m antenna to be mounted on the ETS-VI, which we have conducted on the basis of vibration analysis and modal tests.

2. Outline of Structure

Figure 1 shows the configuration of the antenna to be mounted on the ETS-VI as it is housed prior to launch. The antenna is fixed to the tower by a retention and release mechanism and housed in an H-II rocket at the time of launch. The 3.5 m antenna is divided into three sections—a central wing, a left wing, and a right wing. Each wing consists of a reflector and a truss structure to support it, a stud to couple the reflector and the truss structure, and heat-control material that covers the entire back. In orbit, the left and right wings are extended by the extension mechanism and then the antenna is lifted into the specified position by an ejection mechanism.

3. Vibration Characteristics

The vibration characteristics of the antenna when it is housed are as follows. For the vibration analysis we have assumed that the interface point between the ejection mechanism or the retention and release mechanism and the tower is completely fixed. This antenna is larger in aperture and more complicated in structure than conventional antennas, and it has as many as 30 modes at a

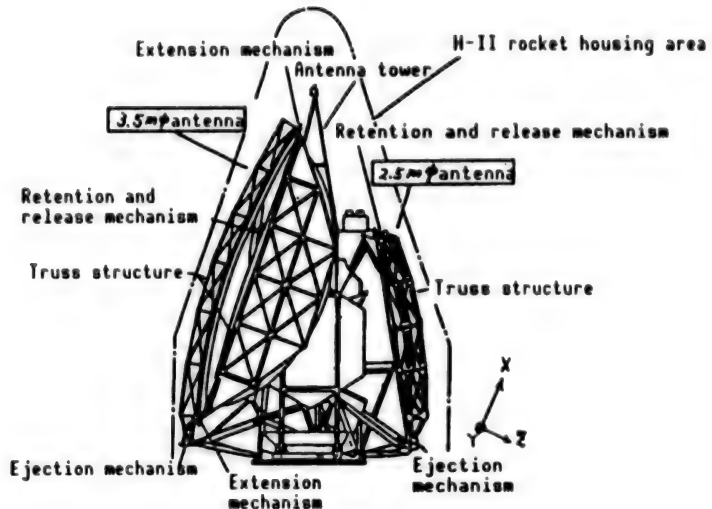


Figure 1. Antenna for Mounting on ETS-VI

frequency of 100 Hz or below, and many of these are local modes. We assume that these vibration modes include some that appear only in analysis, and that, therefore, they cannot always be confirmed by a modal test. It is also difficult to have all resonance points and modes of vibration, which could be confirmed in a modal test, agree with the analysis results. Therefore, in the modal test, we have conducted random one-point vibration tests using a small vibrator in order to identify the vibration mode that is critical for strength. Table 1 shows the results of the vibration analysis. It includes natural frequencies with a margin of safety of one or below and the mode of vibration. The modes of vibration in a vacuum and in the atmosphere differ slightly, but this difference is not sufficiently large to change the mode of vibration.

Table 1. Vibration Analysis Results

Order	Natural frequency (Hz)		Mode of vibration
	In vacuum	In atmosphere	
1	45.4	43.2	Central wing lateral bending
2	50.1	45.2	Central wing out-of-plane bending
3	55.2	49.3	Central wing out-of-plane bending
7	65.5	61.5	- Y wing out-of-plane bending

The modal test results are shown in Table 2. The measured modes of the lower orders are the same as the analysis modes. As for the natural frequency, however, there was a great difference between the test results and the analysis results, with the test results being far lower than the analysis results. Several factors can be cited to explain this discrepancy, but we have found our studies on differences in the rigidity mechanism.

Table 2. Modal Test Results

Order	Natural frequency (Hz)	Mode of vibration
1	33.0	Central wing lateral bending
2	37.4	Central wing out-of-plane bending
3	39.6	Central wing out-of-plane bending

In the middle stage of design, we studied the effect (with no atmospheric effect taken into account) of the antenna components on the natural frequency. As a result of this study, we found that, as compared to the truss diameter, stud diameter, and the rigidity of the retention and release mechanism, the rigidity of the extension mechanism has a great effect. Thus, with the atmospheric effect taken into account, we have computed the natural frequency at the time of changing the rigidity of each axial direction of the extension mechanism, as shown in Table 3. We have calculated these rigidity values on the basis of preliminary test results. The results of the computations are shown in Figure 2. Due to the rigidity of the extension mechanism, the primary natural frequency is somewhat lower than the results shown in Table 1, but it still differs by only 3 Hz from the test results.

Table 3. Analysis Cases Showing Different Values for Extension Mechanism Rigidity

Case	Kx	Ky	Kz
1	300	450	200
2	300	250	100
3	300	450	50
4	300	100	100
5	10	450	100

Unit: kg/mm

Hereafter, we plan to measure the rigidity of the extension mechanism and to confirm the natural frequency by using these data together with the material test results.

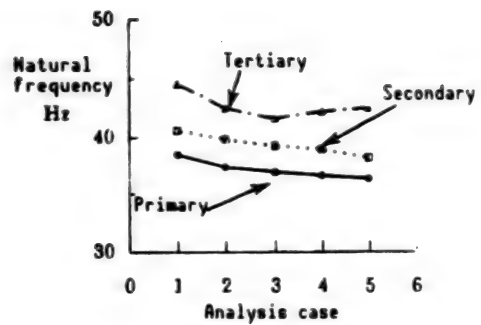


Figure 2. Changes in Natural Frequency Due to Rigidity of Extension Mechanism

References

1. Misawa, et al., "Vibration Characteristics Evaluation of Large Antenna for Mounting on Satellite," DAI31KAI KOAOKYODO NI KANSURU KOENKAI, 3B7, 1989.
2. Ibid., "Structural Characteristics of Large Extensive Antenna for Mounting on Satellite," DAI30KAI KOAOKYODO NI KANSURU KOENKAI, 2B5, 1988.
3. Oda, et al., "Natural Frequency Drop Due to Air of Large Lightweight Antenna," DAI32KAI UCHU KAGAKU GIJUTSU RENGO KOENKAI, 1C5, 1988.

Extension Test Method for ETS-VI Antenna Module

906C3836 Tokyo DAI33KAI UCHU KAGAKU GIJUTSU RENGO KOENKAI KOENSHU in Japanese
31 Oct-2 Nov 89 pp 678-679

[Article by Akira Meguro, Radio System Laboratory, Nippon Telegraph and Telephone]

[Text] 1. Introduction

The greatest obstacle to conducting ground-based extension tests of a large antenna reflector as it is actually mounted on a satellite is gravity. Up to now, with its effect on the extension characteristics taken into account, we have explored ways to overcome this problem. As for the ejection of the overall reflector, we have confirmed that relevant tests can be conducted at the practical level. In this paper, we show, through analysis and test results, the effect of our newly designed gravity compensation method, which is an effective test for the extension of the two wings of the primary reflector.

2. Problems in Extension Test of Divided Primary Reflector

Extension tests of the 3.5 m antenna reflector for the ETS-VI are conducted in two parts—an overall reflector ejection test and a triparted and folded reflector extension test. Up to now, we have conducted gravity compensation extension tests of an antenna actually mounted on a satellite by using a suspension and follow-up system tester. These tests have confirmed the practicality of the equipment and we have conducted a trial test using a structural model with a 2 m aperture.¹ But as for an extension test of the two wings of the divided reflector, little accuracy has yet been attained for the following reasons:

- (1) When the antenna is mounted on a satellite, the extension axis of the two wings is inclined with respect to the vertical axis. When conducting the suspension and follow-up system extension test in this state, a high-accuracy double-degree of freedom control becomes necessary for the follow-up control.
- (2) Since the wing reflector has a smaller moment of inertia than the overall reflector, and since a large driving torque is required to overcome the resistance torque of the large number of latch pawls, its extension speed is 10 or more times greater than the overall reflector erection speed.

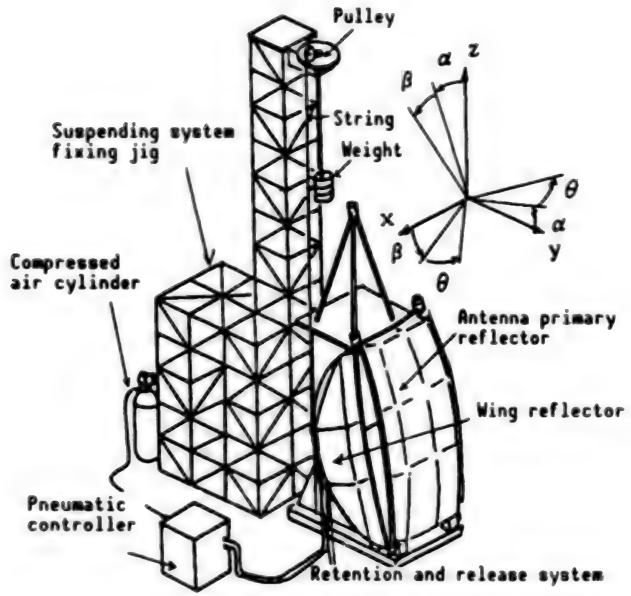


Figure 1. Extension Test Equipment

3. New Gravity Compensation Method for Extension Test of Wing Reflectors

3.1 Composition of Gravity Compensator

Figure 1 is a diagram of the test equipment. The antenna reflector is fixed by the reflector fixing jig so that the extension axis of the two wing reflectors is inclined and the divided wing reflectors of the antenna reflector are retained by the jig in a folded position. Reflector retention and release are effected by the pneumatically operated retention and release system. The wing reflector is suspended from a string and, in order to give this string a tensile force, a weight is attached through a pulley installed above. In the diagram, α and β are inclinations around the x and y axes, respectively, while θ represents the extension angle around the z axis.

3.2 Balance of Force During Wing Reflector Extension

From the difference between M_{og} , the moment around the extension axis due to gravity, and M_{ot} , the moment due to the string:

$$G = \int_{\theta_0}^{\theta_f} (M_{og} + M_{ot})^2 d\theta = \int_{\theta_0}^{\theta_f} (A + T + B)^2 d\theta$$

where,

$$A = \left[T \frac{(x_{sl} - x_{sv})}{L_{sv}} (-\cos\beta\sin\theta) + T \frac{(y_{sl} - y_{sv})}{L_{sv}} (-\sin\alpha\sin\beta\sin\theta + \cos\alpha\cos\theta) \right. \\ \left. + T \frac{(z_{sl} - z_{sv})}{L_{sv}} (\cos\alpha\sin\beta\sin\theta + \sin\alpha\cos\theta) \right] \sqrt{x_{sl}^2 + y_{sl}^2}$$

$$B = -mg(\cos\alpha\sin\beta\sin\theta + \sin\alpha\cos\theta)\sqrt{x_{cg}^2 + y_{cg}^2}$$

This is the error evaluation function. The optimum value of the tensile force, T , can be derived from the stationary condition of G , where $\delta G = \partial G / \partial T$ $\delta T = 0$. In these equations, x_{sl} , y_{sl} , and z_{sl} are the coordinates of the suspending point on the wing reflector; x_{sw} , y_{sw} , and z_{sw} are the coordinates of the upper fixing point; L_{sw} is the distance between the suspending point and the fixing point; and x_{cg} , y_{cg} , and z_{cg} are the coordinates of the gravitational center position.

As in the case of the tensile force, T , the x and y coordinate values x_{sw} and y_{sw} of the upper fixing position to minimize the value for G are:

$$\delta G = (\partial G / \partial x_{sw}) \delta x_{sw} = 0, \delta G = (\partial G / \partial y_{sw}) \delta y_{sw} = 0$$

It has been proven by numerical analysis that the fixing point position that will minimize gravity compensation error is located vertically above the most stable position (where the gravity torque becomes 0) of the wing reflector.

4. Effect of Gravity Compensation

Figure 2 shows the gravity compensation error when the extension axis inclinations $\alpha = 18.96^\circ$ and $\beta = 4.12^\circ$. The amount of error is within 0.04 Nm and 1 percent or less of the driving circuit torque. Thus, a sufficient compensation accuracy is acquired. In order to confirm the effect of the gravity compensation method, we have conducted an extension test using a prototype extensible antenna reflector. Figure 3 shows the results of a test when the same antenna reflector and suspension conditions as those in Figure 2 were used and these results are compared to the results of a test where the extension axis was set in the vertical direction ($\alpha = 0$, $\beta = 0$) and effected no gravity compensation. If the gravity compensation characteristics shown in Figure 2 were actually obtained, these two sets of test results ought to agree completely, but in fact they differ somewhat from each other. The principal reason for this is the error in setting the fixing point position. Also, since an error is included in the perpendicularity of the axis, we would like to conduct further confirmation tests.

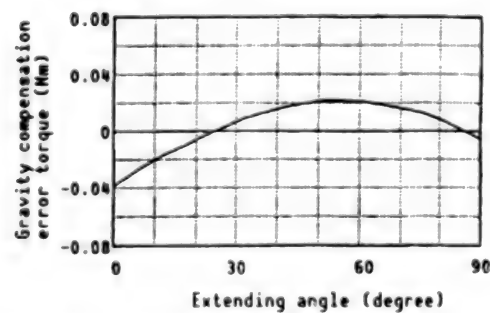


Figure 2. Gravity Compensation Error

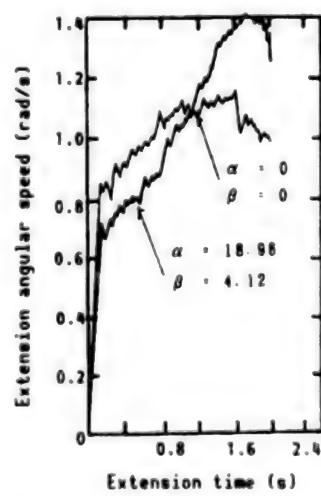


Figure 3. Extension Test Results

5. Conclusion

The most outstanding characteristics of this gravity compensation method are that gravity compensation for an extendible structure with an inclined extension axis can be effected using simple equipment and that its effect on the dynamic characteristics of the extension process is small. However, when there is an error in the initial setting, particularly in the fixing point setting, sufficient accuracy cannot be acquired, and thus we must be careful in determining the setting.

References

1. Meguro, DAI31KAI KOZOKYODO NI KANSURUKOENKAI ZENSATSUSHU, July 1989, pp 348-351.

Ejection, Extension Characteristics of ETS-VI Primary Antenna Reflector

906C3836 Tokyo DAI33KAI UCHU KAGAKU GIJUTSU RENGO KOENKAI KOENSHU in Japanese
31 Oct-2 Nov 89 pp 680-681

[Article by Akira Meguro, Hitoshi Miyoshi, and Shokichi Misawa, Radio System Laboratory, Nippon Telegraph and Telephone]

[Text] 1. Introduction

An ejection and extension system is required for the primary antenna reflector that is to be mounted on the ETS-VI because the antenna reflector is housed in a rocket during launch. Extension of the antenna reflector in orbit is one of the most important events for the satellite mission. However, it is impossible to confirm the system's on-orbit extension characteristics directly through ground tests. Thus, we must predict them by using test data gathered on the characteristics of the parts and the mechanism unit. With these test data we can simulate an environment that is as close to the orbital environment as possible. In this paper, we compare our prediction of its ground extension characteristics based on simulation data with actual ground extension test results. We also compare the mechanism characteristics acquired by parameter identification of the ground test data with the mechanism test results. This enables us to clarify the relationship between its characteristics as a mechanism unit and those of the system and to verify the accuracy of our prediction of its characteristics in orbit, which is based on the mechanism characteristics.

2. Ejection and Extension Mechanism

In this paper, the ejection mechanism means the hinged drive mechanism that ejects the overall antenna reflector. The extension mechanism means the hinged drive mechanism that extends the divided and folded reflector. The driving force is the restoring force of a coiled spring.

2.1 Characteristics of Mechanism Components

The parts characteristics are measured under a variety of conditions, including different pressures, temperatures, loads, and working conditions. Figure 1 shows the measured torque distribution values. In the diagram, the driving torque is from the spring and the resistance torque is the total of

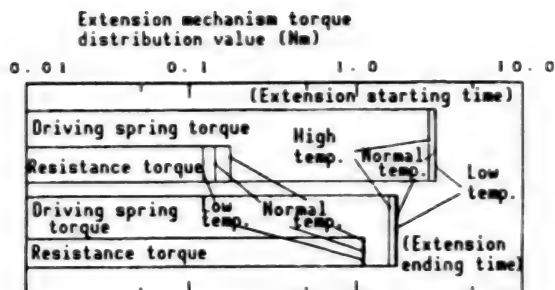


Figure 1. Extension Mechanism Torque Distribution Values

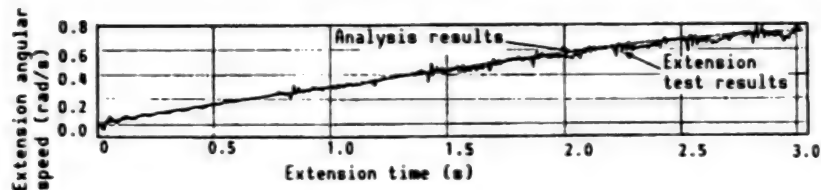


Figure 2. Extension Test Results of Extension Mechanism Unit

the values for bearing friction, friction between the spring and its guide cylinder, harness resistance, and latch resistance.

2.2 Prediction of Mechanism Characteristics and Mechanism Unit Test Results

Figure 2 shows a comparison between the mechanism characteristics of the extension mechanism predicted from the component parts and the extension test results of the mechanism assembly conducted in a vacuum vessel. For the mechanism test, an inertia dummy was installed. Because the inertial of the dummy differs from that of the real reflector, its extension movement also differs from that of the real reflector. Nonetheless, the test results and the analysis results agree very well.

3. Ground Extension Test

Our report is based on the extension test of the reflector components, which of the tests conducted to date is the closest to the system level.

3.1 Ground Extension Test Method

The extension test method for which the effect of tester errors on the reflector components is smallest is to extend the reflector in the horizontal direction thus perpendicularly intersecting the gravitational direction.¹ The reflector is set so that its extension axis agrees with the perpendicular direction. Thus, the load on the mechanism part is canceled by suspension.

Identification of Extension Parameters

In order to identify the system parameters of the nonlinear equation of motion, a value for the discrete time status is computed by numerical integration and the system parameters are retrieved on the basis of the evaluation

function by the steepest ascent method, etc.² The equation of motion, which controls the ground extension motion, can be expressed as follows:

$$\ddot{\theta} = K_0 - k\theta - A\dot{\theta}^2 - F_0 - f\theta + mgr(\sin\Delta\alpha\cos\theta + \sin\Delta\beta\sin\theta)$$

where, I represents the moment of inertia, K_0 the initial spring torque, k the spring constant, A the air resistance coefficient, F_0 the friction torque, f the friction constant, m the mass, g the gravitational acceleration, r the distance from the extension axis to the gravitational center, $\Delta\alpha$ and $\Delta\beta$ the extension axis inclination, and θ the extension angle.

3.3 Prediction and Test Results of Ground Extension Characteristics

Figure 3 shows the extension test results in comparison with the extension behavior prediction results based on the parts characteristics data. The test results and the prediction results show some difference in the final angular speed, but it is believed that this will have no great effect on the mechanism characteristics.

3.4 Identification of Extension Parameters

In order to examine more minutely the difference in the results in the above paragraph, we have estimated the parameters of the equation of ground extending motion by using the angle profile acquired from the test. The extension profile computed on the basis of the estimated parameters is shown on top of the test results in Figure 3. Table 1 shows the acquired extension parameters in terms of their ratio to the parts characteristics values. Values other than those of the driving and friction torque and the air resistance torque virtually can be ignored.

4. Study of Mechanism Characteristics

As shown in Table 1, there is almost no change in the values of the parts characteristics when the antenna is housed, but there is a decrease in the values of the parts characteristics at the time of extension, which causes a difference in the final angular speed.

Table 1. Changes in Characteristics Values of Extension Mechanism Component Parts

Parts characteristics values*/Estimated parameter values**	
Extension starting time	Extension ending time
0.971	0.498

* Difference between driving spring torque and resistance torque

** Difference between $(K_0 - k\theta)$ and $(F_0 - f\theta)$

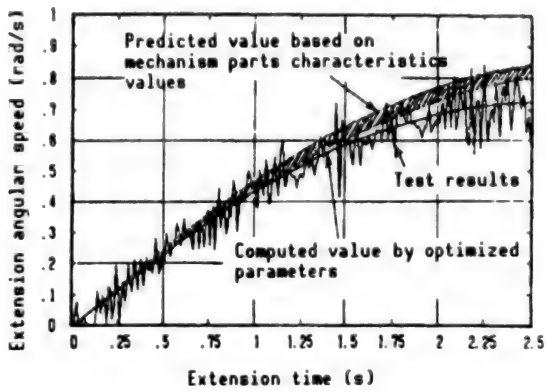


Figure 3. Antenna Reflector Extension Test Results

However, there is no change in the spring torque and resistance torque at extension starting time and the difference in the angular speed profile increases rapidly with the approach of extension ending time. This difference is believed to reflect the fact that although the resistance of the latch pawl is not incorporated in the predicted values based on the parts characteristics values, the latch movement part has been included in the range of the test data used for parameter identification.

5. Conclusion

As described above, we have been able to demonstrate that it is possible to predict the assembly characteristics and hence the antenna reflector extension characteristics from the mechanism component parts characteristics. Since, however, it is also conceivable that in studying the mechanism characteristics there might be changes in characteristics due to handling and environmental hysteresis conditions, etc., we must acquire far more test data in order to carry out further comparative studies.

References

1. Meguro, NIPPON KOKU UCHU GAKKAISHI, Vol 36 No 414, July 1988, pp 326-332.
2. Miyoshi and Meguro, UCHU KOZOBUTSU KENKYUKAI (DAI4KAI) GOSATSUSHI, July 1988, pp 113-116.

Extension Test Method for 5 m ϕ Satellite Antenna

906C3836 Tokyo DAI33KAI UCHU KAGAKU GIJUTSU RENGO KOENKAI KOENSHU in Japanese
31 Oct-2 Nov 89 pp 682-683

[Article by Yasumasa Hisada and Satoshi Kusama, National Space Development Agency; and Tatsukichi Osaka, Kunihiro Nakamura, and Seiji Ohashi, Toshiba Corp.]

[Text] 1. Introduction

Development of a 5 m ϕ petal extensible antenna for satellite-to-satellite communications is under way. In order to conduct ground extension tests on such an extensible antenna, it is necessary to cancel the effects of gravity. In this paper, we report on a basic extension test that we conducted as part of our effort to elaborate a ground extension test method of the 5 m ϕ antenna and to confirm that test method.

2. Extension Test Method

The extension of an antenna on the ground differs from the same operation in space due to the effect of gravity and atmosphere. Therefore, in order to predict the extension functions and characteristics of an antenna in orbit accurately, it is necessary to conduct ground-based tests in which the effects of gravity and atmosphere are eliminated. The effects of the atmosphere can be removed by slowing the extension speed as much as possible or by conducting tests in a vacuum. Thus, it is necessary to develop a gravity compensation method to remove the effects of gravity.

For our extension tests of the 5 m ϕ extensible antenna, we designed a new method of compensating for gravity that involves an overhang arm, a suspension wire, and a motor, with consideration given to the antenna extension sequence.

3. Extension Test of 5 m ϕ Extensible Antenna

3.1 Outline of Extensible Antenna

As shown in Figure 1, the petal extensible antenna has an aperture of 5 meters and its primary reflector is composed of 24 petals divided obliquely along the radial direction and the tangential direction. These petals are extended by rotating them about an axis.

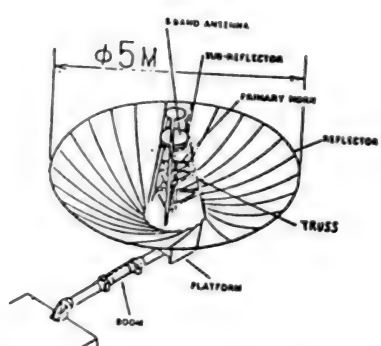


Figure 1. Diagram of Antenna System

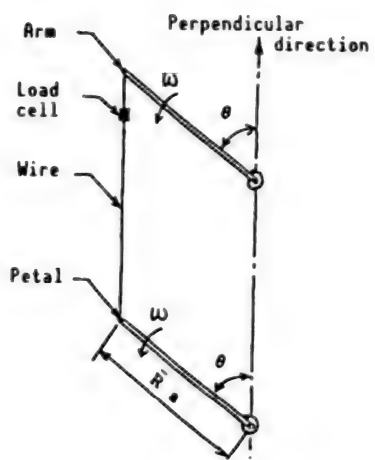


Figure 2. Concept of Extension Test Method

3.2 Extension Test Method

Figure 2 shows the concept for the newly designed extension test method. As shown in the diagram, a petal is suspended from above by an arm through which a suspension wire is passed. The effect of gravity on the petal is canceled by turning the arm in a direction corresponding to the extension of the petal. (This is called the "arm suspension system.") This system is structured so that the arm, wire, petal, and the distance between the centers of rotation of the arm and the petal form a parallelogram for any angle of rotation. Should the tensile force measured by a load cell attached to the suspension wire be fixed, it means that the effect of gravity has been canceled.

The friction moment in the bearing unit is basically unavoidable, but it is small and is believed to have no great effect on the extension process.

As for atmospheric effect, since reducing extension speed reduces the moment of the drag acting on the segment until it becomes the same order of magnitude as the friction moment of the bearing unit, it is believed that there is no great effect on the antenna extension process.

Figure 3 shows the extension test configuration.

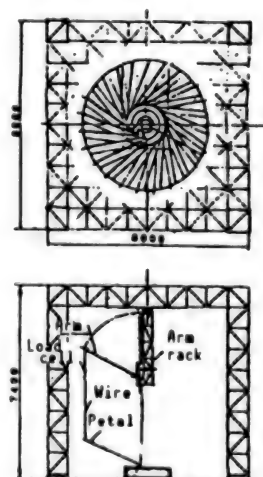


Figure 3. Extension Test Configuration

4. Basic Extension Test

With regard to the "arm suspension system," that we have test manufactured for the extension test of the 5 m ϕ extensible antenna, we have conducted a basic extension test to confirm the functions of the system and the test equipment. In the test, we used an aluminum pipe as the specimen. The extension test demonstrated that, as shown in Figure 4, the tensile force of the wire is roughly fixed with respect to changes in the angle of rotation, and thus the gravity compensation of the specimen has been fully attained.

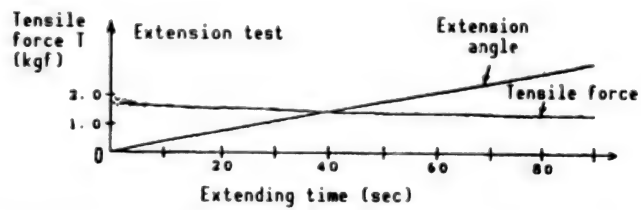


Figure 4. Results of Basic Extension Test

5. Conclusion

Through studies on the extension test method and the basic extension test, we have confirmed the characteristics and functions of the "arm suspension system."

Development of Synthetic Aperture Radar Antenna Retention, Release Mechanism

906C3836 Tokyo DAI33KAI UCHU KAGAKU GIJUTSU RENGO KOENKAI KOENSHU in Japanese
31 Oct-2 Nov 89 pp 684-685

[Article by Hideo Hino, Mitsuru Takei, and Yukiaki Nemoto, Remote-Sensing Observation System R&D Organization; and Yoshiteru Ogata, Noriko Kanai, Nobuyuki Tajika, and Hiroyuki Naruki, Kamakura Works, Mitsubishi Electric Corp.; this research has been conducted as part of a large-scale project entitled "Remote-Sensing Observation System R&D" of the Agency of Industrial Science and Technology, Ministry of International Trade and Industry]

[Text] 1. Introduction

The synthetic aperture radar antenna unit (SAR antenna) that will be mounted on the Earth Resources Satellite 1 (ERS-1) is a large extensible structure of the folding-screen type. Currently, we have verified and somewhat revised its design using the retention and release mechanism of the engineering model (EM), which has roughly the same electrical, mechanical, and thermal performance characteristics as the real thing. This report describes the results we obtained.

2. Functions of Retention and Release Mechanism

The retention and release mechanism is one of the essential systems for the extensible structure. It must fulfill two functions: 1) to hold the extensible structure, which is folded in the rocket nose fairing, firmly in place with multipoint constraints; and 2) to release the constraints at the specified orbit upon command from the ground. The first function is called the retention function; its purpose is to ensure that a lightweight, extensible structure can endure the stressful mechanical environment conditions of a rocket launch. The second function is called the release function, which is often effected by using ordnance (a detonating fuse).

One type of ordnance that can directly fulfill the requirements for multipoint constraint (retention function) and its removal (release function)—the effective operation of the retention and release mechanism—is a split nut. The split nut is designed so that the nut side of a bolt/nut breaks and releases the bolt. By arranging the split nut at every constraint point should make it possible to obtain the desired functions. Also required is an ordnance capable

of performing only the release function. One kind of ordnance that fits this requirement is the line cutter. A line cutter cuts wire and rods with a guillotine knife. This device requires a configuration in which the wire and rod invariably serve as part of the loading route for multipoint constraint and bear a tensile load. A mechanism in which there is a state of multipoint constraint when this tensile load is applied and in which the constraint is removed when it is removed has many variations. The retention and release mechanism for the SAR antenna is based on one of these variations.

The extending movement sequence of the SAR antenna is not described here, because it has been given in a previous report,¹ but the retention and release mechanism must be arranged so that the release function operates at the start of the 90° turn, the first stage extending movement, while the retention function must hold it in the stored state until that point. The SAR antenna, which has an aperture of about 12 m, is divided into eight antenna panels, which are folded during the launch. The retaining pin of the retention and release mechanism fixes the folded panel package by passing through its six spots. The arrangement of these six spots is optimized so as to raise the natural frequency to a range where it will not interfere with the pattern printed on the antenna surface and the buried feeder circuit. The effectiveness of this arrangement has been reported in a previous report.²

3. Relationship Between Retaining Force and Releasing Force

Figure 1 is a cross sectional diagram of the retaining pin piercing part of the folded panel package. We have designed it so that the retaining pin clamping force is the panel package retaining force and, at the same time, its horizontal component becomes the releasing force. The wedge pin is pushed in the opposite direction by a force larger than the releasing force until the ordnance works, but, depending on the cone angle selection and the friction coefficient of the sliding part, the releasing force is balanced with the frictional force, thereby resulting in no release regardless of the presence of external forces. Also, when the retention load increases, flaws in the sliding surface and elastic deformation of the pin can be a cause of concern, but, as shown in Figure 2 and Figure 3, the test results have been satisfactory. We have reviewed the design by using the friction coefficient identified in the experiment.

4. Conclusion

We have acquired data that supports our ability to guarantee the reliability of the release function of the retention and release mechanism, which is also important structurally as the loading route. These results have been incorporated in the flight product design of the SAR antenna.

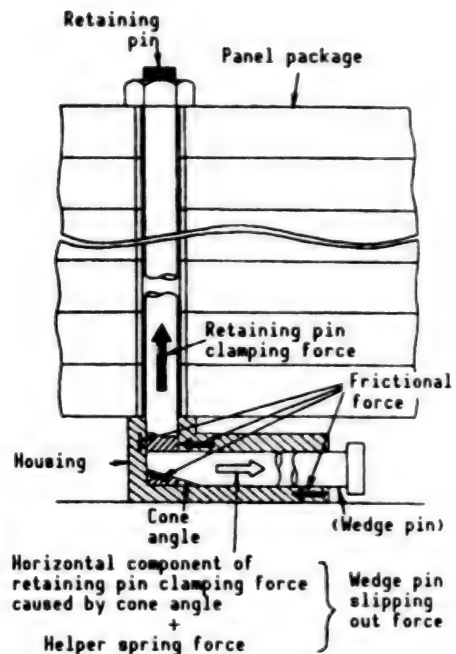


Figure 1. Cross Sectional Diagram of Panel package Retention Position

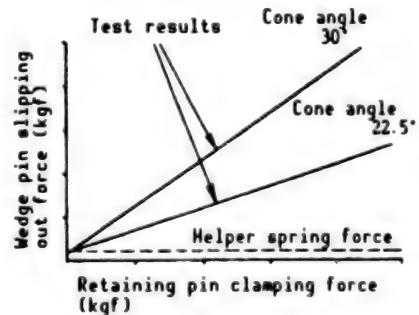


Figure 2. Horizontal Component (Including spring) Vs. Clamping Force

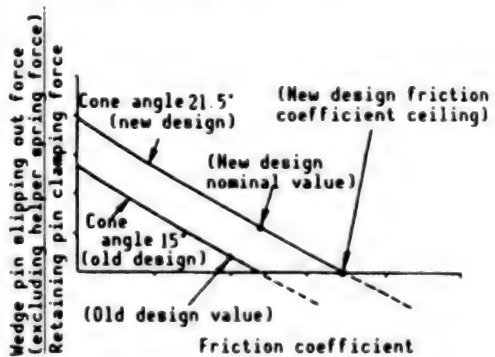


Figure 3. Horizontal Component/Clamping Force Vs. Friction Coefficient

References

1. Hino, H., et al., "Extension Test Results of Development Model of Synthetic-Aperture Radar Antenna for Mounting on ERS-1," DAI31KAI UCHU KAGAKU GIJUTSU RENGO KOENKAI, 3C1.
2. Ibid., "Vibration Test Results of Development Model of Synthetic-Aperture Radar Antenna for Mounting on ERS-1," 3C2.

Orbital Extension Characteristics of ERS-1 Synthetic-Aperture Radar Antenna

906C3836 Tokyo DAI33KAI UCHU KAGAKU GIJUTSU RENGO KOENKAI KOENSHU in Japanese
31 Oct-2 Nov 89 pp 686-687

[Article by Hideo Hino, Mitsuru Takei, and Yukiaki Nemoto, Remote-Sensing Observation System R&D Organization; and Noriko Kanai, Yoshiteru Ogata, Takashi Takada, and Masatoshi Toyosawa, Kamakura Works, Mitsubishi Electric Corp.; this research has been conducted as part of a large-scale project entitled "Remote-Sensing Observation System R&D" of the Agency of Industrial Science and Technology, Ministry of International Trade and Industry]

[Text] 1. Introduction

The synthetic aperture radar (SAR) antenna designed for the earth resources satellite 1 (ERS-1) is a large extensible structure that resembles a folding screen. In order to carry out a comprehensive evaluation of its structure, we conducted a series of developmental tests on an engineering model (EM), which has roughly the same electrical, mechanical, and thermal performance characteristics as the real thing. Further, we have analyzed its extension motion characteristics in orbit. This analysis includes the results of the ground extension and thermal balance tests we conducted. This article reports on the results of our tests and prediction analysis.

2. Reliability of Extension Hinge Function

The SAR antenna extension sequence consists of three steps: 1) a 90° turn; 2) extension of the two wings; and 3) off-nadir inclination—as shown in the previous report.¹ The functions required for the extension mechanism to effect each of these movements—as described in previous reports^{1,2}—consist of: 1) a retention function to maintain the shape of the antenna before extension and to provide a load-resisting capability; 2) a release function to initiate the extension motion; 3) a power function to guarantee the supply of extension energy and the degree of freedom required for extension; and 4) a latching function to maintain the shape of the antenna after extension. This paper, however, deals with extension functions 3) and 4) only as they are directly responsible for the action of the SAR antenna extension hinge.

The basic principle of the SAR antenna extension hinge is as follows. The two metal fittings are designed to be moved by the extension energy provided from

a preloaded spiral spring and then to be locked in a specified position after making a relative motion with the bearing axis of rotation as the center. This motion stops and locking occurs when the pins move into the slots. This simple mechanism can have a very high degree of reliability, but only if there are no defects in the hardware. In other words, function 3) requires that a large amount of energy be provided to ensure that extension occurs. At the same time, however, it is necessary to ensure that the antenna has sufficient structural strength so that it can withstand the stresses created during launch and then during latching (function 4)). One effective way to minimize impact load is to control the extension speed through the use of a damper or a motor instead of reinforcing the antenna structure. This approach, however, was not adopted for the SAR antenna because our first priority was to create a simple structure. In either case, the basic problem is to create lightweight hardware and to guarantee extension. For that purpose, we have been engaged in a reductive analysis of the antenna's extension motion characteristic. The output parameters for prediction and analysis are represented by the time required for extension and the final angular speed of extension. The latter directly affects the magnitude of the impact load. Input parameters, meanwhile, include the positive extension torque caused by preload release of the spiral spring. This is canceled by the negative extension torque caused by bearing friction and the bending resistance of cables. Therefore, whichever is the larger of the two has the greatest effect on extension reliability. In general, antennas are designed so that a positive margin is allowed for the extension torque. However, the negative extension torque factor can also be large and is particularly affected by temperature dependency. Consequently, it is important to estimate orbit temperatures accurately, to be aware of parameter changes within the range of those temperatures, and to guarantee the proper extension motion characteristics for those changes.

3. Temperature Before In-Orbit Hinge Extension

We carried out a predictive analysis of the temperatures before extension in orbit using the EM. This analysis reflected the results of the thermal balance test. With regard to the center hinge, which is involved in the first and third steps of the extension sequence, we have added a heater primarily to provide bearing clearance control, but also ensure a proper temperature margin even if one of the two thermostats malfunctions. As for the double hinge/panel hinge involved in the second step of the extension movement sequence, we have confirmed that this presents no problems. We have also predicted temperatures for the cables and have used these results to determine the size and fluctuation width of the resistance torque (negative extension torque).

4. Extending Motion Characteristics

By using the predicted temperatures of the extension hinge and cables immediately before each in-orbit extension movement together with the data on resistance torque acquired from separate experiments, we have calculated the predicted values shown in Table 1 for the in-orbit extension motion characteristics.

Table 1. In-Orbit Extension Characteristics

Sequence	Extension time (S)		Final extension angular speed (deg/s)	
	Resistance minimum	Resistance maximum	Resistance minimum	Resistance maximum
(1)	18	21	10	8
(2)	12	15	45	34
(3)	10	14	7	5

5. Conclusion

By conducting a predictive analysis of the in-orbit extension characteristics of the SAR antenna, while taking into account the results of good extension and thermal balance tests using the EM, we have been able to guarantee that the actual device will have the reliability to ensure extension and the structural strength necessary to withstand extension impact.

References

1. Hino, H., et al., "Extension Test Results of Synthetic-Aperture Radar Antenna Development Model for Mounting on ERS-1," DAI32KAI UCHU KAGAKU GIJUTSU RENGO KOENKAI, 3C1.
2. Ibid., "Development of Retention and Release Mechanism of Synthetic-Aperture Radar Antenna for Mounting on ERS-1," DAI33KAI UCHU KAGAKU GIJUTSU RENGO KOENKAI.

Creation of Data Base for Research on Functionally Gradient Materials

906C3836 Tokyo DAI33KAI UCHU KAGAKU GIJUTSU RENGO KOENKAI KOENSHU in Japanese
31 Oct-2 Nov 89 pp 706-707

[Article by Akio Moro, Yoshisato Ishibashi, Katsuhito Kisara, Takayuki Sudo,
and Masayuki Niino, Tsunoda Branch Office, National Aerospace Laboratory]

[Text] 1. Introduction

Since FY 1987, about 30 research institutions interested in promoting science and technology have been working together on a project entitled "Research on Fundamental Technologies To Develop Functionally Gradient Materials To Reduce Thermal Stress." Functionally gradient materials are heat-resistant materials with good thermal insulation properties. Potential uses include the thermal protection system of a space plane, rocket combustor walls, etc. We plan to synthesize these materials using ceramics for the high-temperature side and metals for the low-temperature side. Also, the structure of the materials will be controlled so that the mixing ratio and microstructure of these two groups of materials will form a continuous and optimal distribution for their functional environment.

In developing these materials, material design, which includes a determination of material combination and optimal material distribution, is important. Also, not only a synthesis method but a method for evaluating the characteristics of these heterogeneous materials must be developed. Thus, it has been decided to divide the participating research institutions into three groups—one for design, one for synthesis, and one for evaluation. This will make it possible for them to carry out independent research on different subjects.

However, if so many research institutions are to push ahead efficiently in different directions, they must take steps to ensure a smooth flow of information and to maintain close connections among them.

2. Concept for Data Base

Figure 1 shows the flow of data between the data base and each sector. We have designed this data base to be used for the following purposes:

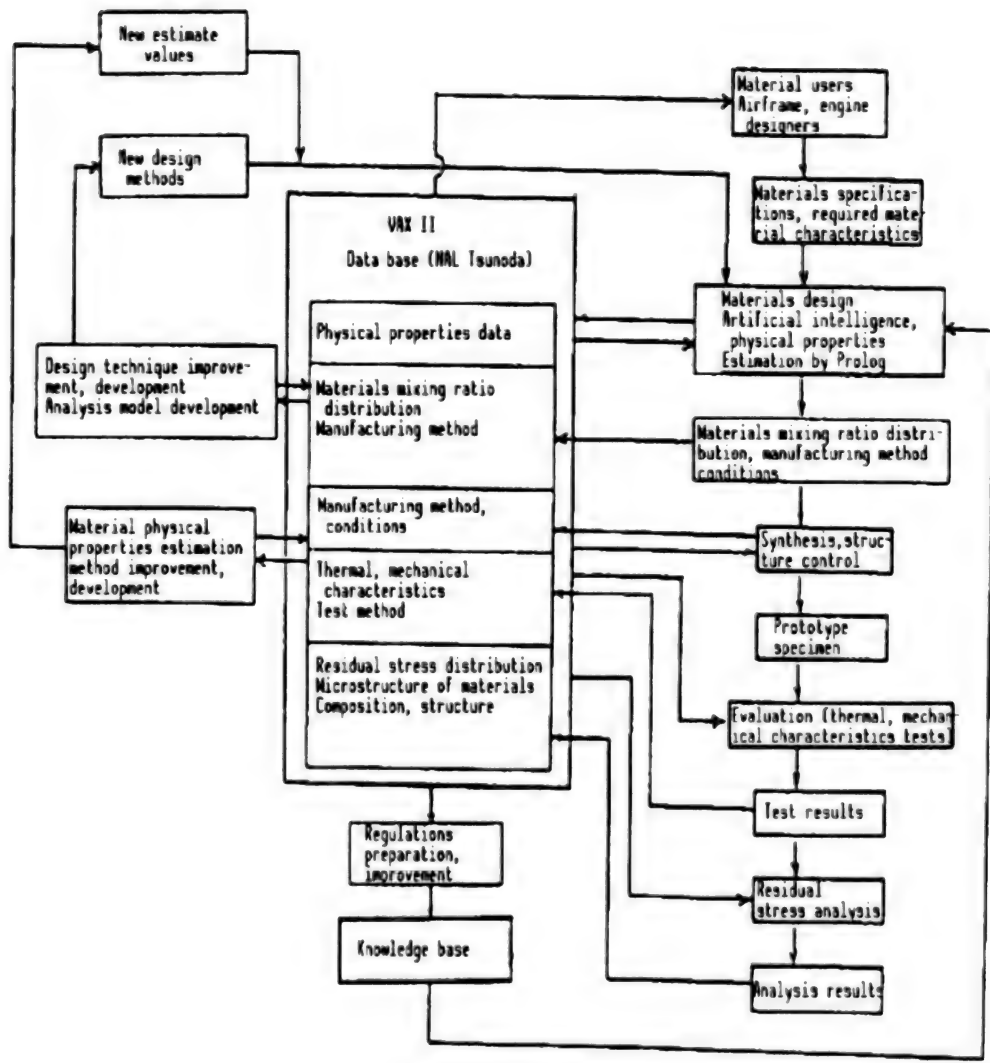


Figure 1. R&D Organization

- (1) To ensure that research institutions in each of the three sectors can have free and immediate access to another's information.
- (2) To provide data to the material design system using artificial intelligence, which is being developed by the design sector.
- (3) To provide for the output of data to the analysis sector to enable it to develop a physical properties estimation method and an analysis method.

To meet the requirements not only data regarding the physical property values of the material but also its microstructure—such as the internal constituent distribution of the material—as well as the control process and data on the testing method and evaluation standards must be inputted into the data base. Also, to enable the research institutions to use this data freely, it is necessary to establish a network and to make the data accessible through this network. Meanwhile, design work must be able to take into account various

network. Meanwhile, design work must be able to take into account various temperature conditions. And for analysis, the problem of unsteady states must be taken into account. Consequently, the physical property values become the functions of multivariables, such as temperature and time, and must be inputted in the form of a matrix and must undergo interpolation or extrapolation at the time of output. Further, in order to control a microstructure based on an optimal design, microstructure research involving such methods as image processing is essential. Therefore, image data inputting and outputting must also be possible.

3. Conditions for Data Base Preparation

Consistent with this concept, we are constructing a data base in the VAX II/GPX workstation of the Tsunoda Branch Office of the National Aerospace Laboratory, using the Boeing RIM as software. In this project, however, individual institutions are conducting research on different synthesis methods and evaluation methods, respectively, and, therefore, the data acquired vary depending on the particular research institution. Such being the case, upon concluding the fundamental data base structure, we held a series of discussions among researchers from all sectors and organized the data base in a way that emphasizes those data items frequently used and which relate to the basic physical properties of the materials being developed. Further, since we are still in the middle of the research, neither a synthesis method nor an evaluation test method has been established, and thus the data points to be acquired also vary as the research progresses. In order to cope with this situation, we must add and change not only the data, but also the data points themselves. At the same time, since material researchers from the research institutions must have direct access through the network, the system operating procedure must also be easy.

Thus, we have built up a network linking the VAX II/GPX of the Tsunoda Branch Office of the National Aerospace Laboratory and the personal PC-9801 computer of each research institution by using a VT emulator. This makes it possible for each institution to have direct access to the data base. Because there is no application program for the RIM, however, operation has not been easy and the need for improvement has become apparent. To cope with this problem, we have developed an application program using the R-base system V for the PC-9801, which is compatible with the RIM, and are trying to conduct input/output by this program.

4. Conclusion

Up through the fiscal year, our work has focused primarily on constructing the data base and improving access performance. Beginning with the next fiscal year, we plan to make an effort to support the development of the design system, to assist in creating a physical properties estimation method and an analysis method, and to improve the network's functions for that purpose.

High-Temperature Evaluation Test of Thermal Insulation Materials

906C3836 Tokyo DAI33KAI UCHU KAGAKU GIJUTSU RENGO KOENKAI KOENSHU in Japanese
31 Oct-2 Nov 89 pp 708-709

[Article by Akinaga Kumakawa, Masaki Sasaki, Mamoru Takahashi, and Tomoyuki Hashimoto, National Aerospace Laboratory; Shuhei Maeda, Sumitomo Heavy Industries; Satoshi Nagata and Naoto Adachi, Mitsubishi Heavy Industries; and Toshiyuki Hashida, Destructive Dynamics Application Laboratory, Tohoku University]

[Text] 1. Introduction

At present, a project entitled "Research on Fundamental Technologies To Develop Functionally Gradient Materials To Reduce Thermal Stress" is being carried out jointly by a number of institutions interested in promoting science and technology. Functionally gradient materials differ from conventional homogeneously mixed composite materials in that in one piece of material the ratio of the components is continuously changed, thereby enabling the functions (characteristics) of the material itself to undergo continuous gradient control. In theory, this should make it possible to create a material that not only eases thermal stress at the interface, but also displays new functions itself. At present, aiming at applying such highly heat-resistant materials in the space plane, development is under way with the goal of creating materials that can resist surface temperatures at 2,000 K and a temperature head of 1,000 K.

The purpose of this test is to evaluate the thermal insulation performance, thermal stress easement performance, and low-cycle thermal fatigue characteristics of specimens of functionally gradient materials test manufactured using various synthesis methods. This report presents the results of a test we conducted as a basic evaluation test. In this test a zirconia thermal insulation coating was subjected to plasma flame spraying.

2. Outline of Test Equipment

Figure 1 is a schematic diagram of the equipment.

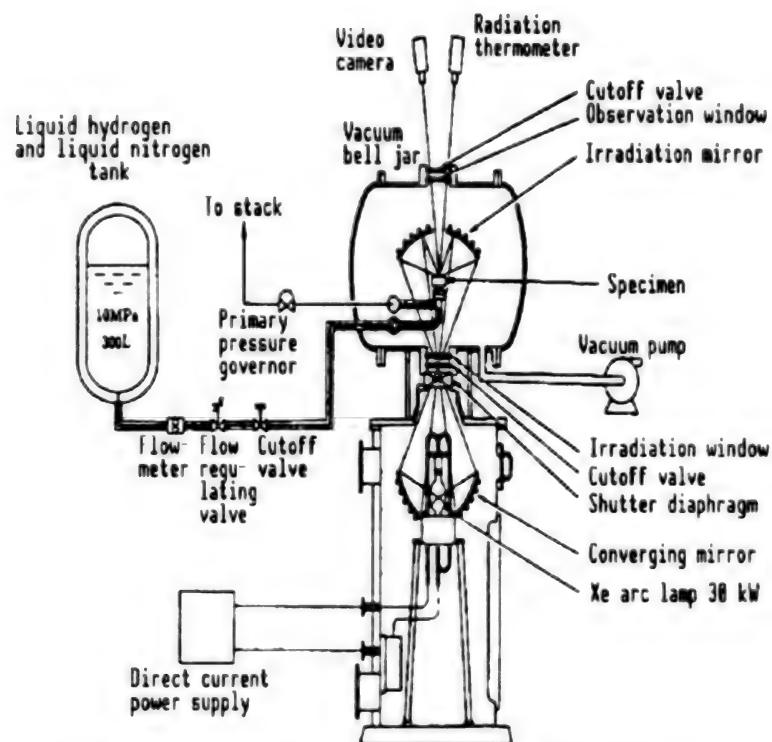


Figure 1. Schematic Diagram of High-Temperature Basic Evaluation Test Device

In this test, the face of the material sample is heated by the convergent beams of a xenon lamp with a maximum output of 30 kW in a vacuum atmosphere (10^{-2} torr or below) while cooling its reverse side with liquid hydrogen or liquid nitrogen. This method makes it possible to obtain a maximum heat flux of 5 MW/cm^2 . Also, it is possible to apply a stepped repetitive heating of 0.3 Hz maximum by opening and closing the shutter.

3. Thermal Insulation Performance of Test Sample

The material sample we used in this test was made by coating a copper base with a homogeneous mixture layer of partially stabilized zirconia ($\text{ZrO}_2 + 8\% \text{Y}_2\text{O}_3$) and NiCoCrAlY using an atmospheric plasma flame spraying technique. A 30- μm thick coating of NiCoCrAlY was used as the undercoating layer, which in turn was covered by a 170- μm thick coating of a nongradient homogeneous mixture layer consisting of four types of constituents—100% ZrO_2 , 80% $\text{ZrO}_2/20\%$ NiCoCrAlY, 60% $\text{ZrO}_2/40\%$ NiCoCrAlY, and 40% $\text{ZrO}_2/60\%$ NiCoCrAlY. We conducted the test by gradually raising the thermal load and measured the steady state at each level. We have defined the effective heat conductivity k_{eff} , which expresses the thermal insulation performance, by the following equation.

$$k_{\text{eff}} = q \cdot t / (T_{ws} - T_{wb})$$

Here, q is the transmitted heat flux, which we have derived from the measured value of the thermocouple buried in the specimen holder. We have designed the coating layer thickness t as fixed at 170 μm . T_{ws} represents the area mean value of the obverse side has measured by the radiation thermometer, while T_{wg} is the temperature of the reverse side coating layer, which is extrapolated from the measured value of the thermocouple in the holder. Figure 2 shows a comparison of temperature dependency of the effective heat conductivity for each mixed layer.

These results demonstrate that for all samples the effective heat conductivity increases as the temperature rises. Also, the higher the percentage of their metal content, the larger their effective heat conductivity becomes and its temperature dependency becomes more pronounced.

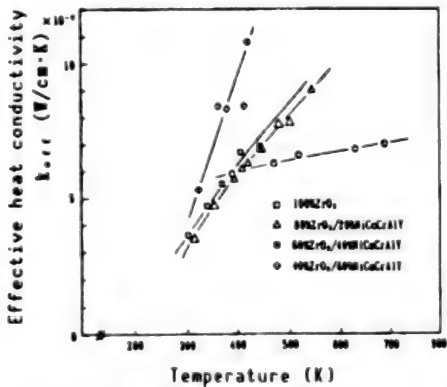


Figure 2. Temperature Dependency of Effective Heat Conductivity for Each Mixed Layer

4. Low-Cycle Thermal Fatigue Test

We have conducted a low-cycle thermal fatigue test on the 100%ZrO₂ material. In this test, sought to determine effective heat conductivity by measuring the steady-state data every 10 cycles and examined its cycle number dependency. As test conditions, we used three types of initial sample obverse maximum temperatures—1,000 K, 1,400 K, and 1,600 K.

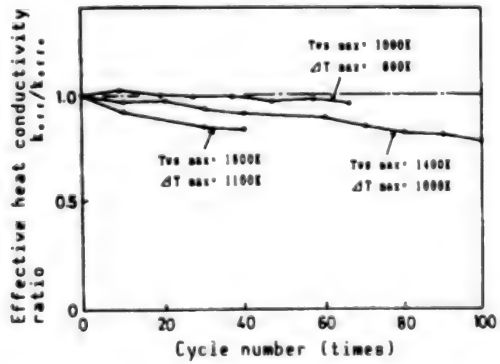


Figure 3. Changes in Effective Heat Conductivity Ratio With Respect to Cycle Number

We used the relationship between the rate of effective heat conductivity after each cycle and the initial effective heat conductivity as the effective heat conductivity ratio. Changes in this ratio with respect to the cycle number are shown in Figure 3. This shows that as the cycle number increases, effective heat conductivity gradually drops and the larger the temperature head, ΔT , is, the larger its gradient becomes. We have found, through observation of the sample cross section after the test, that this drop in effective heat conductivity is caused by the growth and development of longitudinal and transverse cracks with the pore as the starting point. Also, we have examined the relationship between the cycle number at the time of the 10 percent drop in the effective heat conductivity ratio and the temperature head ΔT , and found that there are correlations similar to the life characteristics of metal materials.

Based on these findings, we plan to evaluate the thermal insulation characteristics and structural soundness of functionally gradient materials.

Effects of Electron Beam on Polyimide, Polyetherimide

906C3836 Tokyo DAI33KAI UCHU KAGAKU GIJUTSU RENGO KOENKAI KOENSHU in Japanese
31 Oct-2 Nov 89 pp 710-711

[Article by Ken Abe, Akira Onishi, and Tomonao Hayashi, Institute of Space and Astronautical Science; Keiichiro Furuyashiki, Ube Industries; and Waichiro Kawakami and Yosuke Morita, Japan Atomic Energy Research Institute]

[Text] 1. Introduction

For a long time, (Capton), its Du Pont tradename, has been the preferred material for use as a heat-control material in a space plane. Recently, however, polyimide films, which are the same as or better than this material, have begun to be produced in Japan. The authors are working on the development of heat-control materials, taking note of the particularly high heat-resistant polyimide films UPILEX-R (PI-R) and UPILEX-S (PI-S) produced by Ube Industries.

In a recent series of experiments, together with the PI-R and PI-S, we have irradiated the polyetherimide film (PE) of Sumitomo Bakelite Co., which has outstanding transmission characteristics with an electron beam. Our goal was to evaluate the effects of the electron beam on the films' heat radiation characteristics (solar absorption index α_s , hemispherical emissivity ϵ_H). Meanwhile, UPILEX-R was selected as a heat-control material for the "Akebono" (launched on 21 February 1989).

2. Irradiation Conditions and Evaluation Method

We conducted an evaluation using, as samples, the films shown in Figure 1, on which an evaporation coating has been applied, in addition to the PI-R and PI-S unit films. The thickness of the sample films is 25 μm for the PI-R and PI-S, and 70 μm for the PEI.

We carried out the electron beam irradiation in the atmosphere using accelerators No 1 and No 2 of the Japan Atomic Energy Research Institute (Takasaki Laboratory). Table 1 shows the electron beam irradiation conditions.

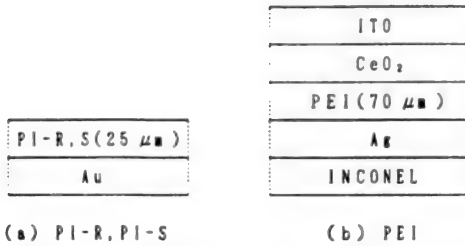


Figure 1. Samples for Evaluation

Table 1. Electron Beam Irradiation Conditions

	Accelerator No. 1	Accelerator No. 2
Irradiation energy (MeV)	0.5	1.0 ~ 3.0
Fluence (e/cm ²)		$1 \times 10^{14} - 1 \times 10^{16}$
Irradiation equipment	Cockcroft-Walton	Cascade

We calculated the value for α_s from the measurement results of the spectral reflectance (incident angle 5°) in the wavelength range of 0.26~2.5 μm. This was done with a special device for measuring dispersion-type spectral characteristics. Also, we determined the value for ϵ_H in a temperature range of -100~+100°C by using the calorimetric method.

3. Results and Study

Because of space considerations, this paper reports only the results of the experiment where the energy of the electron beam was 3.0 MeV with a fluence of 1×10^{16} e/cm².

Table 2. Electron Beam Irradiation Results of α_s

Sample	Electron beam	α_s
PI-R	Before irradiation	0.318
	After irradiation	0.319
PI-S	Before irradiation	0.355
	After irradiation	0.358
PE	Before irradiation	0.157
	After irradiation	0.172

Table 2 shows the values for α_s before and after electron beam irradiation of the PI-R, PI-S, and PEI. With regard to the PI-R and PI-S, hardly any changes could be seen. In the PEI, however, the α_s tended to increase about 9 percent. This is probably because, as shown in Figure 2, the spectral reflectance in the wavelength range of 0.4-0.6 μm decreases. Figure 3 shows the values for ϵ_H before and after electron beam irradiation of the PI-R, PI-S, and PEI. It has been shown that a slight deterioration takes place in the high-temperature and low-temperature regions in the PI-S, and from the low temperature to the normal temperature regions in the PI-R. Also, in the PEI, it was demonstrated that the ϵ_H increases about 3 percent as a whole from the low temperature to the high temperature region.

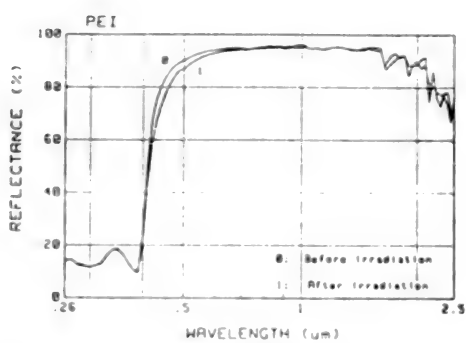


Figure 2. Spectral Reflection Characteristics of PEI

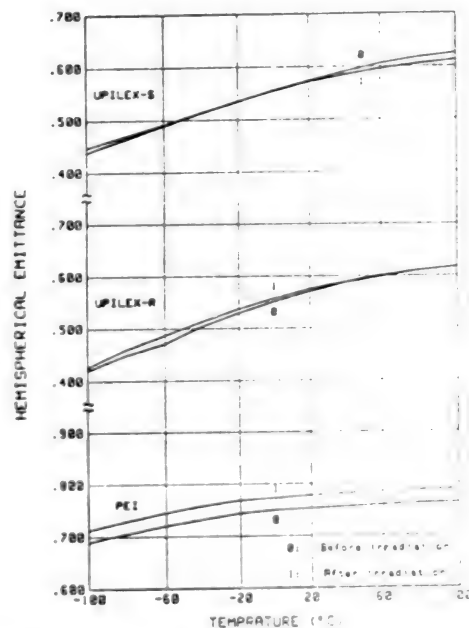


Figure 3. Electron Beam Irradiation Results for ϵ_H of PI-R, PI-S, and PEI

4. Conclusion

As a result of high-energy electron beam irradiation, the polyetherimide film shows a deterioration in the values the α_s , but there is almost no deterioration in the values of ϵ_H . Similarly, for UPILEX-R and UPILEX-S as well, no deterioration in the values for either α_s or ϵ_H were observed. This demonstrates that the high polymer films we evaluated are viable as heat-control materials. Hereafter, we plan to evaluate the effects of low-energy electron beam irradiation and proton beam irradiation.

Research on Deterioration of Paint, Bonding Agent for Space Use

906C3836 Tokyo DAI33KAI UCHU KAGAKU GIJUTSU RENGO KOENKAI KOENSHU in Japanese
31 Oct-2 Nov 89 pp 712-713

[Article by Norihiko Kikuyama, Hideo Oba, and Masahiro Nakao, National Space Development Agency]

[Text] 1. Introduction

Various organic materials are being used in artificial satellites. These organic materials deteriorate while in use in the space environment.

Most of the artificial satellites launched to date have had a design life of 3-5 years, but the current trend is to develop satellites with a longer service life of 7-10 years. In keeping with this trend, it is important to understand the deterioration characteristics of materials while in use in the space environment. Among materials used near the external surface of satellites are solar cells, bonding agents, paint that serves as a heat control material, a (Capton) film, OSR, etc., whose deterioration is due largely to radiation and ultraviolet irradiation.

One example of the effects of material deterioration on the functions of artificial satellites is as follows. Paint is often used as a heat control material. Its characteristics, however, such as reflectance and absorptance, change due to deterioration, thereby affecting the temperature control of the satellite. These effects are depicted in Figure 1, which shows the variation per hour of the antenna surface temperature of the broadcasting satellite.

In order to evaluate the deterioration in the space environment of specially designed equipment and materials, we have examined changes in the characteristics of such materials as heat control paint, (Capton) film, OSR, and bonding agents by irradiating them with electron beams, gamma rays, and ultraviolet light. This paper, however, reports only on paint and bonding agents.

2. Materials for Deterioration Evaluation

From among the heat control paints for artificial satellites, including those that have been actually used and those that are being studied for future use,

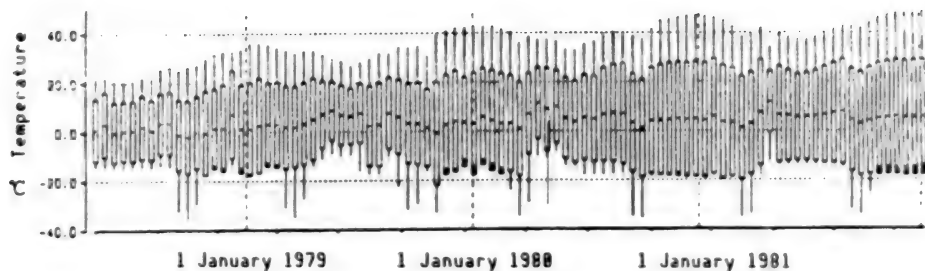


Figure 1. Variation Per Hour at Antenna Surface Temperature of Broadcasting Satellite

The upward trend of antenna surface temperature is thought to be caused by a deterioration of the optical characteristics of the paint.

we chose a total of eight types of paint—six types of white paint and two types of black paint—as the subject materials of deterioration evaluation. These paints are listed in Table 1.

Table 1. Paints Selected for Deterioration Evaluation

Type of paint	Resin
White paint Campe CELA	Silicon resin
" PSG-120FD	Silicon resin
" APA-2474	Silicon alkyde resin
" SPS	Melamine alkyde resin
" Lumifron gloss	Fluorocarbon resin
" Lumifron flat	Fluorocarbon resin
Black paint Lumifron gloss	Fluorocarbon resin
" Lumifron flat	Fluorocarbon resin

As for bonding agents, from among those that have been actually used and those that are being studied for future use for artificial satellites we chose two types of silicon rubber materials and seven types of epoxy materials for evaluation.

3. Irradiation Conditions

In order to simulate deterioration in the space environment, we irradiated the paint with electron beams and ultraviolet light under the following conditions:

(1) Irradiation by electron beam alone.

Irradiation level is 1×10^{16} e/cm² at 10 MeV using the linear accelerator. Atmosphere is a vacuum of $\sim 5 \times 10^{-4}$ torr.

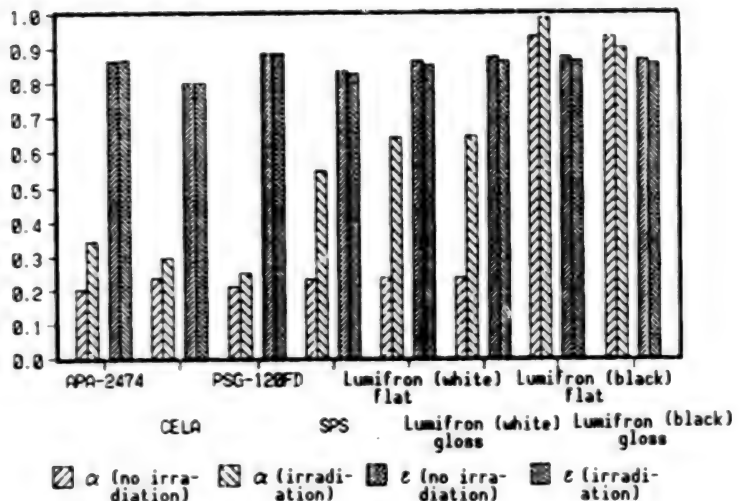


Figure 2. Deterioration of Optical Characteristics of Paint Due to Superimposed Irradiation by Electron Beam and Ultraviolet Rays
After a total electron beam irradiation of 1×10^{15} e/cm², ultraviolet irradiation totaling 300 solar was then applied.
In the white paint based on melamine alkyde and fluorocarbon resins, changes in the α values due to irradiation are large.

(2) Irradiation by ultraviolet rays for a total of 300 solar at a rate of 10 solar/day. Atmosphere is a vacuum of 5×10^{-5} torr.

(3) Irradiation by electron beam under the conditions described in (1) followed by irradiation by ultraviolet rays under the conditions described in (2).

We irradiated the bonding agents under the following conditions:

(1) Irradiation by electron beam alone. The conditions are the same as those described in (1) above.

(2) Irradiation by gamma rays alone. Total irradiation of 10^8 R in at dosage rate of 10^1 R/h.

4. Characteristics Evaluation Test After Irradiation

The most important characteristics of paint used as a heat control material are reflectance, α , and absorptance, ϵ . Figure 2 compares the α and ϵ values of the paint exposed to superposed irradiation by an electron beam and ultraviolet rays under the conditions described in (3) above and those of the paint not exposed to any radiation. It can be seen that, for the white paint, changes in the α values of melamine alkyde and fluorocarbon resins are large.

As for the bonding agents, our evaluation focused on mechanical strength, linear expansion coefficient, and glass transition point.

Deterioration of Composite Resin Materials Caused by Atomic Oxygen

906C3836 Tokyo DAI33KAI UCHU KAGAKU GIJUTSU RENGO KOENKAI KOENSHU in Japanese
31 Oct-2 Nov 89 pp 714-715

[Article by Takayuki Kamiyama, Toshio Sakakibara, Noriaki Sugawara, Akinori Nagao, Katsumi Kamei, and Hiroyuki Takehisa, Aerospace Technology Bureau, Fuji Heavy Industries]

[Text] 1. Introduction

Advanced composite resin material (CFRP) are one of several groups of promising candidates for use as structural space materials. This is because CFRPs have a high level of specific strength and specific rigidity, and also have a small thermal expansion coefficient. In particular, the CFRPs developed as advanced composite materials for use as structural materials for aircraft show good prospects for being useful as materials that can be used in a low-orbit space environment, even when subjected to radiation and thermal shock.¹

It is believed, however, that when CFRP is exposed to an atomic oxygen environment—something that recently has begun to attract attention—it would be eroded by 0.3 cm over 30 years in an environment of 1.4×10^{23} atoms/cm².²

We have investigated, mainly by scanning electron microscope (SEM) observation, the process of deterioration due to the application of atomic oxygen and/or radiation. We have also taken specimens of CFRPs with several different types of matrixes to which aluminum foil was bonded as protective coating by the bonding system that has been actually used in the aircraft structure and subjected them to thermal shock. The following is a report on the results of our tests.

2. Tests

We chose four types of CFRPs with matrix systems that have been actually used as structural materials for aerospace systems. To these we bonded and cured, as a protective coating, a 5052 aluminum foil. This was done using a 350 F curing-type modified epoxy structural film-type bonding agent after prebonding treatment. The prebonding treatment involved either sulfuric acid-sodium dichromate etching (FPL) or the chromic acid anodizing (CAA) treatment that is used for aircraft metal structural bonding.

We cut the prepared specimens into 10 mm x 10 mm testpieces, exposed them to radiation, atomic oxygen, and thermal shock, and then investigated them by SEM and cross section observations.

Table 1 shows the specimens and exposure conditions

Table 1. Specimen Exposure Conditions and Test Evaluation

Specimen		Matrix system	Protective coating	Exposure conditions	Test evaluation
Fiber	Resin				
T-300	3601	Epoxy resin	—	STD, A/O, ² e ⁻ +A/O ³	SEM
IM-6	6376	Modified epoxy resin	— Aluminum foil ¹	STD, A/O, ² e ⁻ +A/O ³ A/O + T/C, ⁴ e ⁻ +A/O+T/C ⁵	SEM Cross section observation
T-800	PMR-15	Polyimide	—	STD, A/O, ² e ⁻ +A/O ³	SEM
T-800	PEEK	PEEK	—	STD, A/O, ² e ⁻ +A/O ³	SEM

- 1) Bonded after metal structure bonding FPL etching or CAA treatment.
- 2) 8 km/s, 3.0×10^{23} atoms/cm².
- 3) Electron beam (2 MeV, 2 mA) (1 KGy \rightarrow 2) exposure.
- 4) 2) exposure \rightarrow thermal shock (-100 \leftrightarrow +100°C) 1,000 CYCLE.
- 5) 3) exposure \rightarrow thermal shock (-100 \leftrightarrow +100°C) 1,000 CYCLE.

3. Results and Assessment

3.1 State of Deterioration on CFRP Surface

We were able to confirm that the 3601 and 6376 epoxy resins are eroded by atomic oxygen, and the thin resin layer on the composite material surface is scraped off. We found that erosion reaches even to the carbon fibers in the very thin part of the resin, but there is less damage to the fibers than to the resin.

In the specimen exposed to radiation before applying atomic oxygen, we were able to confirm roughly the same deterioration tendency. In the current test, however, we were able to observe on the whole a slightly stronger erosion than in the specimen exposed to atomic oxygen alone. It is conceivable that exposure to radiation leaves these materials more vulnerable to the effects of atomic oxygen (Photographs 1, 2, and 3 [not reproduced]).

The T-800/PMR-15 polyimide material displayed the same deterioration tendency as the epoxy resin and were observed a somewhat stronger erosion by applying radiation before the atomic oxygen. As mentioned above, we have concluded that modifying the epoxy or differences between resins have little effect on the deterioration process.

In the T-800/PEEK material, the effect of radiation can be observed as changes in color tone, which are visible by exterior observation. The specimen exposed to atomic oxygen alone had the same color as the material not exposed to radiation, but it was observed that when radiation is applied before atomic oxygen, the specimen whitens. Observation of the specimen surface by SEM shows that cracks on the resin surface, which cannot be observed on the material not subjected to radiation, appear as the result of atomic oxygen application, and, numerically, they seem to increase by applying radiation before atomic oxygen.

3.2 Effect by Protective Coating

Applying atomic oxygen to surfaces treated by FPL etching and CAA causes almost no erosion. However, the surface is rough to the touch and we have observed by SEM that it is slightly eroded. The state of erosion does not differ very much between FPL and CAA, and even in the case of CAA treatment, which is said to be highly resistant to atomic oxygen, the surface felt rough to the touch. Also, as the result of cross section observation of a specimen to which thermal shock was applied after atomic oxygen irradiation, there was no particular effect on the bonding of the protective coating, nor was the development of microcracks observed. In the current test, no falling or peeling of the protective coating due to thermal shock was observed, regardless of the type of pretreatment.

References

1. Kamiyama, T., Seguchi, T., et al., "Evaluation of Tough-Type Matrix CFRP for...," Proceedings of Fourth Japan-U.S. Conference on Composite Materials.
2. Leger, L., et al., "Review of LEO Flight Experiments," Proceedings of the NASA Workshop on Atomic Oxygen Effects.

Deterioration of Composite Materials at Low Temperatures

906C3836 Tokyo DAI33KAI UCHU KAGAKU GIJUTSU RENGO KOENKAI KOENSHU in Japanese
31 Oct-2 Nov 89 pp 716-717

[Article by Seiichi Matsuoka, Akinori Nagao, Kazutaka Nakajima, Takayuki Kamiyama, and Hiroko Oda, Fuji Heavy Industries]

[Text] 1. Introduction

Future space structures, such as a space station, an SFU or a space colony, will generally be operated for long periods of time. In order to develop and evaluate structural materials that meet this requirement for longevity, it is important to clarify the deterioration characteristics of materials in the space environment and also to establish an accelerated test method to assess their life expectancy.

The authors have experimentally demonstrated that composite materials deteriorate when exposed to a heat cycle, which is one element of the space environment. In terms of test periods, however, we have been able only to conduct tests up to 3,000 cycles, which is a far smaller number than the 60,000 heat cycles a space station will have to endure during its 10-year operating period.

For this reason, it becomes particularly important to develop an accelerated heat-cycle test method to be able to accurately assess long-term operations in a short period.

The deterioration of composite materials due to a heat cycle is believed to be caused primarily by the internal stress that results from the different thermal expansion characteristics of the fiber and the resin.

The temperature range of a heat cycle in the space environment (in low orbit) is about +100--100°C. The curing temperature of the composite materials to be assessed is 177°C (350°F). At or below this temperature, the fiber-resin thermal expansion difference causes internal stress, and the lower the material temperature becomes, the larger the stress becomes.

Based on this idea, the purpose of our research was to study whether an accelerated test is possible by assessing the material deterioration behavior on the low-temperature side where the internal stress is greatest.

In this paper, we report on the assessment of material deterioration behavior of a composite material (CFRP) after exposure to a low-temperature environment. We conducted this test as part of the first round of our research.

2. Specimen and Test Method

The material used for test was an epoxy CFRP reinforced with general high-strength fibers and cured at 350°F. Its lamination structure is ($\pm 45^\circ/0_2^\circ/\pm 45^\circ/0^\circ/90^\circ/0^\circ$), 18 PLY. It was prepared by using a prepreg tape material and cured in an autoclave. After molding, we cut out the specimens, exposed them to low temperature under the conditions shown in Table 1 and then assessed their material deterioration characteristics through a strength test (four-point bending strength test) and cross section observation (investigation of crack development). The "bending load applied" in Table 1 means that an attempt was made to increase mechanically the internal stress that develops during exposure to low temperatures by exposing the specimen to low temperatures while a bending force is being applied.

Table 1. Low-Temperature Exposure Conditions

Exposure temperature	-100°C		-150°C	
State of exposure	Load not applied	Bending load applied	Load not applied	Bending load applied

3. Test Results and Evaluation

Figure 1 shows the changes in bending strength after exposure to temperatures of -100°C and -150°C. Table 2 shows the state of crack development as determined by cross section observation.

Table 2. Cross Section Observation Results (State of crack development)

Environmental conditions	Exposure time	100 hours	200 hours	300 hours
-100°C	Load not applied	No	No	No
-100°C	Bending load applied	No	No	No
-150°C	Load not applied	—	No	—
-150°C	Bending load applied	—	Yes	—

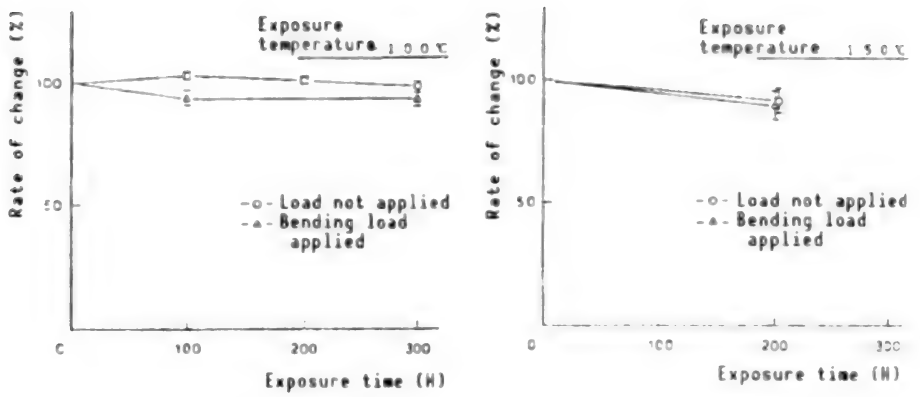


Figure 1. Bending Strength Changes After Exposure to Low Temperature

We will forego an assessment of the results of each test here for want of space, but will report them at the lecture meeting.

References

1. Bunsell, Anthony R., Laroche, Daniel, and Valentin, Daniel, "Damage and Failure in Carbon Fiber Reinforced Epoxy Resin," American Society for Testing and Materials, Special Technical Publication 813.
2. Sugawara, Nagao, et al., "On the Dynamic Characteristics of Structural Composites During the Early Stages of Heat Cycle Load Materials," DAI3IKAI KOZO KYODO NI KANSURU KOENKAI, July 1988.
3. Matsuoka, Nagao, et al., "Deterioration Characteristics in Space Environment of CFRP Materials (2)," DAI3IKAI UCHU SUTESHON KOENKAI, April 1987.

Hydrogen Embrittlement of Ni-Radical Alloy for Liquid Hydrogen Fueled Rocket Engine

906C3836 Tokyo DAI33KAI UCHU KAGAKU GIJUTSU RENGO KOENKAI KOENSHU in Japanese
31 Oct-2 Nov 89 pp 718-719

[Article by Kiyoshi Yokokawa, Government Industrial Research Institute, Chugoku, Agency of Industrial Science and Technology; and Yoshio Yamada, Tsunoda Rocket Development Center, National Space Development Agency]

[Text] 1. Introduction

The first-stage main engine of the H-II rocket, the LE-7, is currently being developed in Japan. The LE-7 is a two-stage combustion engine capable of producing 120 ft of thrust in a vacuum. It uses liquid oxygen and liquid hydrogen as the propellants. A high-strength, lightweight Ni-radical alloy is used for many of its component parts, which are exposed to a high-pressure hydrogen environment of 30 MPa. However, it is generally thought that this Ni-radical alloy easily becomes brittle in a hydrogen environment. Thus, it is necessary to understand the process of how this material becomes brittle and to take measures to cope with it. To this end, we have carried out tensile and other tests on Inconel 718 and Udiment 720, the primary component materials, in a room-temperature high-pressure hydrogen environment, thereby studying the effect of hydrogen in their mechanical properties.

2. Outline of Test

We have conducted tensile tests, fracture toughness tests, and fatigue crack tests on two materials mentioned above in a 19.7 MPa hydrogen atmosphere and a 1.1 MPa argon atmosphere (comparison atmosphere) at room temperature. As part of the test, we examined what effect the contained hydrogen has on the embrittlement process. This was done by letting the samples occlude hydrogen in an autoclave. Table 1 shows the tensile test results.

The testpiece in hydrogen and the hydrogen-occluded testpiece have almost the same values for maximum tensile strength as those in the comparison atmosphere. But after exceeding the elastic limit, there are many instances of ruptures caused by small strains on the plane at a right angle to the axis. We confirmed to AMS Standards, ASTM Standards, etc., for the heat treatment and shape of the testpieces.

Table 1. Tensile Test Results for Room-Temperature High-Pressure Hydrogen

Specimen	Hydrogen pressure (MPa)	Hydrogen atmosphere			Comparison atmosphere			Hydrogen effect: Hydrogen/comparison		
		UTS	ϵ	ψ	UTS	ϵ	ψ	UTS(%)	$\epsilon(%)$	$\psi(%)$
Incl. 718 (occlusion)	19.7	1285	4	3	1297	9	10	99	44	30
	19.7	1283	2	2	1283	2	2	—	—	—
U 720 (occlusion)	19.7	1130	4.4	7	1357	13	14	83	31	50
	19.7	1114	3.6	3	1114	4	3	—	—	—

Note: UTS: Maximum tensile strength (MPa); ϵ : Elongation (%);

ϕ : Reduction of area (%); Comparison atmosphere: Argon

Table 2. Fracture Toughness Values in Room-Temperature High-Pressure Hydrogen

Specimen	Hydrogen pressure	Hydrogen atmosphere	Comparison atmosphere	Hydrogen effect: Hydrogen/comparison
Incl 718	19.7 MPa	$K_G: 89.4, K_{THE}: 53$	$K_G: 104.5, K_{THE}: 75$	$K_G: 86\%, K_{THE}: 71\%$
U 720	19.7 MPa	$K_G: 86.8, K_{THE}: 50$	$K_G: 109.5, K_{THE}: 109$	$K_G: 79\%, K_{THE}: 46\%$

Note: The unit for the fracture toughness values is MPa·m^{1/2} and the comparison atmosphere is argon.

Table 3. Fatigue Crack progress in Room-Temperature high-Pressure Hydrogen da/dn(m/cycle)

Specimen	Hydrogen atmosphere and occlusion	Comparison atmosphere	Hydrogen effect: Hydrogen/comparison	Conditions: f = 0.05 Hz $\Delta K = 50 \text{ MPa} \cdot \text{m}^{1/2}$
Incl. 718	5.8×10^{-6}	2.3×10^{-6}	2.5 times	
U 720	4.6×10^{-6}	6.3×10^{-7}	7.3 times	

Table 2 shows the fracture toughness values. We can observe drops in the fracture toughness values due to the hydrogen environment.

Table 3 shows the fatigue crack progress. Here again, the extent of hydrogen embrittlement is remarkable.

3. Hydrogen Embrittlement Behavior

We have minutely observed the development and growth of cracks by interrupting the tensile test midway and observing the testpieces by SEM. The rupture process is such that cracks develop in the carbide portions of the structure at the elastic limit and grow through the matrix slip line. As deformation increases, cracks also develop in the slip line of the δ phase and the γ' phase, and join those from the carbide. The cracks grow rapidly and rupture occurs when the crack conditions exceed the fracture toughness values. It is believed that since hydrogen acts to stimulate the development and growth of cracks on the slip line in a hydrogen atmosphere cracks develop when only a small strain factor is present and will move quickly to rupture (Table 4).

Table 4. Crack Development Behavior in Hydrogen and Argon

Mate- rial	Atmo- sphere	Crack development strain factor (%)			Rupture- time strain factor (%)	Starting point of rupture
		Carbide	δ , γ' phase	Slip line		
Incl 718	Hydrogen	Elastic limit	δ :1	4	4	Surface carbide
	Argon	Elastic limit	δ :4	9	9	Surface carbide
U 720	Hydrogen	Elastic limit	γ' :1.8	4.4	4.4	Surface carbide
	Argon	Elastic limit	γ' :2.4	13	13	Surface carbide

4. Hydrogen Embrittlement Prevention Technology

Based on the results of this research, we have incorporated the following hydrogen embrittlement prevention technology in the LE-7 design with regard to these materials:

- (1) Setting the allowable stress at 85 percent or below the elastic limit.
- (2) Applying a gold or copper coating to prevent the entry of hydrogen into those parts where the elastic limit has to be exceeded.
- (3) Thoroughly eliminating latent surface cracks.
- (4) Eliminating residual hydrogen and residual stress.

5. Conclusion

We have analyzed the process of hydrogen embrittlement and identified the behavior of an Ni-radical alloy in a high-pressure hydrogen environment. This has made it possible to elaborate guidelines for the prevention of hydrogen embrittlement for the present. However, since the effect of hydrogen on a metal structure is complicated, it is necessary to accumulate further data in order to shed more light on the problem.

References

1. CHUKOSHI/NASDA KYODO KENKYU HOKOKUSHO, "Research on Hydrogen Embrittlement of Rocket Materials," MRP88-57, S62.
2. Fukuyama, et al., "Progress of Fatigue Cracks in Ni-Radical Alloy in Room-Temperature, High-Pressure Hydrogen Environment," ZAIRYO, Japan Society of Materials, Vol 38 No 428, 1989, pp 539-545.

Research on Neutron CT Image Processing Method Using Small Cyclotron

906C3836 Tokyo DAI33KAI UCHU KAGAKU GIJUTSU RENGO KOENKAI KOENSHU in Japanese
31 Oct-2 Nov 89 pp 720-721

[Article by Kazuo Maeno and Yutaka Hanaoka, Department of Technology, Muroran Institute of Technology; Morio Shimizu, National Aerospace Laboratory; and Toshiki Kabutomori, Yuichi Wakisaka, and Keizo Onishi, Muroran Laboratory, Japan Steel Works]

[Text] 1. Introduction

The X-ray CT is now widely used as a medical diagnostic tool and, further, efforts are being made to adopt its use for such purposes as material analysis and defect inspection. Meanwhile, resin products and bonding materials in metal tubes, like rocket workpieces, or composite materials, are inspected using conventional X-ray techniques often in conjunction with inspection by neutron beams. This latter technique is used because neutron beams have the inherent absorption coefficient of the element being inspected. In our research, we have tried to develop a neutron CT using a small cyclotron as the neutron source. This is a report on the results of reconstructed images acquired by this CT.

2. Experimental Equipment and Measurements

Figure 1 shows a diagram of the neutron CT system. Neutron beams¹ acquired by the small cyclotron, moderator, Be target, and collimator are applied to the model set on the rotary table. Images of the neutron beams passing through the subject emit light when they strike the fluorescent screen. These light images are photographed by an ultrahigh-sensitivity camera and converted to data by an image processor. After acquiring 180 pieces of projection data of the subject from 1 degree to 180 degrees of angle of rotation, we transferred them to the host computer and reconstructed the images. Figure 2 shows three sample specimens: (a) is a hollow round Fe bar, (b) is a model of a turbine blade, and (c) is a round Fe bar with large and small artificial defects.

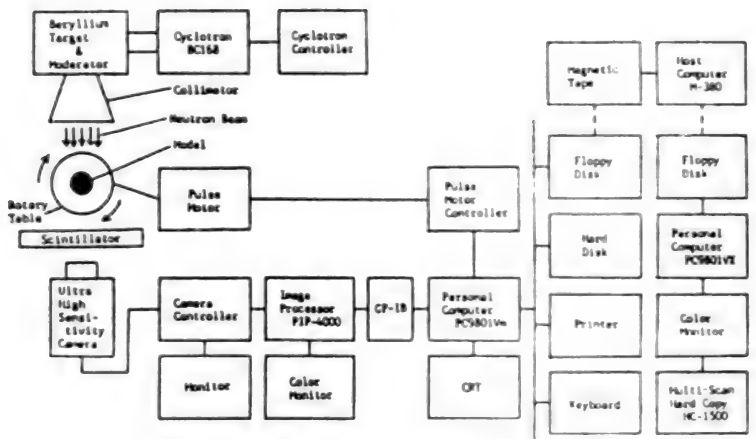
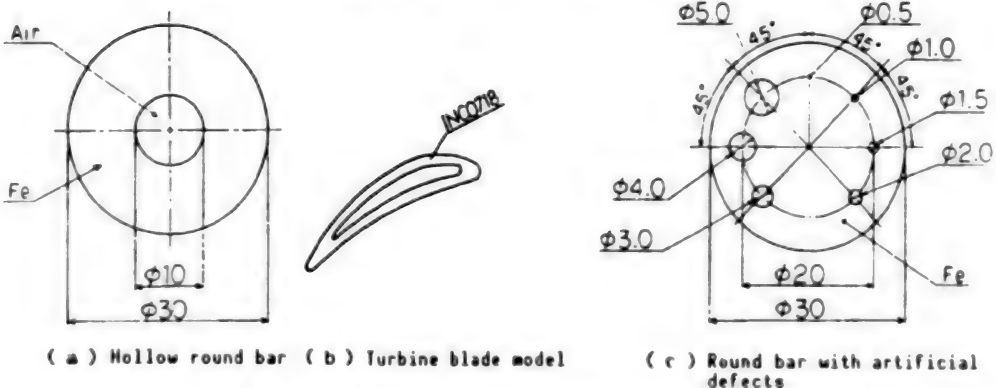


Figure 1. Diagram of Neutron CT System



(a) Hollow round bar (b) Turbine blade model (c) Round bar with artificial defects

3. Results and Evaluation

Figure 3 shows the neutron absorption coefficient reconstruction distribution of the hollow round bar (a). The hollow part at the center can be discerned, but the decrease in the absorption coefficient of Fe from the round bar periphery to the hollow part is also remarkable. This is believed to be attributable in part to the inadequacy of CT development software, but also to the presence of energy distribution in the neutron beams. The results of reconstruction absorption coefficient distribution for the turbine blade (b) are shown in Figure 4. As can be seen, the blade profile has been reconstructed. Further studies must be conducted on the disagreement between the absorption coefficients of the upper and lower surfaces of the blade. Finally, the two-dimensional reconstruction absorption coefficient distribution for the round Fe bar with artificial defects (c) is shown in Figure 5 [not reproduced]. Although the peripheral blur still remains unsolved, we have been able to detect defects as small as about 1 mm. Possible causes of this blur include the effect of distance from the thermal neutron beam source to the subject, the relative distance with respect to the fluorescent screen, and the effect of neutron beam density and energy distribution. Thus, we are now examining various improvements. However, now that the neutron CT is beginning to be used for composite materials, there are good possibilities that it can be applied to many other areas as well.

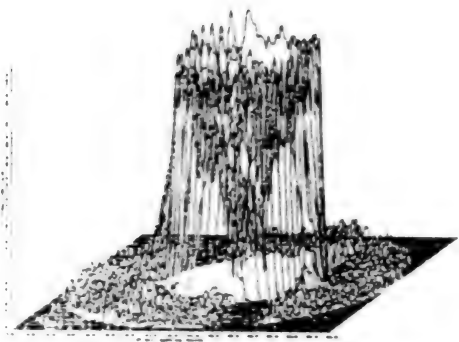


Figure 3. Reconstruction Absorption Coefficient Distribution of Hollow Round Bar

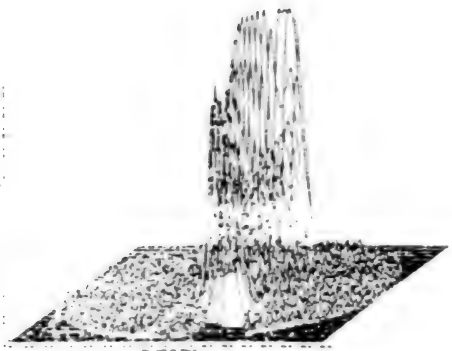


Figure 4. Reconstruction Absorption Coefficient Distribution of Turbine Blade

References

1. Toda, et al., SHINZOZAI OYABI SONO SEIHINNO HIHAKAIKESA SHIMPOJUMU RONBUNSHU, Japan Nondestructive Test Association, 1988, p 113.

Development of 32 GHz Traveling-Wave Tube Power Amplifier

906C3836 Tokyo DAI33KAI UCHU KAGAKU GIJUTSU RENGO KOENKAI KOENSHU in Japanese
31 Oct-2 Nov 89 pp 734-735

[Article by Ryoji Tanaka, Toneo Kawanishi, and Yokichi Mizoguchi, National Space Development Agency of Japan, (Toneo Kawanishi is now assigned to the Space Communications Basic Technology Laboratory)]

[Text] 1. Introduction

A communications service utilizing a data relay tracking satellite (DRTS) will be considered in Japan in the near future. A design study of a traveling-wave tube amplifier (TWTA) and the test manufacture of a traveling-wave tube (TWT) were conducted for the purpose of assessing the prospects for developing a 32 GHz TWTA, which is the major component of the K-band communications equipment that will be on board the user spacecraft involved in communicating with the DRTS. In this report we will describe the development policy and the establishment of design specifications for these items.

The Advanced Earth Observation Satellite (ADEOS) has been selected to be the first user spacecraft for the DRTS. Development of the TWTA will be carried out as part of the ADEOS program. This development effort looks beyond the immediate target. Its design will be reflected in user spacecraft to be used after DRTS, including, for example, the Japanese experiment module (JEM), which will be mounted on a space station.

2. Design Specifications

The predicted transmission demand of user spacecraft for the DRTS communication service is shown in Table 1.

These transmission demands were then used in an initial calculation of circuit requirements, which also took into account the fact that the antenna diameter of the user spacecraft was to be more than 1 m ϕ .

As a result, a transmission power of 10 W for the user spacecraft became one of the design requirements (Table 2).

Table 1. Prediction of KSA Return Link Transmission Demands

User spacecraft	Demanded transmission bit rate
ADEOS: Advanced Earth Observation Satellite	2.6 Mbps/120 Mbps
ATCP: Applied technology common orbit platform	50-70 Mbps
HOPE: Space plane to be launched by H-II rocket	About 30 Mbps
JEM: Japanese experiment model for attachment to a space station	About 100 Mbps (Possesses possibility of 300 Mbps)
OSV: Orbiting satellite vehicle	50-70 Mbps
JPOP: Japanese polar orbiting platform	300 Mbps

Table 2. Antenna Diameter and Transmittable Bit Rate

Transmission power	Transmittable bit rate	Corresponding antenna diameter
32 GHz 10 W (The antenna diameter of the data relay and tracking satellite has been set at 5 m)	Less than 100 Mbps	1 mφ
	100 Mbps~300 Mbps	1~2 mφ

It can also be assumed that the KSA return link frequency will be 26 GHz. This is because of the international cooperation associated with the DRTS. The problem here is that the antenna gain will decrease when the antenna diameter is made the same size. It is not possible given K-band acquisition and tracking restrictions to compensate for the reduction of antenna gain by increasing the antenna diameter. (The necessary condition is a sufficiently wide beam-width.) Therefore, it is necessary to compensate by using the power amplifier and not change the antenna diameter when the return frequency is set at 26 GHz.

Consequently, it proved necessary to increase the output to about 17 W for the 32 GHz band and to 10 W for the 26 GHz band. The development specification for the transmission power of the 32 GHz TWTA has been set at 20 W.

In addition, with a transmission power of 20 W the antenna diameter can be reduced and there is an enhanced capability for acquisition and tracking at a frequency of 32 GHz.

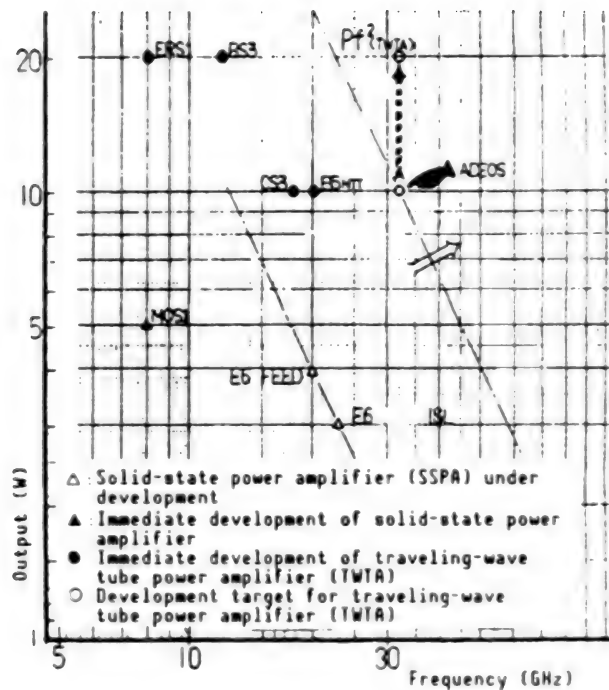


Figure 1. Comparison of Power Amplifiers

3. Selection of Power Amplifier

A transmission power of 20 W has become a design specification for the power amplifier. It appears that this amplifier will have to be either a solid-state power amplifier (SSPA) or a traveling-wave tube power amplifier (TWTA). For the SSPA, the relationship between frequency and output can be expressed by the equation (Output) \times (Frequency) 2 = Fixed. Thus, output decreases as frequency increases. A comparison of the SSPA and TWTA is shown in Table 3 and Figure 1.

An increase of about 1 W is possible in the 32 GHz SSPA at the present technical level. Development of an SSPA with an output greater than 20 W will be difficult, even taking into account the technical progress that will be made over the next several years. Therefore, we have chosen the TWTA and we have decided to begin our development work by subsuming currently existing small-sized TWTA communications technology. The development specifications are shown in Table 4.

Table 3. Comparison of Electric Power Amplifier

Item	Traveling-wave tube power amplifier (TWTA)	Solid-state power amplifier (SPPA)
(1) Fundamental parts	• Traveling-wave tube	• Semiconductor device
(2) Life/reliability	• There is a lifetime part (cathode) • Reliability is inferior due to high-voltage power source	• Excels in long life • Does not require a high-voltage power source
(3) Output	• High output is possible	• About 1 W at present level of technology
(4) Power source efficiency	• Better than SSPA in the 20 W class	• Power source efficiency is inferior
Overall evaluation	•	X

Table 4. Development Specifications

Item	Target specification	Remarks
Frequency range	32~33 GHz	• In accordance with frequency allocation rule
RF input	-5 dBm	• From standard interface level
RF output	More than 20 W	• In accordance with circuit design
Gain	More than 48 dB	
Efficiency	More than 21%	
Weight	More than 4 kg	
Cooling system	Conduction cooling	

4. Conclusion

We have presented an outline of the development policy for a 32 GHz TWTA to be mounted on the user spacecraft for the DRTS. An increase in circuit margin, i.e., an increase in the degree of freedom of system construction, can be expected by setting the target value for transmission power at 20 W. Reports on the test manufacture will be presented in another section.

Test Manufacture of 32 GHz Traveling-Wave Tube Power Amplifier

906C3836 Tokyo DAI33KAI UCHU KAGAKU GIJUTSU RENGO KOENKAI KOENSHU in Japanese
31 Oct-2 Nov 89 pp 736-737

[Article by Ryoji Tanaka, Toneo Kawanishi, and Yokichi Mizoguchi, National Space Development Agency of Japan, (Toneo Kawanishi is currently assigned to the Space Communications Basic Technology Laboratory); and Toshimoto Kikuchi, Sadanori Hamada, Seiichi Otsuka, and Yoshitomo Iwanami, Nippon Electric Co.]

[Text] 1. Introduction

The development of a 32 GHz traveling-wave tube amplifier (TWTA) to be mounted on the user satellite for the data relay tracking satellite (DRTS) is under way. This report will focus on the design, test manufacture, and evaluation of a TWT with an output of more than 25 W. An efficiency rate of more than 30 percent has been achieved from the first test manufactured device.

2. Target Characteristics and Design

The target characteristics are listed in Table 1. To achieve the performance targets of an output greater than 25 W and an efficiency rate greater than 30 percent, the TWT must have a high level of output and must be highly efficient in the millimeter waveband. Therefore, the design has emphasized realizing high beam efficiency and heat resistance in the slow-wave circuit together with reduced electricity consumption by the collector. The principal design specifications are given in Table 2. The inner helix diameter of the slow-wave circuit is 0.74 mm. Heat dissipation and beam transmission become difficult as the helix becomes extremely small. Therefore, together with adopting an integral pole piece (IPP) structure and eliminating the eccentricity between the helix and the beam convergent magnetic field, sufficient contact pressure has been secured by high-precision machining of parts and helix insertion by shrinkage fit. The helix pitch profile has adopted a speed taper on the output side for improving both beam efficiency and AM/PM transfer characteristics. Moreover, the output side of the helix is gold-plated to reduce RF loss. The electron gun is of a pierced type and an ion barrier electrode has been provided to protect the cathode from ion impact.

Table 1. Target Characteristics

Item	TWTA	TWT
Frequency	32-33 GHz	32-33 GHz
Output	Greater than 20 W	Greater than 25 W
Efficiency	Greater than 21 %	Greater than 30%
Gain	48 dB	49.3 dB
AM/PM conversion	5 deg/dB	5 deg/dB
Weight	Less than 4.5 kg	Less than 1 kg
Life	Design target 10 years	Design target 10 years

Table 2. Principal Design Specifications

Slow-wave circuit	: Helix type Speed taper pitch Integral pole piece structure BN pole support
Electron gun	: Pierce type Ion barrier electrode arrangement M cathode
Beam focusing device	: PPM (Sn-Co magnet)
Collector	: Two-step potential lowering collector Conduction cooling
High-frequency I/O circuit	: Wave guide (WRI-320)

In addition, an M cathode has been adopted and the cathode current density has been set at 1 A/cm² to ensure a long operational life.

The collector is a two-stage potential lowering device designed to achieve an overall efficiency of 30 percent.

3. Test Manufacture Results

The operational characteristics of representative examples of test manufactured devices are shown in Table 3 and their frequency characteristics are shown in Figure 1. An output of 31.9 W, a beam efficiency of 8.1 percent, and an overall efficiency of 31.4 percent were obtained at a frequency of 32.5 GHz. Moreover, the AM/PM transfer coefficient was 4.1 deg/dB at the saturated output level and the beam efficiency and AM/PM transfer characteristics were improved by the speed taper. The beam transmission rate was 99.5 percent at saturated output and superior beam transmission characteristics were noted. Further, the helix current in the prescribed temperature range of -20-50°C was less than 0.3 mA and the temperature characteristic was superior.

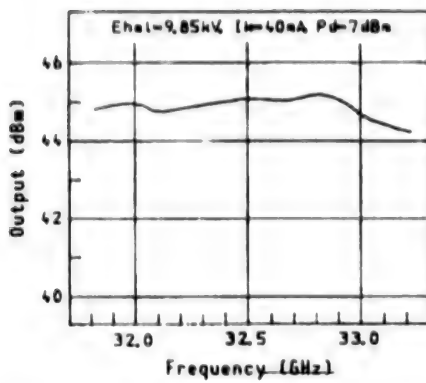


Figure 1. GHz Frequency Characteristics

Table 3. Operational Characteristics of Representative Samples

f	32.5 GHz
Ef/If	4.48 V/0.9 A
Ea/Ia	6.75 kV/0 mA
Eib/Iib	Ehel+0.1 kV/0 mA
Ehel/Ihel	9.85 kV/0.2 mA
Ecl/Icl	3 kV/15.5 mA
Ec2/Ic2	2 kV/24.5 mA
Ik	40 mA
Pd/Po	7 dBm/31.9 W (45 dBm)
Saturated gain	38 dB
Electricity consumption	101.5 W
Efficiency	31.4 %
AM/PM conversion coefficient	4.1 deg/dB
NF	35.3 dB
Weight	1.08 kg
External dimensions	365 x 85 x 55 mm

We prepared an evaluation sample and measured the heat resistance between the helix and the IPP to evaluate the helix temperature. We obtained a result of 8°C/W/cm. We assume from this that the helix temperature at saturated output is less than 200°C. Moreover, the measured result of TWT thermal fading was 0.03 dB, which is extremely small. Therefore, the helix temperature is low and can be assumed to be sufficiently heat-resistant. Photograph 1 [not reproduced] shows the appearance of the TWT prototype. It weighs 1.08 kg, but can be made lighter by reconsidering the potting material and the package.

4. Conclusion

The helix of the text manufactured TWT displayed superior heat-resistant properties. Also, we were able to meet the temperature requirements for the TWT as well as the requirements for other basic characteristics. Thus, we met our goal and confirmed the adequacy of the design. We will continue to work to improve performance further and will evaluate the TWT's resistance to vibration, heat and vacuum conditions, etc.

Thermal Analysis of Radiation-Cooled Four-Stage Collector for TWT

906C3836 Tokyo DAI33KAI UCHU KAGAKU GIJUTSU RENGO KOENKAI KOENSHU in Japanese
31 Oct-2 Nov 89 pp 738-739

[Article by Susumu Atsukawa, Masao Kato, Yoshihiko Kitano, and Nobuo Ishitsu,
Space Communications Basic Technology Laboratory]

[Text] 1. Introduction

As part of the effort to develop a small, lightweight radiation-cooled four-stage collector for the 22 GHz, 250 W TWT that is to be used on board the direct broadcasting satellite (DBS), we have constructed a new type of collector. This was accomplished by attaching a strut supporting the entire body from the exterior and by simplifying the structure. We also have conducted studies using nonlinear thermal analysis by the finite element method and have sought to improve heat radiation to space efficiency by making the surface temperature of the outer peripheral equipment as high as possible while maintaining uniformity.

2. Thermal Analysis Simulation Model

An actual collector is nonaxisymmetric; thus it has been simplified for two-dimensional analysis. Figure 1 depicts such an analytic two-dimensional model. Molybdenum was used for collectors 1 through 4. The plate thickness of the collectors was 2, 1, 1, and 0.5-1 mm, respectively. SUS was used for the outer peripheral equipment. Kovar was used for the strut, while beryllium oxide and aluminum were used for the electrode insulator spacers. A nonlinear analysis of the heat transfer characteristics of various materials was conducted. Heat transfer for the various parts occurred in a stationary state and consisted of conduction and radiation as shown below. The radiation link has been simplified to the extent possible.

$$\text{Conductance} \dots Q = KA(T_2 - T_1)/L$$

Q: Heat flow K: Thermal conductivity A: Area

L: Length T_1, T_2 : Temperature

$$\text{Radiation} \dots Q = \sigma\epsilon FA(T_1^4 - T_2^4)$$

Q: Heat flow σ : Stefan-Boltzmann constant ϵ : Radiation rate

F: Somato coefficient A: Area of radiation surface

T_1, T_2 : Absolute temperature of emission surface and absorption surface

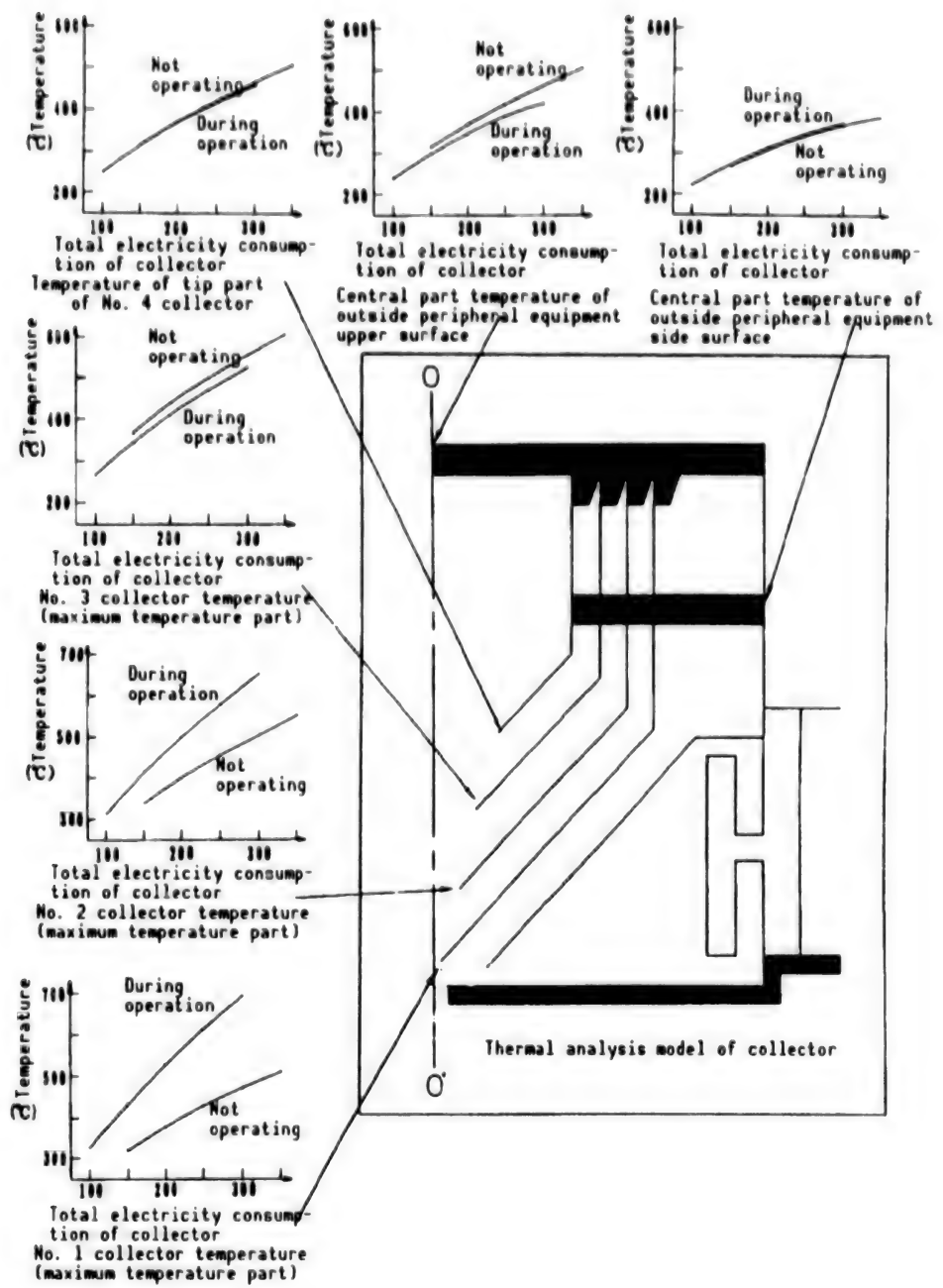


Figure 1. Model Shape and Temperature of Various Parts of the Satellite-Mounted Radiation-Cooled Four-Stage Collector for TWT

3. Thermal Analysis Results

The relationship between the change in temperature of various parts and electricity consumption is shown in Figure 1. The highest temperature of the collector electrode in rated operation is 550°C at the tip of the No. 1 collector and the highest temperature of the outer peripheral equipment is

450°C during nonoperation on the upper surface of the outer peripheral equipment. The heat flow to various parts of the heat sink is shown in Table 1. The heat flow on the upper and side surfaces of the outer peripheral equipment represents heat flow into space, while the heat flow on the base side is heat flow to the satellite body. We obtained superior values one-sixth to one-third greater than those for conventional types.

Table 1. Heat Flow to Heat Sink at Rated Operation
(At loss of 216.5 W)

Attached outer peripheral spacecraft upper surface	Outside peripheral equipment side surface	Base side
88 W	117 W	11.5 W

4. Conclusion

We have obtained good prospects for the development of small, lightweight collectors with a weight of about 1.5 kg. The thermal distribution patterns of these collectors take into consideration both production conditions and the thermal analysis that we conducted. A dramatic improvement of 0.5~1 kg has become possible by redesigning the shape of conventional collectors.

Study of PPM of 22 GHz TWT for Satellite-Mounted DBS

906C3836 Tokyo DAI33KAI UCHU KAGAKU GIJUTSU RENGO KOENKAI KOENSHU in Japanese
31 Oct-2 Nov 89 pp 740-741

[Article by Masao Kato, Susumu Atsukawa, Yoshihiko Kitano, and Nobuo Ishizu,
Space Communications Basic Technology Laboratory]

[Text] 1. Introduction

The 22 GHz, 250 W TWT for the satellite-mounted DBS uses a coupled cavity (CC) slow-wave circuit to obtain high output. This type of CC, as compared to the helix type, has a bigger external slow-wave circuit and the volume and weight of the magnet for generating the prescribed electron beam converging magnetic flux density in the interaction space are correspondingly greater. This is not desirable for a device that needs to be small and lightweight for mounting on a satellite. Therefore, we used the finite element method and conducted a nonlinear analysis on a periodic permanent magnet (PPM) aimed at making the cavity bulkhead the magnetic path in order to overcome the problem of size.

2. Required Magnetic Field for 220 GHz, 250 W TWT

The Brillouin magnetic field required for electron beam convergence of the interaction space drift part of this TWT is given by the following equation:

$$B_0 = \left\{ \frac{\sqrt{2} I_0}{\pi \epsilon_0 \eta^{3/2} V_0^{1/2} I_o^2} \right\}^{1/2}$$

Here, ϵ_0 : Vacuum dielectric constant

η : Electron specific charge

The Brillouin magnetic flux density becomes 848 Gauss, as calculated from the items listed in Table 1. In an actual TWT, however, a magnetic field 1.5~2 times greater than the Brillouin value is necessary because of such factors as the incident condition to the drift space, density modulation of the electron beam, and lowering of electron speed. Thus an effective value of 1,700 Gauss becomes the guideline for the required magnetic field.

Table 1. Specifications for the Magnetic Field Calculation of a 22 GHz, 250 W TWT

Frequency band:	22.5-23.0 GHz
Beam voltage (V_0):	12 kV
Beam current (I_0):	140 mA
Beam radius (r_0):	0.35 mm

3. Studies and Results of Analysis by Nonlinear Two-Dimensional Finite Element Method

The shapes of these three types of magnetic circuits used in these studies are shown in Figure 1. The part represented by the oblique line in the diagram consists of pure iron while the part represented by the dotted line in the diagram is a rare earth magnet (HICOREX-20SV). In the A type and B type devices the cavity bulkhead becomes the magnetic path and the magnets are arranged for each 2 and 1 cavity, respectively. Moreover, the coupling hole of the cavity bulkhead has been ignored here. The generated magnetic fields of the various PPMs are shown in Figure 2. With regard to the A type and B type shown in the diagram, the change in the interaction space radius direction is great and the values for the beam passing hole diameter ratio at 0.7 and 1.0 from the center are represented as (a) and (b). The magnet operating point of the various PPMs is shown in Figure 3. The magnet interior operating points are dispersed in the oblique line range. Thus a stabilizing magnetization of 10-20 percent is essential for the conventional type based on the distribution state, while it has been demonstrated that this is virtually unnecessary for both the A and B types.

4. Conclusion

There are good prospects for the development of a surprisingly small and lightweight PPM with a high degree of reliability and high level of performance for use on a satellite-mounted CC TWT. By comparison with the conventional type, the new device has a high degree of stability and weighs only one-tenth to one-twentieth as much as the conventional type.

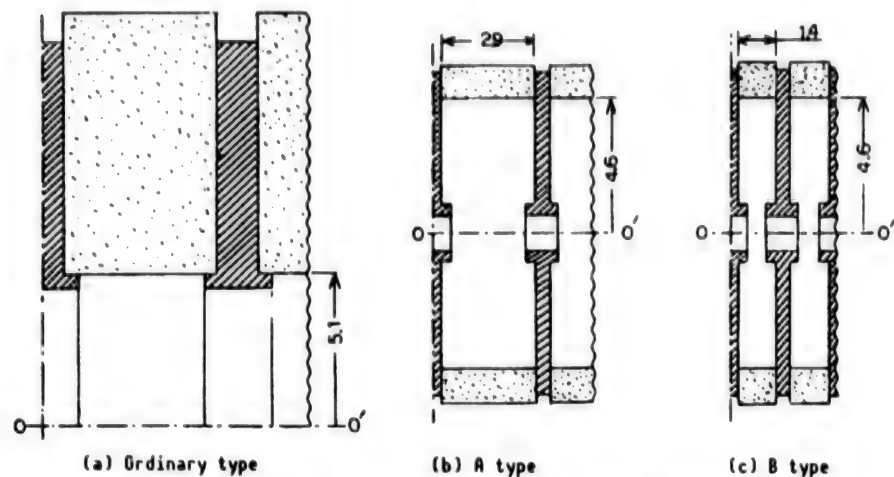


Figure 1. Shape of Various Types of PPMs for 22 GHz TWT (Unit: mm)

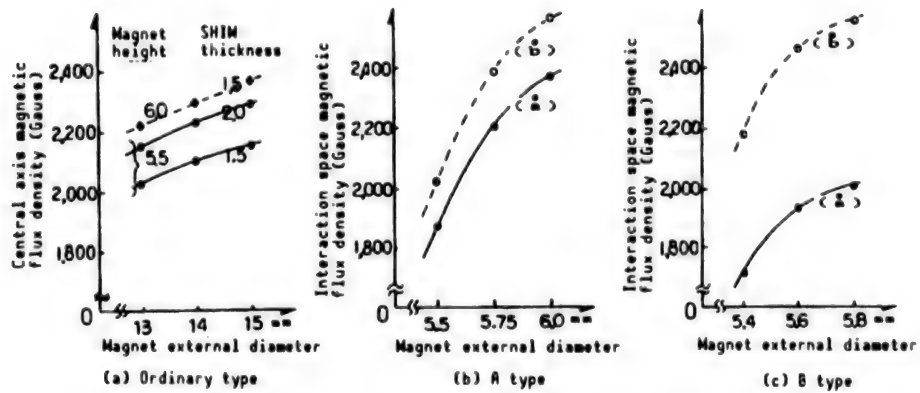


Figure 2. Generated Magnetic Field of Various PPMs (Effective values)

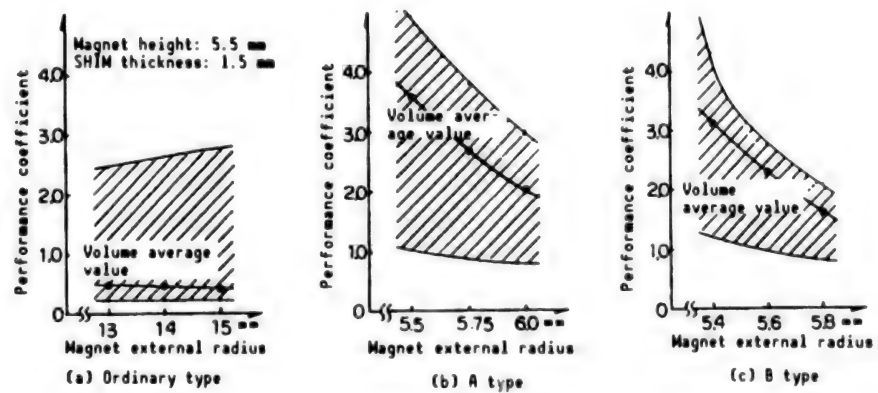


Figure 3. Magnet Operating Point of Various PPMs

Precision Acquisition, Tracking System for Laser Communications Between Satellites

906C3836 Tokyo DAI33KAI UCHU KAGAKU GIJUTSU RENGO KOENKAI KOENSHU in Japanese
31 Oct-2 Nov 89 pp 742-743

[Article by Hiroshi Arikawa, Yasumasa Kubota, Hiroshi Anekawa, and Eiichi Hashimoto, National Space Development Agency of Japan; and Masahide Hamuro, Koichi Shiratama, Yoshio Ogushi, and Motoo Shimizu, Nippon Electric Co.]

[Text] 1. Introduction

An intersatellite laser communications system^{1,2} has less mutual interference than other systems. Although it offers good prospects as a future inter-satellite communications system because it provides a large transmission capacity, it must also have a high-precision acquisition and tracking mechanism for the optical beam. Such an acquisition and tracking system consists of two parts—a rough acquisition and tracking system for directional control of the beam over a wide range and at low speed, and a precision acquisition and tracking system for directional beam control with a high degree of precision and at high speed. We have test manufactured a precision acquisition and tracking system. This system is a mirror-driven mechanism based on the laminated piezoelectric actuator method. This article describes this acquisition and tracking system.

2. Performance Goal

The performance goal for tracking precision was set at tracking within $\pm 1 \mu\text{rad}$ assuming a sine wave change of $\pm 40 \mu\text{rad}$. It is difficult to correct a frequency variation as small as 1 Hz by changing the attitude of a satellite with a thruster or other mechanical device, which is how the rough acquisition and tracking system operates. Design conditions incorporating an open loop gain of more than 32 dB for 1 Hz and more than 52 dB for 0.1 Hz, also including the hysteresis correction of the mirror drive mechanism, are necessary if the control system is to satisfy this control requirement.

In addition, the tracking angle range needs to be $\pm 300 \mu\text{rad}$ to compensate for the tracking error angle of the rough acquisition and tracking system.

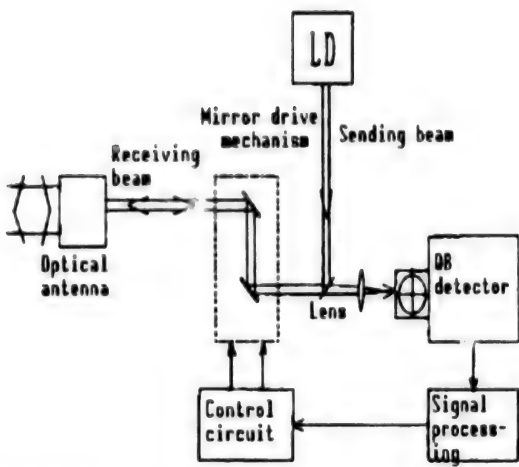


Figure 1. Block Diagram of Precision Acquisition and Tracking System

3. System Composition

Figure 1 is a block diagram of the precision acquisition and tracking system. The structure of the precision acquisition and tracking system is such that the entire system can be rotated by the rough acquisition and tracking system. The optical antenna sharply narrows the transmitted beam expansion angle, condenses the receiving beam, and effects high-precision directional control. The beam direction angle of the precision acquisition and tracking mechanism is magnified by the optical antenna and is many times greater than the antenna incident beam angle.

The mirror drive mechanism aligns the angle of the transmitted beam with that of the receiving beam. Because this requires a high-precision beam direction mechanism, we adopted a mirror drive mechanism that incorporates a laminated piezoelectric actuator in the angle change mechanism. The angle change mechanism used here is for changing the displacement of the laminated piezoelectric actuator, which expands and contracts depending on the applied voltage into a deflection angle of the mirror by using a lever. By combining this with the laminated piezoelectric actuator, we have created a mirror drive mechanism that provides high resolution, high speed, low electricity consumption, low noise, and is virtually wear free.

A quadrant detector (QD) is used to detect the angle error of the receiving beam. Feedback from the output detection signal is provided to the control circuit after undergoing signal processing. It is used to control the mirror drive mechanism so that the receiving beam strikes the center of the QD. A modulation signal detection method that is not easily affected by the DC optical level and that can detect a modulated signal (degree of modulation about 10 percent, about 20 kHz) that is superimposed with the beam was adopted as the detection method for the receiving beam. We also devised measures to protect against background light.

Moreover, a PID controller has been used in the control circuit and the open loop characteristic of the control system has been designed to satisfy the design conditions described above.

4. Test Results of Trial Manufactured Device

(1) Unit characteristic of mirror drive mechanism

The trial manufactured mirror drive mechanism is shown in Figure 2 [not reproduced]. It has the following characteristics: A driving angle range of about 73 mrad, a maximum hysteresis of about 9 mrad, and the resolving power was less than the resolving power ($3 \mu\text{rad}$) of the measuring system. Since the angles mentioned above were reduced to one-twentieth when converted into the photo antenna incident beam angle when the magnification of the optical antenna was set at 20 times, its performance was sufficient to satisfy the target tracking precision of $\pm 1 \mu\text{rad}$. Moreover, the frequency characteristic was the resonance frequency of about 130 Hz (Table 1).

Table 1. Frequency Characteristics of Mirror Drive Mechanism

Item	Characteristic	Remarks
Drive angle range	73 mrad	When applying 0~150 V
Drive angle resolution	Less than $3 \mu\text{rad}$	
Resonance frequency	130 Hz	
Expanded mechanism dimension	45 x 120 x 5 t	
Weight	160 g	

(2) Control characteristics

The control characteristics of the precision acquisition and tracking system that we trial manufactured are shown in Table 2. The tracking characteristics for the angle change of the incident beam are shown in Figure 3. By using a beam that changes at a sine wave of $\pm 40 \mu\text{rad}$, 1 Hz, and by measuring the tracking error angle for the beam, we were able to confirm that it tracked with a degree of precision of about $\pm 0.75 \mu\text{rad}$ when converted into the optical antenna incident beam angle.

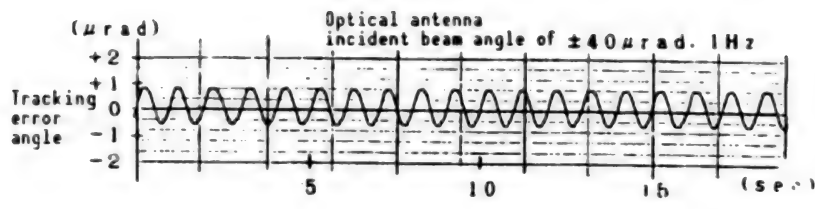


Figure 3. Tracking Characteristics

Table 2. Control Characteristics of Precision Acquisition and Tracking System

Item	Characteristics		Remarks
	Performance targets	Test results	
Drive angle range	$\geq \pm 0.017^\circ$ ($\pm 300 \mu\text{rad}$)	$\pm 0.21^\circ$ ($\pm 3.65 \text{ mrad}$)	Optical antenna incident beam angle
Tracking precision	$\pm 1 \mu\text{rad}$	$\pm 0.75 \mu\text{rad}$	Same as above
Frequency characteristics Open-loop line	$\geq 32 \text{ dB}$ $\geq 52 \text{ dB}$	36 dB 56 dB	at 1 Hz at 0.1 Hz
Phase allowance	$\geq 30 \text{ deg}$	30 deg	

Conditions

- Optical antenna incident beam angle: $\pm 40 \mu\text{rad}$, 1 Hz
- Optical antenna magnification: $\times 20$

5. Conclusion

Using a mirror drive mechanism that incorporates a laminated piezoelectric actuator enabled us to trial manufacture a precise acquisition and tracking system for intersatellite laser communications. Tests of the new device provided satisfactory results. The device met the requirement for a target tracking precision of $\pm 1 \mu\text{rad}$. We plan to conduct studies and tests of a future detailed system that takes the optical receiving level into consideration.

References

1. Hashimoto, et al., SHINGAKUKAI GIHO, SAN87-34.
2. Kubota, et al., The 33rd Space Sciences and Technology Conference, 1988, pp 692-693.

Concept for Intersatellite Laser Communications

906C3836 Tokyo DAI33KAI UCHU KAGAKU GIJUTSU RENGO KOENKAI KOENSHU in Japanese
31 Oct-2 Nov 89 pp 744-745

[Article by Hiroshi Arikawa, Yasumasa Kubota, and Hiroshi Anekawa, National Space Development Agency of Japan]

[Text] 1. Introduction

Optical (laser) communications offer the following advantages:

- (1) The volume of information that can be transmitted is great.
- (2) The beam is sharp and mutual interference is small.
- (3) The communications system can be made compact and lightweight.

Therefore, optical communications systems are widely expected to emerge as effective communications systems in the future. The weakness of optical communications is that attenuation is great in the atmosphere, but this does not apply in the vacuum of space. Mutual interference can be minimized by making the beamwidth sharp and it is believed that this will be an optimum system for communications among space planes. Important technologies that need to be developed for laser communications include a high output and long life LD, a high precision pointing system, and highly sensitive light-intercepting devices. Research on laser communications among satellites will be conducted along two lines. The first will focus on an "immediate system," which is aimed at the development of the pointing system. The second involves the "future system," which is aimed at long distance/large capacity communications. Research is presently under way to accumulate the basic data needed for the acquisition and tracking mechanism of the high precision pointing system of the "immediate system."

2. Development Targets

Taking into account the results of system study and trends in the development of ground-based optical devices, it has been decided to conduct the research and development of intersatellite optical communications efficiently and in stages by dividing it into the "future system" aimed at large-capacity communications and the "immediate system," which is narrowed to the development of an acquisition and tracking system possessing a high precision pointing system

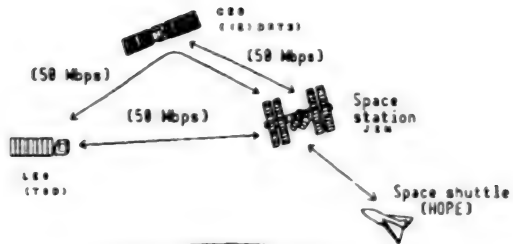


Figure 1. Block Diagram of Inter-satellite Laser Communications (Example)

for establishing the communication link. A conceptual drawing of the immediate system is shown in Figure 1 and the target specifications for both the future system and the immediate system are shown in Table 1.

Table 1. Principal Target Specifications for Intersatellite Laser Communications System

Item		Future system	Immediate system
Communications line		GEO-LEO GEO-GEO	GEO-LEO
Optical system	Antenna diameter	GEO less than 50 cm ϕ LEO less than 20 cm ϕ	GEO 30 cm ϕ LEO 20-30 cm ϕ
Communications system	Wavelength	0.85 μ m band or 1.3 μ m band	0.85 μ m band
	Output	100-200 mW	More than 100 mW
	Transmission rate	More than 1 Gbps	More than 50 Mbps
	Communications distance	GEO-LEO 43,000 km GEO-GEO 82,000 km	GEO-LEO 43,000 km
Acquisition and tracking system	Beacon wavelength	0.85 μ m band	
	Beacon output	50-100 mW	
	Drive range	GEO-GEO X/Y; $\pm 50^\circ$	
		GEO X/Y; $\pm 15^\circ$ LEO Az; $\pm 180^\circ$ El; $\pm 120^\circ$	GEO X/Y; $\pm 15^\circ$ LEO Az; $\pm 180^\circ$ El; $\pm 120^\circ$
	Precision	(Antifluctuation $\pm 0.01^\circ/0.4$ Hz) Within $\pm 1 \mu$ rad	
Electric power		TBD W	150 W
Weight		TBD kg	100 kg

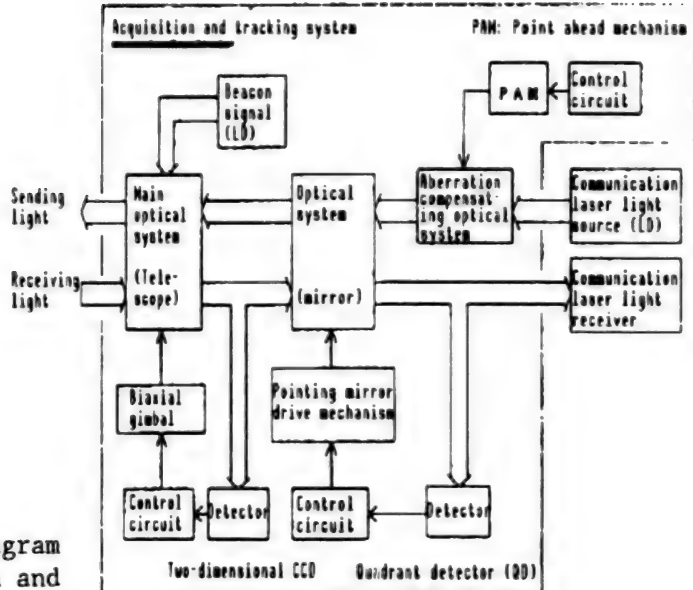


Figure 2. Functional Diagram of Acquisition and Tracking System

The immediate system aims at the development of an acquisition and tracking system having a pointing precision of less than $1 \mu\text{rad}$, envisages optical communications between the GEO and LEO satellites to demonstrate this system and aims ultimately at mounting an engineering/communication experiment mission on the DRTS satellite and the Japan Experimental Module for the space station. After demonstration and confirmation of the acquisition and tracking system's performance, development of the "future system" centered around the communications system will be tackled. This will lead to long-distance/large-capacity communications and preparations will be made for the era of large capacity data communications among satellites.

3. Development of Acquisition and Tracking System

Since it was difficult to effect acquisition using a single control loop with respect to pointing precision in a test manufactured acquisition and tracking system, acquisition is carried out in two stages—rough acquisition and precise acquisition. A CCD was used as the sensor for rough acquisition and while a QD (quadrant detector) was used as the sensor for precise acquisition. Figure 2 is a functional block diagram of this system.

The present phase of the trial manufacture test of the acquisition and tracking system involves a partial trial manufacture of the acquisition and tracking system including the biaxial gimbal and FPM to be carried by the LEO, which demands a wider acquisition and tracking range than the GEO. It is now in the stage of basic data acquisition for basic performance parameters. In this partial trial manufacture test of the acquisition and tracking system, the biaxial gimbal system has been replaced by a uniaxial device, while the mirror drive mechanism, which is the nucleus of the FPM, has a built-in piezoelectric electric system and a moving coil system that have completed primary trial manufacture.

The technical requirements for the acquisition and tracking system include a laser source with a long life and high output, a high precision biaxial gimbal, a long wavelength applicable CCD, and a quadrant detector with a high signal to noise ratio and a wide field of vision.

4. Conclusion

Research on laser communications among satellites has been divided into two stages, an "immediate system" and a "future system." As part of the work on the "immediate system," a partial trial manufacture test of an acquisition and tracking system with a high precision pointing system for establishing the optical link has been conducted. It is necessary to consider the effect of aberration in this acquisition and tracking system. A partial trial manufacture test will be conducted for a system that incorporates an aberration compensation device and basic data will be acquired. Upon observing the results of these tests, the next step will be to move to a full-scale trial manufacture. After the partial trial manufacture test of the acquisition and tracking system, a future task will be to determine the manner in which the evaluation system will be constructed.

Meanwhile, it will be necessary to conduct a series of studies regarding the potential applications of optical communications in the future and also on the use of space planes, including space shuttles, to carry the "immediate system" as demonstration test beds for the high precision pointing system.

Checkout System for Multibeam Satellite-Mounted Transponder

906C3836 Tokyo DAI33KAI UCHU KAGAKU GIJUTSU RENGO KOENKAI KOENSHU in Japanese
31 Oct-2 Nov 89 pp 746-747

[Article by Koji Horikawa, Katsuhiko Araki, Masayoshi Tanaka, Kazuichi Yamamoto, and Kazuyasu Okada, NTT Radio System Laboratory]

[Text] 1. Introduction

There has been a number of studies on the possibility of creating a multibeam satellite communications system. Such a system offers the advantages of large capacity and more economical use of communications satellites. However, when performing an evaluation test of a large multibeam satellite it becomes very difficult to assess the state of the onboard transponders because of the expansion of functions of the satellite switch (Figure 1). In addition, the number of transmission paths increases to the point where it cannot be compared to that of single-beam satellites. Therefore, it is necessary to improve evaluation test efficiency. Based on the development results of an automatic evaluation test system for a single-beam satellite-mounted transponder,¹⁻³ the COSMOS (checkout system for multibeam onboard transponder)

system, which is capable of performing an evaluation test of the multibeam satellite onboard transponder with a high degree of precision in a short period, has been developed.⁴ This paper describes the composition, functions, and characteristics of this evaluation system.

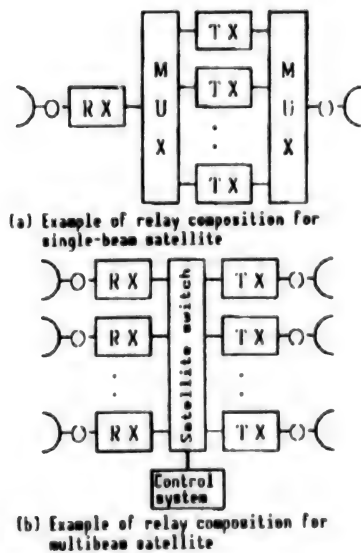


Figure 1. Complication of Relay Composition Multibeaming

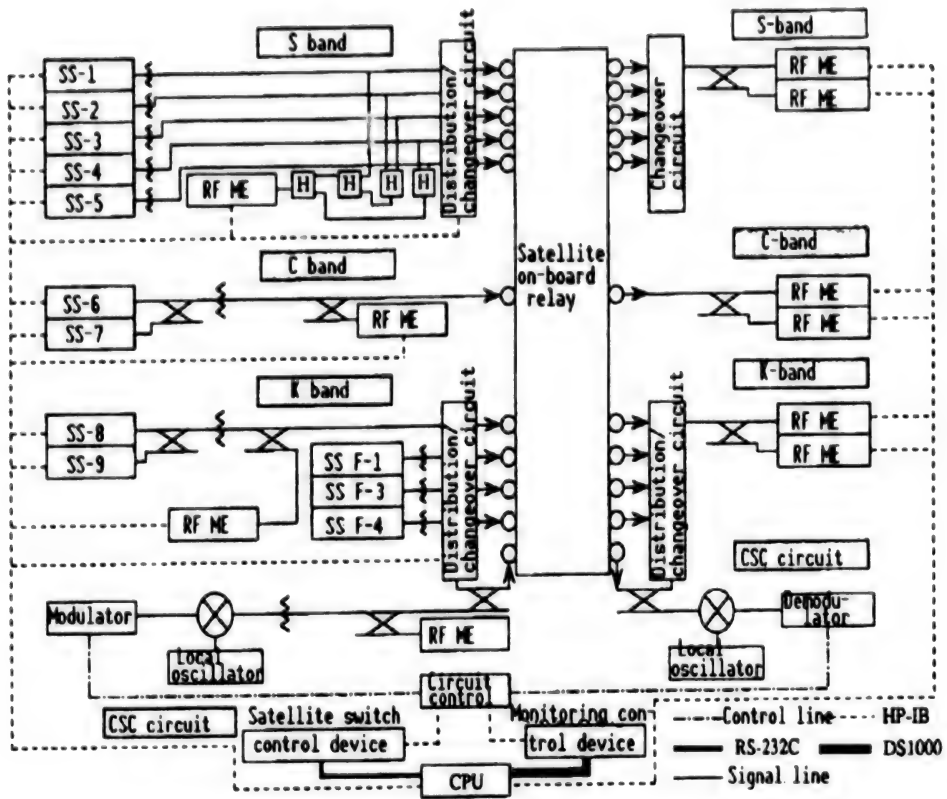


Figure 2. Block Diagram of Checkout System

2. System Composition

The composition of the COSMOS system is shown in Figure 2. The communications equipment control and characteristic evaluation tests are further complicated by having a satellite switch onboard. The evaluation test has been made fully automatic by using a computer. It is a system capable of efficiently evaluating transponder characteristics for a limited period and with limited resources.

Dividing and allotting the complicated functions into three subsystems made it possible to change settings independently for each subsystem and thus overcame the problem of complexity. The three subsystems are:

- (1) transponder characteristic measuring function;
- (2) setting and monitoring functions for equipment operation mode; and
- (3) sending and receiving functions for satellite switch control data.

The first function provides computer control of the measuring equipment and measures the various RF characteristics of the transponder. The second function involves setting the transponder by a command sent in accordance with the command pattern registered in advance and conducts set state monitoring by telemetry reception.⁵ Moreover, the telemetry data after engineering value conversion are combined with the RF measured data. The third function controls the satellite switch according to the data base and the registered switch

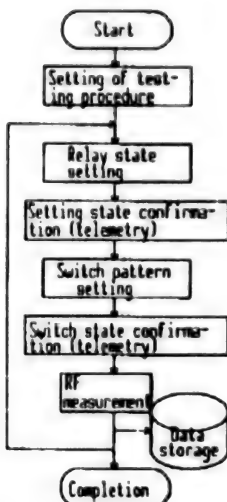


Figure 3. Measurement Sequence

pattern, and monitors the setting state.⁶ These three functions were organically joined together and full automation was achieved by unitary computer processing.

A switch network was arranged in the input/output parts of the RF measuring circuit of this system connected to the transponder so that connection to optional beams was possible.

3. System Functions and Characteristics

The measuring procedures for this system are shown in Figure 3. The state setting and monitoring of the transponder, control of the satellite switch, state monitoring of the testing system, and measurement of transponder characteristics are carried out according to testing procedures set in advance and are fully automated. Examples of main RF measuring items, measurable ranges, and required time are shown in Table 1.

Because of its composition, this system has the following characteristics and advantages:

(1) Labor saving

This is made possible by unitary computer processing and the system can be operated by a single operator.

(2) Automatic setting of switch pattern

Automatic measurement is continuously possible by a different switch pattern.

(3) Simultaneous measurement of different signal transmission paths

Simultaneous measurement of a maximum of three transmission paths is possible.

(4) Suitable for on-orbit checkout

Can be used for transponder performance evaluation after connection with the earth station.

Table 1. Principal Measurement Items, Measurement Ranges, and Examples of Necessary Time

Main RF characteristics of measurement items possible by COSMOS	Measurable range for each measured item (measurable by three frequency bands—Ka, C, and S)	Example of necessary time in case of ETS-VI evaluation
1. I/O characteristics	Input—Less than 20 dBm	About 7 minutes (30 points)
2. Amplitude frequency characteristics	Band less than 3.5 GHz (Ka-band)	About 2 minutes
3. Tertiary intermodulation distortion characteristics	Input—Less than 20 dBm (2-tone)	About 7 minutes (30 points)
4. AM/PM conversion characteristics	Input—Less than 20 dBm (2-frequency method)	About 7 minutes (30 points)
5. Group delay characteristics	Band less than 1 GHz	About 3 minutes
6. Differential gain characteristics	Band less than 1 GHz	About 3 minutes
7. Spurious characteristics	Frequency range 0~40 GHz	About 3 minutes

(5) Real-time display of transponder temperature and measured results
Prompt discovery of abnormality generation is possible by CRT graphic display.

(6) Control of executed measurement items

A computer controls the executed transmission paths for each measured item and it is possible to prevent duplication and effect oversight of measurements by a CRT display.

(7) Improvement of operationability

The test procedure input will be a conversational selective type with the computer and prevention of erroneous operations is possible.

(8) Adaptability

Capable of immediately outputting the measured result and prompt confirmation of transponder performance is possible.

4. Conclusion

We have described the COSMOS checkout system, which is able efficiently to evaluate the characteristics of the transponders onboard a multibeam satellite. This system recently has been applied to the performance evaluation of the ETS-VI onboard transponder. This confirmed that the system performs well

as a multibeam satellite onboard transponder evaluation test system. This system will be continuously used to evaluate the performance of transponders in various space environments and to effect performance confirmation tests after satellite launch. Finally, we express our deep thanks to Department Chief Morita of the Communication Satellite Technical Laboratory for his invaluable guidance.

References

1. Takahashi, et al., "Satellite Onboard Transponder Checkout System Study," SHINGAKU SOZENDAI, 1985, p 2513.
2. Tanaka, et al., "Study of Onboard Transponder Orbital Checkout System," SHINGAKU GIHO, SAT87-70, 1988.
3. Furufuji, et al., "Study of Onboard Transponder Orbital Checkout System," SHINGAKU SPRING ZENKOKUTAIKAI, 1988, pp 1-192.
4. Horikawa, et al., "Multibeam Satellite Onboard Transponder Checkout System," Ibid., 1989, p B-197.
5. Shingenobu, et al., "General Use Satellite Onboard Communication Equipment Monitoring Control Software," Ibid., 1989, p B196.
6. Ono, et al., "Multibeam Satellite Communication Control Data Transmission System," Ibid., 1989, p B228.

Command Decoder for Loading on Future Scientific Satellite

906C3836 Tokyo DAI33KAI UCHU KAGAKU GIJUTSU RENGO KOENKAI KOENSHU in Japanese
31 Oct-2 Nov 89 pp 748-749

[Article by Tomonao Hayashi, Takamoto Ninomiya, and Takahiro Yamada, Space Science Laboratory; and Takeshi Orii, Yoshinari Minami, and Akashi Sugimori, Nippon Electric Co.]

[Text] 1. Introduction

The need to send a large volume of data from the earth to satellites has increased with the increased size of scientific satellites, and the enhanced capability of onboard equipment. A command decoder for a new system that incorporates a new concept has been developed.

This command decoder, which is able to handle hierarchical data, effects transmission control according to the command transmission procedures sent from earth. Adopting this system has made it possible to increase data transmission speed to more than 50 times that of the conventional command decoder.

2. Details of Development

Studies of the command system to be used for future scientific satellites also take into account the command system enacted by the Consultative Committee for Satellite Data Systems (CCSDS) and the results of one such study were reported at the 31st Space Sciences & Technology Conference.¹ Development of the command decoder followed the recommendations presented in this thesis.

3. Functions and Composition

The relationship between the command decoder functions and the hierarchical command data is shown in Figure 1. The command decoder handles three levels of data—the physical layer, the coded layer, and the transmission layer—from among the five hierarchical levels shown in Figure 1. Data processing for the split layer and the application layer is conducted by another device. Since the command decoder handles these three hierarchical data layers, it has the following primary functions:

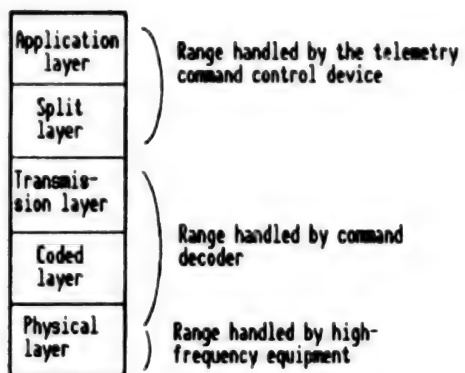


Figure 1. Hierarchical Command Structure

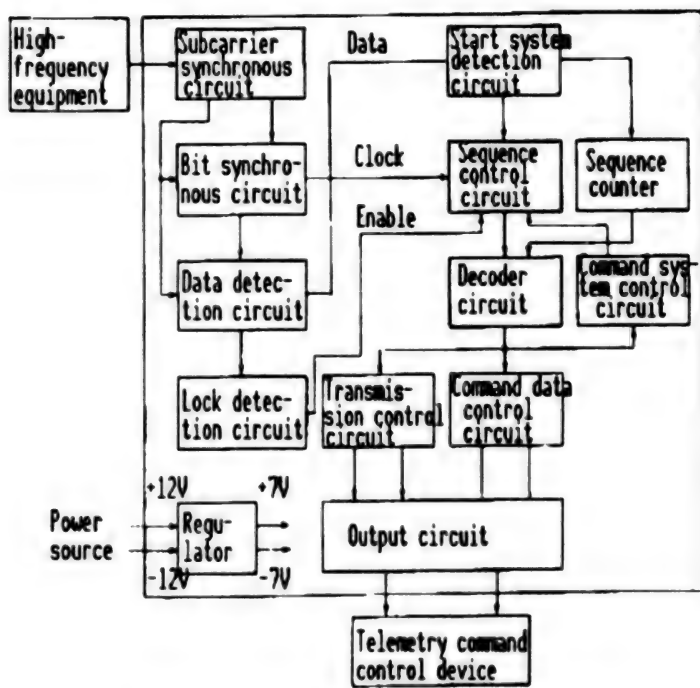


Figure 2. Functional Flow Chart for Command Decoder

- (1) Receives the command base-band signal from the S-band receiver and conducts subcarrier demodulation, bit regeneration and command data demodulation.
- (2) Monitors the demodulated command data column and detects the start sequence, which is the synchronous code. When detecting the start sequence, it demodulates the coded command following the start sequence and conducts bit error correction/bit error detection.
- (3) When a bit error or an invalid command is detected, the command is rejected. Moreover, the sending order of the command is monitored and, together with rejecting the command that has been input in an invalid order, a request for the command to be resent is transmitted to the earth to secure a correct command order.

- (4) Notifies the earth on the acceptance condition of commands

A functional flow chart for the command decoder is shown in Figure 2 while the command decoder itself is shown in Photo 1 [not reproduced].

4. Performance

Table 1 presents a comparison of the major functions for the newly developed command decoder and a conventional command decoder.

Table 1. Principal Performance Characteristics of Command Decoder

	Developed model	Conventional model
Subcarrier frequency	16 kHz	8 kHz
Bit rate	4 Kbps	1 Kbps
Command transmission speed	912 bits/second	16 bits/second
Bit error rate	Less than 1×10^{-5}	Less than 1×10^{-5}
Command resend probability	2×10^{-11}	2×10^{-16}
Command malfunction rate	1×10^{-18}	3×10^{-18}
Electricity consumption	2.5 W	2 W
Weight	2 kg	1.3 kg

5. Characteristics

In developing the command decoder, we took into account a number of important points, including versatility and the possibility of functional expansion in the future:

- (1) The command data length has been made so that it can be changed for each satellite.
- (2) The process of changing the coding method for commands has been simplified.
- (3) PLL controlled by a crystal oscillator was adopted to improve the stability of the subcarrier synchronous circuit.
- (4) The regulation places have been minimized by adopting an all-digital bit synchronous circuit.

6. Conclusion

By developing a command decoder for future scientific satellites and confirming that the results of the electrical performance tests and temperature tests satisfy the design conditions, it will become possible to send a larger volume of data than ever before to onboard equipment. Design of an onboard model is now under way and actual fabrication and tests will be conducted in the future.

Finally, we express our deep thanks to all those who rendered us invaluable guidance.

References

1. Yamada, T., et al., "Future Command System for Scientific Satellites," 31st Space Sciences and Technology Conference Thesis, pp 462-463.

Development of Aurora TV Camera for Scientific Satellite 'Akebono'

906C3836 Tokyo DAI33KAI UCHU KAGAKU GIJUTSU RENGO KOENKAI KOENSHU in Japanese
31 Oct-2 Nov 89 pp 750-751

[Article by Takashi Oguchi, Nagoya University; Eisuke Kaneda, Tokyo University; Zenki Ejiri, Polar Region Laboratory; Susumu Sasaki, Space Science Laboratory; and Katsuhiko Tsuno, Nihiko Okamoto, and Yoshihiko Kameda, Toshiba Corp., Komukai Plant]

[Text] 1. Introduction

The aurora TV camera (ATV) mounted on the scientific satellite "Akebono," which was launched in February 1990, was developed for aurora imaging from the visible range to the vacuum ultraviolet range from satellite orbit. It was designed for aurora phenomenon observation and research, and, together with other onboard observation sensors, for observing aurora particles, wave motion, electromagnetic field, etc.

Since the aurora is a faint light-emitting phenomenon, the ATV must be highly sensitive in order to image its objective. This sensitivity is attained by storage imaging of 0.1-0.6 second by using a highly sensitive CCD and by using an image intensifier. In addition, a despun mirror system (DMS) capable of a maximum of 0.6 second image storage was included in the sensor package on the "Akebono" satellite, which is a spin satellite that rotates about 7.5 rpm.

2. Outline of ATV

The ATV, as shown in the functional block diagram in Figure 1, consists of the sensor element (ATV-S), a high-voltage power source (ATV-HV), and an electronic circuit (ATV-E). The principal specifications of the ATV are listed in Table 1. When mounted on a satellite, the field of vision of the sensor is perpendicular to the spin axis.

The appearance of the sensor element and the high-voltage power source part are shown in Photo 1 [not reproduced]. The sensor element is equipped with two types of CCD cameras. The visible range camera is sensitive in the 557.7 nm band thanks to an image intensifier for the visible wavelength band a lens provided with a wavelength filter. The ultraviolet camera is sensitive in the 115-160 nm band thanks to the mirror reflectivity of the catoptric system

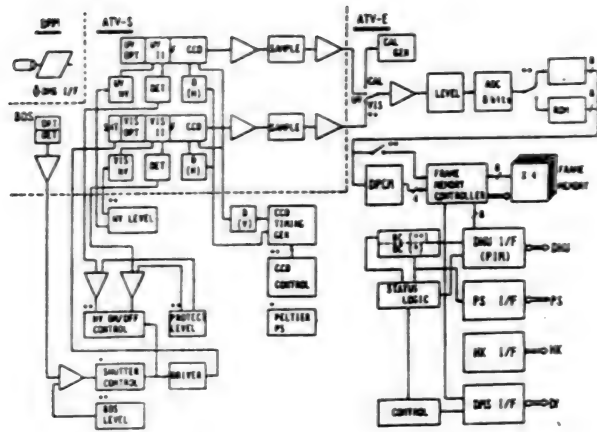


Figure 1. ATV Functional Block Diagram

Table 1. Principal Specifications of ATV

1. Ultraviolet camera performance Effective observation wavelength range Detection level Angle of visibility Effective pixels	115~160 nm More than -300 R 40 deg x 36 deg 376 x 244
2. Visible camera performance Observation wavelength Observation range Angle of visibility Effective pixels	557.7 ± 10 nm 100 R ~ 100 kR 30 deg x 40 deg 244 x 376
3. Weight and electric power Weight Electric power	11.6 kg Less than 12.6 W

and a vacuum ultraviolet image intensifier. The output image of each image intensifier is enhanced by the area CCD. A CCD with a fiber that adheres to a fiber face plate on the chip of the Toshiba-made area CCD (TCD 205C; 376 pixels x 488 pixels) was developed for this CCD and an optical coupling of the image intensifier and CCD has been obtained. Moreover, the high voltage power source supplies the maximum high voltage of about 7 kV independently to each image intensifier for the visible and ultraviolet cameras.

The electronic circuit has an interface with the data handling unit (DHU) and, in addition to conducting command and HK telemetry processing and image data output, it generates the CCD drive signal, synchronizes with the DMS and conducts DMS interface for acquiring the image at the prescribed phase angle of the satellite spin. It also includes the frame memory for buffering the image data.

ATV imaging generally features 188 horizontal pixels x 244 vertical pixels (8 bits per pixel) for read, adding 2 horizontal pixels and 2 vertical pixels in the CCD interior. In addition to this mode, tn can be set for a mode that condenses the 8-bit data to one-half of the data volume or 4 bits by PCM-izing and imaging the horizontal direction pixels at 376 pixels (2 times) while the 188 pixels x 244 pixels data are condensed by DPCM-izing and reducing the time resolution by one-half. The imaging rate will also depend on the setting of the telemetry frame format of the "Akebono" satellite, but an imaging minimum of 8 seconds per image plane is possible.

3. Conclusion

The ATV was given a high voltage charge about one month after being launched. It has completed its basic operational checkout and is performing aurora observation. Photo 2 [not reproduced] shows an example of the aurora oval imaged by the ultraviolet camera.

Despun Mirror for 'Akebono' Satellite Imaging System

906C3836 Tokyo DAI33KAI UCHU KAGAKU GIJUTSU RENGO KOENKAI KOENSHU in Japanese
31 Oct-2 Nov 89 pp 752-753

[Article by Kenji Hiraishi, Haruki Ayada, and Noriko Terada, Nippon Electric Co.; Takashi Koguchi, Nagoya University Atmospherics Laboratory; Eisuke Kaneda, Faculty of Science, Tokyo University; Zenki Ejiri, National Polar Region Laboratory; and Susumu Sakai, Space Science Laboratory]

[Text] 1. Introduction

The despun mirror system (DMS), which is mounted on the No. 12 scientific satellite "Akebono" (EXOS-D) launched this February, is designed to offset the movement of the ATV field of vision caused by satellite rotation when acquiring an image by the aurora television (ATV) camera and to fix the field of vision in a given direction in the inertia space. This report describes the despun mirror system and presents the results of a performance evaluation test.

2. Composition

The DMS consists of a vacuum ultraviolet (VUV) surface reflecting mirror, a stepping motor, a harmonic gear, a mirror position sensor, a mechanical unit (despun mirror mechanical unit: DMM unit) consisting of a frame for supporting the components, and the electronics unit (despun mirror electronics unit: DME unit) (Figures 1 and 2 [not reproduced]). A functional block diagram of the DMS is shown in Figure 3.

2. Functional Performance

The ATV field of vision faces a fixed direction in inertial space. This is done through the medium of the mirror, which rotates in the opposite direction at one-half of the angular velocity of the satellite spin rate. Thus, the ATV is able to acquire a still picture. The ordinary imaging action of the DMS is that it spins in a direction opposite to the satellite spin for a period of about 0.8 second (more than the maximum required time of 0.6 s) out of a satellite single spin period of about 8 seconds after receiving an imaging demand signal for the ATV. The ATV rewinds in the same direction as the satellite spin after stopping for about 4 seconds, conducts a reciprocating

motion for mirror deflection of about 18°, and returns to the initial (STANDBY) position. The phase angle data that specifies the field of vision direction in inertial space can be stored up to 2K bytes in the memory and a continuous program operation of 18.2 hours is also possible with an automatic update made every 32 seconds. In addition, the star direction standard pulse and geocentric direction standard pulse can be selected by the command as the phase angle standard direction. The principal functional performance specifications are shown in Table 1.

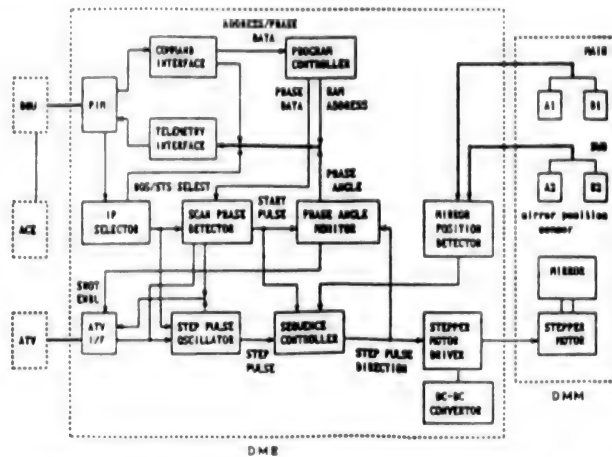


Figure 3. Functional Flow Sheet for DMS

Table 1. Principal Functional Performance Specifications

Principal functions	Imaging sequence operations (STAND-BY→DESPUN→STOP→REWIND→STANDBY) Mirror close function, mirror check function, motor automatic OFF function (at abnormality)
Despun precision	Within 0.04° (precision in 1 pixel of obtained image)
Despun operating range	Satellite spin rate 7.5 ± 0.5 rpm
Standard phase	HOS-IP or STS-IP (Selection by CMD)
Phase assigned resolution	1.41 deg
Phase data memory	2 Kbyte (Equivalent to program operation of 18.2 hours)
Phase data update time	Every 32 seconds (Data update start/stop possible by CMD)
Weight and approximate dimensions	DMM 1.5 kg $\phi 140 \times 273$ DME 3.7 kg 250 x 260 x 116
Electricity consumption	During DMS ON and mirror stop 1.6 W During DMS ON and mirror drive 7.3 W 1 spin average (at 20 percent operation rate of motor) 2.7 W
Command	Telemetry command 19 items Block command 2 items
Telemetry items	Status 2 WORD 13 items Data 3 items (among the 3 items, 2 items are at RAM check)

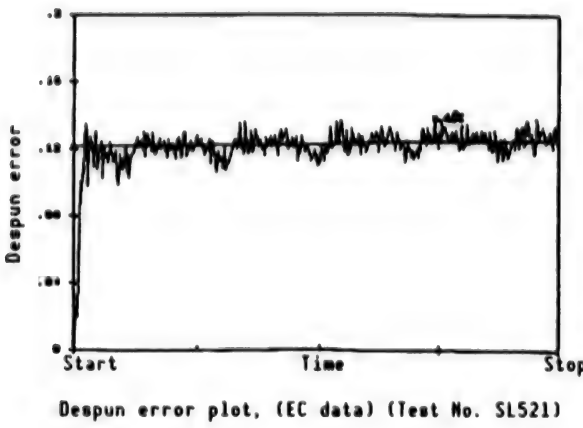


Figure 4. Example of Despun Precision Measured Data

3. Despun Precision

A despun precision within 0.04° is demanded of the DMS in order to hold down the deflection of the acquired image to within one pixel. Measurement was conducted by attaching a rotary encoder to the mirror shaft to evaluate the despun precision of the DMS unit. The measurement results are shown in Table 2. Moreover, an example of the acquired data is shown in Figure 4. Despun errors are attributable primarily to spin rate measurement error, step angle error of the stepping motor and angle transfer error of the harmonic gear. The measured spin rate error of the DMS unit has been held down to within $0.008^\circ/\text{s}$ when converting into the mirror angular velocity, and the precision of the motor plus gear has been held down within $\pm 0.014^\circ$. The results of the measurement confirm that the demand for a despun precision of less than 0.04° is satisfied.

Table 2. Despun Precision Measurement Results

Satellite spin rage	Despun precision (σ)	Remarks
7.0 rpm	$0.006 \pm 0.001^\circ$	$\sigma = \sqrt{\frac{\sum (\Delta\theta_i)}{n-1}}$
7.5 rpm	$0.008 \pm 0.003^\circ$	
8.0 rpm	$0.010 \pm 0.003^\circ$	

[4.] Conclusion

After the launch of the spin satellite "Akebono" and upon completion of an operational check, an aurora image was obtained over the South Pole by the ATV-DMS in April and the functional performance of DMS has been confirmed.

Development of Optical Communications Acquisition, Tracking System

906C3836 Tokyo DAI33KAI UCHU KAGAKU GIJUTSU RENGO KOENKAI KOENSHU in Japanese
31 Oct-2 Nov 89 pp 754-755

[Article by Kenichi Takahara, Shitta Niimiya, Tsuyoshi Kosugi, and Seiichi Hashimoto, Toshiba Corp.; and Hiroshi Arikawa, Yasumasa Kubota, and Hiroshi Anegawa, National Space Development Agency: "Third Report—Design and Basic Characteristics of Point-Ahead Mechanism"]

[Text] 1. Introduction

Optical communications in space are viewed as a promising means to cope with the increasing need for communication capacity that can be expected to grow in the future and for large capacity data transmission by various kinds of observation equipment. To this end, studies of systems including acquisition and tracking systems and communications systems, are being promoted.^{1,2} Optical communications among satellites enjoy a number of advantages, such as the fact that there is no need to allocate radio frequencies, they are not easily affected by mutual interference and they do not suffer atmospheric effects. However, since optical communications are carried by a highly directive laser beam, an optical drive system that conducts high precision acquisition and tracking becomes necessary.^{3,4} In particular, a mirror drive mechanism, i.e., a point ahead mechanism (hereinafter called PAM) that emits a sending beam in a direction that anticipates the movement of the other satellite within the transmit-receive time is necessary for this acquisition and tracking system. Therefore, it is required that the mirror of this PAM face in a certain fixed direction with a high degree of accuracy, although the drive range may be narrow. A piezoelectric element has been selected as the actuator conforming to this requirement and a PAM has been test manufactured. This report will describe the design, basic characteristics, and test results of this PAM.

2. Mechanism Design

The main design problem is not how to design an actuator that is sufficiently strong but to design a highly precise mirror drive mechanism that will compensate for any weakness in resistance to the bending and tension of the piezoelectric element. This is done by taking advantage of the fact that the drive resolution of the piezoelectric element is high. Moreover, since a hysteresis exists between the relationship of the supplied voltage and

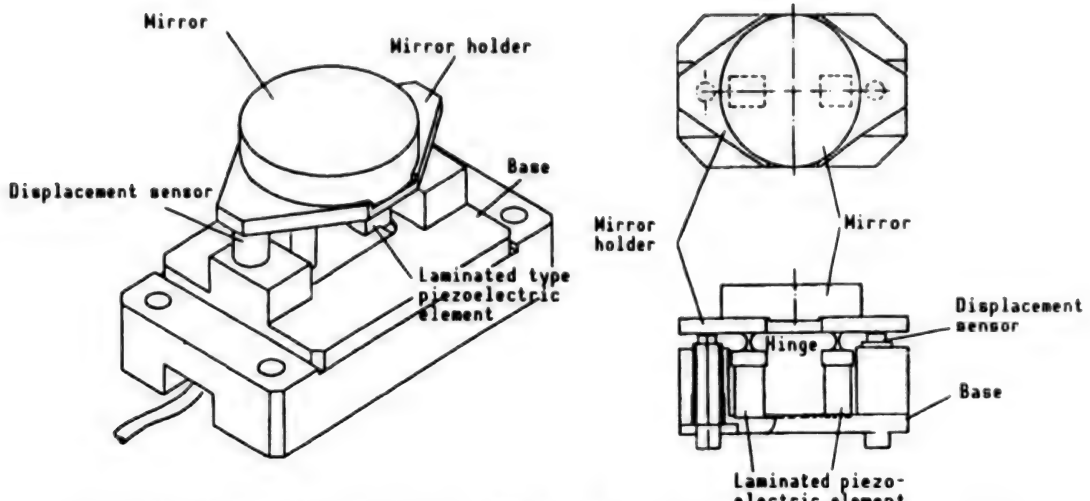


Figure 1. General View of Aberration Correction Mechanism Figure 2. Composition of Aberration Correction Mechanism

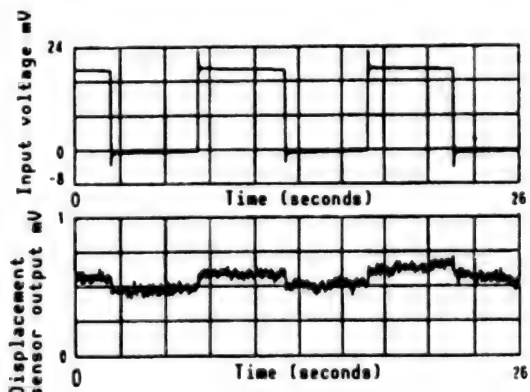


Figure 3. Drive Resolution

displacement in the piezoelectric element, a high precision angle sensor that measures the angle of the mirror becomes necessary.

The newly designed PAM is shown in Figure 1. Since this PAM is a direct drive type in which rotation of the mirror is effected directly by two piezoelectric elements, its composition is simple and its reliability is high. As shown in Figure 2, an elastic hinge has been adopted in the coupling part of the piezoelectric element and the mirror base and is made so that a bending stress is not applied to the piezoelectric element. In addition, the mirror angle is detected by the differential output of the two overcurrent-type noncontact displacement sensors that have been attached to the bottom left and right of the mirror base. When it is composed in this manner, the translational movement of the mirror base caused by temperature rise is not detected.

The specifications of the test manufactured PAM are arranged in Table 1. Its overall dimensions are 20 x 40 x 25H mm and its weight, including the mirror, is 50 g.

Table 1. Specifications of PAM

Item	Characteristic value
Degree of freedom	1
Drive range	± 0.01 deg
Drive frequency (Simplex)	1 kHz
Drive resolution	2.4×10^{-5} deg
Dimensions	20 x 40 x 25H mm
Weight	0.05 kg

3. Basic Characteristic Tests

Various tests to measure step response, frequency response, and drive resolution were conducted to determine the basic characteristics of the PAM. The test results for drive resolution are shown in Figure 3 as an example. The upper diagram in Figure 3 shows the input microrectangular wave and the lower diagram shows the detected displacement sensor. The drive resolution converted from the displacement sensor output was 2.4×10^{-5} degrees.

4. Conclusion

The point ahead mechanism that has been test manufactured is a lightweight and highly reliable mechanism that uses piezoelectric elements. The basic characteristics tests have confirmed that it has sufficient drive resolution.

References

1. Kubota, et al., "Studies of Laser Communications System Among Satellites," 31st Space Sciences and Technology Conference, 1987.
2. Kubota and Hashimoto, "Studies of Optical Communications Among Satellites," 32nd Space Sciences and Technology Conference, 1988.
3. Shimamoto, et al., "Development of Optical Communications Acquisition and Tracking Mechanism," 31st Space Science sand Technology Conference, 1987.
4. Takahara, et al., Ibid., (Second Report), 33rd Space Sciences and Technology Conference, 1988.

Development of Antenna Directional Control System for Earth-Orbiting Spacecraft

906C3836 Tokyo DAI33KAI UCHU KAGAKU GIJUTSU RENGO KOENKAI KOENSHU in Japanese
31 Oct-2 Nov 89 pp 756-757

[Article by Shinichi Otani, Tomomi Koseki, Katsuhiro Yamashita, Akio Mochizuki, and Takeshi Ono, Nippon Electric Co.]

[Text] Introduction

Development of the data relay and tracking satellite (DRTS) system, most recently represented by the TRDSS, is being pursued as the means of transmission for mission data and control signals from spacecraft orbiting at low and medium altitudes. Since this system forms a high speed and large capacity data transmission path, it is necessary for the high gain antenna to be directed toward the relay satellite at all times from the user spacecraft side. Thus, the antenna directional control system has attracted attention as an important element technology. Primary studies and trial manufacture of an antenna directional control system have been conducted and the design base line has been confirmed. This article presents the results of these efforts.

Principal Functions

The principal functions demanded of the antenna directional control system, taking into account the basic demands from the user spacecraft and also considering various operational aspects, are as follows:

- Pointing the antenna in the proper direction.
- Two modes of open-loop control and closed-loop automatic tracking must be included in directional control.
- Changeover from closed-loop automatic tracking to open-loop control is possible by earth command.
- Forecasting angle information for the antenna direction can be input from earth and stored in the memory.
- Time information can be input from the satellite.

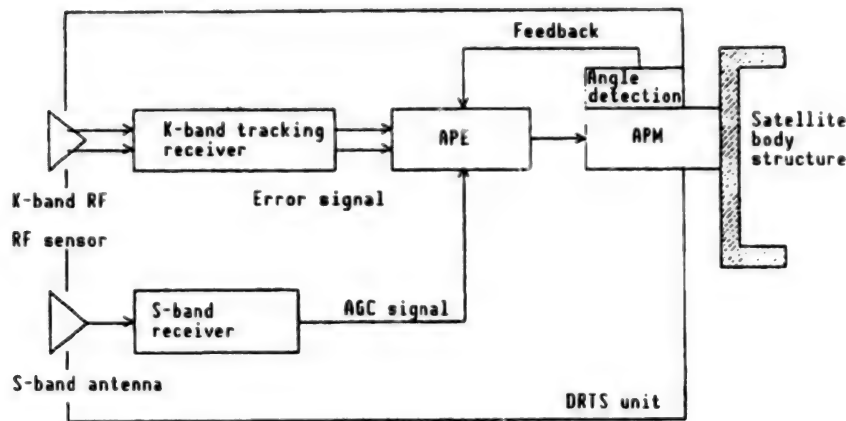


Figure 1. Functional Flow Diagram

- The feed forward signal is sent to AOCS.
- Compensation for initial acquisition and the ability to expand the acquisition range.
- Reacquisition can be effected by switching over to open-loop control when the target has been lost during closed-loop tracking.
- Capability to monitor and check software and hardware malfunctions for both open-loop and closed-loop controls.

Composition

Efforts to devise a system that would satisfy the functions listed above and that would be compatible with EDRTS and ETS-VI, which will be used as the relay satellites, led to the concept for the basic composition shown in the functional flow diagram in Figure 1. This structure assumes a two-wave composition using the S- and K-bands.

Acquisition and Tracking System

It is possible to conceive of cases where open-loop control can be considered, depending on the requirement for tracking precision of the acquisition and tracking system. However, if an antenna of about $2 \text{ m}\phi$ is used and if there is a severe demand for tracking precision, the following method is thought to be the optimal sequence to cover all stages from initial acquisition upto final high precision tracking.

- Open-loop control \rightarrow (Initial acquisition backup) \rightarrow Closed-loop automatic tracking

A flowchart depicting this acquisition and tracking system is presented in Figure 2. The results of a special study on using the generation method of drive information for open-loop control are shown in Table 1. When the orbit determination values for both the user satellite and the data relay/tracking satellite are sent to the onboard computer, a precise orbit generation like

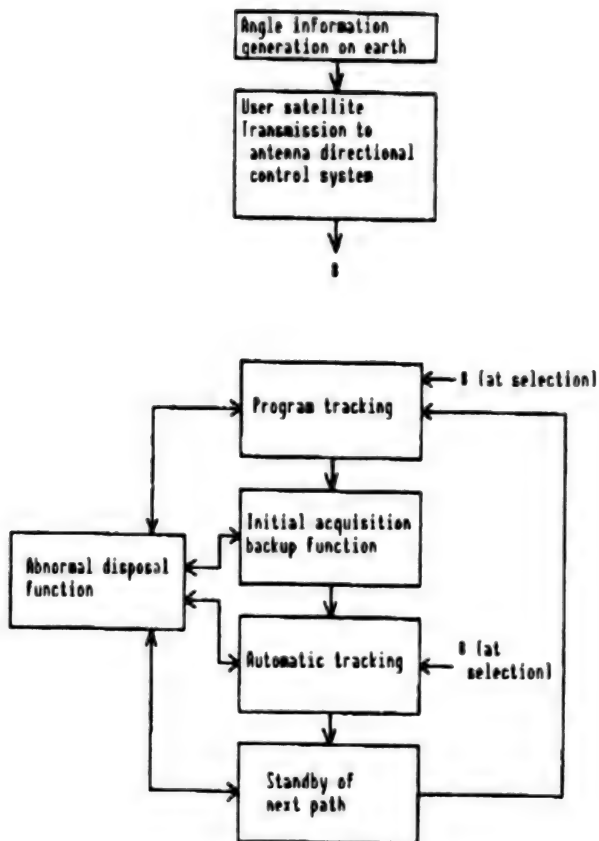


Figure 2. Flowchart for Acquisition and Tracking System

that made by the earth computer is difficult to achieve because of limited processing capability. Meanwhile, if the data for Az and El are sent directly, the onboard computer must have an extremely large memory capacity. Therefore, we devised a method calculating the directional angle based on a precise orbit generation from earth. This is done by approximating the results with a polynomial expression by dividing the data into short periods, sending the set of expansion coefficients to the onboard computer, and generating the drive angle information (Table 1 (3)). In view of the operational characteristics, including capacity, scale, and reliability of the onboard computer, it is believed that this method is suitable as the directional control system for the DRTS system user spacecraft. The results of obtaining the polynomial expression when the calculation time for the expansion coefficients is made every 5 minutes and compared to the standard deviation of the approximate errors as determined by simulation are shown in Table 2. This table indicates that a sufficiently high degree of precision control can be achieved by using a polynomial expression above a biquadratic equation.

Conclusion

Our research has confirmed the adequacy of the design base line for the DRTS system user spacecraft antenna directional control system.

It was generally confirmed that the basic performance characteristics were available. This was confirmed by conducting a partial trial manufacture of the antenna tracking system based on this base line. Taking into account the results of the partial trial manufacture, we expect that more detailed studies will be conducted in the future.

Table 1. Drive Information Generation System Tradeoffs

	(1)	(2)	(3)
Item System	Az, El data transmission	Orbital element transmission	Az, El polynomial approximate expansion coefficient transmission
Onboard processor processing load	Small o	Large x	Small o
Onboard memory capacity	Large x	Small o	Medium Δ
Processing load on earth	Medium Δ	Small o	Large x
Data transmission frequency	Large x	Medium Δ	Small o
Evaluation order	3	2	1

Table 2. Standard Deviation of Order and Error of Approximate Polynomial Expression

Order of polynomial expression	Standard deviation of angular error
Secondary	0.145 degree
Tertiary	0.0297 degree
Quaternary	0.00596 degree

Development of Failure Resistance Onboard Processor

906C3836 Tokyo DAI33KAI UCHU KAGAKU GIJUTSU RENGO KOENKAI KOENSHU in Japanese
31 Oct-2 Nov 89 pp 758-759

[Article by Keiichi Yamasaki and Toshio Kikuchi, Nippon Electric Co.]

[Text] 1. Introduction

Given the increasing size of satellites and the growing complexity of their missions, it has become necessary to automate satellites and to provide for the self-containment of operations that used to be conducted by commands from earth. In keeping with these demands, it has become necessary to provide the satellite subsystem with intelligence. In such a satellite, any data processing failure would have a tremendous impact. Therefore, it is necessary to ensure that satellites are failure resistant. This report will describe a failure resistant onboard processor that we have developed for this purpose.

2. Outline

One way to prevent failure is to provide redundant systems. Variations of this idea include standby redundancy, comparison by two system operations, and majority by three system operations. In the standby redundancy scheme, when one-point failure is detected, the spare system is automatically activated. However, there is a fear that in this case an erroneous result will be output and that a suspension of processing occurs at switchover. The erroneous result is masked and is not output when the comparison method is used, but processing is suspended. The erroneous result is corrected and processing is continued when the majority scheme is used. Moreover, in contrast to static redundancy for masking the failure by majority and error correction codes under a fixed composition, a dynamic redundancy system recovers or degeneracy operates the detected or masked failure by the error correction signal, etc., under a composition that is capable of changing dynamically. Various levels of failure resistance are demanded for onboard processing according to the demand from the system for which the processor is used. The failure resistant onboard processor that we have developed can be used for a wide range of purposes. It is designed so that it is possible to freely establish its composition. This makes it possible to adopt the various redundant compositions mentioned above as well as the single system composition without redundancy. The appearance of the trial manufactured onboard processors is shown in Photo 1 [not reproduced].

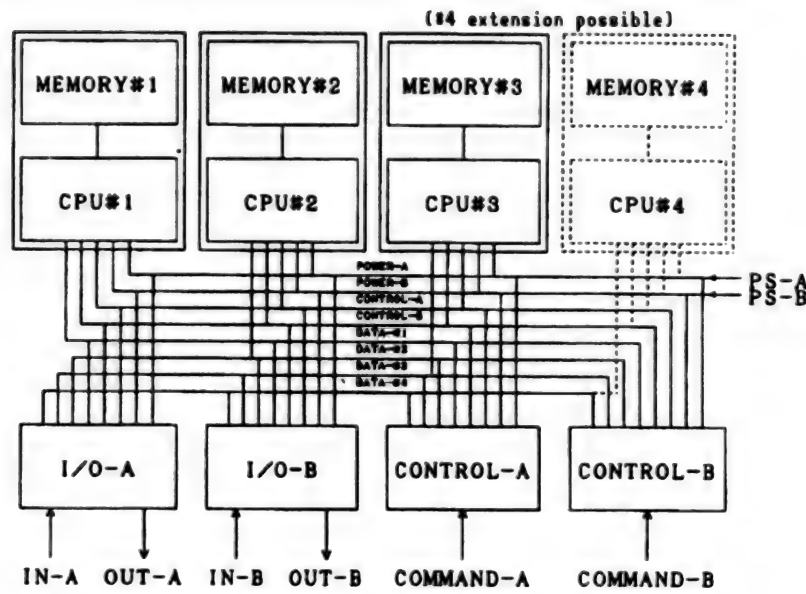


Figure 1. Block Diagram of Failure Resistant Onboard Processor

Both hardware and software techniques can be used to achieve synchronization among CPUs conducting the same processing by using several CPUs to ensure failure resistance. In the former case (hardware spacecraft), CPUs are synchronized by the same clock and results are obtained by the comparator or majority circuit of the hardware. Meanwhile, in the latter case (software technique), the CPU exchanges data with other CPUs via the software and conducts comparison or majority processing. When considering these methods for controlling a processor incorporated and used in a satellite subsystem, it is judged that the realization by hardware is most suitable from the point of view of software development and overload of CPU processing at execution.

3. Characteristics

A block diagram of this device is shown in Figure 1. This device consists of a maximum of four CPU modules (three CPU modules were packaged in the developmental model). Each CPU consists of the CPU board and memory board, and operations are synchronized with the clock supplied from the CONTROL module. An error correction scheme by positive coding is written on the RAM to provide for software corrective actions generated by radiation.

From the output signals generated by the four CPUs, the I/O module selects the output from only one CPU, conducts either the operation of output comparison of two CPUs or the operation of output majority of three CPUs and outputs to the output port. Moreover, in the case of input the I/O module outputs the signals imported from the input port to all CPUs. Since it is necessary to determine the redundancy composition scheme of the I/O module depending on the redundant composition of the other equipment to be connected, it is conducted by the I/O module unit.

The CONTROL module performs power input and disconnection, setting the redundant composition, etc., for each module, in addition to supplying the

synchronous clock for the entire device. The composition setting can be changed by an external command, by an internal failure detection signal or by the CPU software. It has become possible through this function to change the composition dynamically at the time of trouble generation according to the procedures incorporated in advance. Internal redundancy is provided on the synchronous clock generating circuit for failures of the CONTROL module itself, and it is also possible to prepare two systems for the entire CONTROL module and to switch over and use by command.

The main specifications of the developed model are shown in Table 1.

Table 1. Main Specifications for Developed Model (At 3 CPU)

Composition	CPU 3 systems, I/O 2 systems
CPU	Space CMOS 16 bit MPU used
CPU performance	0.82 MIPS (RTM) 0.24 MIPS (SGM)
Memory capacity (per CPU)	RAM 128K bytes ROM 4 KB bytes
Failure resistance technology	Duplicating comparison, triplicating majority Error correction coding, watchdog timer
Dimensions	W 270 x L 200 x H 130 mm
Weight	5.9 kg
Electricity consumption	24 W (maximum)

4. Conclusion

We plan to promote studies of the processor system, including software for actual satellite operation, based on the model we have developed.

Development of MUSES-A Attitude, Orbit Control Processor

906C3836 Tokyo DAI33KAI UCHU KAGAKU GIJUTSU RENGO KOENKAI KOENSHU in Japanese
31 Oct-2 Nov 89 pp 760-761

[Article by Takamoto Ninomiya, Space Science Laboratory; and Akito Watanabe,
Nippon Electric Co.]

[Text] 1. Introduction

There is an increasing demand for high-performance satellite equipment that reflects the growing pace of space development. Satellite equipment must meet stringent requirements for environmental resistance, small size, lightweight, and low electricity consumption. To satisfy the requirements for high performance amid such conditions and environments, an onboard 16-bit processor was developed in which the CPU and the peripheral circuits comprise a radiation-resistant space gate array. It includes a RAM with a 64K bit MOS, while the error correction coding circuit designed to cope with single event upset (SEU) of the RAM caused by radiation also comprises a space gate array. For this, a bipolar 16K bit ROM is used.

This processor incorporates the control unit and data memory of the optical navigation sensor (ONS). It will be used for the first time as an attitude and orbit control processor (AOCP) on the No. 13 scientific satellite that will be launched in January 1990. The appearance of this processor is shown in Figure 1 [not reproduced] and a block diagram is provided in Figure 2.

2. Composition of AOCP

2.1 CPU

The CPU has extended the basic floating-point instruction to the instruction set equivalent to the 16-bit microprocessor V30 made by the Nippon Electric Co. Moreover, it uses a space 16-bit MPU provided with a channel function at the microcommand level. The microcommand is planted in the four externally attached 16-bit ROMs. The clock operates at 6.29 MHz, while the operation speeds are 0.64 MIPS (real time mix) and 0.20 MIPS (Gibson mix).

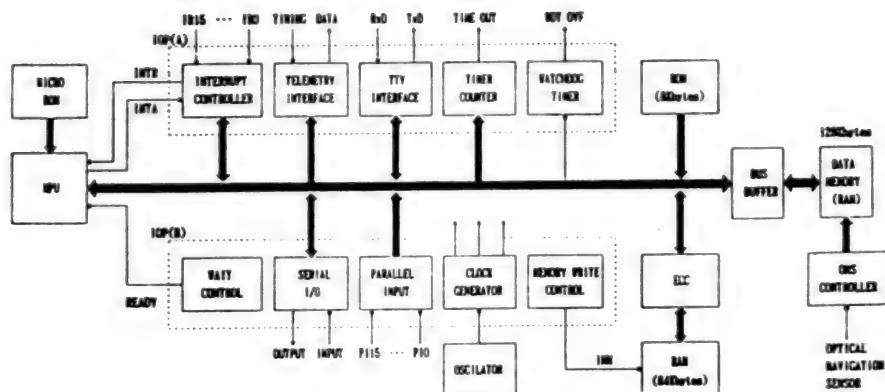


Figure 2. Block Flow Diagram of MUSES-A AOCP

2.2 Peripheral Circuit

A space LSI with the following functions was developed as the peripheral circuit of the CPU:

- (1) Interrupt control function. Conducts interrupt priority control and multiple interrupt control for 16 interrupt inputs.
- (2) Timer function. The resolution is 15.3 μ sec and an optional setting up to 1 sec is possible.
- (3) Watchdog timer function. A watchdog timer has been provided for the detection of software abnormalities.
- (4) WAIT control function. WAIT cycles of 0, 1, 2, and 3 cycles, respectively, can be inserted independently for the I/O and memory access commands.
- (5) Parallel input port. Possesses a function capable of reading one-word data on the parallel input port from the software.
- (6) Telemetry interface function. Reads out the telemetry data stored in the memory by the CPU channel function according to the telemetry timing signal and performs serial output.
- (7) TTY interface function. Used primarily for debugging or when conducting regulations test; also used for connecting to personal computers, etc. It is an asynchronous system and the bit rate is 9,600 bps/4,800 bps.
- (8) General purpose serial I/F. Used for serial I/O between the external hardware circuit. The port address is 6 bits and the data length is 16 bits.
- (9) Memory write inhibit function. Possesses a function capable of performing write inhibit setting at 4K byte units from the least significant address.
- (10) Clock generation. Generates various frequency clocks.

2.3 Memory

Packaging of ROM by 8K byte and RAM by 64K byte are made as the AOCP of MUSES-A. The RAM performs one-bit error correction and two-bit error detection. Moreover, a 128K byte RAM also has been provided as the optical navigation sensor memory.

2.4 Environmental Resistance

The AOCP of MUSES-A has undergone a continuous temperature test, vibration and impact tests, and a vacuum test. These are basic environmental tests. These tests confirmed that it functioned normally during launch and in the orbital environment.

2.5 Electricity Consumption

Electricity consumption reaches 9.5 W (maximum) when turning on the AOCP while operating the software.

2.6 Software

A real-time monitor was newly developed for the execution of the flight software. A floating-point arithmetic library was also prepared. In addition, a debugger was developed as part of the software development for the actual equipment.

3. Conclusion

The space gate array has made it possible to use LSIs for satellite equipment and a high-performance 16-bit processor has been developed. We expect that the processor will perform its functions for attitude and orbit control after the launch of the MUSES-A AOCP. Moreover, a further improved 16-bit processor based on this processor also will be used as the attitude (orbit) control processor in various other satellites, including SOLAR-A, GEOTAIL, ASTRO-D, and MUSES-B. We expect that this type of processor will be widely used in the future to provide satellites with artificial intelligence. In addition, we expect that this technology will be utilized also for more advanced processors, such as the SFU onboard processor, the DEP, etc.

References

1. "Attitude and Orbit Control Processor for MUSES-A and GEOTAIL," Proceedings of PISSTA, 1987.

Development of Small Data Handling Unit for Satellite Use

906C3836 Tokyo DAI33KAI UCHU KAGAKU GIJUTSU RENGO KOENKAI KOENSHU in Japanese
31 Oct-2 Nov 89 pp 762-763

[Article by Yoshinari Minami, Tadaaki Morimura, Makoto Otsuka, Hiroki Hinohara, Ryoichi Chiba, and Takeshi Orii, Space Development Headquarters, Nippon Denki Co.]

[Text] 1. Introduction

Experiments conducted in environments peculiar to space, such as in a vacuum or in a microweight environment, have attracted considerable attention in recent years. However, since experiments utilizing ordinary artificial satellites, space shuttles, or space stations are extremely expensive and require a long preparation period, it is difficult to conduct extremely small-scale experiments on a timely basis. This article describes a data handling unit (DHU) that we have developed for use on small satellites. This DHU is cheap and makes execution possible in a short period even though the scale of the experiment may be limited.

2. Example of Small Satellite

The small satellite shown in Figure 1 is a hexahedron where each side is about 30 cm. It weighs about 17 kg and it performs a spin axial control so as to complement the sun. Since the satellite itself is extremely small, launch requires only a small launching rocket. The small satellite itself does not have a body structure; rather, each component of the rectangular parallelopiped becomes a portion of the body structure. One of these rectangular parallelopipeds is allotted as the DHU.

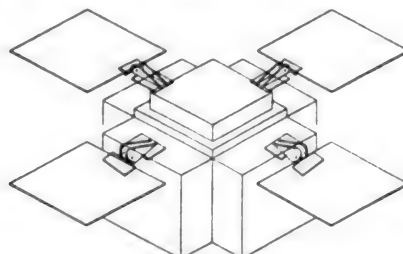


Figure 1. Small Hexahedron Satellite

3. Target Performance Levels of Small Satellite-Mounted DHU

The following values have been established as the target values for miniaturization, lightweight, and low electricity consumption. These conditions must be met if the device is to be mounted on a small satellite weighing only 17 kg.

External dimensions	198 x 198 x 40 (mm)
Weight	1.5 kg
Electricity consumption	1.4 W

In addition, since there are no restrictions on the purposes of small, 17 kg satellites, providing a general-purpose device has been established as another target.

4. Development Tasks for Target Achievement

The following were established as specific tasks in the DHU development process for achieving the targets cited above:

- Miniaturization through the use of LSIs and hybrid ICs.
- Creating appropriate software for the DHU function.
- Simplification of the method for connection with other components.
(Development of a data transfer protocol.)

5. BBM Development Technique

These development tasks have been realized concretely as follows.

5.1 Miniaturization through the use of LSIs and hybrid ICs

- Those suitable for LSI adoption

Space 16-bit CPU
Space I/O processor
Space 64K bit C-MOS RAM
Tiny bus interface (currently under development—to be described later)

- Those suitable for hybridization

Command interface

5.2 Creating appropriate software for the DHU function

Creating software for the DHU function was conducted as another technique for miniaturization.

- Software for the command issuance function
- Software for the telemetry collection/editing function
- Software for the mission data collection function
- Software for attitude control (spin axial control)

These electrical interface conditions and protocols have been systematized in the form of a tiny bus. The tiny bus interface is made by connecting the DHU and other components by three instrumentation lines only and data exchange is conducted with the specified bucket as the unit. This made it possible to achieve a dramatic reduction in the weight of the instrumentation.

6. BBM Development Results

At present, the BBM is in the process of being manufactured and confirmation of the hardware performance (especially the tiny bus interface) functions is nearing completion. The target values for miniaturization have been practically achieved. The layout of the experiment is shown in Figure 2 [not reproduced].

7. Note of Thanks

We express our thanks to Messrs. Sakurai, Oshima, and Sudo of the Nippo Denshi Co. for their cooperation in manufacturing the actual equipment and in other areas during the development of this DHU.

Rocket-Mounted Ku-Band TV Transmission Unit

906C3836 Tokyo DAI33KAI UCHU KAGAKU GIJUTSU RENGO KOENKAI KOENSHU in Japanese
31 Oct-2 Nov 89 pp 764-765

[Article by Tomoki Hayashi, Koji Yokoyama, and Hikaru Onishi, Space Science Laboratory; Masaki Kajikawa and Hideji Fukakura, Nippon Electric Engineering Co.; and Tadanao Kimura, Nippon Electric Co.]

[Text] 1. Introduction

A Ku-band TV image transmission unit was used for operational confirmation and security monitoring of the rocket during the flight of the M-3SII-No. 4 rocket (launched 20 February 1989). This rocket carried three CCD color camera units. Switchover to two-picture plane composition and one-picture plane transmission was made by the video switch. As a result, they succeeded for the first time in photographing the combustion and separation of the auxiliary booster, the first stage motor and the second stage motor; fairing opening; the attitude control state of the second-stage motor; and the actual separation of the third stage motor. This made it possible to obtain valuable image information. This report describes these systems.

2. TV Image Transmission Unit

A functional distribution diagram of this unit is shown in Figure 1. The image obtained by the three CCD camera units after conversion to an NTSC video signal is switched over to either a two-picture plane composition or one-picture plane transmission and sent to the transmitter. The transmitter directly FM modulates the Ku-band carrier wave by the image signal and sends it to the earth station. Transmission power is 2 W.

3. CCD Camera

A head separation-type camera using two-dimensional color CCD solid-state imaging elements was adopted for the camera. The number of imaging elements was about 200,000 pixels and it is assumed that the image is sent at a rate of 60 frames/second. The attachment position and angle of field of the three mounted cameras are shown in Figure 2. The heads of camera A and camera B have been attached in symmetrical positions for photographing the left and right auxiliary boosters and the angle of vision has been respectively set at an

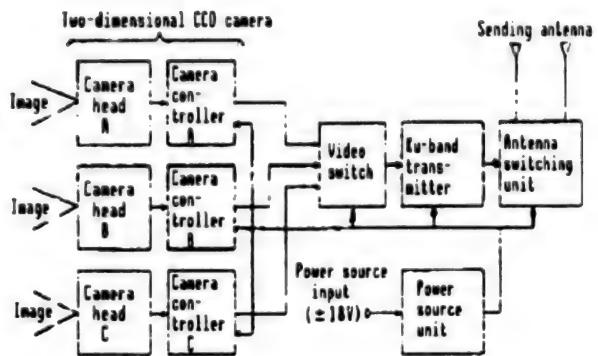


Figure 1. Functional Distribution Diagram of Onboard System

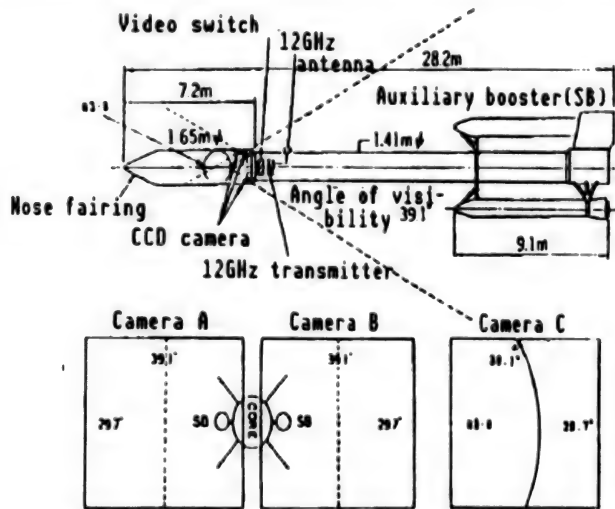


Figure 2. Attachment Position of 12 GHz TV Transmitter

angle of 20 degrees to the outer side from the rocket axis. Meanwhile, the head of camera C has been attached in a position about 30° in the CCW direction from the launcher position and has been set facing practically in an upward direction for photographing the separation state of the third stage motor. Moreover, the synchronization between camera A and B is conducted by the method of sending a synchronizing signal from A to B. Furthermore, a fixed lens was used for cameras A and C, and an automatic diaphragm lens was used for camera B.

4. Video Switch

After dividing the image signals of camera A and camera B into two picture planes, respectively, the video switch has the function of composing it into a one picture plane and the function of performing switchover to the independent image of camera C from the composition image of cameras A and B by receiving the signal of the video switch.

5. Ku-Band Zone Transmitter

The Ku-band zone transmitter consists of an oscillation unit, an FM modulation unit and a power amplification unit. The oscillation circuit adopts the transistor direct oscillation system for dielectric resonator (DR) control and a stability of 2×10^{-5} has been obtained. The modulation circuit is a direct FM system by the varactor diode that has been magnetically coupled to the DR and a modulation sensitivity of 4 MHz/V by transmitter input conversion has been realized. The power amplification unit consists of a GaAs-FET amplifier with four-stage composition. An output of 2 W has been obtained. The main specifications for this equipment are shown in Table 1.

Table 1. Main Performance Characteristics

	Item	Main performance characteristics
Camera	1. Imaging element 2. TV system 3. Resolution 4. S/N 5. Minimum subject illuminance 6. Transmission power	Interline CCD solid-state imaging element Pixels 199, 920 elements (Effective pixels 490 V x 384 H) Japanese Standard TV system Horizontal 285 TV lines Vertical 350 TV lines (field accumulation) More than 50 dB F 1.4, 2 Lux (practical range) 60 photos/second
Transmitter	1. Transmission power 2. Modulation system 3. Frequency 4. Frequency stability 5. Level of spurious signals 6. Modulation sensitivity	2 ± 0.4 W FM 12.8 GHz band Less than $\pm 1 \times 10$ Less than -60 dBc 4 MHz/V
Video switch	1. Number of channels 2. Switchover function 3. Crosstalk	3 systems (A, B, C) A. Switchover function between A and B composition image and C image B. More than 45 dB at 3.58 MHz

6. Conclusion

A composition photograph taken immediately after auxiliary booster separation by cameras A and B is shown in Figure 3 [not reproduced]. A photograph taken immediately after third stage motor separation by camera C is shown in Figure 4 [not reproduced]. The sequence of photographs showing the state of the rocket from third stage motor separation to ignition marked the first time such an effort was successfully completed. Effective results were available in the analysis of the separation mechanism and separation movements.

Current State of Development of Liquid Apogee Propulsion System (LAPS)

906C3836 Tokyo DAI33KAI UCHU KAGAKU GIJUTSU RENGO KOENKAI KOENSHU in Japanese
31 Oct-2 Nov 89 pp 766-767

[Article by Akira Takano, Hideyuki Kobayashi, Ideo Masuda, Kenichi Goto, and Hiroji Terada, National Space Development Agency of Japan; and Masakazu Sato, Takaichi Miyoshi, and Yuichi Hayasaka, Ishikawajima-Harima Heavy Industries Co., Ltd.]

[Text] 1. Introduction

The liquid apogee propulsion system (LAPS) will be mounted for the first time on the ETS-VI, which is scheduled to be launched by an H-II rocket in FY 1993, and is in the authorization test stage of its component parts while the entire system is in the detailed design stage. This paper reports on the present state and technological results of LAPS development.

2. Entire System

LAPS is a 2000N-thrust, two-liquid engine system. Its propellant consists of hydrazine and binitrogen tetroxide. It is also a dual-mode propulsion system that features a 50N-level hydrazine thruster system for attitude control.

The LAPS uses the blow down method to supply the engine and the thruster with propellant. Helium gas is used to pressurize the allege of the propellant tank for system simplification.

LAPS carries out apogee burn three times to disconnect itself from the main body of the satellite after the satellite has been put into stationary orbit.

3. Structure

LAPS is a modular propulsion system built by laying out and fixing a propellant tank, piping, and an engine system on a CFRP truss frame supplied by the maker responsible for development of the ETS-VI system. It is mounted on the lower part of ETS-VI. Figure 1 shows the piping system of the LAPS.

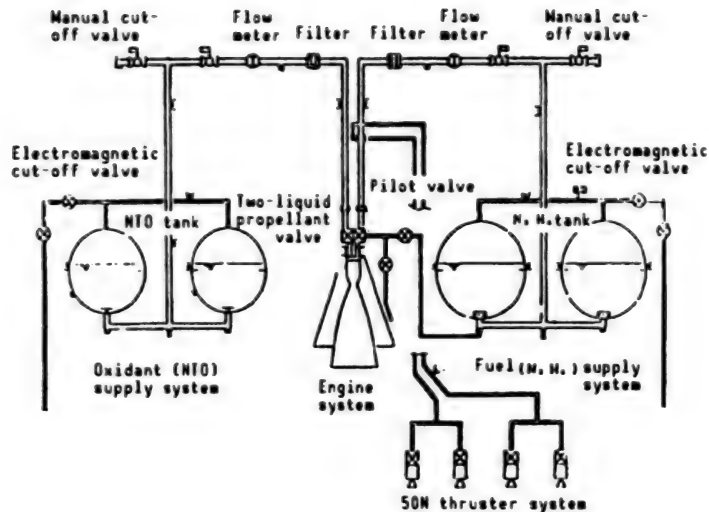


Figure 1. Piping System Diagram of Liquid Apogee Propulsion System

4. Parts Development

Of the main components of the LAPS the propellant filter, the cut-off valve, and the 50N propellant valve had been developed by July of this year. Meanwhile, Ti alloy propellant tanks (two kinds in total: one for hydrazine and the other for NTO), the 50N thruster, the apogee engine, the two-liquid propellant valve, and the flow meter are currently in preparation for authorization tests and are scheduled to be developed within this fiscal year.

5. Development of System Model

As part of the LAPS development program, a system electric model (SEM), a system development model-dynamic (SDM-D), and a thermal development model (TDM) have been produced and delivered to the companies in charge of system development.

Figure 2 [not reproduced] is a photograph of the LAPS SDM-D. It is about 3,400 mm in diameter.

6. Conclusion

The LAPS will pass sequentially through the stages of detailed design, battleship combustion tests, and captive combustion tests and ultimately to performance evaluation. The entire system is scheduled to be delivered to PFM in May 1991. The following companies' cooperation was indispensable to the development of the LAPS. We thank them deeply. Koito Manufacturing Co. (filter development), Fujikin Co. (manual cut-off valve development), Shimadzu Seisakusho (propulsion valve development), Dodwell & Co. (flow meter development), and Hakko Electric Manufacturing Co. (catalyzer layer sheath heater development).

Pop Tests of Apogee Engine for ETS-VI

906C3836 Tokyo DAI33KAI UCHU KAGAKU GIJUTSU RENGO KOENKAI KOENSHU in Japanese
31 Oct-2 Nov 89 pp 768-769

[Article by Yukio Kuroda, Makoto Tadano, and Masahiro Sato, Aviation Research Institute, Sumita; Hideyuki Kobayashi, National Space Development Agency of Japan; and Shigeyasu Iihara and Hiroyuki Ban, Ishikawajima-Harima Heavy Industries Co., Ltd.]

[Text] 1. Introduction

The Engineering Test Satellite VI (ETS-VI), which is scheduled to be launched by an H-II rocket into stationary orbit, will feature a liquid apogee engine that uses a storable propellant (N_2O_4/N_2H_4). This engine must be capable of a high level of performance, and engine research to date has indicated that it is possible to realize such a high-performance engine. However, various problems have occurred in developmental tests. One of these is the problem of high-amplitude vibration combustion (pop). Experiments related to pop were performed on several injectors used in the development of the two-liquid apogee engine and a wide range of data was acquired on combustion pressure and the injection-orifice standard Reynolds fuel number.

2. Samples

Table 1 shows the main features of the injectors used in the test and Figure 1 shows the main parameters of the J01 injector, which was used primarily in this test. The injector has many different two-jet collision elements (doublets) on two concentric rings and film-cooling orifices on the outermost ring. It has a thrust level of 2,000 N. The throat is equipped with various kinds of graphite IG-15 nozzles of different diameters that are inserted from the exit side of the nozzle and fixed. A responsive water-cooling pressure gauge was attached in the combustion chamber to measure the combustion pressure at the time of pop occurrence at high response. Accelerometers were attached to two positions in the axis direction on the back surface of the injector.

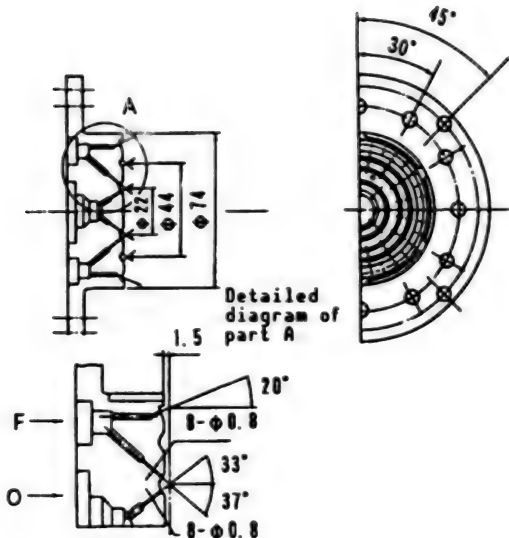


Figure 1. Main Parameters of J01 Injector

Table 1. Principal Features of Injectors

Code	No. of elements (inside/outside)	Fan angle of jet	dF/d0 (mm)	Film cooling rate (%)	No. of film cooling holes	Angle of film cooling hole	Remarks
J01	24(8/16)	0°	0.80/0.82	19.0	32	20° outside	
J02	24(8/16)	7° outside	0.80/0.82	19.6	32	20° outside	
J03	24(8/16)	0°	0.80/0.82	15.6	32	20° outside	
J13	30(10/20)	0°	0.63/0.63	17.0	40	20° outside	
J14	30(10/20)	0°	0.69/0.69	16.1	40	20° outside	
J17	30(10/20)	7° inside/outside alternately	0.69/0.69	18.5	40	20° outside	
J21	30(10/20)	0°	0.67/0.67	21.0*	40	40/20	*S/N:003

3. Test Results

To make it possible to draw inferences from Lawver's jet separation standard, a correlation was obtained between the Reynolds number for the fuel jet (Ref) and the combustion pressure (\bar{P}_c). Figure 2 shows the results of the test. Five kinds of combustion chamber nozzle diameters (D_{th}) were used in the test. As shown in the figure, it was found that pop often occurs at high combustion pressure and high jet speed, but that it diminishes as the number of core elements increases. These results differ from the research results obtained by J. Houseman¹ and L.B. Zung² in the 1970s. Furthermore, the results obtained for the J02 injector, whose cooling rate is greater than that of the J01, show that pop is somewhat easier to produce as the injector orifice diameter and film cooling level increase. As shown in Figure 3, the number of pop occurrences decreases as the combustion pressure becomes smaller, but conversely that the acceleration and the peak value of combustion pressure at the time of pop occurrence are increased. Figure 4 shows the combustion pressure and the popping area on the propellant temperature plane. This figure shows that pop occurs at a combustion pressure higher than the vapor pressure of N_2O_4 .

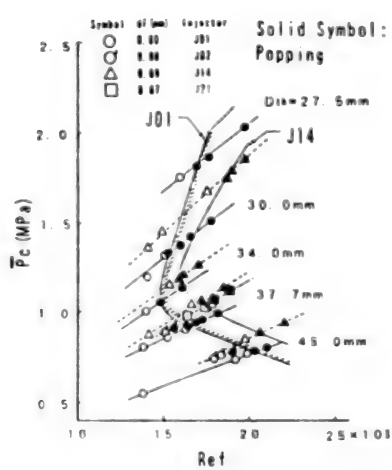


Figure 2. Ref Vs. \bar{P}_c

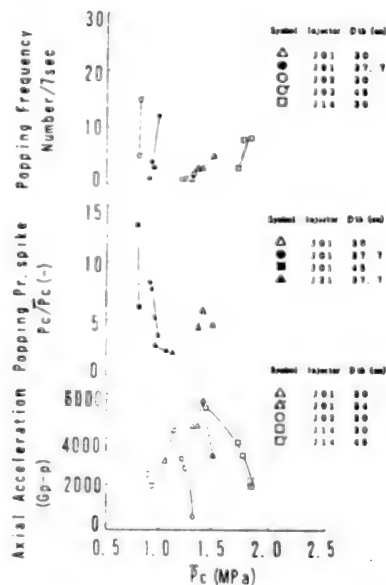


Figure 3. \bar{P}_c Vs. G, P_c/\bar{P}_c , Popping Number

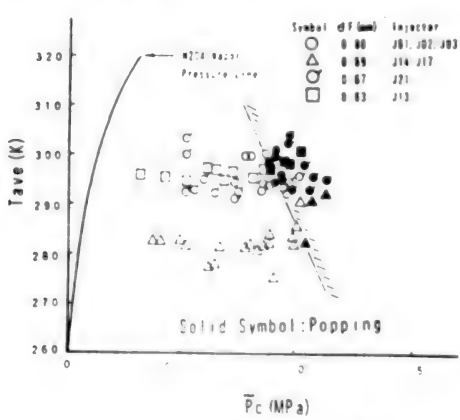


Figure 4. \bar{P}_c Vs. Tave

4. Conclusion

The correlation with jet separation will be examined by comparing the test results of a single-element injector that has the same parameters as those of the injector which was used in the test and those of a multi-element injector.

References

1. Houseman, J., et al., "Popping Phenomena With the Hydrazine Nitrogen-Tetroxide Propellant System," J. SPACECRAFT, Vol 9 No 9, September 1972.
2. Zung, L.B., et al., "Combustion Process of Impinging Hypergolic Propellants," NASA CR-1704, May 1971.

Development of Liquid Apogee Engine for ETS-VI

906C3836 Tokyo DAI33KAI UCHU KAGAKU GIJUTSU RENGO KOENKAI KOENSHU in Japanese
31 Oct-2 Nov 89 pp 770-771

[Article by Kazuo Kusaka, Tatsuo Kumagai, and Katsuto Kisara, Aviation Research Institute, Sumita; Akira Takano and Hideyuki Kobayashi, National Space Development Agency of Japan; and Shigeyasu Iihara and Joji Umeda, Ishikawajima-Harima Heavy Industries Co., Ltd.]

[Text] 1. Introduction

A previous report¹ described the results of evaluating the specific thrust performance and thermal features of the selected apogee engine. Two problems, however, were that the temperature at the constricted part, which is upstream from the combustion chamber throat, is higher than the temporary upper limit temperature and that the shock at the time of ignition is too large. The actual apogee engine must be capable of extended combustion and reignition. Therefore, these problems are important subjects for study in evaluating engine durability. In order to measure these problems, the length of the combustion chamber, injector parameters, and the design of the propellant valve were changed. This report describes the test results.

2. Sample Engine

Table 1 shows the form of the engine that was tested and Table 2 shows the main parameters of the injector that was used. The major differences between the two injectors listed in Table 2 are, first, the jet angles of the J21 injector are 20 and 40 degrees alternately, but are 32 degrees for all the holes of the J16, and second, the orifice diameter of the core element is about 7.5 percent larger for the J21 than for the J16.

3. Test Results

(1) Change of combustion chamber length

Based on the known fact that combustion chamber wall temperature can be lowered by making the combustion chamber length shorter if a drop in performance is acceptable, tests were performed with a J21 injector whose combustion chamber was shortened from 100 mm to 76 mm. Figure 1 shows the

Table 1. Test Configuration

Injector	J21	J21	J16
Combustion chamber length	100 mm	76 mm, 100 mm	76 mm
Nozzle	Flange connection type	Flange connection type	General type
Propellant valve	F-led	O-led	O-led

Table 2. Principal Injector Parameters

	J21	J16
Oxidant core orifice diameter	$\phi 0.67$ mm	$\phi 0.73$ mm
Fuel core orifice diameter	$\phi 0.87$ mm	$\phi 0.72$ mm
Film cooling orifice diameter	$\phi 0.32$ mm	$\phi 0.29$ mm
Film cooling jet injection angle	$20^\circ/40^\circ$ alternately	32°
Film cooling rate	21.1~22.5%	21.4%

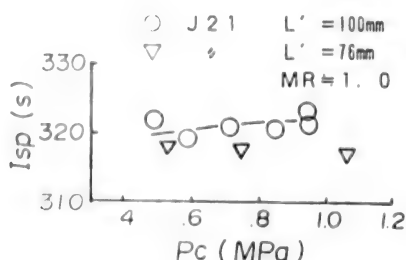


Figure 1. Comparison of Combustion Chamber Length Vs. Performance

results. The specific thrust of target 317s was obtained and the temperature of the combustion chamber was also held within the allowable temperature range. In this test, however, the containing swelled at the exit part of the internal wall of the throat. The cause of this swelling is thought to be as follows: The shortened combustion chamber length caused insufficiently mixed core element fan flow to collide with decomposed hydrazine from the film cooling flow, a hot spot occurred, and unfirm components in the coated surface layer exfoliated and flowed out because the film cooling flow was not sufficiently blocked. The basic material was not damaged, but this combination poses a durability problem.

(2) Change of injector and heat shield

To overcome the malfunction described above, the injector was reviewed and the J16 was adopted (Table 2). Furthermore, the heat shield was improved to make

the opening larger and to lower the rise of combustion chamber wall temperature (Figure 3). The broken line in Figure 2 shows the shape of the heat shield that was used in this experiment. Figure 3 shows that the specific thrust was roughly the same as that for the J21 with a 76 mm combustion chamber, about 317s on the average. Figure 4 shows the data on combustion chamber wall temperature. It indicates that the throat wall temperature (TWA) is higher than the sea-surface altitude data, but the values for the constricted part wall temperatures (TWAB) were about the same level and were sufficiently below the allowable temperature.

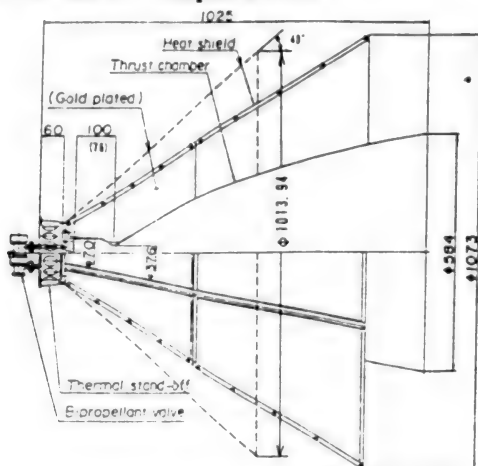


Figure 2. Cutaway Diagram of Apogee Engine

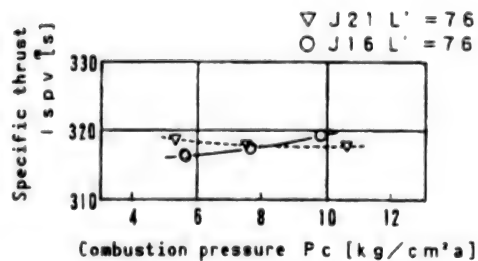


Figure 3. J16 Performance

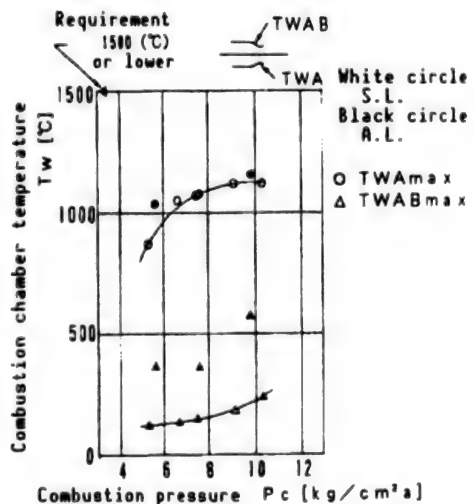


Figure 4. J16 Combustion Chamber Wall Temperature

4. Conclusion

- (1) Using a J16 injector and a 76 mm combustion chamber made it possible to attain an average specific thrust of 317s and demonstrated that it is possible to lower the temperature of the combustion chamber wall. Although not shown here, it was found that the temperature of the throat and the constricted wall

tended to rise sharply during the last stage of combustion (near 160s). The cause cannot be identified and we believe that combustion tests for a longer period of time will be necessary to make such a determination possible.

(2) The tests confirmed that the shock at the time of ignition was sufficiently below the allowable value of 500 G_{p-p} in terms of acceleration. This improvement is due to a switch from a fuel-led ignition sequence to an oxidant-led sequence together with a change in the design of the propellant valve.

References

1. 32nd Space and Technology Conference, 2 October 1988.
2. Aerospace Society's Northern Branch Conference, May 1989.

Extended Test of Mixed-Fuel Reproduction Cooling Engine

906C3836 Tokyo DAI33KAI UCHU KAGAKU GIJUTSU RENGO KOENKAI KOENSHU in Japanese
31 Oct-2 Nov 89 pp 772-773

[Article by Hiroshi Miyajima, Shuichi Ueda, Noboru Sakuranaka, and Takayuki Sudo, Sumita Branch Office, Aviation Research Institute; and Katsuaki Kosaka and Takuo Kuwahara, Nissan Motor Co.]

[Text] 1. Introduction

It has been confirmed that a fuel consisting of a hydrazine-MMH mixture yields a high specific thrust when used in a pressurized gas supply reproduction cooling engine.¹ For practical use in a rocket engine, however, high safety and reliability as well as high performance must be assured. This paper reports on the possibility and problems involved in developing a practical mixed fuel reproduction cooling engine based on measurements of the thermal environment of the engine. These results were obtained by performing extended tests using an improved reproduction cooling combustion chamber.

2. Fuel and Samples

The fuel, injector, and high-expansion nozzle operate at a thrust level of 2000N. These components have been used previously in mixed fuel reproduction cooling engine tests. The fuel consists of 80 percent hydrazine and 20 percent MMH by weight. The injector is a collision-type device that consists of two different jets. Its film cooling rate is 15 percent and the opening ratio of the high-expansion nozzle is 240:1. Combustion tests were performed in a high-altitude combustion test facility. The reproduction cooling burning was improved in several ways in preparation for extended combustion tests. The principal improvements are 1) the reproduction cooling area was expanded on the injector side to prevent the injector from being heated, and 2) the manifold for the entry and exit for reproduction cooling was made smaller in order to increase the flow rate and to reduce the remaining fuel in the cooling groove. Figure 1 depicts the test engine.

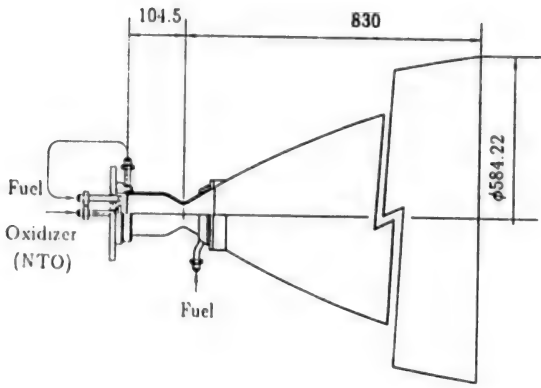


Figure 1. Reproduction Engine (Opening ratio: 240:1)

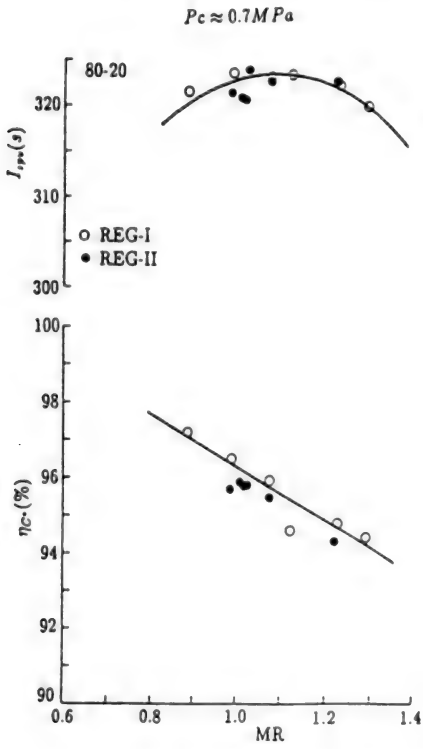
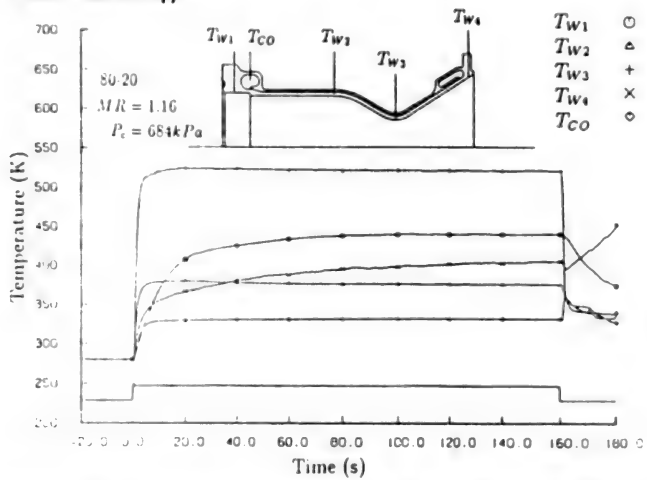


Figure 2. Dependence of Performance on Mixing Ratio
REG-I: Burner before improvement
REG-II: Burner after improvement

3. Test Results

Performance evaluation tests were performed for 30 seconds of combustion time. Figure 2 shows the dependence of performance on the mixing ratio. The vacuum thrust reaches a maximum as the mixing ratio approaches 1:1, yielding a thrust of 322 s or more. There was no difference in performance depending on changes of the burner. Popping occurred in areas other than those expected and the injector can be identified as the probable cause of popping.² Extended combustion tests were performed for 160 seconds of combustion time. Performance

becomes steady after a combustion time of 15 seconds. Figure 3 shows the change in temperature of each part of the burner over time. The temperature of the flange parts of the injector and nozzle rise continuously during the 160 seconds combustion time, but reach an almost stationary state without showing a sudden change. The temperature of the burner wall is below 550 K even in the throat. This temperature level is more than low enough for conventional structural materials. Reproduction cooling using hydrazine is dangerous because an explosion can occur inside the cooling manifold after combustion stops. But no such symptoms were seen in this experiment, which reflects the effectiveness of fuel mixing.



**Figure 3. Change in Temperature of Each Burner Part Over Time
(Measured at a distance of 1 mm from the internal wall.)**

4. Summary

- (1) Extended combustion tests using a mixed fuel reproduction cooling burner confirmed that such an engine is suitable for practical use.
- (2) The performance and the temperature of each part of the engine became almost stationary over a combustion time of 160 seconds.
- (3) An accurate method for predicting the occurrence of popping needs to be established.

References

1. Ueda, et al., 32nd Space Science and Technology Conference, 1988.
2. Ueda, S., Miyajima, H., and Kuwahata, T., IAF 89-286, 40th IAF Spain, 1989.

Dynamic Characteristics of LE-7 Liquid Acid Pump

906C3836 Tokyo DAI33KAI UCHU KAGAKU GIJUTSU RENGO KOENKAI KOENSHU in Japanese
31 Oct-2 Nov 89 pp 774-775

[Article by Takashi Shimura, Mitsuo Watanabe, Yoshiaki Watanabe, and Satoshi Hasegawa, Sumita Branch Office, Aviation Research Institute]

[Text] 1. Introduction

Among the most important data for POGO vibration analysis of the H-II rocket and design of a POGO vibration suppressing device are the dynamic characteristics of the LE-7 engine liquid acid pump. The authors are performing tests for the purpose of investigating response characteristics with pulsating motion given to the pump to obtain this data. We have previously reported the results obtained by laying out a piston pulser at the pump entry and measuring the dynamic flow rate at the main pump exit line as preliminary test results. Subsequently, we have laid out an active POGO suppressing device (APSD), which acts as a piston pulser at the same time, at the pump entry line. We have also laid out a slit-type pulse generating valve at the main pump exit line to give pulsation to the pump. We have performed tests to measure the dynamic flow rate and dynamic pressure at the pump entry line, the main pump exit line, and the preburner pump exit line. This paper describes the results of these tests.

2. Test Equipment and Samples

Figure 1 is a system diagram of the test equipment. APSD absorbs pulsation by putting the piston into or pulling it out of the line branch part with oil pressure. Therefore, APSD becomes a pulse generator or a pulse absorber depending on its direction of operation. Figure 2 shows the structure and principal features of the sample that was used in the tests.

3. Test Results

Figure 3 shows the vibration pressure of each part when the pulse generating valve of the main pump exit line is operated alone and when the valve is operated in combination with the APSD. The APSD was operated only in a sine wave mode at the same frequency as the pulse generating valve while the phase was being changed, but an effect can be seen in suppressing vibration at the entrance. A further effect can probably be produced by feeding back the

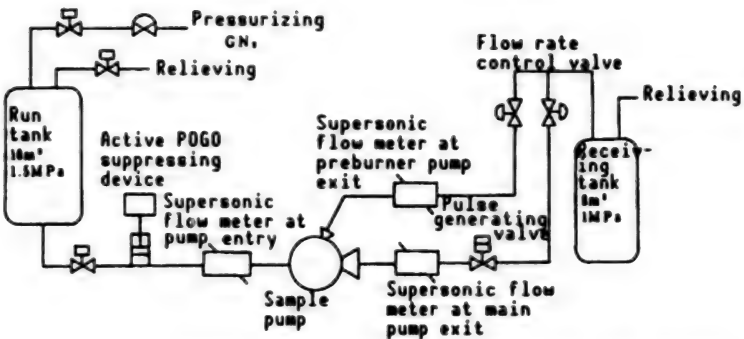


Figure 1. System Diagram of Test Device

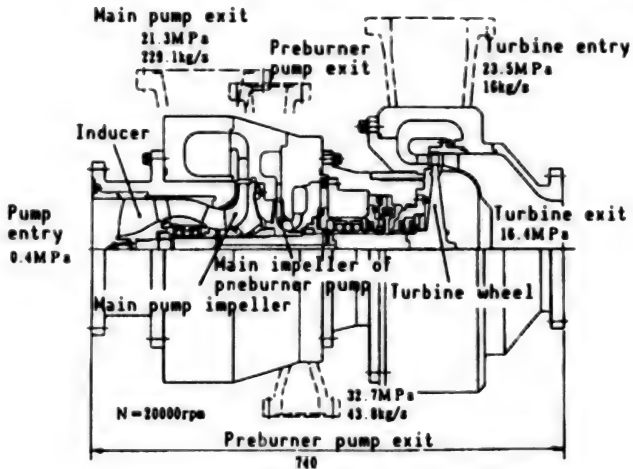


Figure 2. Structure of Test Device and Principal

vibration pressure signal to the oil pressure driving system of the APSD, but this is a subject for future study.

Figure 4 shows the vibration pressure and flow rate fluctuation amplitude for each part when excitation is produced by the pulse generating valve operating alone while the frequency was being changed. In addition, mutually independent data were obtained by causing the pump to pulsate by exciting the APSD alone.

Figure 5 shows the results of Z_{12} component tests when the dynamic characteristics of the main pump is represented by a 2×2 transfer matrix, from expression (1). Pressure valves were divided by twice the circumferential speed at the head of the impeller and the flow rate values were divided by the flow rate—which makes the speed triangle similar to the designed points—to obtain dimensionless values that can easily be ranked.

$$Z_{12} = (\tilde{h}_2 - \tilde{h}_1) / \tilde{Q}_1 \quad (1)$$

where, \tilde{h}_1 : vibration pressure at pump entrance
 \tilde{h}_2 : vibration pressure at pump exit
 \tilde{Q}_1 : fluctuating flow quantity at pump entrance

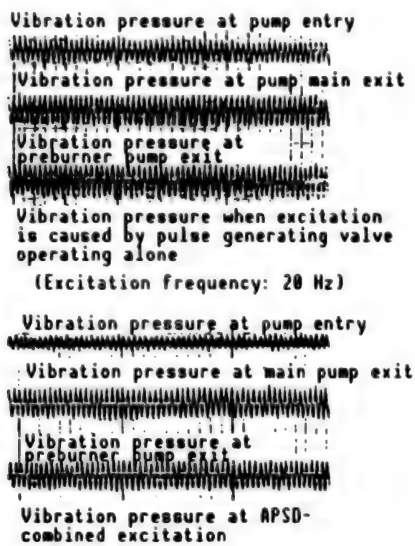


Figure 3. Effects of APSD

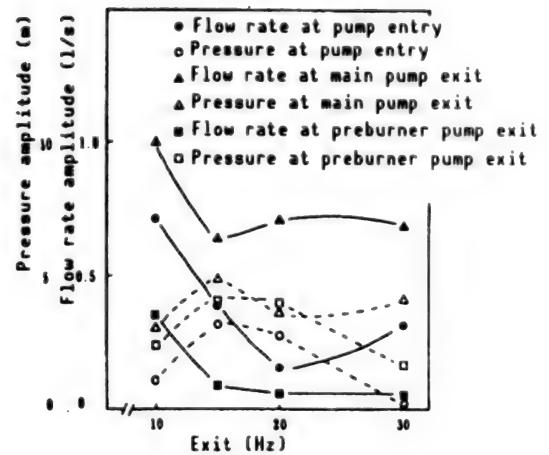


Figure 4. Change of Amplitude as a Function of Frequency

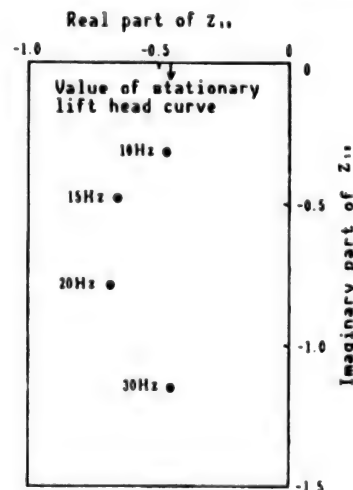


Figure 5. Results of Z_{12} Component Tests

Since the data is test data whose cavitation coefficient is large, $Z_{12} = -R_p - j\omega L_p$ (j : imaginary unit, ω : angular frequency) if it is assumed that cavitation compliance C_b and mass flow gain M_b are both 0 and pump dynamic gain $(1+\mu)$ is 1, and the model which represents the pump transfer matrix is thought of with C_b , M_b , $1+\mu$, pump resistance R_p , and pump inertance L_p . As shown by the real parts in Figure 5, test results of R_p are larger than the values of the stationary head curve at 15 and 20 Hz and are near to the values at 10 and 30 Hz. The imaginary elements in Figure 5 increase in proportion to frequency and L_p shows largely constant values.

Simulation of LE-7 Activation Transient Characteristic (V)

906C3836 Tokyo DAI33KAI UCHU KAGAKU GIJUTSU RENGO KOENKAI KOENSHU in Japanese
31 Oct-2 Nov 89 pp 776-777

[Article by Akio Kanmuri, Takeshi Karita, and Yoshio Wakamatsu, Sumita Branch Office, Aviation Research Institute; Yoshihiro Torii, Takashi Saito, Kazuhisa Kitakura, Masashi Okada, and Takayuki Inoue, National Space Development Agency of Japan; and Keiichi Hasegawa, Mitsubishi Heavy Industries]

[Text] 1. Introduction

Development tests on the LE-7 prototype engine are in progress. To assess the transient characteristic, an activation sequence was established. In particular, the activation and stop times were shortened, and this produced good results. For this experiment, we updated the previously reported LE-7 activation transient characteristic calculation program and examined the activation and stop transient characteristic for development tests. To make the activation time shorter, earlier valve opening timing and realization of quick and stable ignition of the burner are needed. In the simulation calculation used to examine an appropriate sequence, the input of precise element characteristic data and accurate estimates of ignition timing are required. This paper outlines these necessary elements.

2. Engine Schematic and Activation Sequence

The primary control valves are the main fuel valve (MFV), the main oxidant valve (MOV), and the preburner oxidant valve (POV), each of which is provided with openings that are classified as full open and 0/7 to 7/7 (Figure 1). POV has been improved to make the opening process smoother. A high-pressure precooling valve (FCHV) is provided to improve stop transient characteristics. The conventional activation sequence is to ignite the main burner and perform preburner ignition after the expander mode has become stable. But in this experiment we adopted a sequence in which the preburner is ignited immediately after ignition of the main burner to shorten activation time.

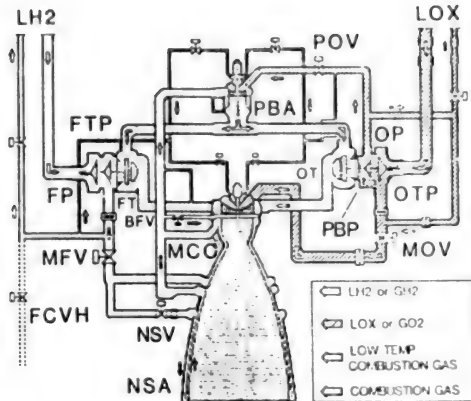


Figure 1. Prototype Engine Schematic

3. Results of the Examination

(1) Influence of MOV/POV opening timing

Figure 2 compares the conventional activation sequence with the results obtained by using the new one (about 65 percent load). Compared to the conventional sequence (a), the sequence adopted this time (b) advances the opening timing of the MOV and POV and, at the same time, raises the O/F immediately after activation by extending the MFV travel time. As a result, quick and smooth activation was achieved.

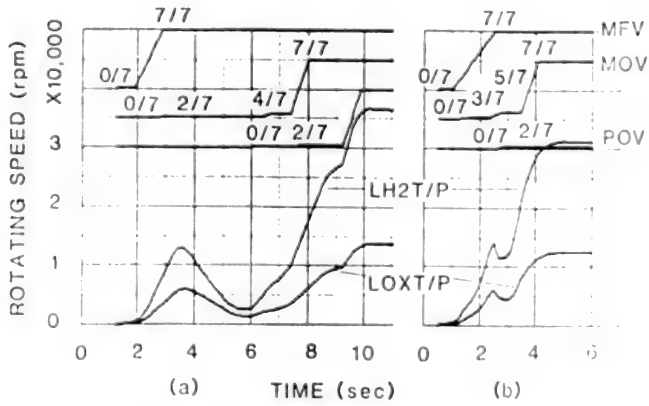


Figure 2. Comparison of Activation characteristics (Simulation)

(2) Influence of MFV travel time

Figure 3 shows the influence exerted on the activation process by the MFV travel timing during partial load operation (65 percent). Rises can be advanced by appropriately extending the MFV travel time (a). IG FLAG represents ignition timing.

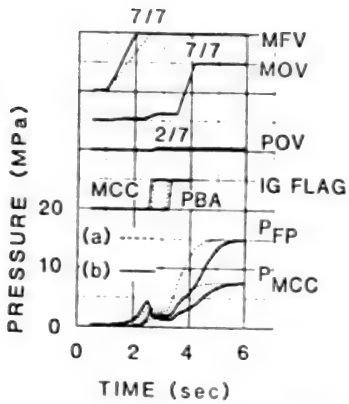


Figure 3. Influence of MFV Travel Time

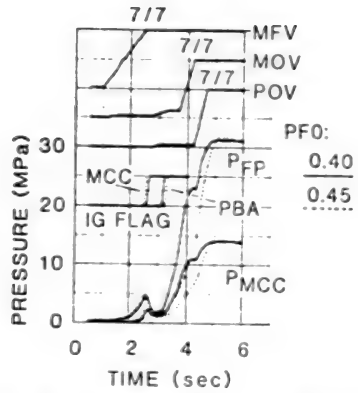


Figure 4. Influence of LH_2 Tank Pressure ($P_{00}=0.7 \text{ MPa}$)

(3) Influence of tank pressure

Figure 4 shows an example of the influence of LH_2 tank pressure (PFO). When LH_2 tank pressure is high, there is an early rise of the expander mode, but it is in the direction of suppressing the preburner mixing ratio. Therefore, the rise of the two-stage combustion cycle is delayed, as shown in the figure.

(4) Rating level simulation

Figure 5 shows the results of the simulation, which supposes a rating level test. Figure 6 shows the data for a 90 percent (Tashiro) load test of the prototype engine for reference.

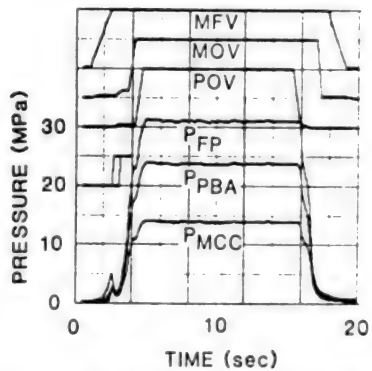


Figure 5. Rating Level Simulation

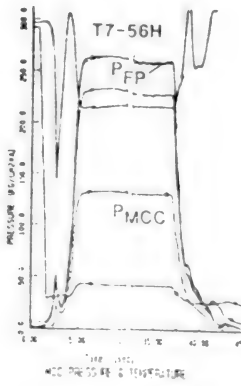


Figure 6. Test Results of Prototype Engine (90 percent load)

4. Conclusion

The activation sequence of the LE-7 prototype engine is thought to be virtually established. There are plans to use a simulation to examine the stop characteristics and the transient characteristics at off-nominal times. The calculation program needs to settle several problems, such as precision settings for engine parameters, and will be further improved.

Model for 'Ionosphere Hole' Generation With Rocket Exhaust Products

906C3836 Tokyo DAI33KAI UCHU KAGAKU GIJUTSU RENGO KOENKAI KOENSHU in Japanese
31 Oct-2 Nov 89 pp 778-779

[Article by Yoshiki Yamagiwa, Junior College of Engineering, Shizuoka University; Yoshio Ishikawa, Faculty of Science and Engineering, Nihon University; and Takashi Nakajima, Graduate School, Nihon University]

[Text] 1. Introduction

It will be unavoidable in the near future, as the scale of space development is, that an increasing number of new rockets that have never been used before will come into use. Thus, rocket exhaust products will become important in terms of their quantity and energy when compared to the component particles of the earth's periphery and can influence the near-earth environment in various ways.

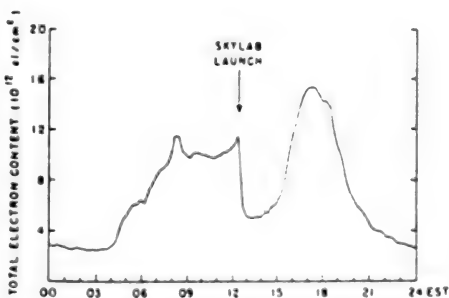


Figure 1. Example of Ionosphere Hole Phenomenon Measurement

One of these is the phenomenon known as the "ionosphere hole." This phenomenon was observed when Sky Lab I was launched on 14 May 1973. It was noticed that the number of electrons in the ionosphere decreased dramatically across a diameter of 1,000 km or more following the lift-off orbit of Sky Lab I and 4 hours or more were needed for recovery (Figure 1).¹ Along with this phenomenon, a fault occurred that disturbed communications between the ground and the satellite for several hours. If this phenomenon were to continue for a long time on a large scale, the impact on the earth's environment would be very large. The degree of the impact exerted on the environment by rocket exhaust products will become an important standard in the selection of thrusters and

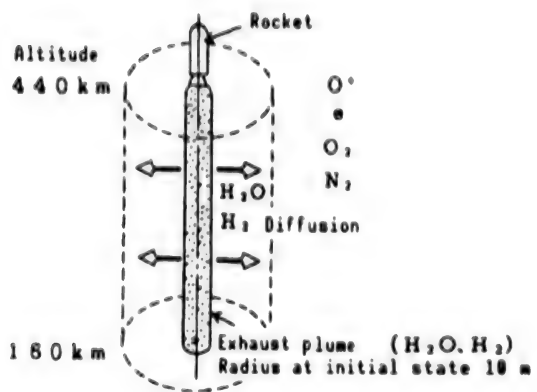


Figure 2. Diffusion Model of Rocket Exhaust Plume

propellants and in the determination of operating methods in the age of mass rocket use. An important task for the new age will be to clarify the generation and disappearance mechanisms of the "ionosphere hole."

This phenomenon has been examined by M. Mendillo¹ and J. Zinn² with various methods ranging from a simple model to complex numerical calculations, but no definitive model has been produced. This paper presents a simple model as the first step in analyzing this "ionosphere hole" and attempts to provide an overall understanding of this phenomenon.

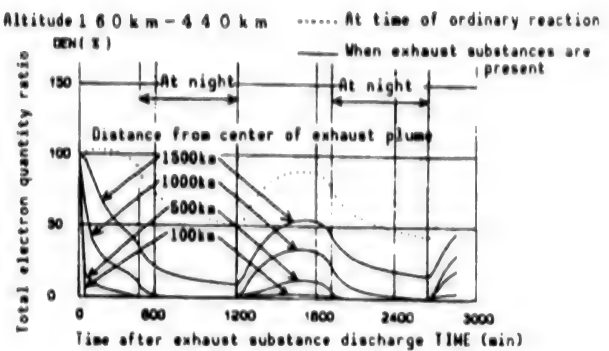
2. Ionosphere Hole Model

The electron density in the ionosphere is determined by the balance between the disappearance of ions through in-atom exchange and dissociation and recombination reactions between particles (N_2 and O_2) and ions and electrons in the ionosphere, and the generation of electrons with solar radiation absorption. When rocket exhaust products are added, electron disappearance by ion-atom exchange and dissociation and recombination reactions with the exhaust products (H_2O_2, H_2) is added to the ordinary reactions mentioned above. It is assumed that rocket exhaust products spread in the radial direction according to a cylindrical diffusion pattern (Figure 2) and that they decrease due to reactions with surrounding particles, ions, and electrons. The particle densities of N_2 and O_2 and electron density at each altitude in the initial state before rocket exhaust products are added were obtained from the atmosphere data of CIRA 1972. Diffusion of exhaust products and electrons in the altitude direction and the influence of wind were not taken into consideration.

3. Analysis Results

Figure 3 shows the results of temporal change analyses of the integral quantity of electron densities in the altitude direction in the case where exhaust products from the second stage of a Saturn V rocket ($H_2: 3.3 \times 10^{27}$ molecules/second, $H_2O: 7.3 \times 10^{27}$ molecules/second) were uniformly scattered at an altitude of 160-440 km (space consisting of ionospheres F1 and F2). The quantity of electrons before the exhaust products were added was set at 100 percent and the time the exhaust products were discharged (EST 12 h 35 mn) at 0 min.

Figure 3. Analysis Results: 1
(Change of total electron quantity over time)



The ionosphere hole is generated because the ion reaction speed is four orders of magnitude faster for H_2O and H_2 than for ordinary N_2 and O_2 . When there is no wind and no diffusion in the altitude direction, 50 percent or more of the electron decrease occurs within a radius of 1,500 km from the center of the exhaust plume and almost no recovery occurs for 30 hours or more in the area closest to the center (about 500 km from the center).

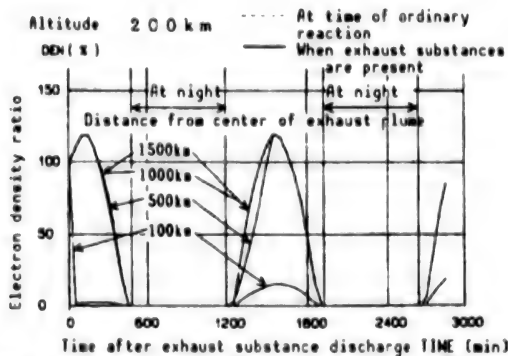


Figure 4. Analysis Results: 2
(Electron density at an altitude of 200 km)

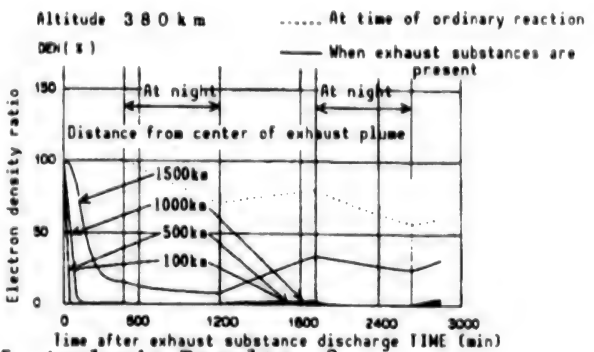


Figure 5. Analysis Results: 3
(Electron Density at an altitude of 380 km)

Figures 4 and 5 show analysis results of the temporal changes of electron density at altitudes of 200 and 380 km, respectively. A comparison of these two figures shows that the influence of electron decrease is larger in space where the background particle density is smaller, electron density is greater and the altitude is higher. It is believed that the diffusion in the altitude direction is an important element in the actual phenomenon because electron density shows a large difference in the altitude direction. At present, work is under way on a model in which the diffusion of exhaust products and electrons in the altitude direction is accounted for.

References

1. Mendillo, M., Hawkins, G.S., and Klobuchar, J.A., "A Sudden Vanishing of the Ionospheric F Region Due to the Launch of Skylab," JOURNAL OF GEOPHYSICAL RESEARCH, Vol 80 No 16, 1975, pp 2217-2228.
2. Zinn, J. and Sutherland, D., "Effects of Rocket Exhaust Products in the Thermosphere and Ionosphere," SPACE SOLAR POWER REVIEW, Vol 1, 1980, pp 109-132.

Dynamic Characteristics of CW Laser Thruster

906C3836 Tokyo DAI33KAI UCHU KAGAKU GIJUTSU RENGO KOENKAI KOENSHU in Japanese
31 Oct-2 Nov 89 pp 780-781

[Article by Hideki Moriai, Graduate School (Atomic Power), University of Tokyo; and Hiroshi Ohashi, University of Tokyo]

[Text] 1. Introduction

In a CW laser propulsion system, the stored propellant gas is heated by a high-power laser installed on the ground or in space, and the increased enthalpy is converted into kinetic energy using a nozzle to produce thrust in space. Unlike conventional chemical and electric rockets, this scheme is not limited by the specific thrust of a chemical reaction; its thrust can be made larger by increasing the laser power. Future use as an interorbit transport propulsion system is being considered because no heavy power source is necessary. Figure 1 depicts the concept.

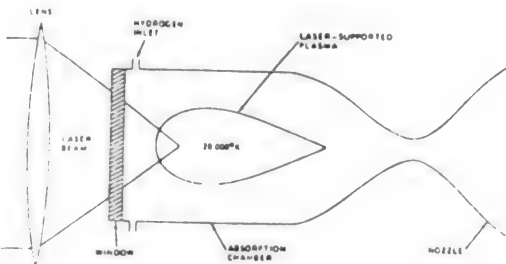


Figure 1. Concept of a Laser Engine¹

A high-temperature laser plasma is created near the focus of laser beam. Radiation from the plasma is absorbed by making a buffer gas flow around the plasma. In this way, the wall surface temperature can be kept low and the plasma temperature can be made high. When conducting research on a laser engine, it is necessary to understand the property of the plasma in the combustion chamber, the temperature around the plasma, and the flow field distribution. Hydrogen is an effective propellant for an actual engine, but in our research we used argon, which makes it possible to analyze the axially symmetric temperature field and the flow field around the plasma.

2. Model and Equation

The problem of maintaining a constant environment in one section of the combustion chamber, as shown in Figure 1, was solved with a cylindrical coordinate system.

- If (1) fluid flow in the radial direction is ignored;
(2) the pressure field is constant; and
(3) an optically thick plasma and heat transportation by radiation approximated with radiation conduction are assumed;

then the equation to be solved is only an energy equation in which the physical property values depend on temperature:

$$\rho C_p(T) \frac{\partial T}{\partial t} = \frac{\partial}{\partial z} (\lambda(T) \frac{\partial T}{\partial z}) + \frac{1}{r} \frac{\partial}{\partial r} (r \lambda(T) \frac{\partial T}{\partial r}) - u \rho C_p(T) \frac{\partial T}{\partial z} + \alpha I - R = 0$$

where, ρ : density; C_p : specific heat at constant pressure; t : time; z : axial distance; λ : thermal conductivity (conduction + radiation conduction); r : radial distance; u : axial speed; α : laser absorption factor; I : laser intensity; and R : radiation loss

The above equation was calculated by the SOR method.

3. Results

Figures 2 to 5 show actual calculations obtained on a scale smaller than the actual engine. Figures 2 and 4 show the temperature fields when the laser output is 5 kW and 8 kW, respectively. Figures 3 and 5 show speed distribution. Isotherms are drawn at nearly 1,000° intervals. In this calculation, the following values were assumed: length of combustion system: 20 cm; radius: 2 cm; laser radius: 1 cm; focal length: 7.5 cm; pressure in engine: 1 atm; inflow gas temperature: 300 K; and speed: 6 cm/second. As expected, the plasma diameter increases as laser output increases. The peak plasma temperature was 14,815 K for a laser output of 5 kW and 17,058 K for a laser output of 8 kW.

The superhigh temperature area is limited to the immediate vicinity of the plasma and heating of the wall surface proved not to be a problem. High-temperature gas and buffer gas are quickly mixed in the lower reaches of the plasma and the gas mixture is expected to reach the nozzle at a uniform speed and temperature.

Analyses which took axial flow and pressure gradient into consideration were also made. These results will be reported in the actual presentation.

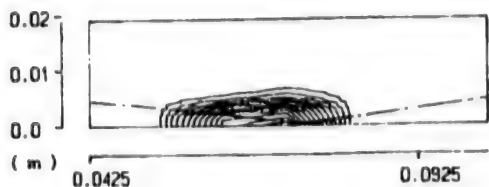


Figure 2. Temperature Field (5 kW)



Figure 3. Speed Field
(5 kW)

\nearrow 5
(m/s)
 \searrow 5

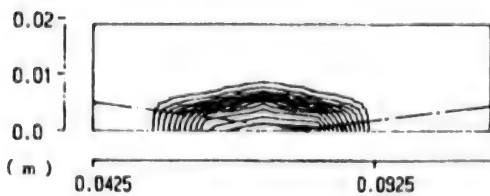


Figure 4. Temperature Field (8 kW)

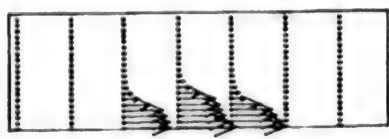


Figure 5. Speed Field (8 kW)

References

1. Jones, L.W. and Keefer, D.R., "NASA's Laser-Propulsion Project," ASTRONAUTICS & AERONAUTICS, Vol 17, 1979, pp 50-58.
2. Glumb, R.J., et al., AIAA-85-1553.

Supersonic Flaw-Detecting Method for Exfoliation Between H-II SRB Liner, Propellant

906C3836 Tokyo DAI33KAI UCHU KAGAKU GIJUTSU RENGO KOENKAI KOENSHU in Japanese
31 Oct-2 Nov 89 pp 782-783

[Article by Morio Shimizu and Katsuya Ito, Aerospace Engineering Research Institute; Yukio Fukushima, National Space Development Agency of Japan; and Takao Maniwa and Satoshi Hirano, Nissan Motor Co.]

[Text] 1. Introduction

The supersonic flaw-detecting method is widely used to detect exfoliation between the case and the liner of a solid rocket motor. The conventional form of this method, however, has not been effective for detecting exfoliation between the propellant and the liner, because of the extensive attenuation of the supersonic waves by the liner layer.

The Aerospace Engineering Research Institute, the National Space Development Agency of Japan, and Nissan Motor Co. have succeeded in detecting exfoliation between the liner and the propellant of the H-I upper-stage motor by adopting a frequency-continuous variable supersonic flaw detecting method and have put this exfoliation detecting method to practical use.

Based on these results, we performed a test to evaluate its detection ability using a test piece modeled on the H-II SRB. The results of this test demonstrated the effectiveness of this inspection technique and confirmed its suitability for practical use.

2. Detection Method

This detection method combines the techniques of multiple reflection and resonance. It uses the reflection of supersonic waves for an exfoliated surface and the resonance phenomenon for the liner layer. For the mechanical boundary conditions in the liner layer, the case side becomes the fixed end and the propellant side (the side which is exposed to air) becomes the free end in the case of exfoliation between the liner and propellant of a solid rocket motor. Therefore, resonance occurs when the thickness of the liner layer is an odd number times one-fourth of the wavelength. That is, exfoliation is detectable by setting the frequency so that an odd number times

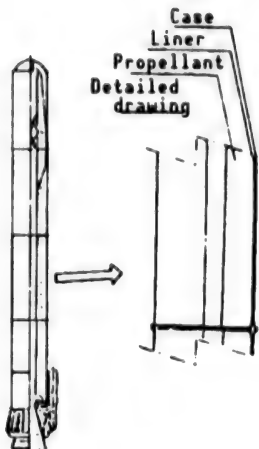


Figure 1. Concept of H-II SRB

one-fourth of the wavelength is equal to the thickness of the liner area and by checking for the presence or absence of a resonant sound.

3. Test Method and Sample

Figure 1 shows a rough diagram of the H-II SRB. The liner thickness and case thickness of the H-II SRB are greater than those of the H-I upper-stage motor. This causes a drop in resonance frequency and makes handling of high-order resonance difficult. For these reasons, the following improvement was tried:

- application of a supersonic probe at low frequency
(probe: 100 kHz)

The two kinds of testpieces shown in Figures 2 and 3 were used in the tests. These testpieces simulate the thickness of an actual motor and exfoliation between case and liner and between propellant and liner. Testpiece A is planar, while testpiece B has the curvature of an actual rocket motor. Tests were performed with supersonic waves in the low-frequency (50 kHz-100 kHz) range, followed by an evaluation as to whether or not exfoliation in the testpieces could be identified.

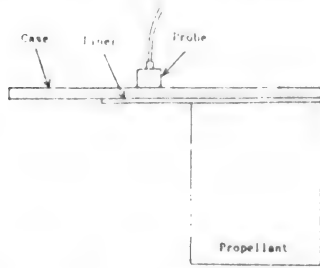


Figure 2. Testpiece A

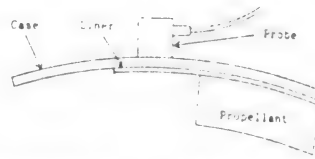


Figure 3. Testpiece B

4. Test Results

The tests confirmed that exfoliation could be identified in the testpiece corresponding to H-II SRB by the frequency-variable supersonic flaw detection method in the low-frequency area as shown in Table 1 and Figure 4.

(Probe: 100 kHz; frequency: 80 kHz)

Table 1. Test Results

Testpiece	Adhesion part	Exfoliated part	Testpiece thickness (Unit: mm)
A Plane	•	•	Case: 5 Liner: 2 Propellant: 150
B Curvature (r=900 mm)	•	•	Case: 4.7 Liner: 6 Propellant: 20

• Identification good; ▲: Identification difficult

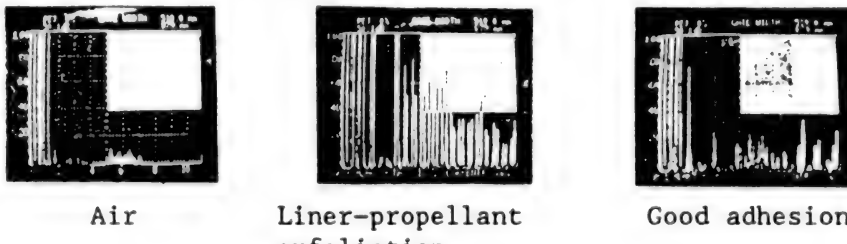


Figure 4. Test Results

5. Conclusion

The effectiveness of the frequency-variable supersonic flaw detection method in detecting exfoliation between the liner and propellant of the H-II SRB was confirmed. In order to apply this technique to an actual sample, repeatability, confirmation of optimum conditions, and enhancement of detection ability will be examined.

References

1. Shimizu, et al., 29th Space Science and Technology Conference, 1985, pp 348-349.
2. Ibid., 30th Space Science and Technology Conference, 1988, pp 492-493.

Combustion Thrust Characteristics of Airbreathing Solid Rocket Motor

906C3836 Tokyo DAI33KAI UCHU KAGAKU GIJUTSU RENGO KOENKAI KOENSHU in Japanese
31 Oct-2 Nov 89 pp 784-785

[Article by Akihiro Eguchi and Yutaka Kaneko, National Space Development Agency of Japan; and Yoichi Yamamoto and Tsuyoshi Mano, Nissan Motor Co.]

[Text] 1. Introduction

The airbreathing solid rocket motor (ASRM) is a propulsion system designed to increase thrust by burning a mixture of the exhaust gas from a solid motor and forced air. Such an engine is expected to have a large thrust and a high-density specific thrust, which are the strong points of a solid rocket, and at the same time to be able to attain high specific thrust. This paper reports the results of our investigation of the thrust characteristics of the ASRM and the combustion characteristics of the mixture of air and motor exhaust gas.

2. Outline of Experiment

In this experiment, combustion tests of an ASRM were performed and thrust data and secondary burner static-pressure data were acquired.

Figure 1 is an outline of the device. The experiment involved changes to the propellant, air to fuel ratio, and secondary burner shape. A conventional propellant, BP-201J (HTPB/AP/Al - 14/58/18), was used as the primary propellant, while the secondary combustion propellant was BP-X (HTPB/AP/A/Mg - 20/30/25/25). Air inflow is handled by the direct connection method and Mach 2 flight above the sea surface was simulated. Three kinds of secondary burners—conical, cylindrical and a hybrid configuration where a cylindrical part is located between two conical sections—were used. The slenderness ratio was 10. The thrust of the main motor was estimated from the combustion pressure and nozzle back pressure, and the secondary burner thrust was estimated from an integral of the static pressure distribution.

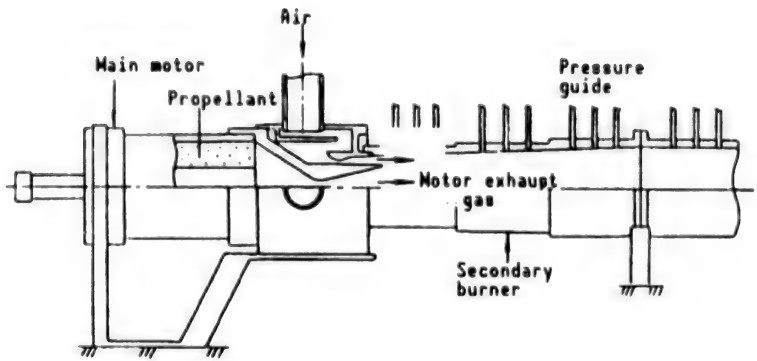


Figure 1. Outline of ASRM Experimental Device

3. Experiment Results

3.1 ASRM Specific Thrust Characteristics

Table 1 shows the specific thrust characteristics of the ASRM. In this table, theoretical values were derived from an analysis that assumed a quasi-one-dimensional flow and completion of mixed combustion in the secondary burner; values are obtained when flow chokes in the secondary burner.

Table 1. Specific Thrust Characteristics of ASRM

Secondary burner shape	Propellant	Air-to- fuel ratio	Experimental values of sea-surface specific thrust (sec)			Experimental values of sea- surface specific thrust for single motor ② (sec)	Theoretical values of sea- surface specific thrust of ASRM ③ (sec)	Increase rate of specific thrust ①, ②	Specific thrust efficiency ①, ③
			Main motor	Secondary burner	ASRM ①				
Conical type	BP - 201J	4.5	230	-53	177	218	-	0.81	
	BP - X	4.5	176	96	272	149	-	1.83	
Cylindrical type	BP - 201J	2	326	29	355	236	334	1.50	1.06
		4.5	319	36	355	218	447	1.63	0.79
	BP - X	2	279	37	316	156	315	2.03	1.00
		4.5	326	64	390*	149	612	2.62	0.61
Conical type with cylindri- cal part	BP - 201J	2	237	8	245	236	257	1.04	0.95
		4.5	230	79	309	218	313	1.42	0.99
	BP - X	2	168	69	237	156	245	1.52	0.97
		4.5	199	233	432	149	529	2.90	0.82

*Since the mixed gas flowed in the opposite direction from the air intake, considerable thrust loss is thought to have occurred.

In this experiment, an extremely high specific thrust, up to 432 seconds, was obtained. For a Mach 2 flight speed, a cylindrical secondary burner is desirable. When the air to fuel ratio is 2, the BP-201J propellant shows higher specific thrust, but when the ratio is 4.5, BP-X is more advantageous. BP-X poses no problems in terms of ignition characteristics and residuals, and is thought to be sufficiently promising for practical use.

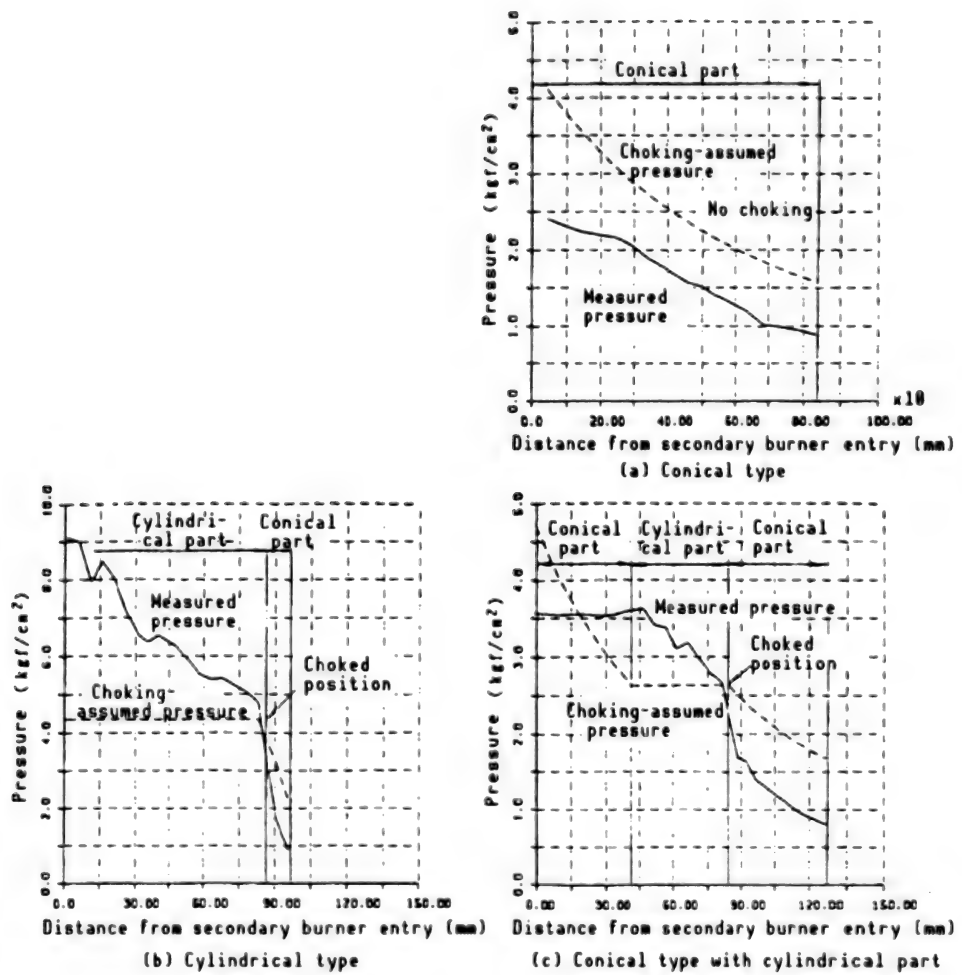


Figure 2. Static Pressure Distribution of Secondary Burner
(Propellant: BP-X, air-fuel ratio: 4.5)

3.2 Mixed Combustion Flow Characteristics in Secondary Burner

Figure 2 shows the static pressure distribution for each secondary burner shape. This figure also shows the static pressure distribution, which was calculated on the assumption that flow chokes at a section.

With the conical type, the flow is supersonic and does not choke. On the other hand, if a conical type has a cylindrical part, flow chokes at the back end of this part. In this case, the mixed combustion is thought to be terminated by the back end.

4. Conclusion

This study confirmed the usefulness of the ASRM. The next step will be to acquire engine design data using semifree jet devices.

Combustion of Carbohydrate, Nitrogen Oxide in Solid Rocket Fuel

906C3836 Tokyo DAI33KAI UCHU KAGAKU GIJUTSU RENGO KOENKAI KOENSHU in Japanese
31 Oct-2 Nov 89 pp 786-787

[Article by Ryoshi Moriyasu and Koichi Hayashi, Faculty of Engineering, Nagoya University; and M.C. Branch, Faculty of Engineering, University of Colorado]

[Text] 1. Introduction

Many solid rocket fuels (nitramines) consist of complex chemical compounds containing carbon, hydrogen, oxygen, and nitrogen. These become carbohydrate and nitrogen oxide after pyrolysis, and burn on the surface of the solid fuel. Therefore, these gaseous reaction products greatly influence the combustion speed of the solid fuel. However, the combustion speed and chemical reaction mechanism of the mixed gas of carbohydrate and nitrogen oxide have not been sufficiently analyzed.

Parker and Wolfhard¹ observed multilayer luminescence in carbohydrate/NO and carbohydrate/NO₂ flames. Similar patterns have been confirmed in the flames generated by pyrolysis of methyl nitrite, methyl nitrate, and ethyl nitrate. Nitrite fuels decompose into carbohydrate and NO, while nitrate fuels decompose into carbohydrate and NO₂. The multilayer characteristics of carbohydrate/NO_x, NO flames indicate that the reaction mechanism is clearly separated into several stages. The combustion speed of such flames can be obtained through numerical analysis. This paper investigates the reaction mechanism and compares the analytical and experimental results.

2. Controlling Equations

The equations which control stationary, constant-pressure, and quasi-one-dimensional planar propagation are as follows:

$$\dot{M} = \rho u A, \quad (1)$$

$$\dot{M} \frac{dT}{dx} - \frac{1}{c_p} \frac{d}{dx} \left(\lambda A \frac{dT}{dx} \right) + \frac{A}{c_p} \sum_{k=1}^K \rho Y_k V_k c_{pk} \frac{dT}{dx} + \frac{A}{c_p} \sum_{k=1}^K \omega_k h_k w_k = 0, \quad (2)$$

$$\dot{M} \frac{dY_k}{dx} + \frac{d}{dx} (\rho A Y_k V_k) - A \omega_k w_k = 0 \quad (k = 1, \dots, K), \quad (3)$$

$$\rho = \frac{P\bar{W}}{RT} \quad (4)$$

where, x: space coordinate;
M: mass flow quantity;
T: temperature;
 Y_k : mass proportion rate of kth kind;
p: pressure;
u: speed of mixed flow;
 ρ : density;
 W_k : Kth molecular mass;
 \bar{w} : average molecular mass;
R: gas constant;
 λ : heat conductivity of mixture;
 c_p : specific heat at constant pressure (mixture);
 h_k : enthalpy of k kind;
 V_k : diffusion speed of k kind;
 c_{pk} : specific heat of k kind at constant pressure;
A: sectional area of the tube which is surrounding the flame;
 ω_k : mol generation rate of k kind per unit volume by chemical reaction

Since evaluation of heat loss is generally difficult, the temperature obtained by an experiment is used as the initial condition. Therefore, what is calculated becomes only the transport equations of a kind. The program that was used is a general purpose flame calculation program (R.J. Kee, etc.³). Incidentally, 20 kinds of chemicals, 57 reaction formulas, and 210 diffusion coefficients were taken into consideration (case of CH₄/O₂/Ar flame).

3. Results

First of all, numerical simulation was performed on the experimental results obtained from the CH₄/O₂/Ar flame to verify the reaction mechanism of methane. Figure 1 shows the results. Since only the temperatures outside the flame were measured, the temperatures inside the flame were obtained by extrapolation. The experimental results agree well with calculated results for the concentration distribution of methane and oxygen. Reasonably good agreement is seen for carbon monoxide and hydrogen in the neighborhood of the burner exit, but the average values show great discrepancies, and no agreement is observed generally for carbon dioxide.

Figure 2 shows the experimental results for the CH₄/NO₂/O₂/Ar flame.² The structure of this flame is such that CH is generated from methane, NO from carbon dioxide, and CN and NH₂ are generated by competitive reactions CH+NO → N_A+CO and CH+NO → CN+OH. Therefore, this part can be said to be the key to verification. A numerical simulation is currently being performed on this flame.

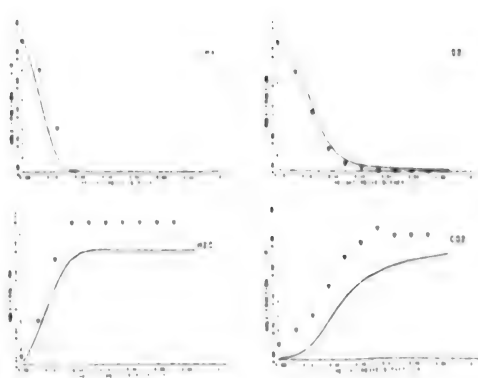


Figure 1. Calculation Results of
 $CH_4/O_2/Ar$ Flame
(∇ : experimental value)

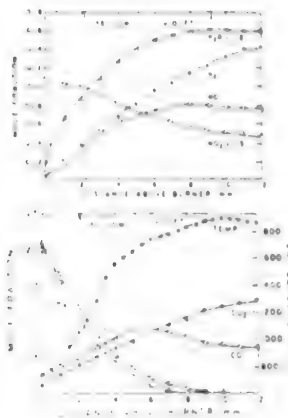


Figure 2. Experimental Results of
 $CH_4/NO_2/O_2/Ar$ Flame

References

1. Parker, W.G. and Wolfhard, H.G., "Some Characteristics of Flames Supported by NO and NO_2 ," 4th Sympo. (Int.) on Combustion Institute, Pittsburgh, 1953, pp 520-528.
2. Sadeqi, M.E., "Structure of Multiple Luminous Zones of Flames of Methane and Formaldehyde With Nitrogen Dioxide and Oxygen," Ph.D. Thesis, Department of Engineering, University of Colorado, 1987.
3. Kee, R.J., Gear, J.F., Smooke, M.D., and Miller, J.A., "A Fortran Program for Modeling Steady Laminar One-Dimensional Premixed Flame," Sandia National Laboratories, December 1985.

Combustion Characteristics of Metal-Added Hydrocarbon Rocket (III)

906C3836 Tokyo DAI33KAI UCHU KAGAKU GIJUTSU RENGO KOENKAI KOENSHU in Japanese
31 Oct-2 Nov 89 pp 788-789

[Article by Hiroshi Sakamoto, Kazuo Sato, Nobuyuki Yatsuyanagi, Fumie Ono, and
Hiroshi Tamura, Sumita Branch Office, Aviation Research Institute]

[Text] 1. Introduction

An earlier report¹ noted that the advantages of a metal-added hydrocarbon fuel include not only enhancement of specific thrust (I_{sp}) and increase of density specific thrust ($\rho_{av} \times I_{sp}$), but also the possibility of improving the combustion characteristics of the hydrocarbon fuel. A second report² showed the combustion stabilizing effect achieved by the addition of Al powder, but did not mention the improvement of combustion efficiency. This report experimentally examined the effect of adding Al powder with an injector for the purpose of enhancing combustion efficiency.

2. Combustion Experiment and Results

The burner used in the experiment is the one described in the previous reports.^{1,2} Two kinds of injectors (i-2, i-3), which differ from the one (i-1) described in the previous reports, were used in this experiment. The i-2 injector is a three-jet collision type (F-O-F), as is the i-1 injector, but it uses smaller particles and promotes initial mixing through a large collision angle and increased collision momentum. The i-3 injector is a gas-liquid coaxial type that uses gaseous oxygen (GO_2) in place of liquid oxygen (LO_2) to create smaller particles of the fuel containing Al powder. Figures 1 and 2 present detailed drawings together with the dimensions of the injectors. The added Al powder was changed from one with an average diameter of $3.9 \mu m$, which was used in the previous experiment to one with an average diameter of $1.9 \mu m$. The experiment conditions were as follows: $P_c \approx 4 \text{ MPa}$, mixing ratio (= oxygen flow rate/(BJ1J+Al) flow rate) $O/F = 1.7 - 4.1$, and Al addition rate = 3-17 percent; and GO_2 is gaseous oxygen at room temperature. The efficiency characteristic (efficiency C^*) was determined by giving heat loss correction to the measured C^* and comparing the obtained value with the theoretical C^* value (transfer-equilibrium theoretical value for LO_2 or GO_2 , RJ1-J, and Al addition rate). Figure 3 shows the efficiency C^* for the mixing rate of the i-2 injector when Al is added and when Al is not added. First, when Al is not

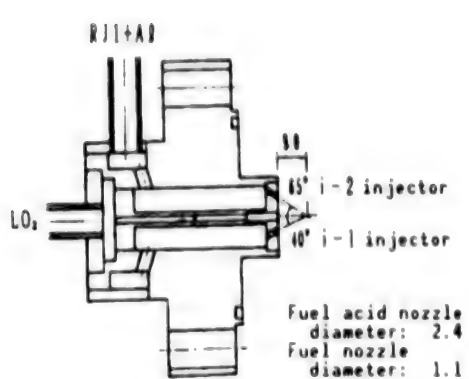


Figure 1. Details of i-1 and i-2 Injectors

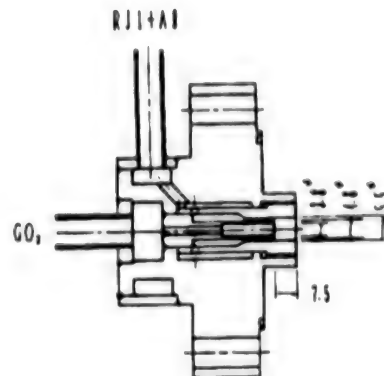


Figure 2. Details of i-3 Injector

added, enhancement of the efficiency C^* is noticeable for all mixing rates, as compared to the i-1 injector, which is of the same collision type as the i-2 injector (about +3 percent when $O/F = 2.5$) In addition, the stable combustion mixing range has been expanded. When Al is added, burning flaws occur on the injection surface. This is probably because the propellant bonds on the surface and because of the increase of collision momentum. This is not consistent with the purpose of Al addition. Since the collision injector that we have examined is generally inferior in terms of making minute particles to the gas-liquid coaxial injector, which uses gaseous propellant for the combustion of LO_2/H_2 , it is believed that combustion of the Al powder contained in the fuel drops is not completed. According to Wong,³ et al., the combustion mechanism for kerosene-group fuel slurry liquid drops containing Al powder is as follows: First, the kerosene evaporates and burns, then the Al particles in the liquid drops gather to form a lump, the lump is heated, and diffusion combustion of the Al vapor phase occurs. To cause the Al that is contained in liquid fuel drops to burn, therefore, the particle diameter of the fuel mist needs to be sufficiently small. For this reason, a gas-liquid coaxial injector (i-3) which uses GO_2 in place of LO_2 was selected. (GO_2 assumes reproduction cooling with LO_2 for injector cooling, but O_2 gas at room temperature was used in this experiment.) Figure 4 shows the efficiency C^* of the i-3 injector for the cases where Al is added and where Al is not added. Because of improvements in the minute particle making feature, a higher efficiency C^* (+2 percent when $O/F = 2.5$) was obtained as compared with the i-2 injector, in the range $O/F > 3.3$ when no Al was added. Furthermore, stable combustion occurred in all ranges covered in the experiment independently of whether Al was added or not. When Al was added, the efficiency C^* was improved in the range $O/F > 2.3$. In particular, a 100 percent efficiency C^* was obtained in the range $O/F > 2.7$.

The combined results of the experiments reported to date indicate that the combustion characteristics improve when Al-added hydrocarbon is used as the fuel. This is exemplified by the stabilization of combustion and enhancement of combustion efficiency that occurs with Al addition.

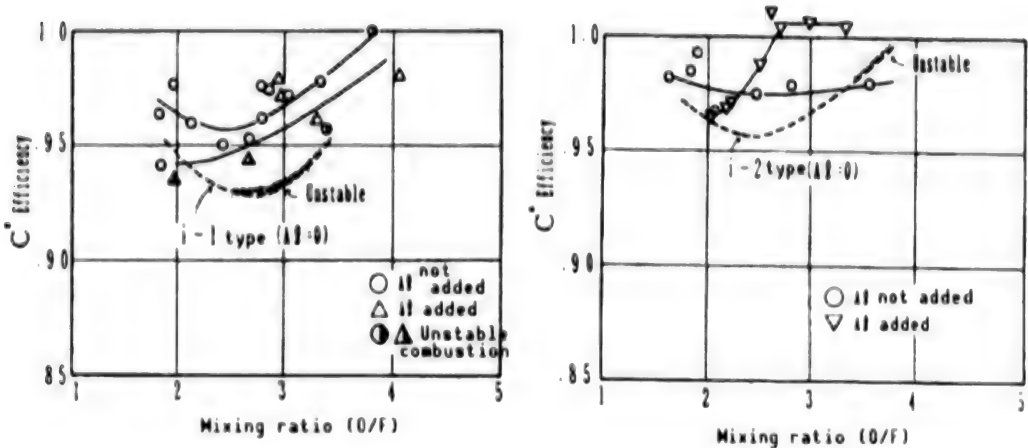


Figure 3. Combustion Performance of i-1 Injector Mixing Ratio

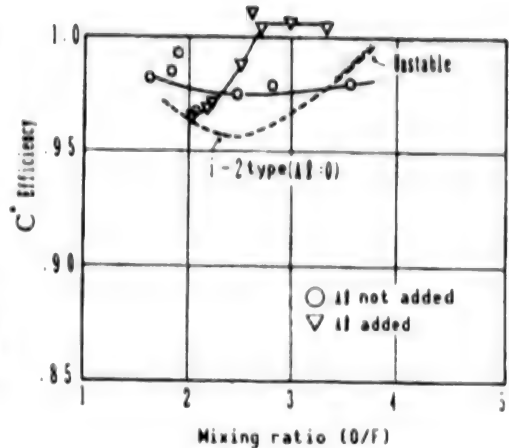


Figure 4. Combustion Performance of i-2 Burner for Mixing Ratio

References

1. Sakamoto, et al., 32KAI UCHU KAGAKU GIJUTSU RENGO KOENKAI KOENSHU, 1988, pp 16-17.
2. Ibid., NIPPON KOKU UCHU GAKKAI KITASHIBU 1989 KOENKAI MAEZURISHU, 1989, pp 36-37.
3. Wong, S.C., et al., COMBUSTION SCIENCE AND TECHNOLOGY, Vol 52, 1987, pp 221-242.

Development of Gas Jet Device for H-II Rocket

906C3836 Tokyo DAI33KAI UCHU KAGAKU GIJUTSU RENGO KOENKAI KOENSHU in Japanese
31 Oct-2 Nov 89 pp 790-791

[Article by Akira Takano and Hideyuki Kobayashi, National Space Development Agency of Japan; and Masata Mako, Hirokazu Kobayashi, Akinori Shimizu, and Katsuki Tachio, Ishikawajima-Harima Heavy Industries Co., Ltd.]

[Text] 1. Introduction

A new gas jet device (H-II RCS) is to be used on the second stage of the H-II rocket, which is scheduled to be launched in 1993 and after. Authorization tests of the component parts for the H-II RES have been almost completed, the detailed design of the entire system has been finished, and a sample device (PM) for authorization testing is now being manufactured. This paper reports on the technical results.

2. Features and Characteristics of H-II RCS

The H-II RCS is a hydrazine single-liquid thruster, as is the H-I rocket second-stage gas jet device (H-I RCS). It is also an adjustable pressure device (Table 1).

The H-II RCS differs from the H-I RCS in three important respects:

- (1) All the principal components are of Japanese manufacture.
- (2) As the H-II rocket is larger, the thrust has been increased.
- (3) It is possible to add thrusters and to increase the total thrust to cope with multiple satellite launches.

3. Overall Structure Design

Since the weight increase that accompanies the increase in the quantity of propellant is greater for the box-type frame structure (Figure 1), a structure consisting of supporting panels reinforced by ribs with supporting rods (Figure 2) has been adopted for the H-II RCS.

Table 1. Principal Features of H-II RCS

Item	Basic mission	Expanded mission (maximum)	H-I RCS (reference)
1. Type	Module type (axes I and III one each)	No change	Module type (axes II and IV one each)
2. Propellant	Hydrazine (N_2H_4)	No change	No change
3. Dry weight	45.0kg or less (both modules)	TBD kg or less (both modules)	42.7 kg (both modules)
4. Total thrust	9,583 kgf·sec or more	14,000 kgf· second or more	10,732 kgf·second or more
5. Thrust	18N thruster x 2 50N thruster x 8	18N thruster x 2 50N thruster x 18	18N thruster x 12
6. Propellant supply system	Pressurizing gas adjusting system	No change	No change
7. Specific thrust (Isp)	18N thruster and continuous mode 210 seconds or more 50N thruster continuous mode 215 seconds or more Pulse mode* 180 seconds or more	No change	18N thruster continuous mode 210 seconds or more Pulse mode** 180 seconds or more
8. Quantity of propellant	50.02 kg	70.94 kg	53.42 kg

*0.1 second-ON/4.0-period pulse mode

**0.1 second-ON/1.0-period pulse mode

Table 2. Characteristic Frequency

Axis	Required value	Analytic value
X		112 Hz
Y	64 Hz or more	87 Hz
Z		77 Hz

Table 3. Experimental Conditions for H-II RCS

Item	Experimental conditions		
Constant acceleration	Machine axis: 9.1 GMAX Horizontal axis: 2.8 G -3.5 MIN		
Sine wave vibration	(1) Machine axis direction Frequency (Hz) Level Sweep level (G ₀ -P) (oct/min) 5-15: 1.5: 2 15-21: 3.5: 2 21-100: 1.0: 2 (2) Radial and tangential directions 5-15: 1.0: 2 15-20: 1.4: 2 20-100: 1.0: 2		
Random vibration	Frequency (Hz)	Level	
	20-220:	5 dB/oct	
	220-450:	0.5G ² /Hz	
	450-2000:	-6 dB/oct	
	Grms(reference):	18.3	
	Duration:	120 sec	
Impact	Frequency (Hz)	Level	
	50-2600:	6 dB/oct	
	2600-10000:	1250 G ₀ -P	
Sound	Octave band central frequency (Hz)	Sound pressure level (dB)	
	31.5	131	
	63	142	
	125	144	
	250	145	
	500	143	
	1000	137	
	2000	129	
	4000	124.5	
	8000	121	
	OASPL	150.5	
	Duration: 120 sec		

For this structure, the first-order characteristic frequency was obtained from the structure model and was found to satisfy the rigidity requirement (Table 2). Furthermore, it was determined that the H-II RCS satisfies the strength requirements. This determination was made on the basis of a stress analysis performed by obtaining dynamic load from the given environment (Table 3) and forecasting response magnification and characteristic frequency.

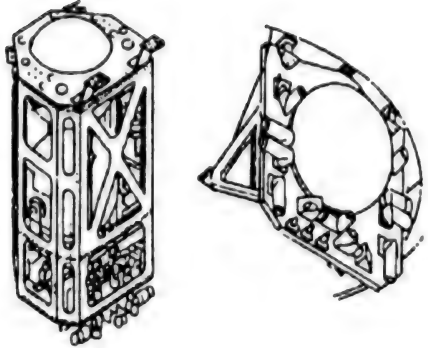


Figure 1. Outline of H-I RCS

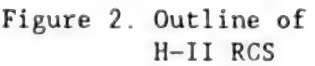


Figure 2. Outline of H-II RCS

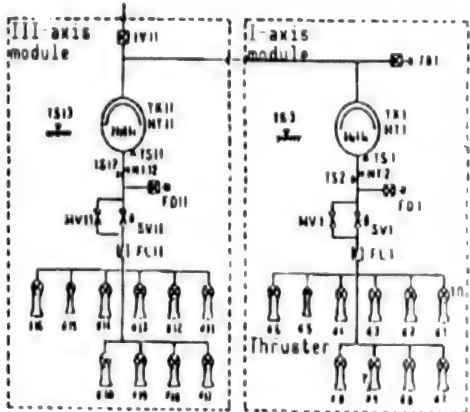


Figure 3. Piping System of H-II RCS

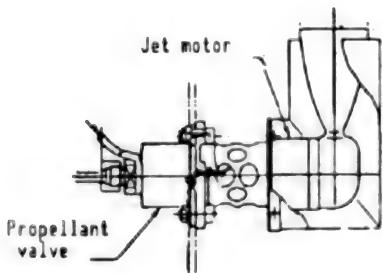


Figure 4. Outline of 50N Thruster

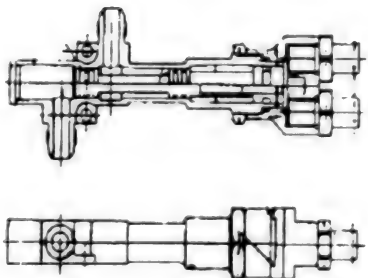


Figure 5. Structure of Pilo Valve

Before manufacturing the PM, a series of preliminary vibration tests were performed. These tests indicated that the structure satisfies the rigidity requirements and poses no problem in terms of its own strength. However, the response level at the end of the panel is high for random vibration in the Y-axis direction and the allowable vibration levels of some components were found to be unsatisfactory. At present, a review of the structural design of the panel is under way.

4. Development of Components

Figure 3 shows the piping system of the H-II RCS. The principal components of the H-II RCS developed in this country are outlined below:

(1) Propellant tank

This tank is made of titanium alloy (Ti-6Al-4V), as is that of the H-I RCS, but super plastic forming (SPF) has been adopted as the manufacturing method. The advantage of SPF is that processing costs can be sharply reduced, while almost the equivalent mechanical strength can be obtained.

(2) 50N thruster

The thruster consists of a jet motor and a propellant valve (Figure 4) and is designed on the basis of the H-I RCS 18N thruster. The friction resistance for the core part of the propellant has been reduced by changing the plunger shape to enhance durability.

(3) Pilo valve

A pilo valve has been adopted as the cut-off valve to reduce the weight and cost of the conventional electromagnetic valve. As shown in Figure 5, this valve has a complex shape inside the body, which makes it difficult to finish the processed surfaces and to clean it. Therefore, the possibility of contamination posed a problem in the development process, but several improvements resolved the problem.

(4) Filter

Development of the filter was completed without any special technical difficulties.

(5) Others

Other important development products include hydrazine anhydride and catalysts, but these will be reported in a separate paper.

5. Conclusion

The H-II RCS is being developed with Ishikawajima-Harima Heavy Industries Co., Ltd., as the principal developer, but the following companies have also made important contributions to composite material development. The authors would like collectively to thank the following companies: Nichiyu Technical Industry Co. (pilo valve); Koito Manufacturing Co. (filter); Shimadzu Corp. (propellant valve); and N.E. Chemcatt, Inc. (catalyzer).

Development of Hydrazine Decomposition Catalyzer for Gas Jet Thruster

906C3836 Tokyo DAI33KAI UCHU KAGAKU GIJUTSU RENGO KOENKAI KOENSHU in
Japanese 31 Oct-2 Nov 89 pp 792-793

[Article by Akira Takano and Hideyuki Kobayashi, National Space Development Agency of Japan, Takashi Sakuratani, Kenji Toyota, Hiroo Ayabe, and Jiro Ueno, Ishikawajima-Harima Heavy Industries Co., Ltd.; and Isamu Toyoshima, Hokkaido University]

[Text] 1. Introduction

Since FY 1985 the National Space Development Agency of Japan had been promoting the development of a hydrazine decomposition catalyzer, a common part, that could be used in the H-II rocket gas jet device. This catalyzer passed its authorization test in November 1989 and is scheduled to complete the development process. This paper reports on the results of the development effort.

2. Required Elements for Catalyzer Development

The hydrazine decomposition catalyzer is filled in the gas jet thruster, decomposes the propellant (hydrazine) by catalytic action, and creates a high-temperature jet gas consisting of NH₃, N₂, and H₂. This catalyzer requires a number of characteristics that differ from those of catalysts used in ordinary chemical processes. These include high reactivity, usability in reactions that accompany high-volume changes from liquid phases to gaseous phases, durability for a wide variety of operations ranging from the pulse thruster jet mode in a cool state to the continuous jet mode in a warm state.

As the common parts for space development, catalysts are being developed to meet specific requirements on the basis of common specifications (NASDA-QTS-1047). The main requirement is durability, with 10,000 or more pulse jets (injection pressure: 20 kg/cm²a; on-time: 0.1 second; period 1 second) and a continuous jet of 10³ seconds or more using a 50N-level jet test jig. This is needed because of the mission duty cycle requirement for the H-II rocket's 18N and 50N thrusters.

3. Physical Properties

The catalyster is structured so that a 14-18 or 25-30 mesh alumina carrier distributively carries a catalyster metal. Figure 1 [not reproduced] is a photograph of the catalyster and Table 1 lists its principal physical properties.

Table 1. Principal Features of Catalyster

Carrier	Active alumina
Carrier metal	Ir or Ir alloy
Bulk density	1g/ml or more
Ir content	28 wt% or more
Specific surface area	60 m ² /g or more
Compressive strength	80 percent or more
Coefficient of thermal contraction	3.0 volume percent or less

Incidentally, a high-strength structure has been adopted for catalysters to reduce cracking deterioration and to protect against explosive hydrazine decomposition during cold start.

Alumina hydrate is the most suitable raw material for the carrier in terms of catalyster life. The variety selected is from commercial alumina hydrate that has been separated from the alkali side. A carrier of the prescribed grain size is fabricated by cracking this raw carrier material and forming spherical grains.

4. Evaluation of Performance

As of August, catalyster development was in the preparatory stages for detailed design examination in parallel with the development of the 50N thruster for the H-II rocket and is scheduled to enter the development confirmation test stage beginning in September. Therefore, this paper is unable to report on its performance, including limit life test results, but we can report that a 20N-level thruster whose performance drop is small to about 90,000 pulses has been obtained with a test manufactured catalyster that was used for testing in the developmental stages. Figure 2 shows the jig (50NFT thruster) used for catalyster evaluation in parallel with an actual 50N thruster in a development confirmation test.

5. Conclusion

In the development of this catalyster, the cooperation of N.E. Chemcatt, Ltd. (formerly Japan Engelhardt, Ltd.) was indispensable. The authors thank this company.

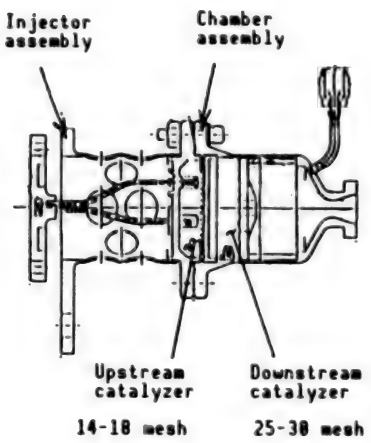


Figure 2. 50N FT Thruster

Development of Anilineless Hydrazine Anhydride for Gas Jet Thruster

906C3836 Tokyo DAI33KAI UCHU KAGAKU GIJUTSU RENGO KOENKAI KOENSHU in Japanese
31 Oct-2 Nov 89 pp 794-795

[Article by Akira Takano and Hideyuki Kobayashi, National Space Development Agency of Japan; Takashi Sakuratani, Atsushi Hasegawa, and Kuniyoshi Miura, Ishikawajima-Harima Heavy Industries Co., Ltd.; and Takafumi Masuda, Masaaki Okudaira, and Hiromi Hirata, Masuda Chemical Industry Co.]

[Text] 1. Introduction

Since 1984 Ishikawajima-Harima Heavy Industries Co., Ltd., has been the prime contractor for the National Space Development Agency of Japan in the development of monopropellant-grade hydrazine anhydride for use in the H-II rocket gas jet device. A manufacturing plant was constructed in FY 1988 and development was completed in June 1989. This paper reports on the results of the development effort.

2. Manufacturing Method

There are various methods for manufacturing hydrazine anhydride from industrial-use hydrazine (water-containing hydrazine). These include: 1) heating and distilling a mixture of water-containing hydrazine and caustic soda; 2) distilling an azeotropic mixture of water-containing hydrazine and aniline; and 3) steam-dehydrating water-containing hydrazine. Since the imported products that have been used to date were manufactured by the second method, they contain about 0.5 percent or less aniline. Since this aniline becomes a catalyst poison for the gas jet thruster, the use of these imported catalysts is not desirable especially for low-powered thrusters.

The new domestically developed hydrazine anhydride manufacturing method refines water-containing hydrazine of about 64 percent purity by dehydrating it with caustic soda and is characterized by use of toluene as the carrier in the reaction system. Incidentally, the toluene also serves to prevent explosions by diluting the hydrazine gas in the reaction system.

In the reaction vessel, the toluene and the hydrazine anhydride first evaporate. The vapor mixture is cooled and liquefied in the condenser and it is further separated into toluene and 94 percent hydrazine anhydride by using

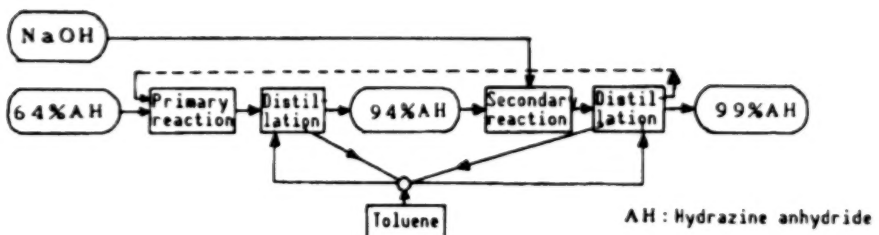


Figure 1. Manufacturing Process Flow of Hydrazine Anhydride

the difference in their specific gravities. Hydrazine anhydride that 98.5 percent pure is obtained as the final product by repeating this process. Figure 1 shows the flow of the manufacturing process.

The hydrazine manufacturing equipment has been installed in Ishikawajima-Harima Heavy Industries Co., Ltd.'s Aioi Factory. This equipment is capable of manufacturing about 400 kg of hydrazine anhydride per month.

3. Quality of Product

Table 1 shows the product standard for hydrazine anhydride and sample results of the test manufacture.

Table 1. Hydrazine Anhydride Component Standard and Example of Results of Trial Manufactured Hydrazine Anhydride

Component	Unit	Prescribed value	Value of trial manufactured hydrazine anhydride
Hydrazine (N_2H_4)	wt%	98.5 MIN	98.9
Moisture (H_2O)	wt%	1.0 MAX	0.8
Particle	mg/l	1 MAX	0.3
Chloride (Cl^-)	wt%	0.0005 MAX	0.0001
Toluene ($C_6H_5CH_3$)	wt%	0.50 MAX	0.3
Iron (Fe)	wt%	0.002 MAX	0.0002
Nonvolatile remaining substance NVR	wt%	0.005 MAX	<0.005
Carbon dioxide (CO_2)	wt%	0.02 MAX	0.001
Other volatile carbon-containing substances	wt%	0.02 MAX	0.003
Sodium (Na^+)	wt%	0.01 MAX	0.0010
External appearance	—	Colorless, transparent	Same as left

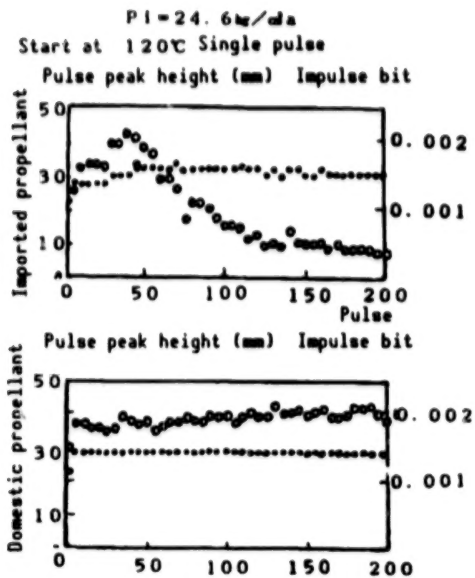


Figure 2. Occurrence of Aniline Poisoning for Different Propellants

The standard (JEQ1B-015) corresponds to the monopropellant grade of MIL-P-26536C Amendment 1 and the difference between these products is that the domestic product contains toluene in place of aniline.

4. Performance

The domestically produced hydrazine was used in development tests of the gas jet thrusters and the ETS-VI apogee engine. These tests confirmed that its performance is equivalent to that of the imported products. Furthermore, its use in jet tests with a 1N thruster confirmed that it does not show any deterioration in performance similar to that caused by the aniline poisoning of imported products (Figure 2).

5. Conclusion

The authors succeeded in the development of a domestically produced hydrazine anhydride, and its toluene content can be removed with comparative ease. Hereafter, therefore, the authors want to explore the manufacture of high-quality hydrazine equivalent to the highly pure hydrazine used for satellites.

- END -

END OF

FICHE

DATE FILMED

5 April 1991